Aspects of gas-phase anion spectroscopy

Marcus Kettner

Aspects of gas-phase anion spectroscopy

Construction of a VMI spectrometer and theoretical studies of carbonyl oxides

Marcus Kettner

This thesis is presented for the degree of Doctor of Philosophy of Chemistry
of The University of Western Australia

> A central lesson of science is that to understand complex issues (or even simple ones), we must try to free our minds of dogma and to guarantee the freedom to publish, to contradict, and to experiment. Arguments from authority are unacceptable.
>
> (Carl Sagan)

Kettner, Marcus
Aspects of gas-phase anion spectroscopy
PhD Thesis, School of Chemistry and Biochemistry
University of Western Australia, September 2015

Abstract

This thesis describes a combined experimental and theoretical approach towards anion spectroscopy.

Motivated by the rich chemistry occurring in the Earth's atmosphere, the first part of thesis describes the design, construction and implementation of an improved anion photoelectron spectrometer based on the velocity map imaging (VMI) principle. This instrument was attached to an existing time-of-flight mass spectrometer and conventional anion photoelectron spectrometer. When coupled with a tunable laser, the new spectrometer will allow for high-resolution studies similar to the slow-electron velocity map imaging (SEVI) experiments described by Neumark and co-workers. The spectrometer has been constructed, and preliminary tests have been undertaken.

Complementary to the instrument development, a theoretical methodology for the prediction of electron affinities and photoelectron spectra based on the W3-F12 protocol published by Karton and Martin was established. The methodology is applied to methanal-oxide, *cis*-ethanal-oxide and *trans*-ethanal-oxide yielding electron affinities of 0.57 eV, 0.18 eV and 0.34 eV, respectively. For all of these molecules as well as their anions, total atomisation energies, harmonic frequencies and heats of formation (at 0 K and 298 K) were calculated alongside.

Finally, a relatively inexpensive computational analysis of the anharmonic frequencies and intensities for methanal-oxide resulting from vibrational second-order perturbation theory (VPT2) CCSD(T) calculations with different basis sets were compared against experimental IR data as well as high-level vibrational configuration interaction (VCI) calculations. Surprisingly, the VPT2 calculations are on a par with computationally more expensive vibrational configuration interaction (VCI) calculations and hence the first simulation of a high-level IR spectrum of *cis*-ethanal-oxide is presented.

Table of Contents

Acknowledgements

I would like to express first and most profound gratitude to my principal supervisor and friend **Duncan Wild**. It was inspiring to see him handle lasers optics, high vacuum equipment and hugely complicated electronic components with such ease. Always leaving a solder trail behind, he managed to keep his group motivated with the aid of his wide scientific knowledge and delightfully Australian sense of humour.

I would also like to express my great appreciation to **Allan McKinley** who was the most valued support I could rely on when things would not work out the way they should have; to **Dylan Jayatilaka** without whom I would not know half of the theoretical chemistry, who was always there to answer the silliest questions and argue about crazy theories over exquisite selections of craft beer; and to **Amir Karton**, a well-respected, most ambitious mind – teeming with ideas who was generously patient with all of my detailed enquiries on thermochemical protocols.

I am particularly grateful for the hospitality I received from *Henrik Kjærgaard*, *Kasper Mackeprang*, *Rasmus Farber* and the rest of the Kjærgaard group during my time in København. I would like to acknowledge *Kim Lapere*, my PhD buddy as well as the rest of the Wild group: *Stephen*, *Richard*, *Duncan* as well as *Peter* and thank them for all the productive discussions and exciting times we had. Furthermore, assistance provided by *Graham Chandler* and *Mark Spackman* was also greatly appreciated.

I must thank the mechanical workshop crew – specifically *Nigel* and *Damien* who helped constructing so many of the components needed for our Lab; my early mentors *Alex Gentleman* who shared his knowledge about Franck–Condon simulations and my Diplom supervisor *Alex Auer* who helped out with CFOUR related questions. I wish to acknowledge the C++ support provided by *Michael Turner* as well as *Jim Williams* for lending us the Fluxmeter. The *School of Chemistry and Biochemistry* and the *Faculty of Science* are acknowledged for generous funding which allowed for the construction of the VMI spectrometer described in this thesis. I would also like to thank the *the University of Western Australia* and the *School of Chemistry and Biochemistry* for enabling this PhD project.

Finally, I wish to thank my parents, my partner *Sarah* as well as my friends *Richard, Julia, Owen, Ellen, Sandy* and the rest of the Uni / Fremantle crew from the bottom of my heart for their support and encouragement throughout my study.

Publications

The following publications were produced from the work presented in this thesis.

M. Kettner, A. Karton, A. McKinley, and D. Wild. The CH_3CHOO "Criegee intermediate" and its anion: Isomers, infrared spectra, and W3-F12 energetics. *Chemical Physics Letters*, **621**: 193 – 198, 2015. DOI: `10.1016/j.cplett.2014.12.037`

A. Karton, M. Kettner, and D. A. Wild. Sneaking up on the Criegee intermediate from below: Predicted photoelectron spectrum of the CH_2OO^- anion and W3-F12 electron affinity of CH_2OO. *Chemical Physics Letters*, **585**: 15 – 20, 2013. DOI: `10.1016/j.cplett.2013.08.075`

The following publication was also produced during the period of PhD candidature.

D. Beckham, S. Conran, K. Lapere, M. Kettner, A. McKinley, and D. Wild. Anion photoelectron spectroscopy and high level ab initio calculations of the halide-acetylene dimer complexes. *Chemical Physics Letters*, **619**: 241 – 246, 2015. DOI: `10.1016/j.cplett.2014.11.058`

K. M. Lapere, R. J. LaMacchia, L. H. Quak, M. Kettner, S. G. Dale, A. J. McKinley, and D. A. Wild. Anion Photoelectron Spectra and Ab Initio Calculations of the Iodide–Carbon Monoxide Clusters: $I^-\ldots(CO)_n$, $n = 1\text{-}4$. *The Journal of Physical Chemistry A*, **116**: 3577 – 3584, 2012. DOI: `10.1021/jp300471x`

K. M. Lapere, R. J. LaMacchia, L. H. Quak, M. Kettner, S. G. Dale, A. J. McKinley, and D. A. Wild. The Bromide–Carbon Monoxide Gas Phase Complex: Anion Photoelectron Spectroscopy and Ab Initio Calculations. *Australian Journal of Chemistry*, **65**: 457 – 463, 2012. DOI: `10.1071/CH12007`

M. Kettner, W. B. Schneider, and A. A. Auer. Computational Study of Pt/Co Core–Shell Nanoparticles: Segregation, Adsorbates and Catalyst Activity. *The Journal of Physical Chemistry C*, **116**: 15432 – 15438, 2012. DOI: `10.1021/jp303773y`

Chapter 1

Introduction

With the invention of quantum mechanics we opened a new box of 'possibilities' describing electronic and atomic behaviour which would otherwise be beyond our reach. We developed methods and approximations to deal with the chaotic nature arising from its assumptions, which can be employed to describe chemical processes. Whilst methods such as the Hartree–Fock theory, density functional theory or coupled cluster theory each have their place, we need constant feedback from experimentation and especially experiments on systems where our predictions disagree allowing for a constant improvement of these methods. Motivated by processes occurring in our atmosphere, it is the area of small molecule gas-phase spectroscopy where theory and experiment are closer than in any other of the chemical sciences – where errors of experiment are as small as those predicted by theory.

Our atmosphere is a vast dynamic system of chemical reactions delicately balanced, and hugely interdependent. Predictions of how we influence this system can only be made once we understand fundamental interactions, not only between different atoms and molecules but also the effects of radiation and temperatures. It is then, that these chemical reactions are profoundly influenced by the comparatively weak interactions and the very nature of the electronic structure of their constituents. For example, the carbonyl oxide class of molecules which occur as intermediates in tropospheric ozonolysis reactions play an important role as an oxidant in our atmosphere.[1] The human-induced warming of Earth's biosphere causes a larger emission of their source compounds which ultimately yields a higher concentration of carbonyl oxides and therefore causes a disruption to the balanced equilibrium state that is our atmosphere.[2]

Smaller varieties of this class of molecules can be investigated with high accuracy and precision, both theoretically and experimentally. The present PhD project is aimed at creating a foundation for the exploration of such types of unstable molecules or weakly bound complexes by means of high-resolution anion spectroscopy and high-level quantum mechanical calculations. For this an anion velocity map imaging (VMI) spectrometer is designed and constructed, as an attachment to an already existing time-of-flight mass spectrometer.[3] Similar to an anion photoelectron spectrometer, this device allows precise investigation of vibronic transitions and therefore provides insight into nuclear and electronic structure for selected atmospherically and otherwise relevant molecules.

Complementary to the experimental studies, a theoretical methodology based on the W3-F12 protocol will be developed allowing for the prediction of the resulting VMI spectra.[4] This cross-link between experiment and theory will hopefully improve atmospheric models and, since this is rather fundamental

---

[1] R. Criegee. *Angew. Chem., Int. Ed. Engl.*, **14**: 745 – 752, 1975.

[2] A. Arneth et al. *Nat. Geosci.*, **3**: 525 – 532, 2010.

[3] A. T. J. B. Eppink and D. H. Parker. *Rev. Sci. Instrum.*, **68**: 3477 – 3484, 1997.

[4] A. Karton and J. M. L. Martin. *J. Chem. Phys.*, **136**: 124114, 2012.

research, also contribute some far reaching insights into electronic binding behaviour. A special focus is devoted to the theoretical exploration of methanal and ethanal oxide, since they have been characterised experimentally for the first time only recently.[5]

The means by which the connection between the experimental world of anion photoelectron spectroscopy and the theoretical realm of the wave function are connected is through the Born–Oppenheimer approximation, which enables a separation of electronic, vibrational and rotational wave functions introducing the concept of a potential energy surface. In anion photoelectron spectroscopy, a negatively charged particle undergoes laser excitation, thereby losing an electron, transitioning from the anionic to a neutral potential energy surface. The energy of the remaining electron then contains the information into which state of the neutral descended. This kind of spectroscopy can therefore be understood as tool to probe such a neutral surface which in turn can be modelled by theoretical means and consequently compared to the natural world.

During this project theoretical and experimental techniques are employed spanning a large variety of different expertise. A brief review on the details behind theoretical methodologies and experimental techniques is therefore presented in Chapter 2. The process of designing and constructing the VMI spectrometer is described in Chapter 3. Finally, the work undertaken towards determining the electron affinities and vibrational transitions which serve as a precedent case for future spectrum simulations are provided in Chapter 4.

---

[5] Y.-T. Su et al. *Science*, **340**: 174 – 176, 2013.

Chapter 2

Theoretical foundations

2.1 Electronic structure methods

2.1.1 Basics

The electronic problem

Basic quantum theory provides an approach to calculate the behaviour of a system by solving the many-body Schrödinger equation. The non-relativistic time independent expression of this equation can be written as:

$$\hat{H}\,|\Psi\rangle = E\,|\Psi\rangle \tag{2.1}$$

The many-body wave function Ψ depends on the electronic spin and spatial coordinates (σ and $\boldsymbol{r}$, respectively), as well as on the coordinates of the nuclei $\boldsymbol{R}$. E represents the total energy of the system. In its non-relativistic form, the Hamiltonian $\hat{H}$ contains terms for the kinetic and potential energy of both electrons and nuclei. Using atomic units (see Appendix A.1.1), the Hamiltonian can be written as follows:

$$\hat{H} = \underbrace{\sum_{i=1}^{N}\sum_{i>j}^{N}\frac{1}{r_{ij}} \overbrace{-\sum_{i=1}^{N}\frac{1}{2}\nabla_i^2 - \sum_{i=1}^{N}\sum_{A=1}^{M}\frac{Z_A}{r_{iA}}}^{\sum_{i=1}^{N}\hat{h}_i}}_{\hat{H}_{\mathrm{el}}} + \sum_{A=1}^{M}\sum_{B>A}^{M}\frac{Z_A Z_B}{R_{AB}} - \sum_{A=1}^{M}\frac{m_A}{2}\nabla_A^2 \tag{2.2}$$

Electrons are denoted as i, j and the nuclei are labelled through A, B (N and M refer to the number of electrons and nuclei, respectively); r_{ij}, r_{iA} and R_{AB} are the distances between electrons, electrons and nuclei and nuclei, respectively; $\frac{m_A}{m_e}$ refers to the mass ratio of nucleus A to an electron and Z_A denotes its proton count.

Born–Oppenheimer approximation

Due to the large mass difference between nuclei and electrons ($\frac{m_A}{m_e} \gg 1$), the electrons move much faster than the nuclei. Therefore, as an approximation, the electrons can be considered to be moving through a field generated by fixed nuclei. This is called the Born–Oppenheimer approximation (BOA).[6] Due to this approximation, the kinetic energy of the nuclei, in Equation (2.2), can be neglected (for an electronic case), while the repulsion between the nuclei can be considered a constant. This enables a separate treatment of an electronic wave function ψ_{el}:

$$\hat{H}_{\mathrm{el}} \left|\psi_{\mathrm{el}}\right\rangle = E_{\mathrm{el}} \left|\psi_{\mathrm{el}}\right\rangle \tag{2.3}$$

The electronic wave function ψ_{el} explicitly depends on the electronic coordinates $\boldsymbol{r}$ and parametrically on the nuclear coordinates $\boldsymbol{R}$. This is often denoted as $\psi_{\mathrm{el}}(\boldsymbol{r};\boldsymbol{R})$. Hence, the Hamiltonian for the nuclear motion $\hat{H}_{\mathrm{nuc}}$ can be approximated as motion through an average field generated by the electrons.

$$\hat{H}_{\mathrm{nuc}} = -\sum_{A=1}^{M} \frac{m_A}{2} \nabla_A^2 + \underbrace{E_{\mathrm{el}}(\boldsymbol{R}) + \sum_{A=1}^{M} \sum_{B>A}^{M} \frac{Z_A Z_B}{R_{AB}}}_{E_{\mathrm{pot}}(\boldsymbol{R})} \tag{2.4}$$

$E_{\mathrm{pot}}(\boldsymbol{R})$ constitutes a potential of nuclear motion and is often referred to as the Born–Oppenheimer potential energy surface (BO-PES)[•] which is the result of the electronic structure of the system. To account for the translational, vibrational, and rotational energy of a given system (included in E_{tot}), the nuclear Schrödinger equation has to be solved.

$$\hat{H}_{\mathrm{nuc}} \left|\psi_{\mathrm{nuc}}\right\rangle = E_{\mathrm{tot}} \left|\psi_{\mathrm{nuc}}\right\rangle \tag{2.5}$$

Within the BOA, the corresponding total wave function is therefore a product:

$$\Psi(\boldsymbol{r};\boldsymbol{R}) = \psi_{\mathrm{el}}(\boldsymbol{r};\boldsymbol{R})\,\psi_{\mathrm{nuc}}(\boldsymbol{R}) \tag{2.6}$$

As a fundamental approximation, the BOA is central to all well established electronic structure determination methods and forms the foundation of our understanding of general chemistry. Its shortcomings are for example present in high-resolution spectroscopy where it manifests itself through rovibronic coupling, i.e. coupling between the electronic and vibrational and rotational motions. Other non-adiabatic approximations that can correct for some of the errors such as the Born–Huang approx-

---

[6] M. Born and R. Oppenheimer. *Ann. Phys.*, **389**: 457 – 484, 1927.

[•] The BO-PES is often only referred to as potential energy surface. However, since this can cause confusion between the also discussed photoelectron spectroscopy, it will be denoted as BO-PES.

imation or the diagonal Born–Oppenheimer correction are available.[7,8] However, these methods will not be discussed in the present work.

Antisymmetry postulate

As described in Section 2.1.1, the electronic Hamiltonian only depends on the coordinates $\boldsymbol{r}$ to describe electrons. However, a complete description of this particle also features a *spin* coordinate, $\alpha\,(\omega)$ for spin up and $\beta\,(\omega)$ for spin down. Both functions are orthonormal with respect to each other:

$$\begin{aligned} \langle \alpha | \alpha \rangle &= \langle \beta | \beta \rangle = 1 \\ \langle \alpha | \beta \rangle &= \langle \alpha | \beta \rangle = 0 \end{aligned} \tag{2.7}$$

An electron can now be described through both, its spacial coordinates $\boldsymbol{r}$ and through its spin variable ω. The resulting set of variables $\{\boldsymbol{r}, \omega\}$ shall from now on be denoted as $\boldsymbol{x}$. According to the *antisymmetry principle*, one of the postulates of quantum mechanics, the wave function of an N particle fermionic system $\Psi_\mathrm{f}\left(\boldsymbol{x}_1, \boldsymbol{x}_2, ..., \boldsymbol{x}_N\right)$ has to change its sign upon interchange of two fermion coordinates.

$$\Psi_\mathrm{f}\left(..., \boldsymbol{x}_i, ..., \boldsymbol{x}_j, ...\right) = -\Psi_\mathrm{f}\left(..., \boldsymbol{x}_j, ..., \boldsymbol{x}_i, ...\right) \tag{2.8}$$

In order to describe a many electron wave function, it is necessary to introduce the concept of *orbitals*. An orbital is a wave function of a single particle; in molecular species, it is referred to as molecular orbital $\chi(\boldsymbol{x})$ which is a product of a spacial wave function $\phi(\boldsymbol{r})$ and spin function $\alpha(\omega)$ or $\beta(\omega)$. The simplest mathematical form combining multiple molecular orbitals to obtain a many-electron wave function which still satisfies the antisymmetry principle is the determinant. An N-electron wave function• ψ is therefore defined via the Slater determinant.[9]

$$\psi(\boldsymbol{x}_1, \boldsymbol{x}_2, \ldots, \boldsymbol{x}_N) = \frac{1}{\sqrt{N!}} \begin{vmatrix} \chi_1(\boldsymbol{x}_1) & \cdots & \chi_N(\boldsymbol{x}_1) \\ \vdots & \ddots & \vdots \\ \chi_1(\boldsymbol{x}_N) & \cdots & \chi_N(\boldsymbol{x}_N) \end{vmatrix} = \hat{A} \prod_i^N \chi_i(\boldsymbol{x}_i) \equiv |\chi_1 \cdots \chi_N\rangle \tag{2.9}$$

---

[7] N. C. Handy, Y. Yamaguchi, and H. F. Schaefer. *J. Chem. Phys.*, **84**: 4481 – 4484, 1986.

[8] M. Born and K. Huang. *Dynamical Theory of Crystal Lattices*, ISBN: 9780198503699 1954.

•For reasons of clarity, the ‘el’ index was dropped and all of the following discussions shall only concern the electronic part of the wave function.

[9] V. Fock. *Z. Angew. Phys.*, **61**: 126 – 148, 1930.

$\widehat{A}$ is the antisymmetrisation operator defined as

$$\widehat{A} = \frac{1}{\sqrt{N!}} \sum_{u}^{N!} \sigma_u \widehat{P}_u \,, \tag{2.10}$$

where σ_u is the parity of the permutation (-1 for odd and 1 for even permutations) and $\widehat{P}_u$ the permutation operator, e.g. $\left\{ \widehat{E}, \widehat{P}_{12}, \widehat{P}_{123}, \dots \right\}$.

The Slater determinant intrinsically incorporates an *exchange correlation* effect as the probability of finding two electrons with the same spin close to each other is very small and finding them at the same positions strictly zero (this is sometimes referred to as a Fermi hole).

2.1.2 Hartree–Fock method

Hartree–Fock energy expression

As introduced in Equation (2.2), the electronic Hamiltonian $\widehat{H}_{\mathrm{el}}$ consists of the one-electron terms $\hat{h}_i$ and the two-electron component $\frac{1}{r_{ij}}$. Hence, the energy expectation value for the electronic Schrödinger equation can be expressed as:

$$E = \left\langle \psi \middle| \widehat{H}_{\mathrm{el}} \middle| \psi \right\rangle = \left\langle \psi \middle| \sum_{i=1}^{N} \sum_{i>j}^{N} \frac{1}{r_{ij}} - \sum_{i=1}^{N} \hat{h}_i \middle| \psi \right\rangle \tag{2.11}$$

The electronic wave function is now chosen to be a Slater-determinant (see Equation (2.9)). Using the Slater–Condon rules, which were derived using an antisymmetrisation operator $\widehat{A}$ on the wave function in order to account for the permutability, the equation can then be rewritten to separate the electron-electron interactions into Coulomb-repulsion and Exchange-interaction terms.[10] This is illustrated in the following for the restricted Hartree–Fock (RHF) case (The detailed justification for this can be

---

[10] J. C. Slater. *Phys. Rev.*, **34**: 1293 – 1322, 1929.

found in Appendix A.1.3).

$$
\begin{aligned}
E_{\mathrm{RHF}} &= 2\sum_{i}^{\frac{N}{2}} \left\langle \phi_i(\boldsymbol{r}_i) \,\middle|\, \hat{h}_i \,\middle|\, \phi_i(\boldsymbol{r}_i) \right\rangle + \sum_{i>j}^{\frac{N}{2}} \left\langle \phi_i(\boldsymbol{r}_i)\phi_j(\boldsymbol{r}_j) \,\middle|\, 4\hat{J}_{ij} - 2\hat{K}_{ij} \,\middle|\, \phi_i(\boldsymbol{r}_i)\phi_j(\boldsymbol{r}_j) \right\rangle \\
&= 2\sum_{i}^{\frac{N}{2}} \left\langle i \,\middle|\, \hat{h}_i \,\middle|\, i \right\rangle + \sum_{i>j}^{\frac{N}{2}} 4\langle ij \mid ij\rangle - 2\langle ij \mid ji\rangle
\end{aligned}
\tag{2.12}
$$

In these equations, the Coulomb operator $\hat{J}_{ij}$ and the Exchange operator $\hat{K}_{ij}$ as well as the physicists' integral notation were introduced. An overview of the different notations can be found in Szabo and Ostlund's *Modern Quantum Chemistry*.[11] Whereas $\hat{h}_i$ and $\hat{J}_{ij}$ both have classical counterparts, $\hat{K}_{ij}$ does not. $\hat{K}_{ij}$ can be understood as an *Exchange correlation*, an interaction between two electrons of the same spin. In a two-orbital–two-electron system, this can cause the paired system to be higher in energy than the unpaired case as the paired electrons can get closer together and hence experience a larger Coulomb repulsion. This is shown in the restricted open-shell Hartree–Fock (ROHF) case, where the single determinant is built from $N = n_\alpha + n_\beta$ spin orbitals. There are $n_s = |n_\alpha - n_\beta|$ singly occupied orbitals denoted by s and t as well as $N - N_s$ orbitals that, since they have a paired configuration, follow the same notation as the RHF case.

$$
\begin{aligned}
E_{\mathrm{ROHF}} = {} & 2\sum_{i}^{\frac{N-n_s}{2}} \left\langle i \,\middle|\, \hat{h}_i \,\middle|\, i \right\rangle + \sum_{i>j}^{\frac{N-n_s}{2}} 4\langle ij \mid ij\rangle - 2\langle ij \mid ji\rangle \\
& + \sum_{s}^{n_s} \left\langle s \,\middle|\, \hat{h}_s \,\middle|\, s \right\rangle + \sum_{i}^{\frac{N-n_s}{2}} \sum_{s}^{n_s} 2\langle is \mid is\rangle - \langle is \mid is\rangle \\
& + \frac{1}{2}\sum_{st}^{n_s} \langle st \mid st\rangle - \langle st \mid ts\rangle
\end{aligned}
\tag{2.13}
$$

Fock operator and Hartree–Fock equations

So far, three approximations have been made. First, the assumption that there are no relativistic effects (the non-relativistic Schrödinger equation was used); second, the BOA; and thirdly, the assumption that the wave function can be expressed in terms of a single Slater determinant. In order to reduce the

---

[11] A. Szabo and N. S. Ostlund. In: *Modern quantum chemistry: Introduction to Advanced Electronic Structure Theory*. chap. 2, 68. Dover Publications, 1996.

two-electron interactions $\hat{J}_{ij}$ and $\hat{K}_{ij}$ to effective one-electron interactions $\hat{J}_j(i)$ and $\hat{K}_j(i)$, respectively, an additional approximation is used.

This *mean-field approximation*• (see Appendix A.1.2 for a more detailed analysis) can now be used to generate the Fock operator $\hat{f}(i)$ by combining one-electron operator $\hat{h}$ and the effective one-electron Coulomb and exchange operators $\hat{J}_j(i)$ and $\hat{K}_j(i)$ in the following manner.

$$\hat{f}(i) = \hat{h}(i) + \sum_{j}^{N} \left(\hat{J}_j(i) - \hat{K}_j(i) \right) \tag{2.14}$$

In order to obtain the Hartree–Fock (HF) equations, one has to minimise the energy of a single determinant wave function with respect to spin orbitals. Applying the method of the variational theorem (See Appendix A.1.4) within a Lagrangian multiplier formalism (to ensure the orthogonality of the orbitals) it can be shown that

$$\hat{f} \left| i \right\rangle = \sum_{j}^{N} \lambda_{ji} \left| j \right\rangle , \tag{2.15}$$

where λ_{ji} are the Lagrangian multipliers. The derivation for this can be found in Appendix A.1.5. Diagonalising the matrix formed by them can be achieved by applying a unitary transformation.

$$\boldsymbol{U} \lambda \boldsymbol{U}^{+} = \varepsilon , \tag{2.16}$$

where ε is a diagonal matrix. This holds true for a certain set of canonical orbitals $\left\{ \chi_i' \right\}$ that give a decoupled form of the HF equations:

$$\hat{f} \chi_i' = \varepsilon_i \chi_i' \tag{2.17}$$

Every spin orbital χ_i' has an orbital energy ε_i associated with itself. The lowest N orbitals are the *occupied* ones, whereas the remaining orbitals are known as *virtual* orbitals.

• Technically, the single Slater determinant approach is also part of the mean-field approximation, as shown later when discussing the configuration interaction approach.

Roothaan–Hall equations

In order to solve the HF equations, it is now necessary to introduce a basis describing the orbitals. By using the linear combination of atomic orbitals (LCAO) method, these orbitals can be described analytically by a combination of hydrogen-like *atomic orbitals* to form *molecular orbitals*.[12]

$$\phi_i = \sum_{\mu=1}^{K} c_{\mu i} \varphi_\mu \tag{2.18}$$

Coefficients $c_{\mu i}$ are introduced as parameters stating the proportion of the single hydrogen-like atomic orbital φ_μ to form a molecular orbital φ_i. The hydrogen-like atomic wave functions are given by a set of Slater functions or Gaussian functions. In an exact representation an infinite amount of basis functions would be needed. For a practical approach however, a finite number K of basis functions is used, introducing yet another approximation. Using the LCAO approach, Roothaan and Hall modified the HF equations (see Equation (2.17)) accordingly to derive the following equations known as Roothaan–Hall equations.[13,14]

$$\sum_{\mu\nu} c_{j\mu} c_{\nu i} \left\langle \varphi_\mu \middle| \hat{f} \middle| \varphi_\nu \right\rangle = \sum_{\mu\nu} \varepsilon_i c_{j\mu} c_{\nu i} \left\langle \varphi_\mu \middle| \varphi_\nu \right\rangle \tag{2.19}$$

The matrix representation displays a pseudo-eigenvalue equation:

$$\begin{gathered} \boldsymbol{FC} = \boldsymbol{SC\epsilon} \\ \text{with } \sum_{\mu\nu} \left\langle \varphi_\mu \middle| \hat{f} \middle| \varphi_\nu \right\rangle = \boldsymbol{F} \quad \text{and} \quad \sum_{\mu\nu} \left\langle \varphi_\mu \middle| \varphi_\nu \right\rangle = \boldsymbol{S}\,, \end{gathered} \tag{2.20}$$

where $\boldsymbol{C}$ denotes the coefficient matrix (a $K \times K$ square matrix of the expansion coefficients $c_{\mu i}$) and $\boldsymbol{F}$ is the Fock matrix. $\boldsymbol{S}$ and $\boldsymbol{\epsilon}$ describe the overlap matrix and the eigenvalue matrix ($\boldsymbol{\epsilon}$ is a diagonal matrix of the orbital energies ε_i), respectively. It is now possible to orthogonalise the atomic orbitals to render the overlap matrix $\boldsymbol{S}$ to a unitary matrix. This reduces the Roothaan–Hall equations to a matrix eigenvalue problem.

$$\boldsymbol{FC}' = \boldsymbol{\varepsilon C}' \tag{2.21}$$

---

[12] J. E. Lennard-Jones. *Trans. Faraday Soc.*, **25**: 668 – 686, 1929.

[13] C. Roothaan. *Rev. Mod. Phys.*, **23**: 69 – 89, 1951.

[14] G. G. Hall. *Proc. R. Soc. London, Ser. A*, **205**: 541 – 552, 1951.

One should note that the Roothaan–Hall equations describe closed-shell molecules only. The open shell approach is realised through the Pople–Nesbet–Berthier equations, where two separate Fock matrices, one for each spin, are solved simultaneously.[15,16]

The Fock matrix ultimately depends on a coefficient matrix which defines a set of orbitals. The orbitals, however, are not known at the beginning of the calculation and thus an initial guess has to be conducted. From these, a new Fock matrix is built and diagonalised, yielding a new set of orbitals. This procedure is repeated until self consistency is achieved and hence called self consistent field (SCF) procedure.

Electron correlation

From the variational theorem, it follows that the eigenvalue obtained from the SCF cycle is only an upper bound to the "true" energy. Assuming an infinite basis set, the major contributions to the difference in energy between the HF energy E_{HF} and the true energy are, in most cases, the mean field (including the single Slater determinant or single reference) approximation. The difference between a system with and without these two approximations is often called the electron correlation energy E_{corr}. One should note however that the HF method already accounts for some correlation between electrons of the same spin (*exchange correlation*) and should therefore not be confused with the totally uncorrelated system.

$$E_{\text{corr}} = E - E_{\text{HF}}, \tag{2.22}$$

where E is the energy eigenvalue of the non-relativistic time independent Schrödinger equation (only applying the BOA).

In order to account for correlation effects, various post-HF methods such as Møller–Plesset perturbation theory (MP-PT), the configuration interaction (CI) method and the coupled cluster (CC) method were developed, all of which are introduced briefly in the following sections.

2.1.3 Configuration interaction

When analysing the aforementioned electron correlation, one has to keep in mind that the term describes the errors introduced by the mean-field approximation and is thus an entirely non-observable

---

[15] G. Berthier. *Compt. Rend. Hebd. Seances Acad. Sci.*, **238**: 91 – 93, 1954.
[16] J. A. Pople and R. K. Nesbet. *J. Chem. Phys.*, **22**: 571 – 572, 1954.

quantity. The first part of the approximation is introduced as a simple way to render the two-particle interaction $\frac{1}{r_{12}}$ in $\widehat{H}_{\mathrm{el}}$ into an effective one particle interaction accounting for an average field of all other electrons (this is described through the Fock operator). Moreover, the solution of the HF eigenvalue Equation (2.17) is a set of orthonormal spin orbitals of which the energetically lowest lying ones, the occupied orbitals $\{ \cdots, \chi_a, \chi_b, \cdots \}$, form the variationally approximated ground state wave function Φ_0. However, in reality electrons are not bound to one orbital. Transitions between the different orbitals and therefore change in occupation leads to a change in orbital energetics, i.e. Φ_0 is not the best description of the true ground state. Both of these approximations are manifestations of the same problem of the interdependency of the electron movement. One approach to address this issue is the configuration interaction approach.[17]

Reference and excited determinants

From a complete set of orthonormal spin orbitals $\{ \chi_k \}$, one can use all possible N-electron Slater determinants $\{ \Phi_i \}$ to find an exact expression for any N-electron wave function. This is often realised through a linear combination

$$|\psi\rangle = \sum_{i}^{K} c_i \, |\Phi_i\rangle \,, \tag{2.23}$$

where K is the number of basis functions.

In the CI approach, these determinants are usually described via a HF ground state wave function Φ_0 and additional *excited determinants*. The excited determinants are categorised in terms of how many orbitals are changed (i.e. how many electrons are excited at once). For example, they can be separated into single excitations Φ_a^r, double excitations Φ_{ab}^{rs}, triple excitations Φ_{abc}^{rst}, et cetera.• This enables a description of the CI wave function ψ_{CI} in reference to Φ_0.

$$|\psi_{\mathrm{CI}}\rangle = c_0 \, |\Phi_0\rangle + \sum_{ra} c_a^r \, |\Phi_a^r\rangle + \sum_{\substack{a<b \\ r<s}} c_{ab}^{rs} \, |\Phi_{ab}^{rs}\rangle + \sum_{\substack{a<b<c \\ r<s<t}} c_{abc}^{rst} \, |\Phi_{abc}^{rst}\rangle + \cdots \tag{2.24}$$

Given an infinite basis set, ψ_{CI} would hold an infinite amount of N-electron determinants Φ_i; yet in reality, one is often confronted with a limited amount of basis functions K, limiting the amount of N-electron determinants to $\binom{2K}{N}$. A procedure involving all possible N-electron determinants is called full configuration interaction (FCI) and only feasible for the smallest of systems (depending on

---

[17] C. D. Sherrill ‘An Introduction to Configuration Interaction Theory’ 1995

• $\{ a, b, c, \cdots \}$ denotes ground state orbitals and $\{ r, s, t, \cdots \}$ denotes virtual orbitals.

the basis set used). It is also possible to only include certain excitations, e.g. only single and double excitations to form the CISD method. However, these truncated CI methods are not size extensive, i.e. two infinitely separated systems will not have the same CI energy as the sum of two single systems.

2.1.4 Møller–Plesset perturbation theory

Rayleigh–Schrödinger perturbation theory

MP-PT is a special case of the Rayleigh–Schrödinger perturbation theory (RS-PT) which was developed in order to express complicated quantum systems, e.g. systems described by Equation (2.1), in terms of a simpler one.[18] The basic assumption is that there is an operator $\widehat{H}$ which can be described in terms of a perturbing operator $\widehat{V}$ and a simpler operator $\widehat{H}^{(0)}$, which can be solved to give a complete set of eigenfunctions.

$$\widehat{H} = \widehat{H}^{(0)} + \lambda \widehat{V}\,, \quad \text{with} \quad 0 \leq \lambda \leq 1\,, \tag{2.25}$$

where λ is a dimensionless parameter, supplying a continuous way to relate the unknown eigenvalues of the perturbed system to the known eigenvalues of the unperturbed system. Expanding ψ, the ground state electronic wave function and E, its eigenvalue, as a Taylor series around λ gives:

$$\begin{aligned} \psi &= \Phi^{(0)} + \lambda \left.\frac{\partial \Phi^{(0)}}{\partial \lambda}\right|_{\lambda=0} + \frac{\lambda^2}{2!} \left.\frac{\partial^2 \Phi^{(0)}}{\partial \lambda^2}\right|_{\lambda=0} + \cdots \\ &= \Phi^{(0)} + \lambda \Phi^{(1)} + \lambda^2 \Phi^{(2)} + \cdots \\ E &= E^{(0)} + \lambda \left.\frac{\partial E^{(0)}}{\partial \lambda}\right|_{\lambda=0} + \frac{\lambda^2}{2!} \left.\frac{\partial^2 E^{(0)}}{\partial \lambda^2}\right|_{\lambda=0} + \cdots \\ &= E^{(0)} + \lambda E^{(1)} + \lambda^2 E^{(2)} + \cdots \end{aligned} \tag{2.26}$$

where $\Phi^{(n)}$ and $E^{(n)}$ are the nth order corrections to $\Phi^{(0)}$ and $E^{(0)}$, respectively. Combining the time independent non-relativistic Schrödinger Equation (2.1) with Equation (2.25) and Equation (2.26), one

---

[18] E. Schrödinger. *Ann. Phys.*, **385**: 437 – 490, 1926.

can account for the various orders (equating the coefficients λ of like powers).

$$\hat{H}^{(0)}\left|\Phi^{(0)}\right\rangle = E^{(0)}\left|\Phi^{(0)}\right\rangle \tag{2.27a}$$

$$\hat{H}^{(0)}\left|\Phi^{(1)}\right\rangle + \hat{V}\left|\Phi^{(0)}\right\rangle = E^{(0)}\left|\Phi^{(1)}\right\rangle + E^{(1)}\left|\Phi^{(0)}\right\rangle \tag{2.27b}$$

$$\hat{H}^{(0)}\left|\Phi^{(2)}\right\rangle + \hat{V}\left|\Phi^{(1)}\right\rangle = E^{(0)}\left|\Phi^{(2)}\right\rangle + E^{(1)}\left|\Phi^{(1)}\right\rangle + E^{(2)}\left|\Phi^{(0)}\right\rangle \tag{2.27c}$$

$$\vdots$$

It is now possible to solve Equations (2.27a) to (2.27c) by multiplying with $\Phi^{(0)}$ on the left side and and subsequent integration. It is required that the wave function ψ is orthonormal to the zeroth order term $\langle\psi|\Phi^{(0)}\rangle = 1$ (intermediate normalisation), which also implies that $\langle\Phi^{(0)}|\Phi^{(m)}\rangle = \delta_{0m}$. For Equation (2.27b), the only remaining term is

$$E^{(1)} = \left\langle \Phi^{(0)} \middle| \hat{V} \middle| \Phi^{(0)} \right\rangle . \tag{2.28}$$

This shows that the first order correction to $\hat{H}^{(0)}$ is simply the expectation value of the perturbing operator $\hat{V}$. Applying the same procedure to Equation (2.27c), it follows, that

$$E^{(2)} = \left\langle \Phi^{(0)} \middle| \hat{V} \middle| \Phi^{(1)} \right\rangle . \tag{2.29}$$

The first order correction to the wave function can be expressed as a linear combination of a complete and orthonormal set of unperturbed eigenfunctions $\Phi_i^{(0)}$ of $\hat{H}^{(0)}$:

$$\left|\Phi^{(1)}\right\rangle = \sum_i c_i^{(1)} \left|\Phi_i^{(0)}\right\rangle, \text{where } c_i^{(1)} = \left\langle \Phi_i^{(0)} \middle| \Phi^{(1)} \right\rangle \tag{2.30}$$

Equation (2.27b) can then be multiplied by $\Phi_j^{(0)}$, integrated and simplified using Equation (2.30):

$$c_i^{(1)} = \frac{\left\langle \Phi_i^{(0)} \middle| \hat{V} \middle| \Phi^{(0)} \right\rangle}{E^{(0)} - E_i^{(0)}} \tag{2.31}$$

This procedure can be carried out in a similar manner to obtain higher order expansions. For this short review, the second order shall suffice.

Møller–Plesset perturbation

In order to explore electron correlation of systems relevant to quantum chemistry, Christian Møller and Milton Plesset applied the results of the HF approximation to the RS-PT.[19] In their approach, the zeroth order Hamiltonian corresponds to the sum of Fock operators $\hat{f}_i$, as defined in Equation (2.14):

$$\hat{H}_0 = \sum_i^N \hat{f}(i) = \sum_i^N \left(\hat{h}(i) + \sum_j^N \left(\hat{J}_j(i) - \hat{K}_j(i) \right) \right) = \sum_i^N \left(\hat{h}(i) + \sum_j^N \hat{V}_{\mathrm{HF}}(i) \right) \tag{2.32}$$

The perturbing operator $\hat{V}$ is therefore the difference between the full electronic Hamiltonian (Equation (2.2)) and $\hat{H}_0$ (Equation (2.32)).

$$\hat{V} = \sum_{ij}^N \frac{1}{r_{ij}} - \hat{V}_{\mathrm{HF}}(i) \tag{2.33}$$

The zeroth order wave function is set as the HF wave function. From Equation (2.27a) then, it follows that $E^{(0)}$ is merely the expectation value of $\hat{H}_0$, i.e. the sum of occupied orbital energies ε_i'. The first order energy correction is simply the expectation value of the perturbing operator acting on the HF wave function.

$$E^{(1)} = \left\langle \Phi^{(0)} \middle| \frac{1}{r_{ij}} - \hat{V}_{\mathrm{HF}}(i) \middle| \Phi^{(0)} \right\rangle = -\frac{1}{2} \sum_{ij}^N \langle ij \mid ij \rangle - \langle ij \mid ji \rangle \tag{2.34}$$

Summing $E^{(0)}$ and $E^{(1)}$, one obtains the HF energy. By summing the orbital energies ε_i', the (approximated) two-electron interactions were double counted, while with $E^{(1)}$ this "error" is remedied. Hence, the first correction to the HF energy is introduced with the second order of perturbation theory, for which the first order wave function is needed.

As described in Equation (2.30), the first order wave function $\Phi^{(1)}$ can be expanded using the $\Phi^{(0)}$. Due to Brillouin's theorem,[20,21] the fact that spin orbitals are eigenfunctions of the Fock operator and the two-particle nature of the perturbation,[22] only double excitations Φ_{ab}^{rs} contribute to $\Phi^{(1)}$ and therefore

---

[19] C. Møller and M. S. Plesset. *Phys. Rev.*, **46**: 618 – 622, 1934.

[20] L. Brillouin. *Conductibilité électrique et thermique des métaux*, 1934.

[21] P. R. Surján. In: *Second Quantized Approach to Quantum Chemistry*, 87 – 92, 1989.

[22] A. Szabo and N. S. Ostlund. In: *Modern quantum chemistry: Introduction to Advanced Electronic Structure Theory*. chap. 6, 352. Dover Publications, 1996.

to the second order energy correction.

$$E^{(2)} = -\sum_{\substack{a<b\\ r<s}} \frac{\left|\left\langle \Phi^{(0)} \middle| \frac{1}{r_{12}} \middle| \Phi_{ab}^{rs} \right\rangle\right|^2}{\varepsilon_r + \varepsilon_s - \varepsilon_a - \varepsilon_b} = -\sum_{\substack{a<b\\ r<s}} \frac{|\langle ab\,|\,rs\rangle - \langle ab\,|\,sr\rangle|^2}{\varepsilon_r + \varepsilon_s - \varepsilon_a - \varepsilon_b} \tag{2.35}$$

Due to the size extensivity of the method and the fact that for many important chemical systems it can account for up to 92 % of correlation energy,[23] the second order Møller–Plesset (MP2) method found widespread application in modern quantum chemistry. It should be noted however, that the correlation energies derived from higher order MP-PT methods are not variational; in fact, it has been observed that higher orders energies are alternating and in some cases even diverging.[24] So while MP2 serves as a sound foundation for investigations into the influence of electron correlation, it should be noted that if more accuracy is required, the single determinant approach is an inadequate one to begin with or if weakly bound systems are investigated, other methods (e.g. CC or multi-reference methods) are more beneficial.

2.1.5 Coupled cluster theory

For smaller systems – systems with less than nine heavy atoms – the CC technique offers one of the most accurate, reliable but still computationally feasible methods in quantum chemistry. Starting originally as a method to model the behaviour of atomic nuclei in the late 1960's,[25–27] it was later adapted by Pople and Bartlett for chemical problems.[28,29] The well known coupled cluster singles and doubles method with perturbative inclusion of triples (CCSD(T)) is now the "golden standard" when it comes to calculation where correlation plays an important role.

In this section, a brief introduction into CC theory is given. It will illustrate some of the key points on which the theory is based. A more detailed and rigorous description of the theory and the implementations is found in the work of Crawford and Schaefer III.[30]

---

[23] Y. Jung et al. *J. Chem. Phys.*, **121**: 9793 – 9802, 2004.

[24] M. L. Leininger et al. *J. Chem. Phys.*, **112**: 9213 – 9222, 2000.

[25] J. Čižek. *J. Chem. Phys.*, **45**: 4256 – 4266, 1966.

[26] J. Čižek and J. Paldus. *Int. J. Quantum Chem.*, **5**: 359 – 379, 1971.

[27] J. Paldus, J. Čížek, and I. Shavitt. *Phys. Rev. A*, **5**: 50 – 67, 1972.

[28] J. A. Pople et al. *Int. J. Quantum .Chem.*, **14**: 545 – 560, 1978.

[29] R. J. Bartlett and G. D. Purvis. *Int. J. Quantum .Chem.*, **14**: 561 – 581, 1978.

[30] T. D. Crawford and H. F. Schaefer. *Rev. Comput. Chem.*, **14**: 33 – 136, 2000.

Annihilation and creation operators

Starting from the HF case, one always runs into the problem of electron correlation. As already described in Section 2.1.3, one way of incorporating correlation effects is to account for excitations of electrons from a ground state to an exited state. For CC theory it is helpful to introduce the second quantisation approach in order to deal with excitations. In a Slater determinant, this excitation is described by a replacement of ground state orbital χ_a with the exited orbital χ_r. Mathematically, this is expressed as a combination of annihilation operator $\hat{a}_a$–removing the orbital χ_a from the determinant, and creation operator $\hat{a}_r^\dagger$–spawning a new orbital χ_r where χ_a used to be.

$$\hat{a}_r^\dagger \hat{a}_a \left|\chi_a \chi_b \chi_c \cdots\right\rangle = \hat{a}_r^\dagger \left|\chi_b \chi_c \cdots\right\rangle = \left|\chi_r \chi_b \chi_c \cdots\right\rangle \tag{2.36}$$

In a similar manner, a double excitation can be described.

$$\hat{a}_r^\dagger \hat{a}_s^\dagger \hat{a}_b \hat{a}_a \left|\chi_a \chi_b \chi_c \cdots\right\rangle = \left|\chi_r \chi_s \chi_c \cdots\right\rangle \tag{2.37}$$

In order to describe all possible single excitations of Φ_0, one has to excite each of the N electrons into K orbitals (K represents the amount basis functions). This can be described in operator form through the *total one orbital cluster operator* $\widehat{T}_1$.

$$\widehat{T}_1 = \sum_{a}^{N} \sum_{r}^{K} t_a^r \hat{a}_r^\dagger \hat{a}_a , \tag{2.38}$$

where t_a^r is the called the single excitation *cluster amplitude*. Similarly, the *total two orbital cluster operator* $\widehat{T}_2$ can be expressed as follows.

$$\widehat{T}_2 = \sum_{a>b}^{N} \sum_{r>s}^{K} t_{ab}^{rs} \hat{a}_r^\dagger \hat{a}_s^\dagger \hat{a}_b \hat{a}_a = \frac{1}{4} \sum_{ab}^{N} \sum_{rs}^{K} t_{ab}^{rs} \hat{a}_r^\dagger \hat{a}_s^\dagger \hat{a}_b \hat{a}_a \tag{2.39}$$

In general one can write an expression for the *total n-orbital cluster operator* through $\widehat{T}_n$.

$$\widehat{T}_n = \left(\frac{1}{n!}\right)^2 \sum_{ab\cdots}^{N} \sum_{rs\cdots}^{K} t_{ab\cdots}^{rs\cdots} \; \hat{a}_r^\dagger \hat{a}_s^\dagger \cdots \; \hat{a}_b \hat{a}_a \cdots \tag{2.40}$$

Exponential ansatz

In striking difference to CI theory, the excitations are not directly applied as a sum to the wave function, but rather through the use of an exponential ansatz.

$$\Psi_{\mathrm{CC}} = \mathrm{e}^{\sum_i^N \widehat{T}_i} \Phi_0 = \mathrm{e}^{\widehat{T}_1 + \widehat{T}_2 + \ldots + \widehat{T}_N} \Phi_0 \equiv \mathrm{e}^{\widehat{T}} \Phi_0 \tag{2.41}$$

CC exponential expression

If this gets expanded into a power series it becomes clear how the excitations actually mix into the wave function.

$$\mathrm{e}^{\widehat{T}} = 1 + \widehat{T} + \frac{\widehat{T}^2}{2!} + \frac{\widehat{T}^3}{3!} + \ldots \tag{2.42}$$

Acting on a single HF determinant via

$$\left\langle \Phi_0 \middle| \widehat{H} \left(1 + \widehat{T} + \frac{\widehat{T}^2}{2!} + \frac{\widehat{T}^3}{3!} + \ldots\right) \middle| \Phi_0 \right\rangle = E\,, \tag{2.43}$$

one can see that due to the one-and-two-particle-only nature of the Hamiltonian (Slater rules),[10] the power series is truncated after the $\frac{\widehat{T}^2}{2!}$ part. The resulting expression for the CC energy can be written as

$$\left\langle \Phi_0 \middle| \widehat{H} \middle| \Phi_0 \right\rangle + \left\langle \Phi_0 \middle| \widehat{H}\widehat{T} \middle| \Phi_0 \right\rangle + \left\langle \Phi_0 \middle| \widehat{H}\frac{\widehat{T}^2}{2!} \middle| \Phi_0 \right\rangle = E\,. \tag{2.44}$$

In order to find the specific amplitude $t_{ab\cdots}^{rs\cdots}$ however,

$$\left\langle \Phi_{ab\cdots}^{rs\cdots} \middle| \widehat{H} \middle| \Phi_0 \right\rangle + \left\langle \Phi_{ab\cdots}^{rs\cdots} \middle| \widehat{H}\widehat{T} \middle| \Phi_0 \right\rangle + \left\langle \Phi_{ab\cdots}^{rs\cdots} \middle| \widehat{H}\frac{\widehat{T}^2}{2!} \middle| \Phi_0 \right\rangle = E \tag{2.45}$$

needs to be solved, resulting in a large set of dependent equations. Assuming an infinite basis K, it can be shown that this CC expression is exact within the non-relativistic BOA framework. To be computationally feasible however (K is limited), it is quite common for $\widehat{T}$ to be truncated after a certain amount of excitations, e.g. coupled cluster approach including single and double excitations (CCSD) would involve a cluster operator of $\widehat{T} = \widehat{T}_1 + \widehat{T}_2$ (yet truncated versions are not variational).

It should be noted that the CC method is size extensive due to the nature of the exponential ansatz.

$$\hat{H}\psi_{\mathrm{CC}} = \hat{H}\mathrm{e}^{\hat{T}}\Phi_0 = \hat{H}\mathrm{e}^{\hat{T}_{\mathrm{A}}+\hat{T}_{\mathrm{B}}}\Phi_0 = \hat{H}\mathrm{e}^{\hat{T}_{\mathrm{A}}}\mathrm{e}^{\hat{T}_{\mathrm{B}}}\Phi_0 = (E_{\mathrm{A}} + E_{\mathrm{B}})\Phi_0 \tag{2.46}$$

Explicit correlation

As shown in (2.9) and (2.18), the electronic wavefunction is usually expressed as an antisymmetrised product of one-electron orbitals. In common electronic structure methods, Gaussian type orbitals are employed. However, the resulting electronic wave function does not satisfy the electron cusp-conditions;[31]

$$\lim_{r_{12}\to 0}\left(\frac{\partial\psi}{\partial r_{12}}\right)_{\mathrm{av}} = \frac{1}{2}\psi\left(r_{12}=0\right) , \tag{2.47}$$

where an averaging over all directions is implied. The lack of this property for conventional wavefunctions is thought to be the primary reason for the slow convergence towards a complete basis set limit when increasing the size of the basis sets. A successful solution to this problem is the inclusion of r_{12}-term through a $f\left(r_{12}\right)$ factor in the basis functions ϕ_k

$$\phi_k = \varphi(1)\varphi(2)f\left(r_{12}\right) \tag{2.48}$$

This was first employed by Hylleraas in 1929 to calculate the ionisation potential of helium where $f\left(r_{12}\right) = r_{12}^m$ (at different powers m).[32] The Hylleras approach was subsequently refined and implemented by Kutzelnigg and Klopper and are referred to as R12 methods.[33] An approach pioneered by Boys and Singer where $f\left(r_{12}\right) = e^{-\gamma r_{12}^2}$ (where γ is an adjustable parameter), denoted as explicitly correlated Gaussian method or in its refined form, F12, provided a more successful alternative.[34,35] While the R12 method showed better convergence towards the basis set limit, the basis set usually had to be large and was thus limited to rather small systems. Despite the fact that the wavefunction generated through an F12 method does not satisfy the cusp-conditions, the recovery of the correlation energy is significantly more efficient than for the R12 methods. This is shown by Peterson and co-workers and works particularly well with specifically optimised basis sets.[36] The explicitly correlated methods are usually combined with the previously introduced Møller-Plesset or coupled cluster techniques, e.g. CCSD-F12 or MP2-R12.

---

[31] T. Kato. *Comm. Pure Appl. Math.*, **10**: 151 – 177, 1957.

[32] E. A. Hylleraas. *Z. Angew. Phys.*, **54**: 347 – 366, 1929.

[33] W. Kutzelnigg and W. Klopper. *J. Chem. Phys.*, **94**: 1985 – 2001, 1991.

[34] S. F. Boys. *Proc. R. Soc. London, Ser. A*, **258**: 402 – 411, 1960.

[35] K. Singer. *Proc. R. Soc. London, Ser. A*, **258**: 412 – 420, 1960.

[36] K. A. Peterson, T. B. Adler, and H.-J. Werner. *J. Chem. Phys.*, **128**: 084102, 2008.

2.1.6 Density functional theory

The density functional theory (DFT) has become one of the major tools of larger scale modern day quantum-mechanical property calculations. In this section, a very brief introduction to the basics of this theory will be presented. A sound introduction, is found in the works of Parr, Koch or Burke.[37–39]

Theoretical basis

Compared to wave function based methods, density based methods employ an electron density $\rho(\boldsymbol{r})$ as basic three-dimensional scalar quantity to explore quantum-mechanic behaviour of systems in the atomistic realm. For an N electron system, this electron density is defined as follows.

$$\rho(\boldsymbol{r}) = N \int \cdots \int \left|\psi\left(\boldsymbol{r}, \omega_1, \boldsymbol{x}_2, \dots, \boldsymbol{x}_N\right)\right|^2 d\omega_1 d\boldsymbol{x}_2 \cdots d\boldsymbol{x}_N \tag{2.49}$$

Where ψ is the normalised electronic wave function of the spin orbitals $\boldsymbol{x}_i$ (with spin and spacial coordinates ω_i and $\boldsymbol{r}_i$ respectively, as described in Section 2.1.1).

DFT, as known today, was first introduced by Hohenberg and Kohn in 1964 by formulating and proving two theorems.[40] The *first fundamental theorem* is quoted as follows:

> 'Thus [external potential] $V_{\text{ext}}(\boldsymbol{r})$ is (to within a constant) a unique functional of $\rho(\boldsymbol{r})$; since, in turn, $V_{\text{ext}}(\boldsymbol{r})$ fixes $\widehat{H}$ we see that the full many-particle ground state is a unique functional of $\rho(\boldsymbol{r})$.' [Ref. 40, p. B 865]

The authors prove that for N-interacting electrons, there cannot be two different $V_{\text{ext}}(\boldsymbol{r})$ yielding the same ground state electron density. Therefore, $V_{\text{ext}}(\boldsymbol{r})$ is uniquely specified through $\rho_0(\boldsymbol{r})$. As this external potential is fully defined as an attractive potential of the nuclei M, it is denoted as V_{Ae}. The total ground state electronic energy of a system E_0 is expressed as a sum of electronic kinetic energy T, the energy resulting from the external potential E_{Ae} and the electron-electron interactions E_{ee}.

$$E_0\left[\rho_0\right] = E_{Ae}\left[\rho_0\right] + \underbrace{T\left[\rho_0\right] + E_{ee}\left[\rho_0\right]}_{F_{\text{HK}}\left[\rho_0\right]} \tag{2.50}$$

---

[37] R. G. Parr and W. Yang. *Density-Functional Theory of Atoms and Molecules*, ISBN: 9780195357738 1989.

[38] W. Koch and M. Holthausen. *A chemist's guide to density functional theory*, ISBN: 9783527299188 2000.

[39] K. Burke. *The ABC of DFT*, 2007.

[40] P. Hohenberg and W. Kohn. *Phys. Rev.*, **136**: B864 – B871, 1964.

In this equation, $E_{Ae}\left[\rho_0\right]$ is the only molecule specific part, whereas the remaining terms−often collected as the Hohenberg–Kohn functional $F_{\mathrm{HK}}\left[\rho_0\right]$ −only depend on the electron density. The electron-electron interaction term E_{ee} can furthermore be described by classical known Coulomb part[•] $J\left[\rho\right]$ and a non-classical unknown part $E_{\text{non−classical}}\left[\rho\right]$.

$$E_{ee}\left[\rho\right] = J\left[\rho\right] + E_{\text{non−classical}}\left[\rho\right] \tag{2.51}$$

By introducing a *second fundamental theorem*, Hohenberg and Kohn laid out a way to obtain the ground-state energy E_0:

> '…the problem of determining the ground-state energy and density in a given external potential would be rather easy since it requires merely the minimization of a functional of the three-dimensional density function.' [Ref. 40, p. B 865]

This means that the variational principle can be applied in a similar manner as for the self consistent field cycle employed in the HF method, where instead of a trial wave function, the trial density $\tilde{\rho}$ is used:

$$\frac{\delta \widetilde{E}}{\delta \tilde{\rho}} = 0 \tag{2.52}$$

This can be expressed by using the wave function.

$$\begin{aligned} \left\langle \widetilde{\psi} \middle| \widehat{H} \middle| \widetilde{\psi} \right\rangle &= T\left[\tilde{\rho}\right] + V_{ee}\left[\tilde{\rho}\right] + \int \tilde{\rho}\left(\boldsymbol{r}\right) V_{\mathrm{eff}} d\boldsymbol{r} \\ &= E\left[\tilde{\rho}\right] \\ E\left[\tilde{\rho}\right] &\geq E_0\left[\rho\right] \\ E_0\left[\rho\right] &= \left\langle \psi_0 \middle| \widehat{H} \middle| \psi_0 \right\rangle , \end{aligned} \tag{2.53}$$

where V_{ee} is the electron-electron interaction potential and V_{eff} corresponds to an effective potential describing the electron-nuclei interactions. It can be shown that optimising the density works in a similar manner to the optimisation of the wave function. The exact forms of $T\left[\rho\right]$ and $E_{ee}\left[\rho\right]$, however, remain unknown.

Shortly after the publication of the Hohenberg–Kohn theorems, Kohn and Sham introduced an approach to find an approximation for the exact functional. In this approach, a fictitious auxiliary system

---

[•] $J\left[\rho\right] = \frac{1}{2}\int\int \frac{\rho(r_1)\rho(r_2)}{r_{12}} dr_1 dr_2$

of non-interacting particles, the so-called Kohn–Sham (KS) system, is used. These particles have similar properties to those of electrons, yet they do not interact with each other. A Hamiltonian of a non-interacting N-particle KS system is expressed as follows.

$$\hat{H}^{\mathrm{KS}} = -\frac{1}{2}\sum_{i}^{N} \nabla_i^2 + \sum_{i}^{N} V_{\mathrm{eff}}\left(\boldsymbol{r}_i\right) \tag{2.54}$$

To account for exchange anti-symmetry the ground state wave function is a Slater-determinant constructed from the individual spin orbitals χ_i. This gives rise to the following equation for the spin orbitals.

$$\hat{f}^{\mathrm{KS}} \chi_i = \varepsilon_i \chi_i \tag{2.55}$$

Where the one-electron Kohn–Sham operator $\hat{f}^{\mathrm{KS}}$ is defined as follows.[•]

$$\hat{f}^{\mathrm{KS}} = -\frac{1}{2}\nabla_i^2 + V_{\mathrm{eff}}\left(\boldsymbol{r}_i\right) \tag{2.56}$$

V_{eff} can now be chosen in such a way, that the sum of the squared spin-orbitals χ_i (Kohn–Sham spin orbitals) represents the ground state density.

$$\rho_{\mathrm{KS}}(\boldsymbol{r}) = \rho_0(\boldsymbol{r}) = \sum_{i}^{N} \left|\chi_i(\boldsymbol{x})\right|^2 \tag{2.57}$$

The kinetic energy of the fictitious Kohn–Sham system is therefore as follows.

$$T_{\mathrm{KS}} = -\frac{1}{2}\sum_{i}^{N} \left\langle \chi_i \middle| \nabla^2 \middle| \chi_i \right\rangle \tag{2.58}$$

It is now possible to separate known parts of $T[\rho]$ and $E_{ee}[\rho]$ from the unknown parts. All unknown functionals are combined in the exchange-correlation (XC) functional $E_{\mathrm{XC}}[\rho]$.

$$\begin{aligned} E_{\mathrm{XC}}[\rho] &\equiv \left(T[\rho] - T_{\mathrm{KS}}[\rho]\right) + \left(E_{ee}[\rho] - J[\rho]\right) \\ &= T_{\mathrm{C}}[\rho] + E_{\mathrm{non-classical}}[\rho] \end{aligned} \tag{2.59}$$

[•] It should be noted that the difference between the Fock operator f (see Equation (A.20) in Appendix A.1.5) and $\hat{f}^{\mathrm{KS}}$ depends on ρ_0. The resulting orbitals are also different.

Hence, the ground state energy becomes.

$$\begin{aligned} E\left[\rho\right] &= E_{Ae}\left[\rho\right] + T\left[\rho\right] + E_{ee}\left[\rho\right] \\ &= E_{Ae}\left[\rho\right] + T_{\mathrm{KS}}\left[\rho\right] + J\left[\rho\right] + E_{\mathrm{XC}}\left[\rho\right] \end{aligned} \tag{2.60}$$

The XC functional now contains all the quantities unknown, and for which approximations were developed.

Exchange-correlation functionals

As the XC functional is crucial for a density functional method, different types of XC functionals are often classified according to their complexity–this ranking is also known as Jacob's ladder of XC functionals.[41] In the local spin density approximation (LSDA), one of the simplest models, the XC energy is composed of Dirac's HF exchange and a correlation functional which is built on the homogeneous electron gas (HEG) model.[42]

$$E_{\mathrm{XC}}^{\mathrm{LSDA}}\left[\rho\right] = \int \varepsilon_{\mathrm{XC}}\left[\rho_\alpha\left(\boldsymbol{r}\right), \rho_\beta\left(\boldsymbol{r}\right)\right] \cdot \rho\left(\boldsymbol{r}\right) d\boldsymbol{r}\,, \tag{2.61}$$

where $\varepsilon_{\mathrm{XC}}$ is the XC energy per electron of the HEG; $\rho_\alpha\left(\boldsymbol{r}\right)$ and $\rho_\beta\left(\boldsymbol{r}\right)$ are the separate electron densities for the α and β electron populations, respectively. Using various approaches with different forms of E_{C}, several LSDAs with different forms of correlation functionals were generated through interpolation (since an exact expression for the correlation in the HEG model is also not known), such as those described as Vosko–Wilk–Nusair (VWN)[43] and Perdew–Wang (PW91).[44]

Functionals based on a LSDA are not known for their great accuracy when it comes to molecules; they are succeeded by XC functionals based on a generalised gradient approximation (GGA). In addition to the normal density, the GGA XC functional also incorporates the gradient of the electron density.

$$E_{\mathrm{XC}}^{\mathrm{GGA}}\left[\rho\right] = \int f\left(\rho_\alpha, \rho_\beta, \nabla\rho_\alpha, \nabla\rho_\beta\right) d\boldsymbol{r} \tag{2.62}$$

---

[41] J. P. Perdew and K. Schmidt. *AIP Conf. Proc.*, **577**: 1 – 20, 2001.

[42] P. A. M. Dirac. *Math. Proc. Camb. Philos. Soc.*, **26**: 376 – 385, 1930.

[43] S. H. Vosko, L. Wilk, and M. Nusair. *Can. J. Phys.*, **58**: 1200 – 1211, 1980.

[44] J. P. Perdew and Y. Wang. *Phys. Rev. B*, **45**: 13244 – 13249, 1992.

Common GGA XC functionals usually use Becke's exchange functional (B)[45] exchange and the correlation functional of Perdew (P86)[46] correlation or Lee et al. (LYP)[47] correlation functional to give such methods as B-P86 or B-LYP. However, many others are available.

More modern, higher-order methods such as *Meta* and *Hyper* GGAs also exist. These approaches are often referred to as further steps on the aforementioned Jacob's ladder of density functional approximations.[41]

A somewhat deviating class of XC functionals are the *Hybrid functionals*. Although, through most of these functionals, the ab initio character is removed from the density functional method, they often return more accurate results than GGAs or LSDAs, as they are fitted against a large trial set of atoms and molecules.[•] The most popular Hybrid functional is B3-LYP, which uses a set of three semi-empirical coefficients a, b and c, the LSDA XC functional $E_{\mathrm{XC}}^{\mathrm{LSDA}}$, Becke's exchange functional $E_{\mathrm{X}}^{\mathrm{B}}$, the LYP correlation functional $E_{\mathrm{C}}^{\mathrm{LYP}}$ and elements from the adiabatic connection formula $E_{\mathrm{XC}}^{\lambda=0}$. The latter part of the functional essentially employs the exact HF exchange and is derived using the Hellmann–Feynman theorem (see Appendix A.1.6).[48]

$$E_{\mathrm{XC}}^{\mathrm{B3-LYP}} = E_{\mathrm{XC}}^{\mathrm{LSDA}} + a\left(E_{\mathrm{XC}}^{\lambda=0} - E_{\mathrm{X}}^{\mathrm{LSDA}}\right) + bE_{\mathrm{X}}^{\mathrm{B}} + c\left(E_{\mathrm{C}}^{\mathrm{LYP}} - E_{\mathrm{C}}^{\mathrm{LSDA}}\right) \tag{2.63}$$

Even higher up on this Jacob's ladder are double hybrid GGA funcionals which, in addition to the HF exchange, also account for the MP2 correlation interaction.[49] The parametrisation approach of approximating E_{XC} caused the development of a large variety of functionals. In 2011, Goerigk and Grimme benchmarked a great amount of LSDAs, GGAs, meta-GGAs, hybrid as well as double hybrid functionals for basic thermochemistry, kinetics and non-covalent interactions (via dispersion correction).[50] They could indeed show that despite its popularity, compared to other hybrid functionals, the B3-LYP functional performs rather poorly and should be avoided if one requires accurate energetics. However, due to this popularity, the shortcomings of this functional are reasonably well explored and when dispersion interaction is accounted for, the obtained energies, and energy derivatives are usually an acceptable starting point for further investigations.

---

[45] A. D. Becke. *Phys. Rev. A*, **38**: 3098 – 3100, 1988.

[46] J. P. Perdew. *Phys. Rev. B*, **33**: 8822 – 8824, 1986.

[47] C. Lee, W. Yang, and R. G. Parr. *Phys. Rev. B*, **37**: 785 – 789, 1988.

[•] Arguably, if one moves outside of this fitting set, unexpected results may occur.

[48] R. Feynman. *Phys. Rev.*, **56**: 340 – 343, 1939.

[49] S. Grimme. *J. Chem. Phys.*, **124**: 034108, 2006.

[50] L. Goerigk and S. Grimme. *Phys. Chem. Chem. Phys.*, **13**: 6670 – 6688, 2011.

2.1.7 Molecular vibrations and electronic transitions

The interaction of light with matter can be understood as molecules within that matter responding to a changing electromagnetic field. As this involves both the nuclei and the electrons, it is necessary to go beyond the electronic problem and consider the nuclear Schrödinger Equation (2.5). According to the BOA, the nuclear wave function ψ_{nuc} is a product of translational, rotational and vibrational wave function−ψ_{trans}, ψ_{rot} and ψ_{vib} respectively. As a first approximation, it is possible to treat each of these entities independently. In the following, the theoretical treatment of vibrational and electronic transitions are presented briefly. For a more detailed discussion of the rotational problem, see the work of Atkins et al. and Wilson and co-authors.[51,52]

Mechanical harmonic approximation

The nuclear kinetic energy T_{nuc} in its Cartesian form can be written as

$$T_{\text{nuc}} = \frac{1}{2}\sum_{A=1}^{M}\sum_{i=1}^{3}\frac{1}{M_A}\left(\frac{\partial \Delta x_{iA}}{\partial t}\right)^2, \tag{2.64}$$

where one sums over all nuclei M within three dimensions. Δx_{iA} describes the displacement of a nucleus coordinate from its equilibrium position[▲] x_{i0A}.

It is now advantageous to substitute $M_A^{-1/2}\Delta x_{iA}$ with q_{iA}, the *mass-weighted Cartesian displacement coordinates*. Often through convention, the index A is dropped as it is understood that the summation is carried out over $3M$ coordinates where after a set of three coordinates, an iteration to the next nucleus occurs. Hence T_{nuc} becomes:

$$T_{\text{nuc}} = \frac{1}{2}\sum_{i=1}^{3M}\left(\frac{\partial q_i}{\partial t}\right)^2 \tag{2.65}$$

---

[51] P. W. Atkins and R. Friedman. *Molecular Quantum Mechanics*, ISBN: 9780195672510 2005.

[52] E. B. Wilson, J. C. Decius, and P. C. Cross. *Molecular Vibrations: The Theory of Infrared and Raman Vibrational Spectra*, ISBN: 9780486639413 1955.

[▲] $\Delta x_{iA} = x_{i0A} - x_{iA}$

The potential energy E_{pot} can be represented through a Taylor series around the equilibrium position.

$$\begin{aligned}
V_{\text{nuc}} &= V_0 + \sum_{i=1}^{3M} \left(\frac{\partial V}{\partial q_i}\right)_0 q_i + \frac{1}{2!} \sum_{i,j=1}^{3M} \left(\frac{\partial^2 V}{\partial q_i \partial q_j}\right)_0 q_i q_j \\
&+ \frac{1}{3!} \sum_{i,j,k=1}^{3M} \left(\frac{\partial^3 V}{\partial q_i \partial q_j \partial q_k}\right)_0 q_i q_j q_k + \cdots \\
&= \frac{1}{2!} \sum_{i,j=1}^{3M} f_{ij} q_i q_j + \frac{1}{3!} \sum_{i,j,k=1}^{3M} f_{ijk} q_i q_j q_k + \cdots && (2.66a) \\
&\approx \frac{1}{2} \sum_{i,j=1}^{3M} f_{ij} q_i q_j && (2.66b)
\end{aligned}$$

In this equation, V_0, a constant, was arbitrarily set to zero. The term $\left(\frac{\partial V}{\partial q_i}\right)_0$ vanishes as the derivative is carried out in an extremum. For small displacements from equilibrium, higher-order terms are less important and therefore, a reasonable approximation is the harmonic one where only the second-order term of the Taylor series contributes to the potential. This is often referred to as the *mechanical harmonic approximation*.[53] The force constants $\frac{f_{ij}}{\sqrt{m_i m_j}}$ constitute a matrix of second derivatives, the so-called Hessian, which can be diagonalised using a matrix $\boldsymbol{U}$, resulting in a set of *normal coordinates* Q_i.

$$Q_i = \sum_{i=1}^{3M} U_{ik} q_i \quad \text{hence,} \quad q_i = \sum_{k=1}^{3M} U_{ik} Q_k \tag{2.67}$$

A simplified vibrational Hamiltonian $H_{\text{vib}} = T_{\text{nuc}} + V_{\text{nuc}}$ can now be expressed in terms of these normal coordinates.

$$H_{\text{vib}} = \frac{1}{2} \sum_{k=1}^{3M} \left(-\frac{\partial^2}{\partial Q_k^2} + \omega_k^2 Q_k^2 \right) \tag{2.68}$$

Here, ω_k^2 are the eigenvalues of the Hessian matrix. The energy eigenvalues of the vibrational Schrödinger equation $H_{\text{vib}} \left|\psi_{\text{vib}}\right\rangle = E_{\text{vib}} \left|\psi_{\text{vib}}\right\rangle$ is then expressed through

$$E_{\text{vib}} \left(v_1, \ldots, v_{3M}\right) = \sum_{k=1}^{3M} \hbar\omega_k \left(v_k + \frac{1}{2}\right), \tag{2.69}$$

---

[53] H. P. Figeys and P. Geerlings. In: *Theoretical Models of Chemical Bonding*, 25 – 62, 1991.

where ω_k are the harmonic vibrational frequencies and v_k the vibrational quantum number of the mode k. Depending on whether the molecule under investigation is linear or not, five or six modes will have a vibrational frequency of zero and constitute translations and rotations. For the harmonic approximation, the vibrational wave function ψ_{vib} is described as a product of harmonic oscillator functions. These are used to evaluate the integrals for the transition dipole matrix $\boldsymbol{d}$.

Electrical harmonic approximation

The absorption or emission of an IR, visible or UV-light photon always goes along with a changed wave function from an initial state Ψ'' to a final state Ψ'.

$$\boldsymbol{d}_{\mathrm{trans}} = \left\langle \Psi' \,\middle|\, \widehat{\boldsymbol{\mu}}_{\mathrm{electric}} \,\middle|\, \Psi'' \right\rangle \tag{2.70}$$

In this case, the transition moment operator $\widehat{\boldsymbol{\mu}}_{\mathrm{electric}}$, describes the electric interactions, i.e. the complete multipole moment generating operator. For the prediction of IR and photelectron spectra however, transitions caused by the electric dipole should suffice. When considering vibrational dipole transitions, the remaining transition moment operator $\widehat{\boldsymbol{\mu}}_{\mathrm{nuc}}$ is only a function of the nuclear coordinates and can be expanded as a Taylor series around the equilibrium position.

$$\widehat{\boldsymbol{\mu}}_{\mathrm{nuc}} = \boldsymbol{\mu}_{\mathrm{nuc},0} + \sum_{i=1}^{3M} \left(\frac{\partial \boldsymbol{\mu}_{\mathrm{nuc}}}{\partial Q_i} \right)_0 Q_i + \frac{1}{2!} \sum_{i=1}^{3M} \left(\frac{\partial^2 \boldsymbol{\mu}_{\mathrm{nuc}}}{\partial Q_i^2} \right)_0 Q_i^2 + \cdots \tag{2.71a}$$

$$\approx \boldsymbol{\mu}_{\mathrm{nuc},0} + \sum_{i=1}^{3M} \left(\frac{\partial \boldsymbol{\mu}_{\mathrm{nuc}}}{\partial Q_i} \right)_0 Q_i \tag{2.71b}$$

Equation (2.71b) is called the *electrical harmonic approximation*.[53] Together with the mechanical harmonic approximation, Equation (2.66b), this is known as the *double harmonic approximation*. Since $\boldsymbol{d}_{\mathrm{trans}}^2$ is proportional to the intensity, this approximation is commonly used to obtain a first IR spectrum estimate of a given molecule.

Anharmonic vibrations

For higher-resolution experiments or for investigations into hydrogen weakly bound complexes the double harmonic approximation is insufficient.[54] Not only does one need to account for effects arising

---

[54] J. E. Del Bene and M. J. T. Jordan. *Int. Rev. Phys. Chem.*, **18**: 119 – 162, 1999.

from rotational-vibrational interactions but also for the *anharmonicity of the vibrations* resulting from higher-order terms in Equation (2.71a) and Equation (2.66a).

There have been many attempts to approximate the anharmonic and rotational-vibrational effects. Of these, the most successful general models can be grouped into two categories, perturbation theory based approximations and variational approaches.

In the former one, the nuclear rotational-vibrational Hamiltonian, also known as the Watson Hamiltonian,[55] is expanded in terms of normal coordinates and rotational momenta. By using harmonic oscillator and rigid rotor wave functions as a basis set, it is possible to derive analytic expressions for ro-vibrational energy levels.[56,57] An example of this method is the vibrational second-order perturbation theory (VPT2) developed by Stanton et al. in which the pure vibrational terms of the expanded Hamiltonian up to the fourth order are used.[58,59]

For the variational approach, the Watson Hamiltonian is rewritten in a matrix representation such that it acts on the rotational-vibrational wavefunctions, analogous to the Fock-matrix of the SCF procedure where the vibrations can be interpreted as interacting quasi-particles (phonons). The wavefunctions can be expressed in any basis, e.g. harmonic oscillator functions; and analogous to the SCF procedure, the eigenvalue problem is solved in a variational way. It is for this reason, that the simplest model of the variational approach is called vibrational self consistent field (VSCF), developed by Bowman, Carter and Gerber.[60–62] Borrowing again from electronic structure methods, correlation between vibrational phonons can be achieved by various techniques such as vibrational configuration interaction (VCI),[63,64] vibrational multi-configurational SCF (VMCSCF),[65] vibrational complete-

---

[55] J. K. Watson. *Mol. Phys.*, **15**: 479 – 490, 1968.

[56] D. Papoušek and M. R. Alijev. *Molecular Vibrational-rotational Spectra: Theory and Applications of High Resolution Infrared, Microwave, and Raman Spectroscopy of Polyatomic Molecules*, ISBN: 9780444997371 1982.

[57] R. D. Amos et al. *J. Chem. Phys.*, **95**: 8323 – 8336, 1991.

[58] J. Vázquez and J. F. Stanton. *Mol. Phys.*, **104**: 377 – 388, 2006.

[59] J. Breidung et al. *J. Chem. Phys.*, **110**: 3678 – 3696, 1999.

[60] J. M. Bowman. *J. Chem. Phys.*, **68**: 608 – 610, 1978.

[61] R. Gerber and M. Ratner. *Chem. Phys. Lett.*, **68**: 195 – 198, 1979.

[62] P. Jensen and P. R. Bunker. *Computational Molecular Spectroscopy*, ISBN: 9780471489986 2000.

[63] J. M. Bowman, K. Christoffel, and F. Tobin. *J. Phys. Chem.*, **83**: 905 – 912, 1979.

[64] H. Romanowski, J. M. Bowman, and L. B. Harding. *J. Chem. Phys.*, **82**: 4155 – 4165, 1985.

[65] F. Culot and J. Liévin. *Theor. Chim. Acta*, **89**: 227 – 250, 1994.

active-space SCF (VCASSCF),[66] second order vibrational perturbation theory (VMP2),[67] as well as Christiansen's vibrational coupled cluster (VCC) model.[68,69]

Alternatively if one is only interested in certain vibrational modes, the local mode model (LMM) can provide a better approach, specifically in the form of an improved harmonically coupled anharmonic oscillator model (HCAO).[70−73] Multiple modes can be coupled to give a corrected representation of the individual vibrational states. For the LMM, a certain local mode is mapped out in terms of its potential energy and dipole moment and fitted against an anharmonic oscillator model (e.g. the Morse oscillator or spline fitting functions). The vibrational Hamiltonian is expressed through curvilinear coordinates q_i and q_j,[74,75]

$$\hat{H} = -\frac{\hbar^2}{2} \sum_{ij} \frac{\partial}{\partial q_i} g_{ij} \frac{\partial}{\partial q_j} + V' + V \,, \tag{2.72}$$

where g_{ij} is an element of the Wilson $\boldsymbol{g}$-matrix,[52] V' is the pseudo-potential and V the potential term. Using products of eigenvectors, resulting from the solutions of one-dimensional nuclear Schrödinger equations of a vibration, as basis functions, the Hamiltonian can then be diagonalised, yielding individual vibrational states.

A disadvantage of the variational methods is that an extensive part of the BO-PES needs to be known to obtain accurate frequencies. Furthermore, if the underlying method and basis set are not suitable to describe such a BO-PES accurately (they might be accurate enough to describe the immediate equilibrium region), the predictions through use of the variational methods suffer immensely, e.g. the famous case of a CCSD(T) BO-PES of a fluorine molecule.[76] Due to the smaller force field (semi-quartic in the case of VPT2), a simple perturbation approach can yield much better approximations to the experimentally determined vibrational frequencies. Another advantage is the small amount of computational effort that needs to be put into carrying out a VPT2 calculation compared to a variational variant. Additionally, one should mention that the eigenfrequencies obtained through VPT2 are those of a *Morse oscillator*, implying an excellent treatment of molecular stretching motions.[77]

---

[66] F. Culot, F. Laruelle, and J. Liévin. *Theor. Chim. Acta*, **92**: 211 – 226, 1995.

[67] J. O. Jung and R. B. Gerber. *J. Chem. Phys.*, **105**: 10332 – 10348, 1996.

[68] O. Christiansen. *J. Chem. Phys.*, **120**: 2149 – 2159, 2004.

[69] O. Christiansen. *Phys. Chem. Chem. Phys.*, **9**: 2942 – 2953, 2007.

[70] O. S. Mortensen, B. R. Henry, and M. A. Mohammadi. *J. Chem. Phys.*, **75**: 4800 – 4808, 1981.

[71] M. S. Child and R. T. Lawton. *Faraday Discuss. Chem. Soc.*, **71**: 273 – 285, 1981.

[72] H. G. Kjærgaard et al. *J. Chem. Phys.*, **93**: 6239 – 6248, 1990.

[73] B. R. Henry and H. G. Kjærgaard. *Can. J. Chem.*, **80**: 1635 – 1642, 2002.

[74] R. Meyer and E. B. Wilson. *J. Chem. Phys.*, **53**: 3969 – 3980, 1970.

[75] H. M. Pickett. *J. Chem. Phys.*, **56**: 1715 – 1723, 1972.

[76] P. Piecuch et al. *Comput. Phys. Commun.*, **149**: 71 – 96, 2002.

[77] D. A. Matthews, J. Vázquez, and J. F. Stanton. *Mol. Phys.*, **105**: 2659 – 2666, 2007.

There are of course occasions where the perturbation approach is disadvantageous. This is the case for vibrational modes which involve large amplitudes, as the assumptions in any perturbation theory only allow for small deviations. Moreover, the standard VPT2 algorithm in its different variants,[78] does neither account for Fermi nor for Darling–Denison resonance effects,[79,80] which are non-physical remnants of the underlying uncoupled harmonic oscillator model approximation, analogous to non-dynamic correlation in electronic structure methods.

In VPT2, it is possible to account for Fermi resonance effects by removing the resonant parts of the anharmonic constants (if $2\omega_k \approx \omega_m$ or $\omega_k + \omega_l \approx \omega_m$, where ω represents the harmonic vibrational frequency of mode k, l, and m) from the perturbative treatment and subsequently reintroducing the elements of a diagonalised coupling matrix (coupling between all the resonant modes).[81] Recently, Matthews et al. developed an improved technique of detecting such resonances by 'harmonic derivatives of perturbation theory corrections'.[82] The Darling–Denison resonance can also be accounted for, however it requires the full quartic force field. In most cases however such Darling–Denison resonances affects predominantly overtones of X–H stretching modes (where there is more than one H atom connected to X, e.g. H_2O).[77]

Vibronic transitions in molecules

An electronic state of a molecule can be approximated through the BO-PES model and subsequently this surface describes the vibrational behaviour of the molecule. If the electronic state of the molecule is changed however, it casts itself onto a new BO-PES. This change of electronic state can be caused by an electronic excitation in which case the dimensionality of the BO-PES stays the same; yet if an electron is lost or gained, it would constitute a transition to an $(N{-}1)$ or $(N{+}1)$ surface, respectively.

In comparison to vibrations, a change in electronic state is ca. 10^2 to 10^3 times faster than a vibrational transition, which means that the molecular structure undergoes almost no change during the electronic transition and can be considered adiabatic. This process was first described by James Franck, later extended by Edward Condon and is hence called *Franck–Condon (FC) principle*.[83–85] It is expressed

---

[78] V. Barone. *J. Chem. Phys.*, **122**: 014108, 2005.

[79] E. Fermi. *Z. Angew. Phys.*, **71**: 250 – 259, 1931.

[80] B. T. Darling and D. M. Dennison. *Phys. Rev.*, **57**: 128 – 139, 1940.

[81] S. Califano. *Vibrational states*, ISBN: 9780471129967 1976.

[82] D. Matthews and J. F. Stanton. *Mol. Phys.*, **107**: 213 – 222, 2009.

[83] J. Franck and E. G. Dymond. *Trans. Faraday Soc.*, **21**: 536 – 542, 1926.

[84] E. Condon. *Phys. Rev.*, **28**: 1182 – 1201, 1926.

[85] E. U. Condon. *Phys. Rev.*, **32**: 858 – 872, 1928.

through an expansion of Equation (2.70), where $\widehat{\boldsymbol{\mu}}_{\text{electric}}$ is now expressed as a sum of nuclear transition moment operator $\widehat{\boldsymbol{\mu}}_{\text{nuc}}$ and electronic transition moment operator $\widehat{\boldsymbol{\mu}}_{\text{el}}$.

$$
\begin{aligned}
\boldsymbol{d}_{\text{trans}} &= \left\langle \Psi' \,\middle|\, \widehat{\boldsymbol{\mu}}_{\text{electric}} \,\middle|\, \Psi'' \right\rangle \\
&= \left\langle \psi'_{\text{nuc}}\psi'_{\text{el}} \,\middle|\, \widehat{\boldsymbol{\mu}}_{\text{el}} \,\middle|\, \psi''_{\text{el}}\psi''_{\text{nuc}} \right\rangle + \left\langle \psi'_{\text{nuc}}\psi'_{\text{el}} \,\middle|\, \widehat{\boldsymbol{\mu}}_{\text{nuc}} \,\middle|\, \psi''_{\text{el}}\psi''_{\text{nuc}} \right\rangle \\
&\approx \left\langle \psi'_{\text{nuc}} \,\middle|\, \psi''_{\text{nuc}} \right\rangle \left\langle \psi'_{\text{el}} \,\middle|\, \widehat{\boldsymbol{\mu}}_{\text{el}} \,\middle|\, \psi''_{\text{el}} \right\rangle + \underbrace{\left\langle \psi'_{\text{el}} \,\middle|\, \psi''_{\text{el}} \right\rangle}_{=0} \left\langle \psi'_{\text{nuc}} \,\middle|\, \widehat{\boldsymbol{\mu}}_{\text{nuc}} \,\middle|\, \psi''_{\text{nuc}} \right\rangle && \text{(2.73a)} \\
&\approx \underbrace{\left\langle \psi'_{\text{nuc}} \,\middle|\, \psi''_{\text{nuc}} \right\rangle}_{f_{\text{FC}}} \left\langle \psi'_{\text{el}} \,\middle|\, \widehat{\boldsymbol{\mu}}_{\text{el}} \,\middle|\, \psi''_{\text{el}} \right\rangle && \text{(2.73b)}
\end{aligned}
$$

Since the two electronic states are orthogonal, the addend in Equation (2.73a) involving $\widehat{\boldsymbol{\mu}}_{\text{nuc}}$ is zero. This equation however is an approximation, as $\widehat{\boldsymbol{\mu}}_{\text{el}}$ also depends parametrically on the nuclear coordinates. Using the FC factors f_{FC} in Equation (2.73b), one can approximate the intensity of a transition; the remaining transition moment integral multipliers are the so-called *selection rules* which can be used to predict whether a transition is possible (within the approximations applied) or not.

If, in order to evaluate f_{FC}, it is assumed that a nuclear wave function is a product of harmonic oscillator functions, then the final state needs to be expressed in terms of normal coordinates of the initial state (or vice versa). It follows that f_{FC} is a product of one dimensional *FC integrals*. This approach – known as parallel mode approximation – is reasonable if the normal modes of the initial and final state present a similar displacement (parallel).[86] However, if these modes are significantly different, the parallel approximation fails. Another approach is to obtain f_{FC} as a product of multidimensional FC integrals.[87] Here, mode mixing between the initial and final vibrational states is accounted for by a rotation matrix (Duschinsky matrix) describing the normal mode displacements.[88]

There are of course other methods of solving the described vibronic problem. For the transitions from anion to neutral BO-PES transitions, neutral (N–1) ← anion (N), which are occurring in this work, other methods such as the Dyson orbital approach can yield better descriptions.[89]

---

[86] E. Hutchisson. *Phys. Rev.*, **36**: 410 – 420, 1930.

[87] H. Kupka and P. H. Cribb. *J. Chem. Phys.*, **85**: 1303 – 1315, 1986.

[88] F. Duschinsky. *Acta Physicochim. URSS*, **7**: 551 – 566, 1937.

[89] C. Melania Oana and A. I. Krylov. *J. Chem. Phys.*, **127**: 234106, 2007.

2.2 Experimental techniques

2.2.1 Supersonic expansion

In order to transfer molecules of interest into the gas-phase and form a molecular beam, a variety of techniques can be utilised, e.g. laser ablation, effusive expansion or supersonic expansion. The latter technique is applied in the present work, as it provides the necessary cooling and collimation.

In a supersonic free-jet expansion, one prepares a gas reservoir at pressure p_0, temperature T_0 and density n_0, and passes this through a nozzle with an orifice diameter d_O. The internal energy shall be defined as $U = U_\mathrm{trans} + U_\mathrm{rot} + U_\mathrm{vib} + U_\mathrm{el}$, where U was split up into a translational, rotational, vibrational and electronic part, respectively. For one mole of the gas with the mass m, the total energy will be a sum of the internal energy U, the potential energy pV and the flow energy $\frac{1}{2}m\boldsymbol{u}^2$, where $\boldsymbol{u}$ is the velocity of the beam. In the case of a supersonic expansion, where d_O is much smaller than the mean free path λ of the gas at p_0, parts of the internal energy and almost all of the potential energy are converted into kinetic flow energy. As the gas in the source is mostly stationary, it is fair to assume that its kinetic flow energy is zero. Also, it is assumed that after the expansion, p is very small which renders the potential energy after expansion approximately zero.

$$U_0 + p_0V_0 = U + \frac{1}{2}m\boldsymbol{u}^2 \tag{2.74}$$

While the conversion between potential energy and flow energy is due to the pressure difference, the conversion of internal energy is caused by collisions before, in and shortly after the orifice. Before exiting the nozzle, fast particles are slowed down while slower ones are accelerated, as only a limited flow can pass the orifice. This behaviour leads to a narrowing of z-component of the velocity distribution. The perpendicular r-component of this distribution is also narrowed down to a certain extent. However this is rather due to a geometrical effect showing a decreased likelihood for a particle exiting the nozzle if it has a large v_r; this effect is known as *geometrical cooling*.[90]

If the particles have any molecular structure, they are able to undergo vibrations and rotations. Since rotational transitions require more energy than translation and vibrational transitions even more than rotational transitions, their respective cross sections are much smaller. For this reason, the quenching

---

[90] W. Demtröder. *Laser Spectroscopy Vol.2: Experimental techniques*, ISBN: 9783540749523 2008.

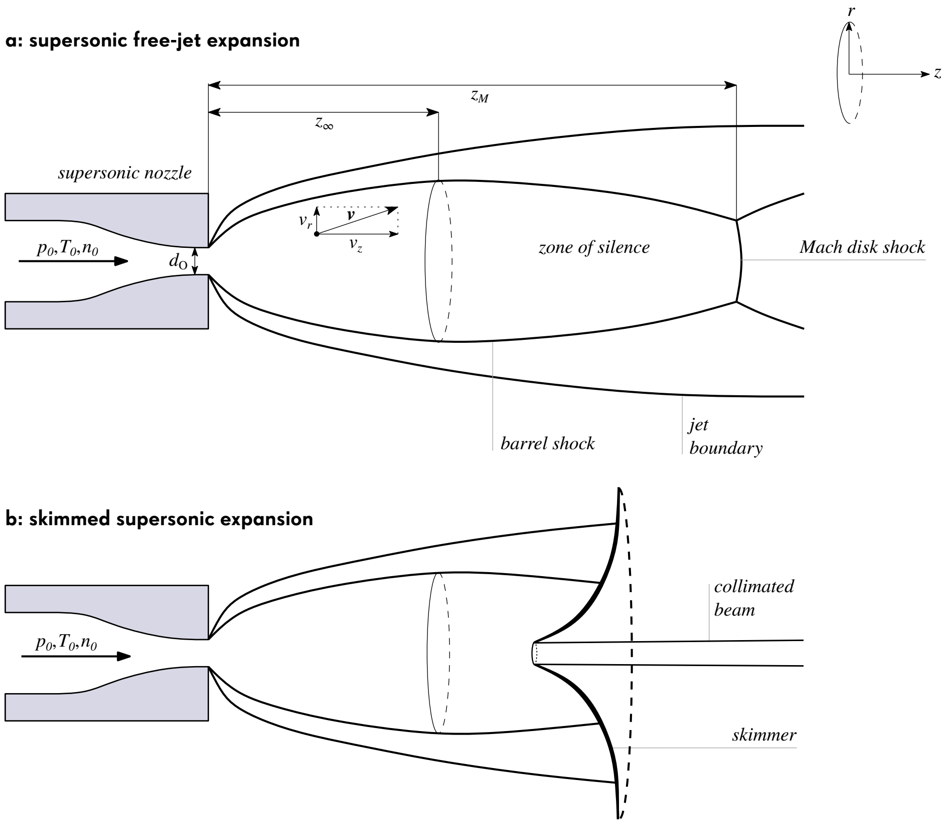

Figure 2.1 | Schematic representation of skimmed and unskimmed supersonic expansions. Adapted and modified scheme sourced from Koperski et al. and Vallence.[91,92]

of internal translational energy is more effective than the rotational quenching, which again is much more efficient than vibrational quenching.[91,92]

When undertaking molecular spectroscopy experiments, it is of advantage to only populate the lowest lying vibrational and rotational states. In order to increase the cooling efficiency, the target molecules are usually seeded in a noble carrier gas (due to their lack in rotations and vibrations), where the partial pressure of the target molecules would normally not exceed 10 % of the total pressure. As an example, it is found that for 3 % NO_2 in Ar (p_0 = 1 bar, d_O = 100 µm), the temperatures are as follows; $T_{trans} \approx 1$ K, $T_{rot} \approx 5$ K to 10 K, $T_{vib} \approx 50$ K to 100 K.[90]

---

[91] J. Koperski and E. S. Fry. , **39**: S1125 – S1150, 2006.

[92] C. Vallence ‘Molecular Reaction Dynamics Lectures 1–4’ Accessed on 01/03/2013

After exiting the nozzle, the gas undergoes an adiabatic expansion which, depending on the number of collision, leads to significant cooling. The value of the beam velocity will thereby exceed the local speed of sound which is the reason for the term supersonic expansion. At some distance z_∞ (as indicated in Figure 2.1a), the density becomes so low that there are effectively no more collisions between the gas particles. The distance z_∞ can be described by an *empirical* equation, where pressures are expressed in atm and distances in cm.[93]

$$z_\infty = 260.586 d_\mathrm{O} (d_\mathrm{O} p_0)^{\frac{3}{5}} \tag{2.75}$$

At this point, the lack of collisions causes the various distributions to be locked in their state, as energy transfer is not possible anymore. Due to its nature the region of the beam after z_∞ is called *zone of silence*. As the expansion is supersonic it causes a series of shock waves. One of these is the barrel shock which, as the pressure acts in all directions, at some point overwhelms the inner Mach shock, forcing it back inwards and causes the formation of a so-called *Mach disk*. One can approximate the distance of the Mach disk shock from the nozzle z_m for a monoatomic gas in an *empirical* way by only accounting for the orifice diameter d_O, the pressure in the vacuum chamber p_1 and the reservoir pressure p_0,[93]

$$z_M = 0.67 d_\mathrm{O} \sqrt{\frac{p_0}{p_1}}, \tag{2.76}$$

where the pressure is expressed in atm and d_O in cm. In the case of helium, Equation (2.76) fails due to predominant quantum effects that increase the cross sections for low energy collisions.[94]

In order to collimate the beam and to prevent the Mach disk from forming, it is necessary to deflect the barrel shock. This can be achieved by placing a skimmer into the zone of silence, as described in Figure 2.1b. By only allowing the very centre of the beam to pass through an orifice in the skimmer, one also removes the outwards moving particles from the beam.

2.2.2 Anion formation

A common way to generate anions for investigation in mass or molecular spectroscopy is by means of electron impact. In the present study, fast electrons intercept the supersonically expanding beam before it reaches the zone of silence. Since the majority of the expanding gas-mixture contains a noble

---

[93] M. D. Morse. In: *Atomic, Molecular, and Optical Physics: Atoms and Molecules*, 21 – 47, 1996.

[94] J. P. Toennies and K. Winkelmann. *J. Chem. Phys.*, **66**: 3965 – 3979, 1977.

gas E as a carrier (in most cases Argon) the probability of an interaction between these and the fast electron are the highest, causing an ejection of a slower electron in a *single ionisation* event.[95]

$$\mathrm{E} + \mathrm{e}^-_{\text{fast}} \longrightarrow \mathrm{E}^+ + \mathrm{e}^-_{\text{scattered}} + \mathrm{e}^-_{\text{slow}} \tag{R 2.1}$$

Reactions with other beam constituents–e.g. double and multiple ionisations, dissociative ionizations as well as ion pair formations–might also occur.[95] The cross sections of these processes are very small and thus play an insignificant role in the present study.

Slow electrons (kinetic energy $E_{e\mathrm{KE}} < 20\,\mathrm{eV}$) generated in reaction (R 2.1), can be captured by molecules X···Y of the expanding particle beam. The resulting transient anions harbour an excess of internal energy (and hence are marked by an asterisk) and might also be in an excited electronic state.

$$\mathrm{X{\cdots}Y} + \mathrm{e}^-_{\text{slow}} \longrightarrow [\mathrm{X{\cdots}Y}]^{-*} \tag{R 2.2}$$

The metastable product $[\mathrm{X{\cdots}Y}]^{-*}$ can undergo a variety of subsequent reactions.[96]

$$\begin{aligned}
[\mathrm{X{\cdots}Y}]^{-*} &\longrightarrow \mathrm{e}^-_{\text{slow}} + \mathrm{X{\cdots}Y} && \textit{elastic scattering} && \text{(R 2.3a)}\\
&\longrightarrow \mathrm{e}^-_{\text{slower}} + [\mathrm{X{\cdots}Y}]^{*} && \textit{inelastic scattering} && \text{(R 2.3b)}\\
&\longrightarrow \mathrm{X}^{*} + \mathrm{Y}^- && \textit{dissociative electron attachment} && \text{(R 2.3c)}\\
&\longrightarrow [\mathrm{X{\cdots}Y}]^- + \text{energy} && \textit{parent negative ion formation} && \text{(R 2.3d)}
\end{aligned}$$

Reaction (R 2.3a) is essentially the reverse of reaction (R 2.2). The inelastic scattering leaves an excited neutral parent molecule and a scattered electron with less kinetic energy than the initially captured slow electron. Most important for the present work is the dissociative electron attachment reaction (R 2.3c), providing a pathway to a fragment anion Y^- with relatively low internal energy. Finally, it is also possible to generate the parent anion via reaction (R 2.3d), the excess internal energy is dissipated through collisions with the surrounding particles. Of course, the products of these reactions can undergo further reactions, which however depend heavily on the involved molecules, their partial pressure and other reactants.

---

[95] T. Märk. In: *Electron-Molecule Interactions and their Applications*, 251 – 334, 1984.

[96] L. Christophorou, D. McCorkle, and A. Christodoulides. In: *Electron-Molecule Interactions and their Applications*, 477 – 617, 1984.

2.2.3 Time-of-flight mass spectrometry and ion optics

It is possible to separate the generated ions by their mass-to-charge ratio *m*/*z* using a time-of-flight mass spectrometer (TOF-MS). In the present work, this technique is used to temporally and spatially isolate a single *m*/*z* which subsequently is subjected to further analysis. To achieve separation, a set of ion optics is necessary, the modes of operation of which are discussed here briefly.

Acceleration

Historically, in conventional TOF-MSs, the acceleration region consisted of a single charged electrode (Voltage V_1, same charge as the ion of interest) with a grounded plate at the end.[97] In the lower panel of Figure 2.2a, the potential V and change in the initial velocity distribution $I_0\left(\boldsymbol{v}, m_{\mathrm{Y}^-}\right)$ of a single particle Y^- is illustrated. For an ideal case, where I_0 is equal to a δ-distribution (non-interacting particles, perfect field structure), all particles would be accelerated to the same speed and mapped onto the same spot of the Micro-channel plate (MCP) detector at the end of the drift area. The repulsion between the particles however causes the accelerated beam to widen (increase in beam diameter d_{b} along $r = \sqrt{x^2 + y^2}$). Indubitably I_0 is not a δ-distribution but rather, depending on the source of the ionised particles distributed in such a way that at the time of acceleration initiation (t_0), some particles feature velocities with positive or negative v_z-components. Hence, those particles with negative v_z need to be turned around by the electric field, which increases their flight time by $t_2 - t_1$ (see upper panel of Figure 2.2a) causing a larger distribution in the arrival times.

The latter issue can be accounted for by a linear electric field in the acceleration region. Implemented first by Wiley and McLaren, the acceleration region is equipped with an additional extractor electrode exhibiting a lower voltage V_2 (in absolute terms) than the repeller electrode.[98] In this set-up, an ion with a negative v_z-component penetrates a region of higher potential and hence experiences a stronger acceleration and subsequently this ion can ‘catch up’ with other ions featuring positive v_z-components. This technique is often refered to as *spatial focusing* as the extractor and repeller voltage have to be chosen carefully in order to establish a temporal coalescence at the MCP detector.[98,99]

---

[97] A. E. Cameron and D. F. Eggers. *Rev. Sci. Instrum.*, **19**: 605 – 607, 1948.
[98] W. C. Wiley and I. H. McLaren. *Rev. Sci. Instrum.*, **26**: 1150 – 1157, 1955.
[99] M. Guilhaus. *J. Mass Spectrom.*, **30**: 1519 – 1532, 1995.

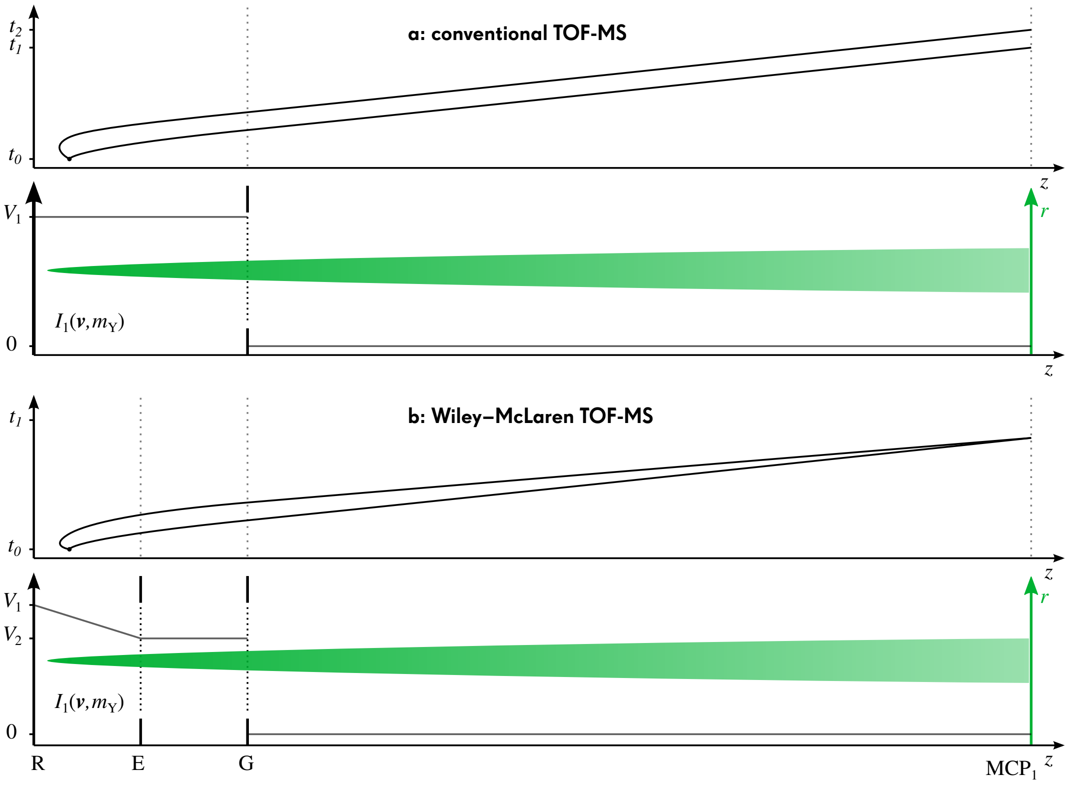

Figure 2.2 | Comparison of potential, time and spacial domains between a conventional (a) and a Wiley–McLaren (b) type TOF-MS; R – repeller electrode, E – extractor electrode, G – grounded electrode, MCP_1 – first micro-channel plate detector.

Electrostatic deflection and lensing

If the initial velocity distribution I_0 is skewed towards one direction, e.g. due to supersonic expansion perpendicular to the z direction, it is necessary to compensate for this using x-y-deflection plates. These create a homogeneous electric field in their respective direction, guiding the ion beam without imparting additional kinetic energy in z-direction.

As illustrated in Figure 2.2, the ion beam is diverging naturally due to inter-ionic repulsion. In order to reduce d_b, *einzel lenses* are commonly used. The electric fields generated by these electrodes cause charged particles to follow a path similar to that of a light beam passing through a convex or concave lens.

An einzel lens consists of cylindrical electrodes arranged along the flight path (see Figure 2.3). The central cylinder exerts a certain potential V_E, while the two outer cylinders would be at the beam reference potential (most likely ground). If V_E carries the same sign as the charge of the passing particles, the einzel lens causes the beam to focus without affecting the kinetic energy in z-direction.[•]

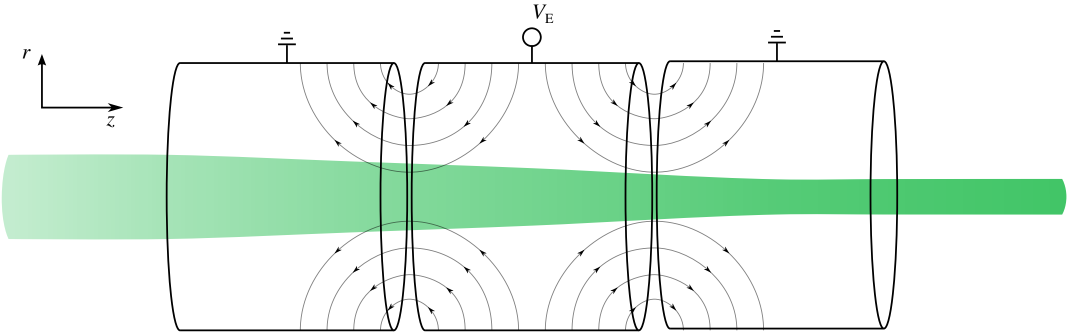

Figure 2.3 | Schematic representation of a charged particle beam passing an einzel lens. The vector field structure is idealised, a more detailed simulation of the vector field electric potential can be found in Equation (A.25).

2.2.4 Photoelectron time of flight spectroscopy

In the laser interaction region, a laser beam of a given energy E_laser interacts with an anionic particle beam. If E_laser is larger than the anion's valence electron binding energy $E_{e\mathrm{BE}}$, photoelectrons are ejected from the cloud of anions, the kinetic energy $E_{e\mathrm{KE}}$ of which are given by the difference between E_laser and $E_{e\mathrm{BE}}$. This was first applied by Brehm et al. and effectively introduced the a new branch of spectroscopy, namely anion photoelectron spectroscopy (PES).[100]

Depending on the polarisation of the laser and the nature of the originating orbital, the electrons exhibit a certain photoelectron angular distribution $I_\mathrm{PAD}(\phi, \theta)$, where θ represents the polar angle and ϕ the azimuthal angle; the distribution can be described through spherical harmonics. In the simplest case, $I_\mathrm{PAD}(\phi, \theta)$ can be of spherical symmetry, which means that a sphere of electrons each with the same speed is ejected from the anion cloud. Although there are many interactions e.g. electrostatic repulsion from the anions and repulsions between the electrons, if the density of particles is low enough,

---

[•] While the final kinetic energy remains unaffected, particles get slowed down and accelerated during the focusing process.

[100] B. Brehm, M. Gusinow, and J. Hall. *Phys. Rev. Lett.*, **19**: 737 – 741, 1967.

the cloud of photoelectrons expand with a constant speed (assuming a field free environment). The electrons drift through a time of flight region and will reach a suitable detector.

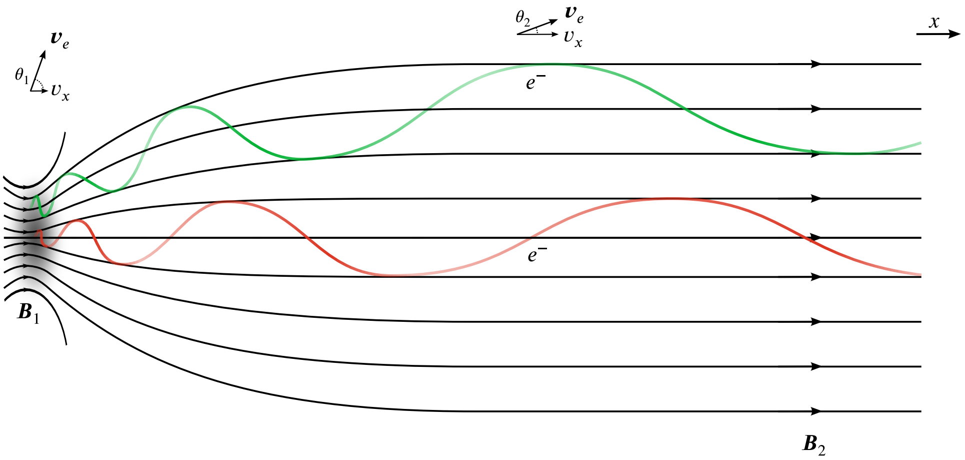

Figure 2.4 | Schematic representation of the magnetic bottle type field structure, where the field changes gradually from a stronger field $\boldsymbol{B}_1$ to a weaker field $\boldsymbol{B}_2$. Photoelectrons ejected from the various points within the (shaded) interaction region, undergo a helical motion and eventually reach parallel trajectories. Illustration adapted from Ref. [101]

A longer the drift region allows for a better temporal separation of the electrons, but it also decreases the solid angle for detection, i.e. the detection efficiency is reduced. Commonly however, a ‘magnetic bottle’ type field is employed.[101,102] As described in Figure 2.4, in the anion-laser interaction region, a strong inhomogeneous magnetic field $\boldsymbol{B}_1$ is applied, while the drift region is engulfed in a weaker homogeneous magnetic field $\boldsymbol{B}_2$. The field gradient forces the electrons to follow a helical trajectory towards the detector in x-direction, the angle of which is given through θ_2,[101]

$$\frac{\sin\theta_2}{\sin\theta_1} = \sqrt{\frac{B_2}{B_1}}\,. \tag{2.77}$$

For the movement of an electron in this magnetic field the energy and the angular momentum in x-direction are conserved entities. Hence, the movement of the electrons is parallelised; also, the absolute value of the electron velocity $\boldsymbol{v}_e$ remains constant. The transverse component v_x is reduced according to the following equation.[101]

$$v_x = |\boldsymbol{v}_e|\sqrt{1 - \frac{B_2}{B_1}\sin^2\theta_1} \tag{2.78}$$

---

[101] P. Kruit and F. H. Read. *J. Phys. E: Sci. Instrum.*, **16**: 313 – 324, 1983.
[102] O. Cheshnovsky et al. *Rev. Sci. Instrum.*, **58**: 2131 – 2137, 1987.

The initial angle of electron ejection θ_1 is not important for electrons that already fly in the direction of the detector (assuming a long flight tube). Electrons starting with a velocity component in negative x-direction however need to be turned around. This leads to different flight paths l for different velocities, i.e. peak broadening in the spectrum, which can be reduced by altering the laser polarisation and reducing the photoelectron kinetic energy. With the magnetic bottle, one is able redirect almost the full solid angle of 4π sr of the ejected photoelectrons at the cost of resolution. Another source of peak broadening is due to the Doppler effect whereby the ejected electrons retain the momentum of the originating ion. This effect can be reduced by slowing down the arriving ions, e.g. by use of an ion decelerator.[102]

In order to transform the electron time of flight intensity distribution $I_{e\mathrm{TOF}}(t)$, which is measured at the detector into the electron kinetic energy domain, $I_{e\mathrm{KE}}(E)$, one can use the following relationship.

$$\begin{aligned} \left| I_{e\mathrm{TOF}}(t)\,\mathrm{d}t \right| &= \left| I_{e\mathrm{KE}}(E)\,\mathrm{d}E \right| \\ I_{e\mathrm{KE}}(E) &= \left| \frac{\mathrm{d}t}{\mathrm{d}E} \right| I_{e\mathrm{TOF}}(t) \end{aligned} \tag{2.79}$$

A typical laser energy is 4.66 eV (frequency quadrupled neodymium-doped yttrium aluminium garnet (Nd:YAG) laser). If a transition from I^- to the ${}^2P_{3/2}$ state of I is excited (requires 3.05 eV), the ejected electrons would move with ca. $10^{-3}c$, a speed where relativistic effects are negligible. The kinetic energy can therefore be expressed as $E_{e\mathrm{KE}} = \frac{m_e l^2}{2t^2}$. When applied to Equation (2.79), one retrieves $I_{e\mathrm{TOF}}(t)$.

$$I_{e\mathrm{KE}}(E) = \frac{t^3}{m_e l^2} I_{e\mathrm{TOF}}(t) \tag{2.80}$$

This equation is an approximation, as the distance an electron flies l varies depending on the initial velocity vector and the structure of the magnetic field. The time of flight t is also not known exactly. For these reasons, the spectrum is calibrated by factors found through fitting an experimental spectrum against known transitions of certain ions.

2.2.5 Velocity map imaging

The previously introduced PES technique exhibits in the best of cases a resolution limit of 5 meV to 10 meV. Due to this ‘low’ resolution, the arising finer features resulting from a dense vibrational structure might be obscured at best. To overcome these limitations, Zero kinetic energy (ZEKE) PES was introduced by Schlag and co-workers.[103,104] While their technique is limited to neutrals, a version for anion spectroscopy was developed shortly after.[105,106] This technique is applied readily and inspired numerous studies.[107–111]

This type of PES involves tuning the laser wavelength in such a way that it produces photoelectrons with no kinetic energy at all (ZEKE electrons). As the laser wavelength is scanned, different amounts of ZEKE electrons are detached from the anions according to the possible vibronic transitions from the anion to the neutral states. For ZEKE spectroscopy, a resolution limit of 0.2 meV to 0.1 meV has been reported,[112] mostly governed by the wavelength width of the tunable laser. However, the Wigner-law implies some further limitations in the applicability of this technique,[113]

$$\sigma \propto \left(h\nu - E_{\mathrm{th}}\right)^{l+\frac{1}{2}} , \tag{2.81}$$

where σ is the cross section for electron detachment (effectively the probability) and E_{th} is the threshold energy. As the angular momentum quantum number l of the electron wave increases, the probability of emission decreases. In practice, p-states ($l = 1$) are almost never detectable. A further disadvantage is the susceptibility of the detached electron to minute stray electric or magnetic fields, which requires a very careful experimental set-up.

To address some of these shortcomings, in 2005 Wolf et al. developed a variation of ZEKE PES. The method also uses a tunable laser; yet it requires for the photon energy to be slightly above threshold, producing slow photoelectrons. A special magnetic bottle design guides these slow electrons to the detector. The resolution of this ‘photoelectron action at constant kinetic energy’ method is with 1 meV slightly below that of anion ZEKE, yet it avoids its major drawbacks.[114]

The arrival of fast cameras enabled another approach to increase the resolution of PES. In 1997, Parker and Eppink introduced of what is known as velocity map imaging (VMI) spectroscopy.[3] For this technique the three-dimensional velocity distribution of the detached photoelectrons is projected onto

---

[103] K. Müller-Dethlefs, M. Sander, and E. W. Schlag. *Chem. Phys. Lett.*, **112**: 291 – 294, 1984.

[104] K. Müller-Dethlefs and E. W. Schlag. *Annu. Rev. Phys. Chem.*, **42**: 109 – 136, 1991.

[105] T. Kitsopoulos et al. *Chem. Phys. Lett.*, **159**: 300 – 306, 1989.

[106] I. M. Waller, T. N. Kitsopoulos, and D. M. Neumark. *J. Phys. Chem.*, **94**: 2240 – 2242, 1990.

[107] C. Bässmann et al. *Int. J. Mass Spectrom. Ion Processes*, **159**: 153 – 167, 1996.

[108] V. Distelrath and U. Boesl. *Faraday Discuss.*, **115**: 161 – 174, 2000.

[109] G. F. Gantefor, D. M. Cox, and A. Kaldor. *J. Chem. Phys.*, **93**: 8395 – 8396, 1990.

[110] T. Lenzer et al. *J. Chem. Phys.*, **110**: 9578 – 9586, 1999.

[111] F. Schlicht, M. Entfellner, and U. Boesl. *J. Phys. Chem. C*, **114**: 11125 – 11132, 2010.

[112] D. M. Neumark. *J. Phys. Chem. A*, **112**: 13287 – 13301, 2008.

[113] E. Wigner. *Phys. Rev.*, **73**: 1002 – 1009, 1948.

[114] I. Wolf et al. *J. Chem. Phys.*, **122**: 141101, 2005.

a two-dimensional screen by an *asymmetric immersion lens*. Using velocity distribution reconstruction methods, one can recover the full three dimensional distribution, therefore also enabling the analysis of the photo-angular distribution $I_{\text{PAD}}(\phi, \theta)$ (as introduced previously). A variety of studies were carried out using this technique,[115–118] including high-resolution ones such as those by Cavanagh and co-workers.[119]

By only accounting for slower electrons that originated from states just above the ZEKE level, Osterwalder et al. were able to resolve the issue arising from the Wigner-law.[120] Incidentally, this subclass of VMI–often referred to as slow-electron velocity map imaging (SEVI) technique–also has the advantage of a much higher data collection rate (as much as two orders of magnitude higher).[112] Generally, multiple SEVI spectra are overlapped, providing a larger range, where each spectrum requires ca. 10^4 events for an adequate quality.

The Abel transform

During a VMI experiment, a polarised laser interacts with a particle beam and the polarisation vector forms an axis of symmetry. Within the space of the interaction region, a strong electrostatic field accelerates the ejected electrons towards an imaging plane. The inhomogeneous property of the field –described by Parker and Eppink as an asymmetric immersion lens– allows for electrons with the same initial velocity vector to be 'mapped on the same point on the detector, irrespective of their initial distance from the ion lens axis'.[3]

The most popular velocity distribution reconstruction method for VMI is the inverse Abel transform. It can be applied since the laser polarisation imparts a cylindrical symmetry onto the emerging three dimensional electron velocity distribution $I\left(x, r\right)$, where $r = y^2 + z^2$. The two dimensional projection in y' and x', $P\left(y', x'\right)$ is given through the Abel integral.[121]

$$P\left(y', x'\right) = 2 \int_r^\infty \frac{I\left(x, r\right) r}{\sqrt{r^2 - y^2}} \,\mathrm{d}r \tag{2.82}$$

---

[115] T. Suzuki and B. J. Whitaker. *Int. Rev. Phys. Chem.*, **20**: 313–356, 2001.

[116] A. Stolow, A. E. Bragg, and D. M. Neumark. *Chem. Rev.*, **104**: 1719–1758, 2004.

[117] M. N. R. Ashfold et al. *Phys. Chem. Chem. Phys.*, **8**: 26–53, 2006.

[118] A. Sanov and R. Mabbs. *Int. Rev. Phys. Chem.*, **27**: 53–85, 2008.

[119] S. Cavanagh et al. *Phys. Rev. A*, **76**: 052708, 2007.

[120] A. Osterwalder et al. *J. Chem. Phys.*, **121**: 6317–6322, 2004.

[121] E. W. Hansen and P.-L. Law. *J. Opt. Soc. Am.*, **2**: 510–519, 1985.

Here, x is the cylinder axis, parallel to which lies the y'-x' plane in some distance along z. An inverse Abel transform therefore allows for the recovery of the original three dimensional distribution.[122]

$$I(x,r) = -\frac{1}{\pi}\int_r^{\infty} \frac{\mathrm{d}P\left(y',x'\right)}{\mathrm{d}y'} \frac{\mathrm{d}r}{\sqrt{y^2-r^2}} \tag{2.83}$$

As such, the Abel transform based velocity distribution reconstruction algorithms all share a common disadvantage, namely the amplification of any noise, especially around the centreline of the image. Alternatives to the transform exist, the most promising of which is the *maximum entropy velocity image reconstruction*.[123] As the name suggests, in the method, the most likely distribution corresponding to the observed image is found and hence does not rely on smoothing or inverting the original data.

---

[122] V. Dribinski et al. *Rev. Sci. Instrum.*, **73**: 2634 – 2642, 2002.

[123] B. Dick. *Phys. Chem. Chem. Phys.*, **16**: 570 – 580, 2013.

Chapter 3

Photoelectron experiments

3.1 General overview and motivation

The invention of the laser and its implementation in photoelectron spectroscopy (PES) in the late 1960s,[100] fertilised a vast ground in physical chemistry. Not only was it one of the first techniques with which one could determine vertical atomic and molecular electron detachment energies; it also allowed investigations into otherwise inaccessible electronic states. Applications include, for example, the characterisation of the electronic structure of small molecular systems such as NO_2^-,[124] but can also shed light on solvation effects that influence small clusters.[125,126]

By combining these data with theoretical modelling it is possible to draw conclusions about the underlying Born–Oppenheimer potential energy surface (BO-PES) which ultimately determines the bonding behaviour of a certain molecular system. However, due to the resolution limit of PES, the fine structure arising from excitation of the low energy intermolecular vibrations can be obscured. To overcome these limitations, Zero kinetic energy (ZEKE) PES and later velocity map imaging (VMI) as well as slow-electron velocity map imaging (SEVI) was introduced (see Section 2.2.5 for a more detailed overview).

3.1.1 A TOFMS-PES-VMI apparatus

In 2008, LaMacchia and Wild constructed a time-of-flight mass spectrometer (TOF-MS) coupled to a photoelectron spectrometer at the Wild laboratory of the University of Western Australia (UWA),[127] which was used for a variety of studies involving chloride,[128] bromide,[129] and iodide carbon monoxide clusters.[130] Recently, a further study on halide acetylene complexes has also been published.[131] Furthermore, $X^-\cdots(N_2)_n$, $X^-\cdots(NO)_n$ as well as $Br^-\cdots(N_2O)_n$ (where X represents Cl, Br or I, n is up to 6 molecules) have been investigated and will be published soon.

One major task for the present project was the development of an improved PES apparatus. Initially, due to limited funding, a ZEKE photoelectron spectrometer was proposed. However, as additional

---

[124] K. M. Ervin, J. Ho, and W. C. Lineberger. *J. Phys. Chem. C*, **92**: 5405 – 5412, 1988.

[125] G. Markovich et al. *J. Chem. Phys.*, **101**: 9344 – 9353, 1994.

[126] A. W. Castleman and K. H. Bowen. *J. Phys. Chem. C*, **100**: 12911 – 12944, 1996.

[127] R. LaMacchia. *Towards Anion Photoelectron Spectroscopy of Complexes and Clusters*. MA thesis. University of Western Australia, 2008.

[128] K. Lapere et al. *Chem. Phys. Lett.*, **504**: 13 – 19, 2011.

[129] K. M. Lapere et al. *Aust. J. Chem.*, **65**: 457 – 463, 2012.

[130] K. M. Lapere et al. *J. Phys. Chem. A*, **116**: 3577 – 3584, 2012.

[131] D. Beckham et al. *Chem. Phys. Lett.*, **619**: 241 – 246, 2015.

Figure 3.1 | Plan view of the TOF-PES-VMI set-up. Red and green colour identifies components added in the course of the 'VMI extension' described in Section 3.3.1. Unaltered ion optics and chambers are outlined in grey and black, respectively (with respect to the machine description in Ref. [127]).

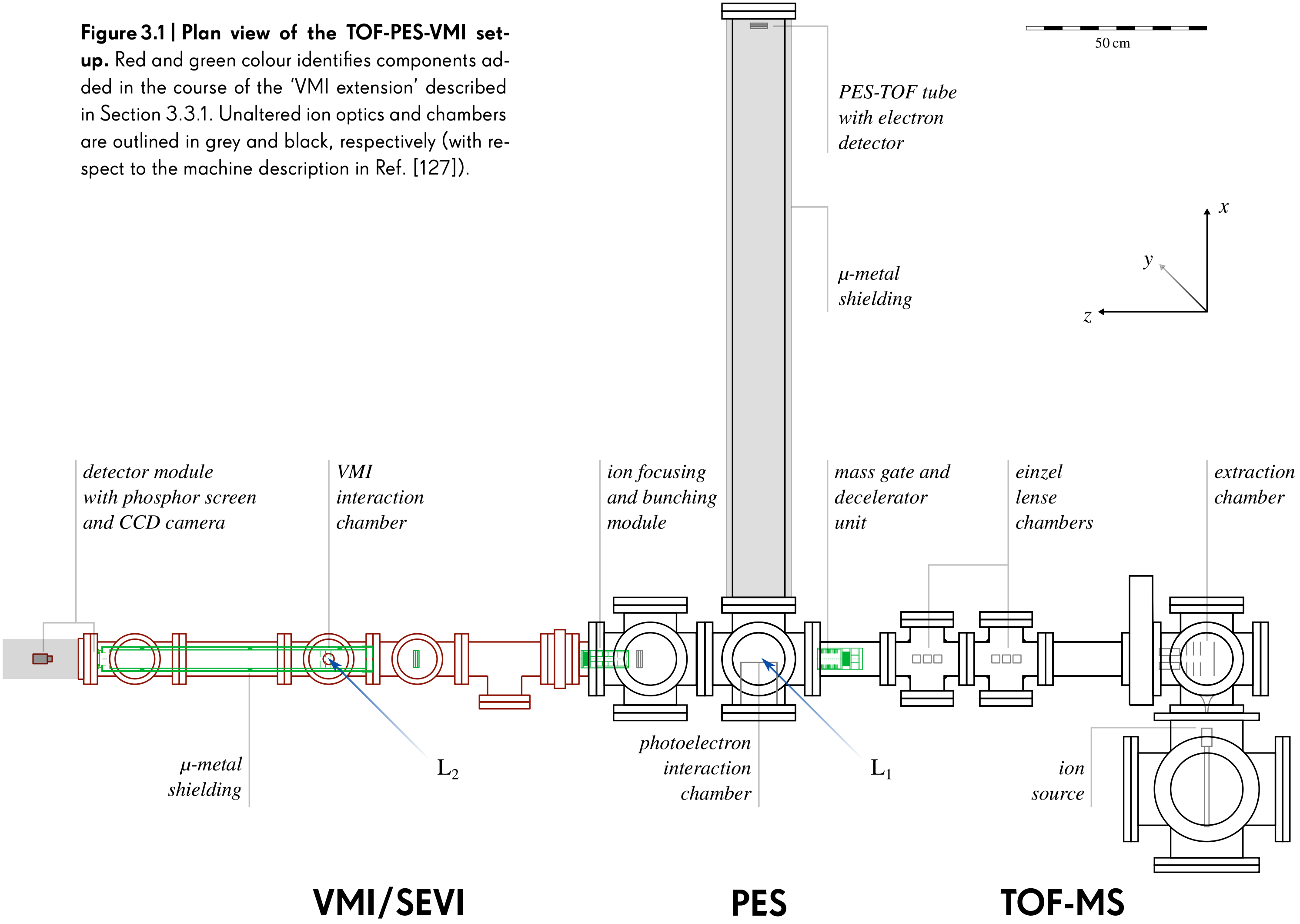

funding became available, it was decided to build a VMI/SEVI photoelectron spectrometer instead. Sections outlined in red colour in the plan view, of the now combined TOFMS-PES-VMI apparatus (see Figure 3.1), mark the new 'VMI extension' next to the photoelectron spectrometer, the TOF-MS and the ion source.

At the point of writing, the construction phase of the VMI spectrometer is completed and preliminary tests have been undertaken. Unfortunately, due to a limited candidature for this project of 3½ years due to the candidate being an International student, the apparatus is still in a prototype stage and requires more testing. Details of the VMI set-up as well as a description of the preliminary testing phase are presented in Section 3.3.

3.2 Existing infrastructure

The VMI spectrometer is designed with the existing TOF-MS-PES apparatus in mind. A detailed overview and description of the different parts of the apparatus can be found in the PhD thesis of Kim Lapere.[132] For purpose of comprehensibility however, a brief overview of the existing spectroscopic infrastructure is still given.

3.2.1 Ion source and extraction

An initial gas mixture is ejected from a reservoir and expanded supersonically through a pulsed solenoid nozzle *(General Valve Series 9, Parker Hannifin)* into the source chamber at a rate of 10 Hz. While the initial gas mixture is kept at a pressure p_0 of 450 kPa, the source chamber, during experiment, reaches a pressure p_1 of ca. 1 mPa (1 μPa at rest). The expanding gas mixture is then intercepted by an electron beam ($E_{e\mathrm{KE}} < 500\,\mathrm{eV}$, ca. 3 mm after ejection) causing an electron impact reaction. The electron beam is generated by a home-built electron pulser consisting of rhenium filament encased by a Wehnelt's cylinder which acts as a cathode directing the thermionic electrons through an einzel lens towards the expanding beam. Since the einzel lens acts as an electron focusing device, it is possible to create a tight point of convergence between the electrons and the expanding gas mixture.

---

[132] K. M. L. Lapere. *Anion photoelectron spectroscopy of halide complexes and clusters*. PhD thesis. University of Western Australia: School of Chemistry and Biochemistry, 2014.

As described in Section 2.2.2, the electron bombardment subsequently leads to the formation of anionic particles (molecules and atoms). Together with the neutral and positively charged particles they form a beam which drifts through a conical skimmer (placed in a distance of ca. 80 mm from the ejection point in order to deflect the barrel shock) into the extraction region of the mass spectrometer.

3.2.2 Time-of-flight mass spectrometer

When the particle beam reaches the centre of the acceleration region of the Wiley–McLaren TOF-MS, the repeller and extractor plate voltages are immediately (rise time of ca. 15 ns) set to $V_\mathrm{R} \approx -1000\,\mathrm{V}$ and $V_\mathrm{E} \approx -900\,\mathrm{V}$, respectively. These two voltages can be varied in order to optimise the space-focusing effect farther down the flightpath. Unaffected by the field, the neutrals continue in a straight line; the cations are accelerated towards the repeller plate and the anions are pushed into the time of flight (TOF) tube (see Figure 2.2). The time it takes for for V_R and V_E to reach their respective maximum voltage is 15 ns.

Along the anion flightpath, outlined in Figure 3.2, there are ion optic elements which are used to optimise the beam trajectory. The first set of optics are the x-y deflection plates which are primarily used to compensate for the drift speed of the particle beam due to the initial expansion, but also serve as positioning aids. The second segment contains two sets of einzel lenses, allowing for focusing and compensation of the slow divergence of the beam. Subsequently, the particle beam drifts through a mass gate as well as an ion decelerator module. Since the design of these two elements have been improved, they are discussed separately in Section 3.3.1. Finally, the mass spectrum can be obtained when the particles hit the first micro-channel plate MCP_1 (*Burle APD 3025MA*, 25 mm diameter, Chevron configuration, 10 µm pore size). Here, the MCP front face is grounded, the back face is floated at

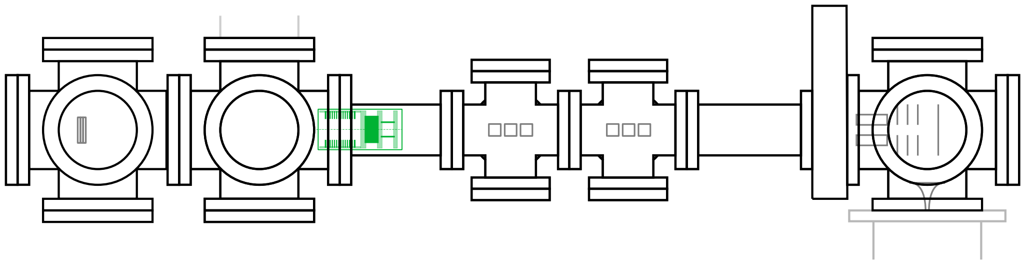

Figure 3.2 | Plan view of the current TOF-MS set-up at UWA. The grey outlines mark the positions of the ion-optics, starting (right) with the Wiley–McLaren extraction optics, followed by x-y deflection plates, two sets of einzel lenses, the mass-gate and ion decelerator unit and finally the MCP ion detector (left).

1700 V and the detecting anode is subjected to 1750 V. MCP_1 is retractable to allow for the passage of the particle beam to the VMI section.

In Figure 3.3 an example of a mass-spectrum at MCP_1 is provided. It serves as an aid to determine the MCP_1 mass-resolution, which is obtained through fitting a Gaussian function through an individual peak. This then provides the standard deviation σ as a fitting parameter. The mass-resolution is then defined through the full width at half maximum (FWHM)

$$\frac{m}{\Delta m} = \frac{m}{2\sqrt{2\ln 2}\,\sigma}, \tag{3.1}$$

which suggests a resolution of 121.74 for $^{37}\mathrm{Cl}^-$ and 124.89 for $^{35}\mathrm{Cl}^-$.

These values do not compare well with other high-resolution spectroscopy, however, one should note that (3.1) is biased towards higher masses, as Δm is not linearly dependant on m. For example, a peak occurring at a mass to charge ratio of 147.4 m/z already yields a resolution of 149.3. For all experiments planned with the present apparatus, this resolution is sufficient.

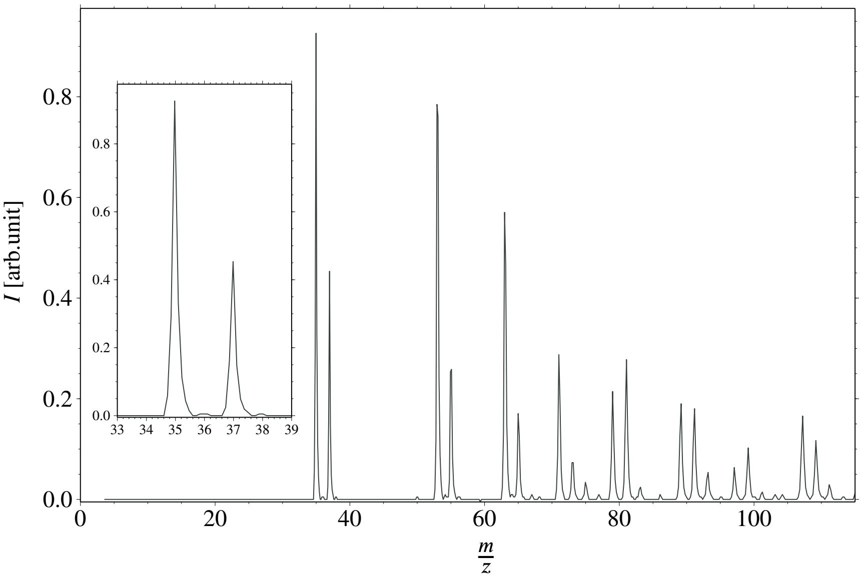

Figure 3.3 | Mass spectrum of ionised CH_2Cl_2 and Ar as buffer gas with traces of Br^- and I^-. Example of a mass spectrum produced by the TOF-MS apparatus at MCP_1 without any gating. The $^{35}\mathrm{Cl}^-$ and $^{37}\mathrm{Cl}^-$ peaks (magnified in the smaller graph) are used to determine the mass-resolution.

3.2.3 Laser

The purpose of the TOF-MS is the separation and classification of a certain selected *m*/*z*. The selected particles are at some stage during an experiment subjected to a laser field. During a standard photoelectron experiment, a neodymium-doped yttrium aluminium garnet (Nd:YAG) laser *(Spectra-Physics Quanta-Ray Pro)* is used.

Internal to the Nd:YAG laser set-up, the fundamental wavelength of 1064 nm can either be frequency-doubled to yield 532 nm or frequency-tripled resulting in 355 nm laser pulses. The pulse frequency is set at 10 Hz and hence the gas pulsing rate is also set to 10 Hz; each of the laser pulses can reach energies of up to 800 mJ pulse^{-1}, but is usually kept at around 500 mJ pulse^{-1} during experiment. Farther along the beam line, the 532 nm laser can be frequency-doubled again (using a larger β-barium borate crystal – BBO) to yield a wavelength of 266 nm. Rather then using a static 266 nm laser wavelength, the 532 nm or 355 nm laser pulses can be passed through a dye laser (*Syrah Cobra-Stretch*), which can be used to produce a variety of different wavelength laser radiation depending on the dyes applied. A list of all available dyes is presented in Table 3.1. These dyes have been carefully chosen to photodetach the halogen anions, thereby allowing for the planned SEVI experiments.

Laser Dye	λ_{pump} [nm]	λ_{low} [nm]	λ_{peak} [nm]	λ_{high} [nm]	**Solvent**
Coumarin 480	355	434	448	463	Ethanol
Pyridin 2	532	691	718	751	Ethanol
Rhodamin B	532	588	596	614	Ethanol
Sulforhodamin B	532	585	591	600	Ethanol
BiBiQ	355	380	390	410	Ethanol / Toluene
DCM	532	602	627	660	Ethanol
	532	626	651	685	DMSO
Rhodamin 6G	355	563	574	597	Ethanol

Table 3.1. | Laser dyes available in the Wild research group. Here, λ_{pump} notes the pumping laser wavelength, λ_{low} and λ_{high} give the range of the output laser wavelength where λ_{peak} denotes the most intense wavelength.

Polarisation and beam energy attenuation of the laser is achieved by passing it through an achromatic half-wave plate (*RAC 1.2.10 from Bernhard Halle Nachfolger GmbH*) and subsequently through a Glen–Laser prism (*Thorlabs GLB10 α-BBO Polariser*, 10.0 mm MgF_2 210 nm to 450 nm).[133] In order to adjust the beam diameter the laser can be passed through a telescope set-up, allowing for laser

---

[133] J. F. Archard and A. M. Taylor. *J. Sci. Instrum.*, **25**: 407 – 409, 1948.

beam diameters of 6 mm to 10 mm. For the VMI experiments the diameter is further reduced to 4 mm by the use of an appropriate aperture. Focusing elements are generally avoided to reduce the probability of multi-photon processes. The laser pulses interacting with the particle beam is Gaussian in shape and can carry different amounts of energy per pulse, depending on the wavelength. Maximum output energies measured directly after frequency multiplication are 500 mJ pulse^{-1} for $\lambda = 532$ nm, 270 mJ pulse^{-1} for $\lambda = 355$ nm and 150 mJ pulse^{-1} for $\lambda = 266$ nm. In the interaction regions, these maximum energies are below 10 mJ pulse^{-1} due to losses within the optic elements along the beam path (largest losses are due to the Glen–Taylor polariser).

3.2.4 Photoelectron spectrometer

As the anionic particle beam drifts along the TOF tube, it eventually reaches a point L_1, onto which a laser beam can be directed. In the immediate vicinity of this point, a permanent magnet has been placed which causes the $\boldsymbol{B}_1$ field necessary to form the 'magnetic bottle' (see Figure 2.4 and Section 2.2.4).

The remanent magnetisation B_r of this neodymium disk magnet ($\mathrm{Nd_2Fe_{14}B}$, diameter $2r_\mathrm{mag}$ is 20 mm, the length l_mag is 14 mm) was extrapolated from measurements to 293 mT.[•] The disk is positioned in such a way, that the centre of the top of the magnet is in a distance of 10 mm to the point L_1. According to Equation (3.2):

$$B_x(x') = \frac{B_\mathrm{r}}{2}\left(\frac{l_\mathrm{mag} + x'}{\sqrt{r_\mathrm{mag}^2 + (l_\mathrm{mag} + x')^2}} - \frac{x'}{\sqrt{r_\mathrm{mag}^2 + x'^2}}\right), \tag{3.2}$$

where x' is the distance from the top of the cylindrical-shaped disk magnet, the x component of $\boldsymbol{B}_1$ due to the magnet at L_1 ($x' = 10$ mm) is 32 mT. In previous experiments a cooled strong electro-magnet was used instead. However, due to its requirement of constant cooling and an inability to maintain a constant cooling rate, the magnetic field spawned by the electro-magnet was unstable and hence affected the transverse component of the photoelectron velocity (see Equation (2.78)). The current permanent magnet will be replaced in near future by a 20 mm × 50 mm rod magnet ($B_\mathrm{r} \approx 1.4$ T to 1.5 T) creating a one order of magnitude stronger magnetic field.

During a photodetachment experiment, the $\boldsymbol{B}_2$ field is created by a copper coil wrapped around the 1.625 m long photoelectron TOF tube. With a current of 5 A passing through the coil, the value of

---

[•] Measured in air, pressure of 1014.0 hPa, temperature of 21 °C, 520A FLUXGATE MAGNETOMETER the $\boldsymbol{B}_2$ field becomes 1 mT and points in the x direction.[▲] On the outside, this tube is encased with a double walled μ-metal shield for the purpose of attenuating the surrounding as well as earth's magnetic field.

At the very end of this 1.6 m long tube, a micro-channel plate detector (*Burle APD 3040MA*, 40 mm diameter, Chevron configuration, 10 μm pore size) is placed intercepting the incoming electrons. Here, the MCP front face has a 200 V bias with a grounded mesh situated approximately 25 mm before the front of the face, the back face is floated at 2300 V and the detecting anode is subjected to a potential of 2500 V. The 200 V bias on the front face improves detection of low energy electrons. The resulting analogue signal is amplified by a *VT120A Ortec Fast Pre-amplifier* and digitised (transformed to NIM logic pulses) by an *Ortec Constant Fraction Discriminator*. A detection sweep is triggered by the leading edge of a photodiode output pulse which sits underneath the laser interaction point L_1. The amplified transformed detector signal is interpreted by a Multiscaler card *(P7888 Fast Comtec GmbH)* which allows for a time bin size of 2 ns. For a typical photoelectron TOF spectrum (histogram of number of electrons arriving per time bin), 10 000 sweeps are averaged. The spectrum then is transformed into kinetic energy domain as per Equation (2.80).

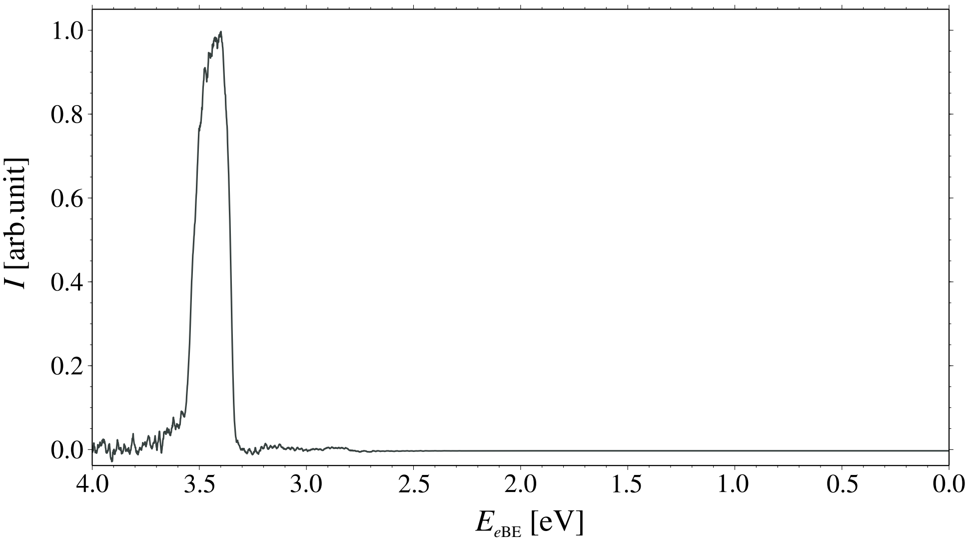

Figure 3.4 | Photoelectron spectrum of $O_2CH_3\cdots I^-$. A 266 nm laser was used for photodetachment.

In Figure 3.4 a PES of what is assumed to be $O_2CH_3\cdots I^-$ treated according to the prior description is presented. The spectrum was obtained by mass-selecting the mass at 174.09 *m*/*z* found in the ionisation

---

[▲] The copper wire is 226 m long, wrapped around the tube 325 times with equal distances between each loop; the value of the field was calculated using the Biot–Savart relationship.

residue of a gas mixture containing CH_3I in the presence of N_2 and O_2 with Ar as a buffer gas (see mass-spectrum in Figure 3.5). The actual mass of $CH_3O_2\cdots I^-$ is 0.15 u lower than found; however the surrounding peaks of $Ar\cdots I^-$, $O_2\cdots I^-$ and $N_2\cdots I^-$ also show a small systematic shift, suggesting a small offset in the mass spectrum calibration.•

The reason why the species at 174.09 *m*/*z* is assumed to be $O_2CH_3\cdots I^-$ is due to the large peak at an electron binding energy of $E_{eEB} = 3.42\,\text{eV}$ which is closer to the electron affinity of iodine ($E_{EA} = 3.059\,\text{eV}$) than that of oxygen ($E_{EA} = 0.448\,\text{eV}$),[134,135] ruling out the alternative where an anionic molecular oxygen is weakly bound to CH_3I.

The observed peak shift between E_{EA} of iodine and the electron binding energy of $O_2CH_3\cdots I^-$ amounts to 0.36 eV which is in line with similar 'solution experiments'. For example, in a recently published study of $OC\cdots I^-$a shift of 0.10 eV was found.[130] The stronger perturbation of the iodide atom might also suggest a shorter $C{-}I^-$ bond. It is unclear however how the oxygen is bound to the methyl group, and for this reason a theoretical investigation is in progress. The resolution of the peak of the presented spectrum is 166 meV (FWHM) which is too low for vibrational resolution. This is an example of where higher resolution in the photoelectron spectrum is necessary for completion of the analysis. Approaches to resolution improvements are presented in the next section.

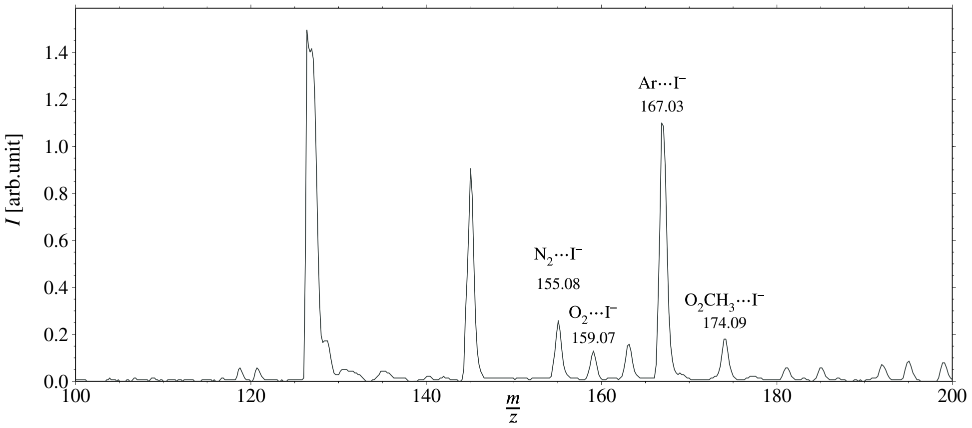

Figure 3.5 | Mass spectrum of ionised CH_3I in the presence of N_2 and O_2 (Ar as buffer gas). The species at 174.09 *m*/*z* is selected for photoelectron spectroscopy presented in Figure 3.4. Note that the bare iodide peak at 127 *m*/*z* is somewhat distorted as it is saturating the detector.

•$Ar\cdots I^-$: 0.18 u, $O_2\cdots I^-$: 0.17 u and $N_2\cdots I^-$: 0.16 u (see Figure 3.5)

[134] R. J. Peláez et al. *J. Phys. B: At., Mol. Opt. Phys.*, **42**: 125001, 2009.

[135] K. M. Ervin et al. *J. Phys. Chem. A*, **107**: 8521 – 8529, 2003.

3.3 A new velocity map imaging segment

The new VMI segment is attached collinearly to the particle beam path and is based on a design published by Cavanagh et al. in 2007.[119] The group achieved resolution of 3.3 meV measuring the $O(^3P_2) \leftarrow O^-(^3P_{3/2})$ transition. In the following, the improvements to the already existing TOF-MS set-up as well as the construction and testing details of the new VMI attachment are discussed.

3.3.1 VMI construction

A plan view of the newly constructed imaging segment can be found in Figure 3.6. The spectrometer is constructed using standard 6” Conflat flanges and fittings. 6” fittings were favoured over 8” flanges due to cost. For a VMI experiment, the incoming particle beam will pass under the retracted micro-channel plate MCP_1 to enter an ‘ion beam optimisation’ module which contains an ion-buncher element, an einzel lens set and a pair of x-y deflection plates. The beam then passes a gate-valve and can subsequently be intercepted by a second retractable micro-channel plate MCP_2, which serves as a targeting aid before the particle beam enters the opening of the µ-metal shielding and VMI interaction region.

The ion beam is overlapped with a laser pulse L_2 between the repeller plate R and the extractor plate, causing the ejection of photoelectrons. Both the particle beam and the generated photoelectrons then pass a grounding plate G to pass through a field free drift region. They are finally projected onto the electron detecting element (el-D), causing an image on the adjacent phosphor screen which is recorded by a CCD camera.

Initially an aperture stack was installed just after MCP_2, which was meant to choke the incoming particle beam down to a diameter of 5 mm to 2 mm. This however was found to be too restrictive, resulting in a complete loss of signal at el-D, which seems to be the result from an improper alignment of the aperture stack. It was hence decided to suspend the implementation of this element in the prototypal version of the VMI attachment.

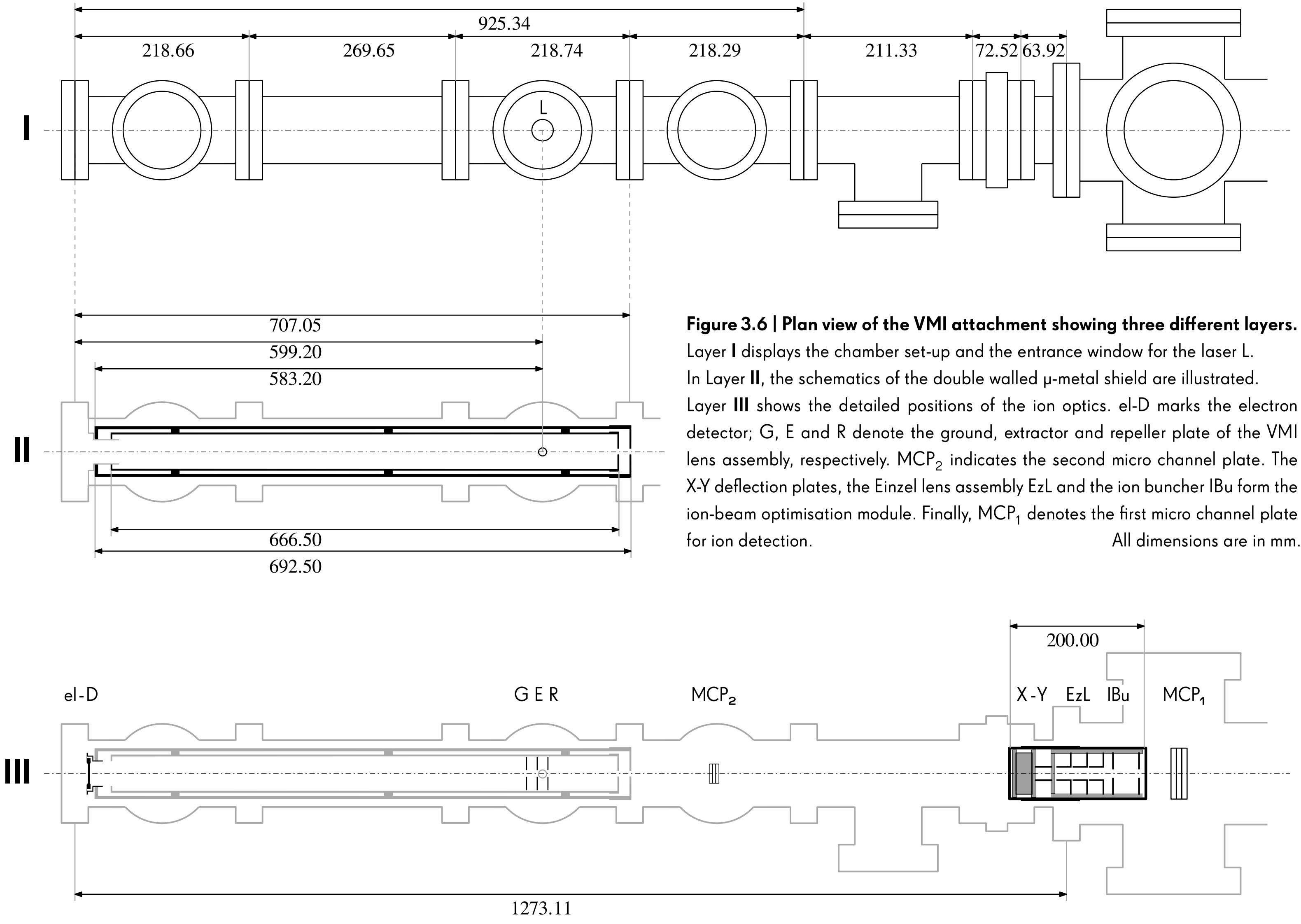

Figure 3.6 | Plan view of the VMI attachment showing three different layers. Layer **I** displays the chamber set-up and the entrance window for the laser L. In Layer **II**, the schematics of the double walled μ-metal shield are illustrated. Layer **III** shows the detailed positions of the ion optics. el-D marks the electron detector; G, E and R denote the ground, extractor and repeller plate of the VMI lens assembly, respectively. MCP$_2$ indicates the second micro channel plate. The X-Y deflection plates, the Einzel lens assembly EzL and the ion buncher IBu form the ion-beam optimisation module. Finally, MCP$_1$ denotes the first micro channel plate for ion detection. All dimensions are in mm.

Improved mass-gate and ion-decelerator module

In order to improve the resolution of the photoelectron spectrometer, a new mass-gate and ion-decelerator has been devised and implemented. The original cylindrical design, described by LaMacchia,[127] has been replaced by a multi-disc based design, similar to the one reported by Kopczynski.[136]

The new unit also features another set of x-y deflection plates. As outlined in Figure 3.7, the ions enter from the right-hand side, pass the new x-y deflection plates, and enter the mass-gate. The gate is floated consistently at a high negative voltage (1 kV to 5 kV) and only 'opened' briefly to allow for a selected mass range to pass. Passing ions then proceed to enter the decelerator region, which consists of 10 plates electrically chained together by 100 kΩ resistors. The first decelerator plate is charged up with a high positive voltage (up to 5 kV) once a pulse of anions passed the mass-gate. Due to the resistor chain the anions move through a linearly decreasing field, which slows them down to a moderate 2 eV to 20 eV. All grounded plates, and the high voltage plate of the mass gate, in this module (see Figure 3.7) are equipped with 90 % transmittance nickel mesh (*Industrial Netting* #BM0700-01 N) allowing for a homogeneous electric field structure along the ion pathway. The design features a tube of Teflon material which acted as both support and isolation of the plates. For mass selection, the rise and fall times of the applied voltage are crucial. Using metal-oxide-semiconductor field-effect transistor (MOSFET) push-pull switches (*Behlke*, HTS 61-01-GSM, 6 kV, 15 A) and appropriate tuning resistors and ballast capacitors the rise and fall time differences are ca. 45 ns.

In Figure 3.8, the capabilities of the improved mass-gate are demonstrated for which a gas mixture containing mainly CH_2Cl_2 and argon as a buffer gas is ionised. The non-gated spectrum was presented Figure 3.3 and as illustrated, the mass gate, which is set to only allow the $^{35}Cl^-$ to pass, performs as expected. It should be noted that the sudden small peak occurring at 25 m/z is caused by switching noise from the mass gate high voltage switch.

Due to laser related issues which occurred late in the candidature (burned out Glen–Laser polariser) it was unfortunately not possible to record a PES with the recently completed ion decelerator.

Ion focusing and bunching module

Further fine control of the particle beam can be established through a beam optimisation module, which contains an ion buncher unit, an additional einzel lens and an x-y deflection plate. The cross-

---

[136] M. Kopczynski. *Femtosekunden Photodetachment-Photoelektronenspektroskopie an isolierten und massenselektierten Halogen-Edelgas-Clustern*. PhD thesis. Georg-August-Universität Göttingen, 2010.

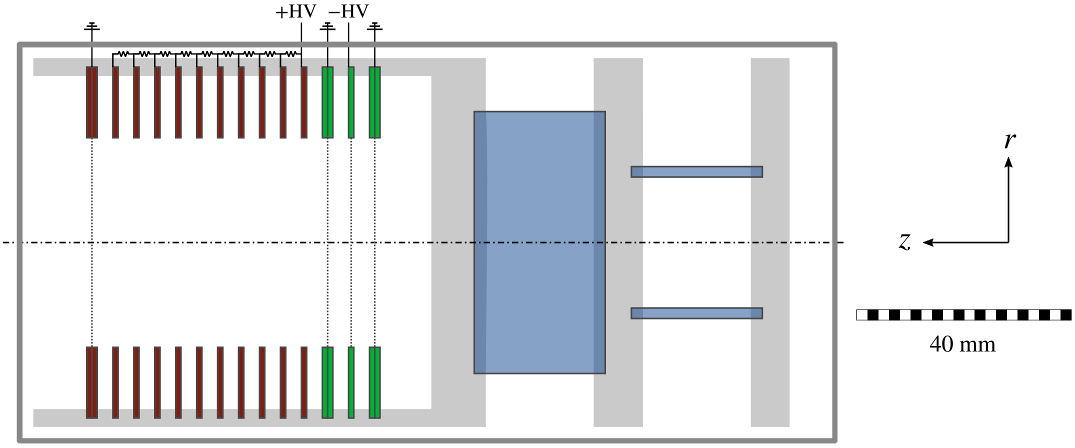

Figure 3.7 | Cross-section of the improved mass-gate and ion-decelerator assembly. Blue shows the deflection plates which are held in place by slotted Teflon disks; green marks the mass-gate plates and red is used to outline the decelerator unit. The latter are mounted within a Teflon tube (grey areas identify the Teflon). Dotted lines represent meshed grids.

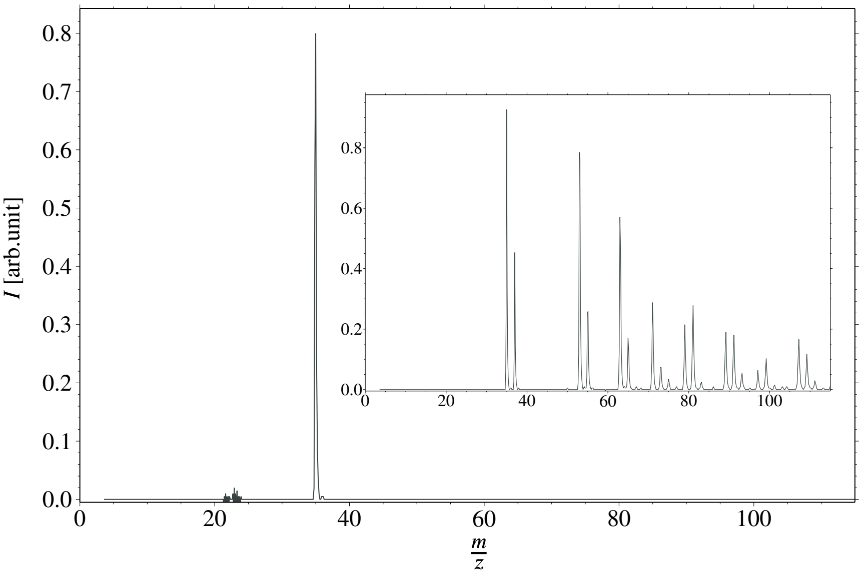

Figure 3.8 | Mass-gated mass spectrum of ionised CH_2Cl_2 and Ar as buffer gas. The spectrum is taken with the same gas mixture as presented in Figure 3.3 with mass-selection for the $^{35}Cl^-$ peak. For comparison the non mass-gated spectrum is presented in the inset.

section through the cylindrical construction is displayed in Figure 3.9. The assembly is supported, and isolated from ground, by a Teflon tube and as in the previously described module, the *x*-*y* deflection plates are also held in place by slotted Teflon plates.

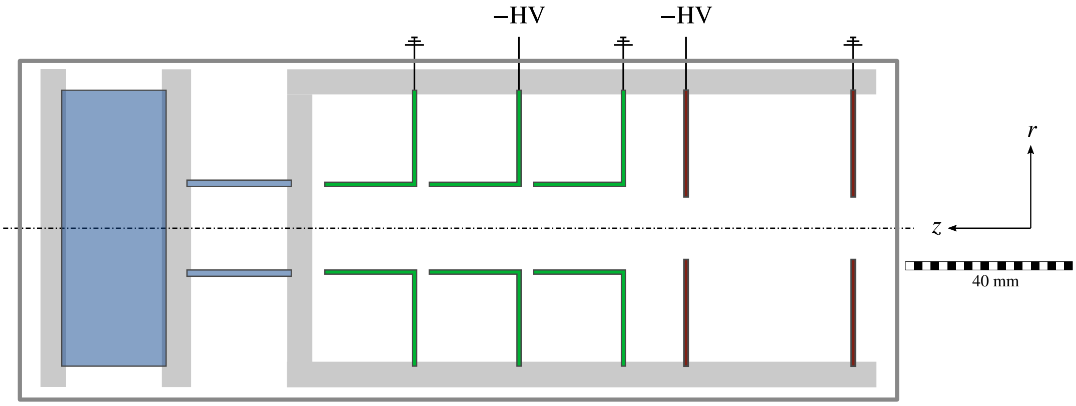

Figure 3.9 | Cross-section of the beam optimisation module. Blue colour shows the deflection plates, green areas identify the einzel lenses and red colour is used to outline the ion bunching unit.

The ion buncher is employed to ensure that a tight ion packet is presented to the incoming laser pulse which is achieved by a briefly occuring linear field between the buncher plates (the ions travel from the ground plate to the negative high-voltage plate) outlined in red in Figure 3.9. Anions farther to the back of the ion package are experiencing less of a deceleration than ions at the front, thereby also adding to the space focussing effect afforded by the TOF-MS plates (see Section 2.2.3). The einzel lens will ensure that the ion beam is focussed laterally, while the additional x-y deflection plates assist in correcting the ion beam direction.

Secondary mass detection

Immediately before the ion beam enters the μ-metal tube, they can be detected by another MCP, labelled as MCP_2 (*Tectra GmbH* MCP-25-D-S-A, 18.8 mm diameter, Chevron configuration, 6 μm pore size) During operation, the MCP front face is connected to ground potential, while the back face is floated at 1800 V and the detecting anode is subjected to 2300 V. Figure 3.10 shows a test mass spectrum resulting from the same gas mixture as described in Figure 3.3. The resolution is of similar quality as for MCP_1.

Multi-layered μ-metal shielding

Rather important to the core operating principle of VMI is the mapping of the electron velocities onto the detector plane. This process requires a nearly field free environment; hence, shielding the

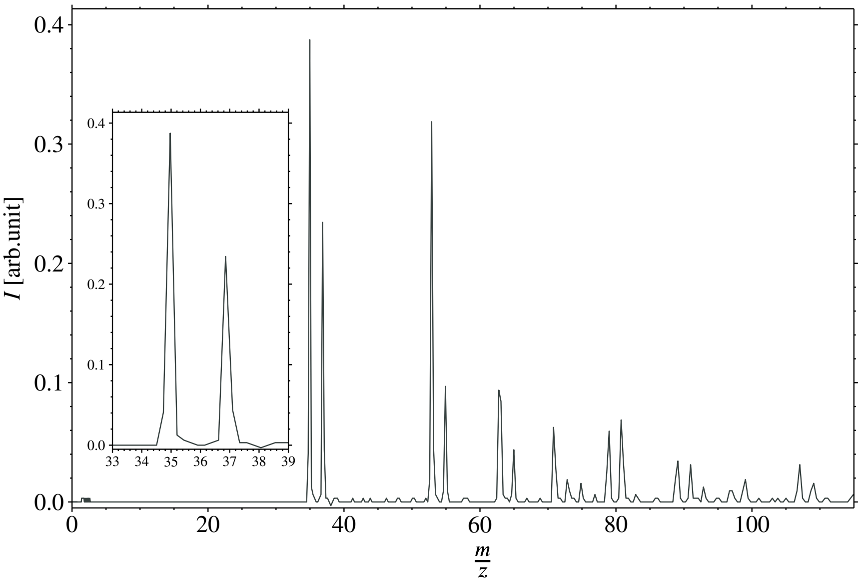

Figure 3.10 | Mass spectrum of ionised CH_2Cl_2 and Ar as buffer gas with traces of Br^- and I^-. Example of a mass spectrum produced by the TOF-MS apparatus at MCP_1 without any gating. The $^{35}Cl^-$ and $^{37}Cl^-$ peaks are magnified in the smaller graph.

expanding electron cloud from earth's magnetic field as well as the surrounding electro-magnetic fields generated by adjacent charged wires or RF noise. Most of the ambient electro-magnetic and electric fields are eliminated by the vacuum chambers, leaving the earth's magnetic field as one of the main reasons for electron deflection.

At UWA the magnetic field intensity is 58.27 µT and shows a decrease of 0.03 $\mu T\,yr^{-1}$ according to the Australian geomagnetic reference field computation, where the field components are: $B_X = 23.54\,\mu T$ ('true' North), $B_Y = -0.67\,\mu T$ ('true' East), $B_Z = -53.41\,\mu T$ (down).[•] One should note that, since the Z component points downwards, the Z direction is equal to the y direction described in Figure 3.1. When measured in the middle of the electron flight tube (point M) without any magnetic shielding B_Z carried a slightly smaller value of −49.92(9) µT,[▲] presumably due to the surrounding metal chambers.

The Z component of the (measured) magnetic field would subject an electron (E_{KE} of 1 keV, flying in z direction) to the Lorenz force, sending it on a circular trajectory with a radius of ca. 2.14 m. Hence, the electron would be vastly displaced on the detector. For an ideal detection, this displacement on the detector should be smaller than 45.3 µm, which is the projected size of a camera pixel. This requires

---

[•] Date: 31/12/2014, magnetic declination: −1.594°; magnetic inclination: −66.255°

[▲] Measured in air, pressure of 1013.6 hPa, temperature of 21 °C, 520A FLUXGATE MAGNETOMETER an absolute value of the magnetic field in Z direction to be smaller than $-28\,\mathrm{nT}$, i.e. a magnetic shielding attenuation $A < -65\,\mathrm{dB}$.[⋆] This maximum field value scales with the square root of the electron kinetic energy. An electron with a low kinetic energy of 1 eV for example (which could be relevant when mapping slow electrons and to gain a higher resolution), would require a $|B_Z|$ to be smaller than 872 pT ($A < -95\,\mathrm{dB}$).

In a cylindrical encased space, the attenuation of a constant transverse magnetic shielding factor S_i can be approximated as,[137]

$$S_i = \frac{\mu}{4}\left(1 - \frac{d^2_{i,\mathrm{inner}}}{d^2_{i,\mathrm{outer}}}\right) + 1\,, \tag{3.3}$$

where μ is the relative magnetic permeability (for µ-metal, μ is up to 100 000 but realistically somewhere between 35 000 to 50 000) and $r_{i,\mathrm{Wall}} = \frac{1}{2}\left(d_{i,\mathrm{outer}} - d_{i,\mathrm{inner}}\right)$ is the wall-thickness of the cylinder ($d_{i,\mathrm{outer}}$ and $d_{i,\mathrm{inner}}$ are the outer and inner shield diameters, respectively). Standard single walled µ-metal cylinders therefore offer shielding factors on the order of 10^3 (attenuations of $-40\,\mathrm{dB}$ to $-60\,\mathrm{dB}$); it can be improved significantly however by enclosing multiple shields within each other. The combined shielding factor of a (long) cylindrical two-layered shield is given through S_{total},[137,138]

$$S_{\mathrm{total}} = S_1 S_2\left(1 - \frac{D^2_{\mathrm{inner}}}{D^2_{\mathrm{outer}}}\right) + S_1 + S_2 + 1\,, \tag{3.4}$$

where D_{outer} and D_{inner} refers to the outer and inner diameter of the space between the first and second layer, respectively. This yields shielding factors, depending on the shield set-up, on the order of 10^5 to 10^7 (attenuations of $-100\,\mathrm{dB}$ to $-140\,\mathrm{dB}$) and is therefore more suited to the requirements of the VMI attachment.

Based on these considerations, a double-walled magnetic shield was designed by the author and subsequently constructed by *Magnetic Shields Ltd.*[•] It consists of two cans of µ-metal nested within each other. The inner shield exhibits a wall thickness $r_{1,\mathrm{Wall}}$ of 2 mm ($d_{1,\mathrm{outer}} = 64$ mm); the outer cylinder is composed of a thicker µ-metal with $r_{2,\mathrm{Wall}}$ of 2 mm ($d_{2,\mathrm{inner}} = 84$ mm). A 52 mm sized hole allows for electron detection on one side of the assembly. On the other side, an end-cap with a central lying 6 mm hole was attached to each cylinder permitting the particle beam to enter along the central axis. 11 cm after the beam entry point, a 10 mm hole, going on a transverse axis through both cylinders, was

---

[⋆] $A = 20\log_{10}\left(B_{\mathrm{att}}/B_{\mathrm{ini}}\right)$ [dB], where B_{ini} is the initial magnetic field (reference) and B_{att} the attenuated magnetic field. $B_{\mathrm{ini}}/B_{\mathrm{att}}$ is often referred to as magnetic shielding factor S.

[137] A. Mager. *IEEE Trans. Magn.*, **6**: 67 – 75, 1970.

[138] D. Dubbers. *Nucl. Instrum. Methods Phys. Res., Sect. A*, **243**: 511 – 517, 1986.

[•] MAGNETIC SHIELDS LTD, TN12 0DS United Kingdom, Price: 721.79 £

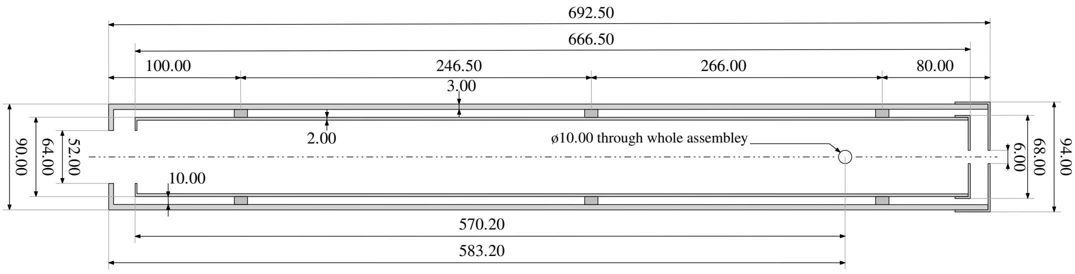

Figure 3.11 | Cross-sectional plan view of the μ-metal shield assembly. The left side is attached to the electron detector unit. The right side features two removable end caps. The positioning of the assembly within VMI attachment is shown in Figure 3.6. All units in mm.

added enabling the laser to enter the shield. A cross-sectional plan view is presented in Figure 3.11; the positioning of the assembly within VMI attachment is described in Figure 3.6.

Using Equations (3.3) and (3.4), the theoretical shielding factor S_{total} is calculated to be between 0.504×10^6 to 1.027×10^6 (assuming the μ to be 35 000 to 50 000) which is equivalent to an attenuation A_{total} of -114 dB to -120 dB. Unfortunately, a magnetometer able to measure such small fields was not available during the time. Using the fluxgate magnetometer which is available to our group, only noise data was obtained. Ultimately however, it is possible to obtain an estimate of the internal magnetic field by measuring the electron beam displacement on the detector at different electron kinetic energies.

Velocity map imaging lens

Within the μ-metal tube, 10.9 cm after the ions entered shield, they reach the photodetachment point L_2. Around it, a VMI lens is positioned in such a way that the detached electrons are accelerated towards the detector at the far end of the μ-metal tube. There is a variety of different lens designs used throughout the literature, two of which are discussed here in more detail.

The design of the first lens was guided by descriptions of Gibson, Cavanagh and co-workers.[119] It seems[•] that the key feature of the groups design is an equal plate spacing and a cylindrical elongation of each lens. Based on this and in order to acquire a compact design configuration, the 'Gibson–Cavanagh' VMI lens design employed in the current set-up consists of repeller, extractor and ground-plate separated by 20 mm. Each plate exhibits a diameter of 58 mm at a thickness of 1 mm. While the

---

[•] A detailed description of their lens is not published at the time of writing.

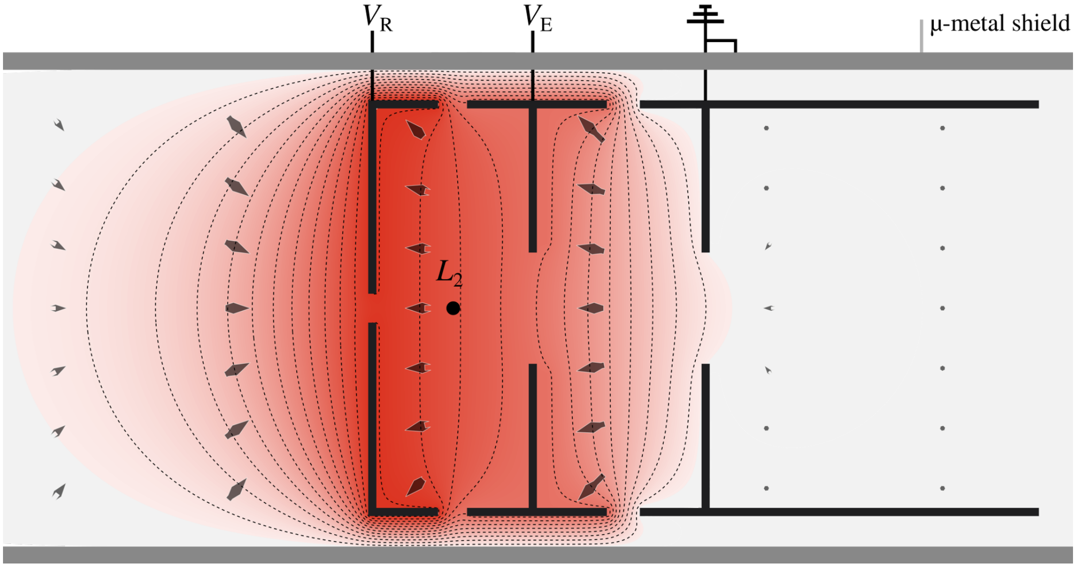

Figure 3.12 | Cross-section through the x-z plane of the 'Gibson–Cavanagh' VMI design. The field was simulated with V_R = 1000 V and V_E = 681 V. The colour density maps the electric field gradient, the dashed black lines are the respective contour (steps of 83 V), the grey arrows point into the direction of the field. Repeller, extractor and ground-plate are separated by 20 mm .

ions have to enter through a rather small aperture of 3 mm in the repeller plate, the opening in the extractor and ground plate are 15 mm each.

In order to explore the effect of the electric field on the detached electrons, the electric potential was calculated and electron flight paths simulated using the SIMION programme suit.[139] The repeller potential V_R as well as the extractor potential V_E have been optimised such that they produce the best resolution on the detector (distance to L_2: 592.1 mm). For our version of the 'Gibson–Cavanagh' VMI design, the ideal voltage ratio V_E/V_R is 0.681. In Figure 3.12, the dimensions as well as the resulting electrostatic potential and vector field at ideal potential ratio are illustrated in a cylindrical cross-sectional view. It clearly displays the inhomogeneity at the extractor and ground plate openings through which the 'projection effect' discussed in Section 2.2.5 is achieved.

Trajectory simulations for a fictitious particle and for the 266 nm laser induced halide detachments (from Cl^-, Br^- and I^-) are presented in Figure 3.13. The purpose of the fictitious particle simulation was to find out whether the VMI lens, when supplied with the ideal voltage ratio, can resolve a 0.01 eV difference in kinetic energies. Due to their simple synthesis, the halide ions have been successfully used

---

[139] D. C. McGilvery and D. A. Dahl *Simion 8.1.1.1* 2012

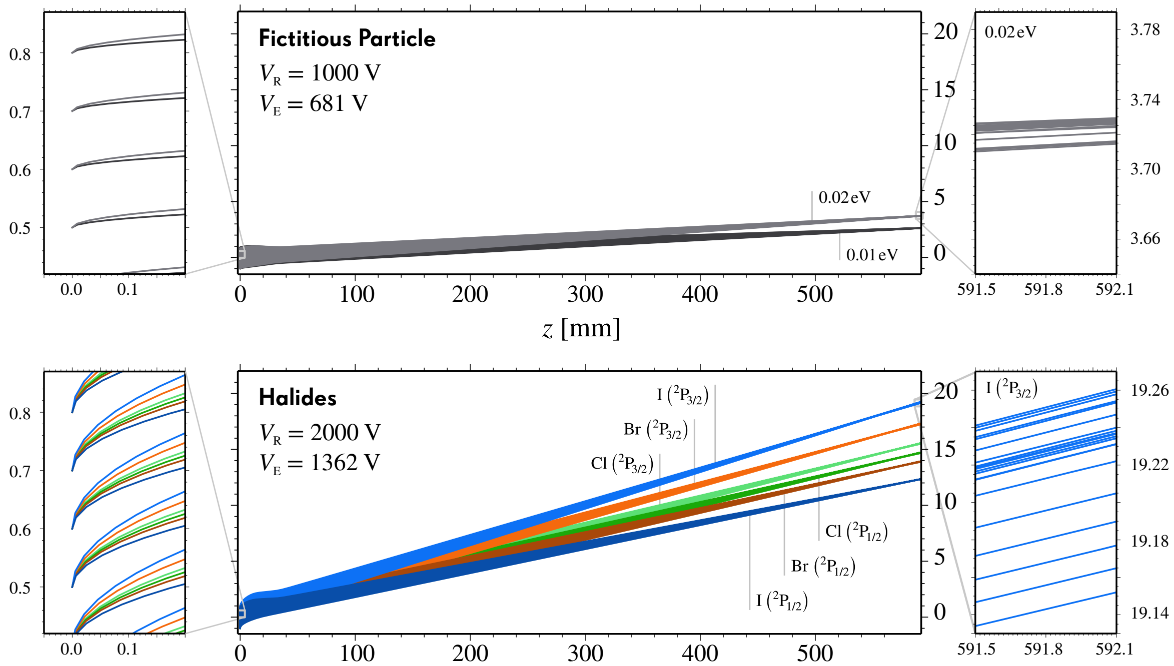

Figure 3.13 | Trajectory simulation with the Gibson–Cavanagh type VMI lens. For each particle type three graphs can be seen. The inner graphs represent the complete electron flight trajectory. The outer graphs are magnifications of the beginning and termination of the flight paths. Halide start from an anionic $^1S_0$ state and transition to a neutral $^2P_{\{3,1\}/2}$ state (labelled). The resulting electron kinetic energies were assigned according to 266 nm induced transition listed in Table 3.2.

to calibrate the PES spectra against their known transition (see Table 3.2) and might serve the same purpose in the VMI case.

For the simulations all electrons are spawned at 21 different positions around L_2 ($z = 0.0$, $r = \{-1.0, -0.9, \cdots, 0.0, \cdots, 0.9, 1.0\}$) with a certain kinetic energy in r direction. The reason for this spread is that the ionic particle beam will arrive at L_1 with a diameter of around 2 mm to 3 mm. In the central panels of Figure 3.13, one notices that during the first 30 mm the particles follow a bent trajectory due to the VMI lens followed by a linear trajectory until they reach the detector at $z = 592.1$ mm. According to the simulations, with this lens design one should be able to discern between electrons separated by 0.01 eV of kinetic energy. The distance between the centre of the two 'spots' on the detector for the fictitious particle is 1.089 mm which is much larger than the projected pixel size of 45.3 µm. It is therefore conceivable to resolve even smaller energy differences. The spread of

Initial state	Target state	E_{trans}	$E_{\text{KE}}^{[266\text{ nm}]}$	Reference
Cl^- $(^1\text{S}_0)$	Cl $(^2\text{P}_{3/2})$	3.6127	1.0483	140
Cl^- $(^1\text{S}_0)$	Cl $(^2\text{P}_{1/2})$	3.7221	0.9389	141
Br^- $(^1\text{S}_0)$	Br $(^2\text{P}_{3/2})$	3.3636	1.2975	142
Br^- $(^1\text{S}_0)$	Br $(^2\text{P}_{1/2})$	3.8205	0.8406	143
I^- $(^1\text{S}_0)$	I $(^2\text{P}_{3/2})$	3.0590	1.6020	134
I^- $(^1\text{S}_0)$	I $(^2\text{P}_{1/2})$	4.0017	0.6593	143

Table 3.2. | Transition energies and resulting kinetic energies for halide-detached electrons. The laser excitation is assumed to be the 4th harmonic of an Nd:YAG laser (266 nm, 4.6611 eV). Isotopic shifts of the electron affinity between ^{35}Cl and ^{37}Cl are on the order of 10^{-7} eV; they are even lower for ^{79}Br and ^{81}Br and therefore not relevant. All transitions in eV.

arriving electrons with the same original kinetic energy is as low as 15 µm (visible as only one pixel) and can be larger than 110 µm (for electrons arriving at larger r) blurring over multiple pixels.

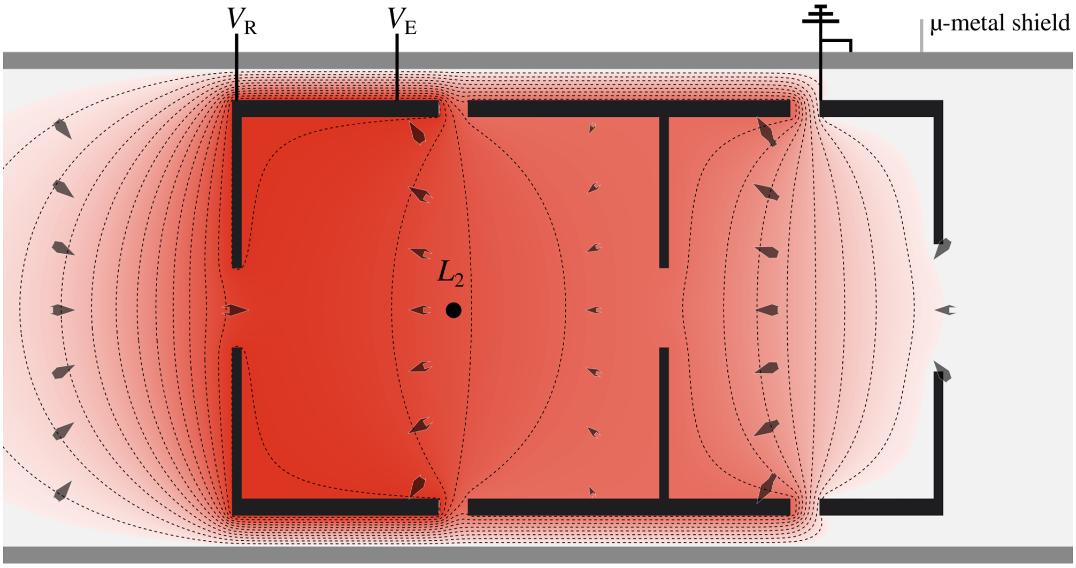

Figure 3.14 | Cross-section through the x-z plane of the Gascooke based VMI design. The field was simulated with V_R = 1000 V and V_E = 701 V. The colour density maps the electric field gradient, the dashed black lines are the respective contour (steps of 83 V), the grey arrows point into the direction of the field.

As an alternative to the Gibson–Cavanagh VMI design, a VMI lens set-up of Gascooke was modified and combined with the cylindrical lens scheme.[144] The plate separation between repeller and extractor plate is now 46 mm and between extractor and ground plate, it measures 34 mm. In Figure 3.14, a cylindrical cross section illustrates the dimensions as well as the arising electrostatic potential and vector field at ideal potential ratio. One should note that the ideal ratio V_E/V_R for this lens set-up is 0.701. Trajectory simulations for this lens suggest a slightly lower resolution, mainly due to the lower field gradient at L_2 resulting in more interactions between the electrons.

The separation between repeller and extractor plate however is an advantage of this set-up over the Gibson–Cavanagh VMI design. As soon as the particle beam passes through the repeller plate, the field is activated. The time it takes for the field to be fully established (ca. 45 ns) might be – depending on the speed of the ion – too long before the ion reaches L_2 for the Gibson–Cavanagh VMI design, therefore causing a distortion in the resulting image. Of course, this can be remedied by either slowing down the particle beam beforehand or by decreasing the rise time of the potential. Both solutions will cause additional problems however (particle beam spread increase or asymmetries in the field), that the Gascooke based design might indeed be the better choice – at least for lighter ions.

Electron detection

The detector at the far end of the electron drift region is comprised of a large MCP (43.5 mm effective diameter, 12 µm sized holes arranged in a hexagonal array with a distance of 15 µm between them in a Chevron configuration) and a ceramic scintillator screen underneath. As a scintillator material P43 – terbium-activated gadolinium oxysulfide ($G_{32}O_2S$:Tb) – was chosen since it has one of the highest emission intensities amongst the commercially available materials. Additionally, its emission maximum lies at 545 nm, which is close to the spectral response maximum of the camera used for capturing the image (510 nm). Furthermore, the time it takes for the phosphorescence to decay to 1 % of its original intensity takes 3 ms – ideal for an experiment pulsed at 10 Hz. This whole assembly was manufactured by *El-Mul Technologies, Ltd.* (E050VP43) and is attached to a 6” Conflat flange which in turn has a 4.58” flange with a glass window in the centre allowing for observation of the screen. The front face of the detector is usually connected to ground. In pulsed mode however, the front face can be set to V_{MF} of 500 V to 800 V (at times when no electrons arrive), resulting in a higher signal gain as other charged particles, e.g. the trailing ion package, get repelled. The back face of the MCP array is floated at constant 2000 V, while the scintillator carries a potential of 6000 V, which is achieved

---

[144] J. R. Gascooke. *Energy transfer in polyatomic rare gas collisions and van der Waals molecule dissociation*. PhD thesis. Flinders University of South Australia, 2000.

through a voltage divider circuit. The end of the µ-metal tube is held in place by custom made hollow aluminium mounting can, which is also attached to the flange sitting over the detector array. It fulfils the additional purpose of shielding the incoming electrons from the high voltages applied to the back face and the scintillator screen. A schematic cross-section of the whole electron detection unit is presented in Figure 3.15.

The camera used to acquire image data features a 1280×960 px sensor capable of supplying a 12 bit image stream at a frame rate of 10 Hz *(IDS UI-2140RE-M-GL)*. It is connected to an optical lens with a focal length of 16 mm. During experiment the aperture value of the lens is set to 1.4. The camera is positioned ca. 20 cm behind the glass window in such a way that the detector area is covers the whole 960 px. This is achieved by a in-house-built adjustable mounting system which attaches to the 6” Conflat flange at the end of the VMI attachment.

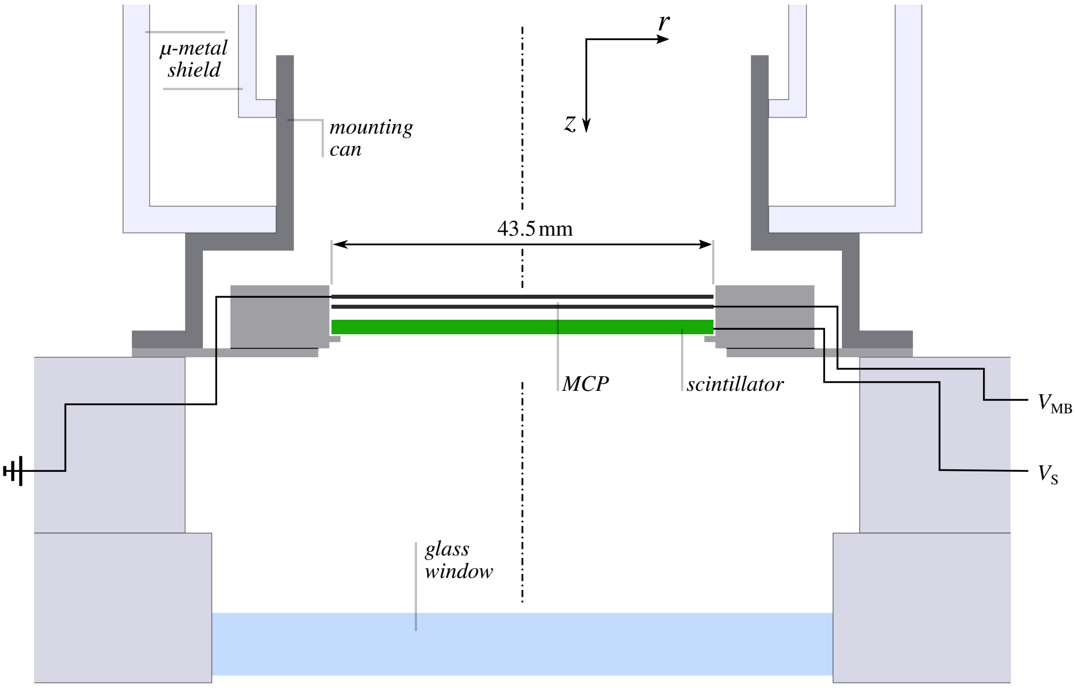

Figure 3.15 | Cross-section through the electron detection assembly. The detector is comprised of an MCP set-up with the front face connected to ground, the back face floated at V_{MB} = 2000 V and a P43 coated scintillator supplied with V_{S} = 6000 V. It is attached to a 6” Conflat flange with a 6.35 mm thick glass window. The µ-metal is held in place by a fitted aluminium mounting can.

3.3.2 Image acquisition software

Recording images is the quintessential process in the quest of obtaining a VMI spectrum. In order to control the camera, to acquire images, and process the data, a custom C++ programme was developed. The final image processing and transformation routine which includes image centring through ellipse detection, correction and subsequent inverse Abel transform has already been developed in prototypical form by Richard Bentley-Moyse.[145] The routine is based on an implementation of the inverse Abel transform provided to us by Jason Gascooke.[144] In future, the inverse Abel transform algorithm should be replaceable by an improved method, i.e. the maximum entropy velocity image reconstruction.[123] Here, a brief overview of the structure of the image acquisition part of the software is given.

All image related work is carried out on a LINUX based operating system. The camera is controlled through the `uEye` library provided by the camera manufacturer IDS and once a frame leaves the camera's internal memory, it is stored and processed as an `OpenCV` array. For the purpose of image collection an image is a picture of a single event, whereas 'frame' is used in the context when n images are stacked, it therefore represents an average image. The amount of images n necessary for a frame depends on the image bit-rate. Since a frame is stored as a 16 bit image, it needs to be a stack of at least 16 individual 12 bit images, otherwise memory is wasted.[•] If a higher number of images per frame is chosen one can decide to either lower the bit-rate of the input images or to create a normalised image (thereby loosing information).

A new image collection sweep is started with the collection of a dark master frame which is constructed from an uneven amount of dark images, i.e. the image detector is not active, but the camera settings are the same as for the normal image collection. The dark master frame will be a median of the uneven amount of dark images, which will prevent incorporation of an unlikely cosmic ray streak into the each frame. The resulting frame is subtracted from each image in order to remove additive noise. Ideally, one also wants to apply a flat-field correction in order to remove multiplicative noise, however this is not yet implemented in the current stage of the software.

After the dark master frame collection, the VMI frames are collected and stored separately, allowing for more fine-control over the final image stacking process – the software will however return an averaged final image of all frames. A single VMI spectrum needs on the order of 10^4 events to be completed and hence the default number of frames collected is 900 with a frame-size of $n = 16$ images.

---

[145] R. J. Bentley-Moyse. *Towards velocity map imaging: Implementation of a self-centering inverse Abel transform script*. MA thesis. University of Western Australia, 2014.

[•] For testing purposes, only 8 bit images were collected the resulting frame is an 8 bit normalised average of 10 images.

```
Mat MedianArray(Mat *mImages, int nDarkFrames)
{
    int med;
    // Creating a resulting image that will contain all the median values.
    Mat DarkMaster;
    DarkMaster.create(mImages[0].size(), CV_8U);

    //addressing each pixel
    for(int j = 1; j < mImages[0].rows - 1; ++j)
    {
        for(int k = 1; k < mImages[0].cols - 1; ++k)
        {
            //initiate a vector for the median
            std::vector<int> v(nDarkFrames, 0);
            for (int i = 0; i < nDarkFrames; i++)
            {
                v[i] = mImages[i].at<uchar>(j,k);
            }
            //Resulting pixel is the median of all pixels in the images array
            DarkMaster.at<uchar>(j,k) = median(v);
        }
    }
    return DarkMaster;
}

int median(std::vector<int> &v)
{
    std::nth_element(v.begin(), v.begin() + v.size()/2, v.end());
    return v[v.size()/2];
}
```

Listing 1 | 8-bit dark master frame generation by using the `MedianArray` subroutine. Here, `*mImages` is a points to the first of `nDarkFrames` images.

3.3.3 Current status

The current set-up is in a prototype state, where the following milestones have been reached:

1. A test run of all the components was completed by which the 266 nm laser was focused on an edge of the inner μ-metal shield to produce photoelectrons which were successfully accelerated with the VMI lens and captured by the camera.

2. An iodide anion beam was directed through the opening of the μ-metal and has been captured by the camera (as presented in Figure 3.16).

3. A 355 nm laser was successfully overlapped with the iodide beam causing photodetachment. With a front face voltage of $-1500\,\mathrm{V}$ on the electron detector, any negatively charged particle was repelled and neutrals were observed.

The characteristic VMI photoelectron detection however has not been achieved yet. This is believed to be due to a number of issues related to the laser and ion beam properties encountered during the testing. Firstly, the laser beam at the point of interception L_2 had a large diameter; in future, the laser will be focused to a plane by using an appropriate cylindrical optical lens and hence causes electrons to emerge in the same region of the field. Of course, great care needs to be taken to ensure that the laser fluence is below the threshold needed for multi-photon processes. Secondly, the image presented in Figure 3.16 was obtained with a rather large ion kinetic energy of 1500 eV. The reason for this is that not all x-y deflection plates were functioning at the time of testing causing the ion beam to drift

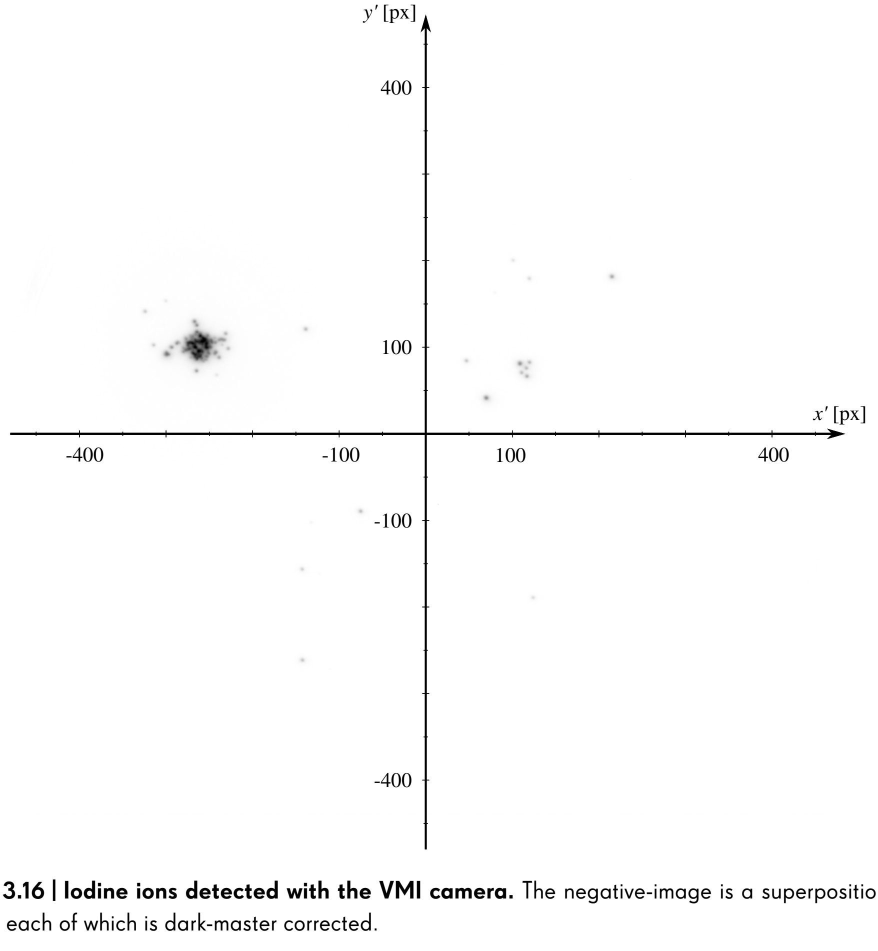

Figure 3.16 | Iodine ions detected with the VMI camera. The negative-image is a superposition of 16 frames, each of which is dark-master corrected.

off centre. If the ion beam energy was lowered, the beam would miss the μ-metal entrance orifice. A 1500 eV fast ion beam however is hard to precisely overlap with the laser pulse as it passes through the interaction region around L_2 (1 cm) within 0.3 μs. Moreover, the beam only remains within the VMI lens for 2.4 μs before it reaches L_2 and hence the electric field which requires up to 45 ns to be fully established needs to be triggered at exactly the right moment. Lastly, at the time of the described VMI test sets, the mass-gate was not working properly, leading to excessive background noise due to other arriving ions.

Unfortunately, the PhD candidature was limited to 3½ years and hence, at the time of writing, no further testing has been done. Most of the previously mentioned issues however have been addressed and fixed, only leaving the focusing and repair of burned out optics to be addressed. It should therefore be possible to produce the VMI spectra in the not too distant future.

Chapter 4

Carbonyl oxide studies

4.1 Carbonyl oxides

4.1.1 Motivation

Carbonyl oxides, also known as Criegee intermediates, are understood to be linking structures in tropospheric ozonolysis reactions. They where first proposed as a possible reaction intermediate by Rudolf Criegee in 1949.[146] Extensive isotopic labelling experiments supported Criegee's initial idea and a full mechanism was published in 1975.[1]

The mechanism features the formation of primary ozonide.

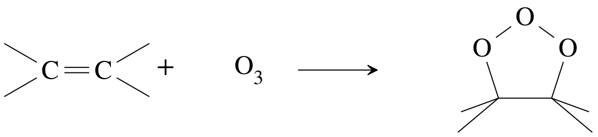

(R 4.1)

This initial step is followed by the carbonyl and carbonyl oxide formation.

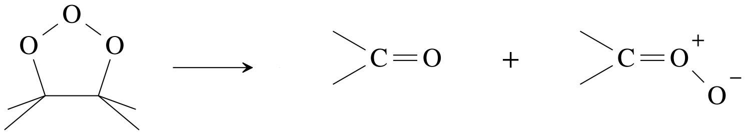

(R 4.2)

Finally, these products can recombine to form a secondary ozonide.

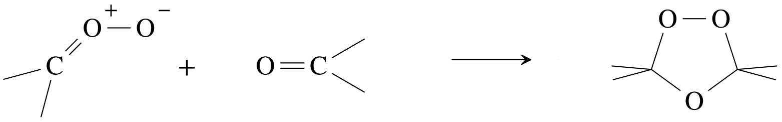

(R 4.3)

The cross section for reaction (R 4.3) is small if the particle density is low, which is the case in our planet's atmosphere where the carbonyl oxide intermediates formed in reaction (R 4.2), are more likely to decompose unimolecularly to •OH radicals.[147–150] As one of the main gas-phase oxidants in our atmosphere, the carbonyl oxides are also likely to react with other carbonyl oxides as well as H_2O,

---

[146] R. Criegee and G. Wenner. *Justus Liebigs Ann. Chem.*, **564**: 9 – 15, 1949.

[147] G. T. Drozd, J. Kroll, and N. M. Donahue. *J. Phys. Chem. C*, **115**: 161 – 166, 2011.

[148] D. Johnson and G. Marston. *Chem. Soc. Rev.*, **37**: 699 – 716, 2008.

[149] R. Gutbrod et al. *Chem. Phys. Lett.*, **252**: 221 – 229, 1996.

[150] R. Gutbrod et al. *J. Am. Chem. Soc.*, **119**: 7330 – 7342, 1997.

SO_2, NO, NO_2, other alkenes or ozone,[151–155] only to name a few examples for the rich chemistry these molecules exhibit.

Carbonyl oxides seem to play an important role as an oxidant in our planet's atmosphere. In those natural atmospheric processes, the precursors to carbonyl oxide formation – volatile organic compounds (VOC) – are for example generated by our forests and as earth's biosphere slowly warms, more VOCs can enter the carbonyl cycle.[2] The reaction of VOCs with ozone creates carbonyl oxides with high internal energy, most of which immediately dissociate through unimolecular rearrangements leading to, amongst others, •OH .[156] Those carbonyl oxides which are stable enough to participate in further reactions (lifetimes of approximately 100 ms were postulated), are often called stabilised Criegee intermediates.[147,157]

Spectroscopic studies on carbonyl oxides

To conclude his article of 1975, Criegee asked about the rather unstable intermediate he discovered: 'Will it become possible to at least detect a carbonyl oxide spectroscopically, or even to isolate one?' [Ref. 1, p. 751]

Although the carbonyl oxide has been observed indirectly, mostly through trapping reactions (e.g. the formation of α-methoxy hydroperoxides with methanol),[158] it took 37 years before it would be observed spectroscopically. The key was the discovery of alternate methods for gas-phase synthesis for the simplest of all Criegee intermediates, the methanal-oxide (MetOx). In 2006, the molecule could be obtained through a chlorine radical initiated oxidation of dimethyl sulfoxide (DMSO) in an oxygen rich atmosphere and was subsequently identified by its photoionisation spectrum.[159]

Eventually, Welz and co-workers discovered a superior synthetic pathway through the reaction of the iodomethyl radical with oxygen.[152] The radical is obtained through photolysis of CH_2I_2.

$$CH_2I_2 \xrightarrow{h\nu} {\cdot}CH_2I + I{\cdot} \tag{R 4.4}$$

---

[151] Y.-T. Su et al. *Nat. Chem.*, **6**: 477 – 483, 2014.
[152] O. Welz et al. *Science*, **335**: 204 – 207, 2012.
[153] H. G. Kjærgaard et al. *J. Phys. Chem. Lett.*, **4**: 2525 – 2529, 2013.
[154] T. Berndt et al. *Atmos. Environ.*, **89**: 603 – 612, 2014.
[155] C. A. Taatjes et al. *Science*, **340**: 177 – 180, 2013.
[156] L. Vereecken and J. S. Francisco. *Chem. Soc. Rev.*, **41**: 6259 – 6293, 2012.
[157] N. M. Donahue et al. *Phys. Chem. Chem. Phys.*, **13**: 10848 – 10857, 2011.
[158] W. H. Bunnelle. *Chem. Rev.*, **91**: 335 – 362, 1991.
[159] C. A. Taatjes et al. *J. Am. Chem. Soc.*, **130**: 11883 – 11885, 2008.

In an oxygen atmosphere, the iodomethyl radical attacks an oxygen molecule to form MetOx and an iodine radical

$$\cdot CH_2I + O_2 \longrightarrow CH_2O_2 + I\cdot \qquad (R\,4.5)$$

A plethora of side and follow-up reactions are possible, examples of which are presented in reference [152].

As a consequence of this new synthetic pathway, the behaviour of MetOx could now be investigated utilising various spectroscopic methods, such as UV adsorption and gas-phase IR experiments.[5,160,161]

Taatjes and co-workers recently extended this technique and could show photoionisation spectrum of ethanal-oxide (EtOx) prepared from the 1-iodoethyl radical prepared in the same way as presented in reaction (R 4.4).[155]

$$CH_3\dot{C}HI + O_2 \longrightarrow CH_3CHO_2 + I\cdot \qquad (R\,4.6)$$

Applying this technique, Nakajima and Endo were able to record an experimental microwave spectrum of both of the ethanal oxide isomers, providing rotational constants.[162,163] Due to its β-carbon, the EtOx also seems more relevant to atmospheric processes than its ‘simpler’ counterpart.[2,150] In a recent study, Liu et al. were able to measure an IR action spectrum of *cis*-ethanal-oxide (^{c}EtOx) in the 5600 cm^{-1} to 6100 cm^{-1} region determining the barrier height for the hydrogen transfer reaction from the methyl group to the terminal oxygen.[164]

Computational studies

Because of their metastable nature, experiments on the carbonyl oxides are indeed rather challenging. The small size of MetOx however allows for a thorough theoretical analysis of its electronic structure and the reactions it can undergo.[156] For instance, Fang et al. studied the potential energy surface of the reaction between CH_2 and O_2 on the singlet and triplet surfaces using CASSCF type calculations.[165] Nguyen et al. obtained the heat of formation and ionisation energy of the Criegee intermediate at the CCSD(T) / CBS level using W1 theory.[166,167]

---

[160] J. M. Beames et al. *J. Am. Chem. Soc.*, **134**: 20045 – 20048, 2012.

[161] M. Nakajima et al. *Chem. Phys. Lett.*, **621**: 129 – 133, 2015.

[162] M. Nakajima and Y. Endo. *J. Chem. Phys.*, **140**: 011101, 2014.

[163] M. Nakajima, Q. Yue, and Y. Endo. *J. Mol. Spectrosc.*, **310**: 109 – 112, 2015.

[164] F. Liu et al. *Science*, **345**: 1596 – 1598, 2014.

[165] D.-C. Fang and X.-Y. Fu. *J. Phys. Chem. C*, **106**: 2988 – 2993, 2002.

[166] M. T. Nguyen et al. *Chem. Phys. Lett.*, **448**: 183 – 188, 2007.

[167] J. M. L. Martin and G. de Oliveira. , **111**: 1843 – 1856, 1999.

In order to discern the IR spectrum of MetOx from other isomers and side products occurring in reaction (R 4.5), Su et al. simulated an anharmonic IR spectrum at a lower level of theory (NEVPT2-MP2 / A'VDZ[•]) and compared it to those of dioxirane, CH_2I_2, *cis*-CH_2IOO and the corresponding biradical methylenebis(oxy).[5] The experimental spectrum and simulations agreed fairly well with a harmonic CCSD(T) / A'VTZ spectrum published by our group (this will be discussed further in Section 4.5.2).[168] Recently, Li et al. published an anharmonic high-level VCI spectrum simulation, further improving upon the prediction accuracy.[169]

4.1.2 Overview

As presented in this section, the main focus of current and past research lies within the neutral carbonyl oxide chemistry. It is however also possible to explore the neutral carbonyl oxides coming from an anionic surface via anion photoelectron spectroscopy. Before one tries to synthesise promising candidates (e.g. anionic MetOx or EtOx) for spectroscopic characterisation, it is worthwhile to simulate the stability and electron affinity of such entities.

In this chapter these ideas will be discussed. High-level calculations are presented for methanal-oxide (MetOx) in Section 4.3 and the two isomers ethanal-oxide (EtOx) in Section 4.4. For all molecules, the W3-F12 method (see Section 4.2) was applied to retrieve neutral and anionic molecular structures, electron affinities, simulations of IR and photoelectron (PE) spectra as well as relative stabilities.

4.2 Methodology

The carbonyl oxides exhibit some non-negligible degree of non-dynamical correlation effects.[165] This is commonly represented as follows.

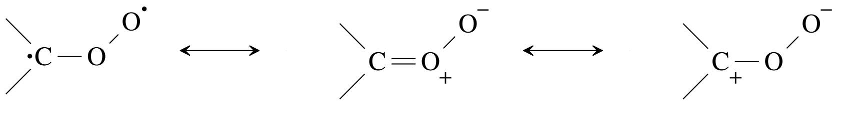

(R 4.7)

[•] for an overview of the basis set notation used in this document, the reader is referred to Table 4.1

[168] A. Karton, M. Kettner, and D. A. Wild. *Chem. Phys. Lett.*, **585**: 15 – 20, 2013.

[169] J. Li et al. *J. Phys. Chem. Lett.*, **5**: 2364 – 2369, 2014.

Anglada and co-workers showed that MetOx is predominantly zwitterionic and that the biradical form only has a small stabilising effect.[170] In order to represent this multi-reference character in the calculations involving carbonyl oxide, a reliable and tested methodology had to be found; one which represented a compromise between accuracy and computational expense.

Composite thermochemistry protocols offer such features and additionally, they are also readily tested against large benchmark sets. Accuracies of less than 1 kcal mol^{-1}, which is often termed chemical accuracy, can be achieved with some of these methods.[171–173] Two sets of protocols stand out: the highly accurate extrapolated ab initio thermochemistry (HEAT) project and the Weizmann (W*n*) protocols.[4,167,171,172,174–176]

For the present work the latter set, namely the W3-F12 protocol has been chosen.[4] Compared to the equivalently accurate HEAT approach (HEAT345-(Q)), W3-F12 is computationally more economical.[•] An overview of other W*n* protocols and a comparison between them can be found in the Appendix A.2.1, specifically Table A.1.

4.2.1 The W3-F12 protocol

The thermochemical W3-F12 procedure describes a method to obtain the total atomisation energy (TAE) of a molecule, $E_{\mathrm{TAE},M}$ at relativistic all-electron CCSDT(Q) / CBS level of theory by means of layered extrapolation techniques. It shows a root-mean-square deviation (RMSD) of 1.13 kJ mol^{-1} against the W4-11 test set and therefore provides more than chemical accuracy.[173] Throughout this work, a variety of correlation consistent basis sets are used and an explanation for their shorthand notation and sources can be found in Table 4.1. In the following the correlation consistent basis set notation often includes a $\{n, n+1\}$ term (where n refers to the cardinal number of a correlation consistent basis set). This indicates the use of a two-point extrapolation equation (4.1) to obtain the energy at basis set limit E_∞.

$$E(L) = E_\infty + \frac{A}{L^\alpha} \tag{4.1}$$

---

[170] J. M. Anglada, J. González, and M. Torrent-Sucarrat. *Phys. Chem. Chem. Phys.*, **13**: 13034 – 13045, 2011.

[171] A. Tajti et al. *J. Chem. Phys.*, **121**: 11599 – 11613, 2004.

[172] A. Karton et al. *J. Chem. Phys.*, **125**: 144108, 2006.

[173] A. Karton, S. Daon, and J. M. Martin. *Chem. Phys. Lett.*, **510**: 165 – 178, 2011.

[174] Y. J. Bomble et al. *J. Chem. Phys.*, **125**: 064108, 2006.

[175] M. E. Harding et al. *J. Chem. Phys.*, **128**: 114111, 2008.

[176] A. D. Boese et al. *J. Chem. Phys.*, **120**: 4129 – 4141, 2004.

[•] This is mainly because there are no explicitly correlated versions HEAT methods, however, W3.2 is also slightly more economical than the equivalently accurate HEAT method.

Here, $E\,(L)$ is the energy resulting from a calculation employing a certain basis set (where L is the highest angular momentum quantum number of that basis set) and E_∞ the energy at basis set limit. The empirical parameter α depends on the method used. In Appendix A.2.1, this equation is derived.

Abbreviations	Basis set description		Ref.
valence basis sets			
V*n*Z	H−Ne:	cc-pV*n*Z	177
AV*n*Z	H−Ne:	aug-cc-pV*n*Z	178
A'V*n*Z	H:	cc-pV*n*Z	177
	B−Ne:	aug-cc-pV*n*Z	178
V(*n*+d)Z	H−Ne:	cc-pV*n*Z	177
	Al−Ar:	cc-pV(*n*+d)Z	179
AV(*n*+d)Z	H−Ne:	aug-cc-pV*n*Z	178
	Al−Ar:	aug-cc-pV(*n*+d)Z	179
A'V(*n*+d)Z	H:	cc-pV*n*Z	177
	B−Ne:	aug-cc-pV*n*Z	178
	Al−Ar:	aug-cc-pV(*n*+d)Z	179
core-valence basis sets			
CV*n*Z	H:	cc-pV*n*Z	177
	B−Ne:	cc-pCV*n*Z	180
ACV*n*Z	H:	aug-cc-pV*n*Z	178
	B−Ne:	aug-cc-pCV*n*Z	180
CV(*n*+d)Z	H:	cc-pV*n*Z	177
	B−Ne:	cc-pCV*n*Z	180
	Al−Ar:	cc-pCV(*n*+d)Z	181
ACV(*n*+d)Z	H:	aug-cc-pV*n*Z	178
	B−Ne:	aug-cc-pCV*n*Z	180
	Al−Ar:	aug-cc-pCV(*n*+d)Z	181

Abbreviations	Basis set description		Ref.
weighted core-valence basis sets			
wCV*n*Z	H:	cc-pV*n*Z	177
	B−Ne:	cc-pwCV*n*Z	181
AwCV*n*Z	H:	aug-cc-pV*n*Z	178
	B−Ne:	aug-cc-pwCV*n*Z	181
A'wCV*n*Z	H:	cc-pV*n*Z	177
	B−Ne:	aug-cc-pwCV*n*Z	181
wCV(*n*+d)Z	H:	cc-pV*n*Z	177
	B−Ne:	cc-pwCV*n*Z	181
	Al−Ar:	cc-pwCV(*n*+d)Z	182
A'wCV(*n*+d)Z	H:	cc-pV*n*Z	177
	B−Ne:	aug-cc-pwCV*n*Z	181
	Al−Ar:	aug-cc-pwCV(*n*+d)Z	182
special basis sets			
ANO2	H:	$[4s3p2d1f]$	183
	B−Ne:	$[5s4p3d2f1g]$	183
A'V*n*Z-DK	H:	cc-pV*n*Z-DK	184
	B−Ne:	aug-cc-pV*n*Z-DK	184
V*n*Z-F12	H−Ne:	cc-pV*n*Z-F12	36
MTsmall	H−Ne:	MTsmall	
wCVTZ (no f)	H:	cc-pV*n*Z	177
	B−Ne:	cc-pwCVTZ	181
	without f functions		

Table 4.1. | Basis sets; their abbreviations and references; $n = \{\mathrm{D}, \mathrm{T}, \mathrm{Q}, 5\}$.

A brief overview of the different components that make up this procedure are presented in Table 4.2 and in the following paragraphs. First, according to the protocol, the initial geometry is calculated at CCSD(T) / A'VQZ (or similar) level of theory. All further calculations are carried out using this geometry.

Segment	**W3-F12**
Reference Geometry	CCSD(T) / A'V(Q+d)Z
SCF	HF* / V({T,Q}+d)Z-F12
SCF extrapolation	$E(L) = E_\infty + A/L^{5.00}$
Valence CCSD	CCSD* / V({T,Q}+d)Z-F12
Valence CCSD extrapolation	$E(L) = E_\infty + A/L^{5.94}$
Valence (T)	(T*) / VTZ-F12 scaled by f
Valence T_3−(T)	CCSDT / V({D,T}+d)Z
Valence T_3−(T) extrapolation	$E(L) = E_\infty + A/L^{3.00}$
Valence (Q)	(Q) / VDZ
CCSD inner shell	CCSD / A'wCV{T,Q}Z
(T) inner shell	(T) / wCVTZ (no f)
Scalar relativistics	DKH-CCSD(T) / AV(Q+d)Z
DBOC	HF / A'VTZ
ZPVE	Best available
RMSD$_{\text{W4-11}}$ [kJ mol^{-1}]	1.13

Table 4.2. | Overview of the different methods that make up the W3-F12 protocol.[4] Basis set abbreviations can be found in Table 4.1.

The first segment is devoted to the acquisition of the CCSD(T) / CBS energy within the frozen core approximation, which is evaluated using the explicitly correlated methods.[185] Within the W3-F12 framework, they comprise of a Hartree–Fock (HF) and a coupled cluster approach including single and double excitations (CCSD) component and are applied using the V{T,Q}Z-F12 ($\alpha = 5.00$ for HF*) basis set of Peterson and co-workers.[36] One should note that the complementary auxiliary basis singles correction is included in the HF energy, which is denoted by the HF* acronym.[186,187] An explicitly correlated coupled cluster variant of the CCSD method, namely diagonal, fixed-amplitude 3C(FIX) ansatz along with the CCSD-F12b approximation, are employed.[185−189] In this variant−denoted as CCSD*− the same V{T,Q}Z-F12 basis set is used (where α = 5.94). Optimal geminal exponents

---

[185] S. Ten-no. *Chem. Phys. Lett.*, **398**: 56–61, 2004.

[186] G. Knizia and H.-J. Werner. *J. Chem. Phys.*, **128**: 154103, 2008.

[187] T. B. Adler, G. Knizia, and H.-J. Werner. *J. Chem. Phys.*, **127**: 221106, 2007.

[188] H.-J. Werner, G. Knizia, and F. R. Manby. *Mol. Phys.*, **109**: 407–417, 2011.

[189] G. Knizia, T. B. Adler, and H.-J. Werner. *J. Chem. Phys.*, **130**: 054104, 2009.

for all VnZ-F12 basis sets were taken from Reference [36]. The quasiperturbative approximation to $\widehat{T}_3$, (T), is taken from a normal CCSD(T) / VTZ calculation, which is then scaled by a factor of $f = 0.987 \cdot E_{\mathrm{MP2-F12\,/\,VTZ-F12}}/E_{\mathrm{MP2\,/\,VTZ}}$. As described in reference [4], this approach performs better than extrapolation; it is denoted as (T*).

In a second segment, the post coupled cluster singles and doubles method with perturbative inclusion of triples (CCSD(T)) contributions are calculated. Here, the CCSDT / V{D,T}Z ($\alpha = 3$) correlation energy is obtained, from which the (T) / V{D,T}Z ($\alpha = 3$) energy is subtracted to give T_3−(T). Additionally, the perturbative quadruples (Q) are determined with a VDZ basis set.

With the aim of approximating the contribution of the core correlation to the energy, the inner-shell contribution to the CCSD is obtained as the difference between an all-electron CCSD / A'wCVTZ and a frozen-core CCSD / A'VTZ calculation. The (T) component is the difference between an all-electron (T) / wCVTZ (no f) and a frozen core (T) / VTZ energy.

The scalar relativistic contribution, using in the second-order Douglas–Kroll–Hess (DKH) approximation,[190,191] is determined from a relativistic DKH-CCSD(T) / A'VDZ-DK calculation (second order direct perturbation theory approach). Atomic spin-orbit coupling terms are taken from the experimental fine structure. It is also necessary to calculate the diagonal Born–Oppenheimer corrections (DBOC); this is done at HF / VTZ level of theory.

Finally, the protocol does not specify a certain method for obtaining the zero-point vibrational energy (ZPVE). It states however that a higher order, preferably anharmonic calculations are needed. Where possible, anharmonic vibrational second-order perturbation theory (VPT2) calculations at a level of theory of CCSD(T) / A'VTZ are obtained. Otherwise, the harmonic CCSD(T) / A'VTZ ZPVE is scaled by a factor of 1.0007.[192]

For the thermochemical analysis it is necessary to calculate the heat of formation at 298 K, $\Delta_\mathrm{f} H_{298}$. Accordingly, one can convert E_TAE of a molecule M to its heat of formation at 0 K, $\Delta_\mathrm{f} H_0$ by subtracting the atomic heats of formation at 0 K, H_0. In order to obtain $\Delta_\mathrm{f} H_{298}$, the enthalpy functions $H_\mathrm{EF}(T = 298\,\mathrm{K}) = H_{298} - H_0$ for each molecule and element have to be subtracted as well. Note that for a molecule (harmonic approximation, ideal gas), $H_\mathrm{EF}(T)$ is the sum of ZPVE thermic, translational, rotational and vibrational energy:

$$H_\mathrm{EF}(T) = k_\mathrm{B}T + E_\mathrm{trans}(T) + E_\mathrm{rot}(T) + E_\mathrm{vib}(T) + E_\mathrm{ZPVE}\,. \tag{4.2}$$

---

[190] M. Douglas and N. M. Kroll. *J. Phys.*, **82**: 89 – 155, 1974.

[191] B. A. Hess. *Phys. Rev. A*, **33**: 3742 – 3748, 1986.

[192] M. K. Kesharwani, B. Brauer, and J. M. L. Martin. *J. Phys. Chem. A*, 141021073335006, 2014.

The heat of formation at 298 K is therefore obtained as

$$\Delta_\mathrm{f} H_{298} = E_{\mathrm{TAE},M} - H_{\mathrm{EF},M}(T = 298\,\mathrm{K}) - \sum_A x_A(H_{0,A} - H_{\mathrm{EF},A}(T = 298\,\mathrm{K}))\,, \tag{4.3}$$

where x_A is the stoichiometric factor of an atom A involved in the formation reaction. Atomic heats of formation at 0 K are sourced from the Active Thermochemical Tables (ATcT),[193–195] the enthalpy functions, $H_\mathrm{EF}(T = 298\,\mathrm{K})$, for the elemental reference states can be found in the CoData database.[196] A data selection for the elements and molecules treated in the present study are shown in Table 4.3. The enthalpy functions for the molecules of interest are obtained within the ridged rotor harmonic oscillator approximation from B3LYP / A'VTZ geometries and harmonic frequencies.[197]

Element	H_0	Molecule	State of matter	$H_\mathrm{EF}(T = 298\,\mathrm{K})$
H	216.034(1)	H_2	*g*	8.468(1)
C	711.38(6)	C	*cr*, graphite	1.050(20)
O	246.844(2)	O_2	*g*	8.680(2)

Table 4.3. | Atomic heats of formation at 0 K and CoData enthalpy functions as H_0 from the ATcTs and $H_\mathrm{EF}(T = 298\,\mathrm{K})$ for the elemental reference states, respectively.[193–196] All values in kJ mol^{-1}.

HF and CCSD(T) calculations are carried with the restricted or restricted open-shell algorithms.[•] For geometry optimisations and all vibrational analyses (harmonic and anharmonic) as well as the DBOC calculations, the CFOUR suite is employed,[198], as it contains an implementation of analytical gradients for the RHF-CCSD(T) as well as ROHF-CCSD(T) algorithm, thus being much more economical than equivalent other programs.[199] MP2, MP2-F12, CCSD-F12b and CCSD(T) single-point energies are

---

[193] B. Ruscic et al. *J. Phys. Chem. A*, **108**: 9979 – 9997, 2004.

[194] W. R. Stevens, B. Ruscic, and T. Baer. *J. Phys. Chem. A*, **114**: 13134 – 13145, 2010.

[195] B. Ruscic et al. *J. Phys. Chem. A*, **110**: 6592 – 6601, 2006.

[196] J. D. Cox, D. D. Wagman, and V. A. Medvedev *CODATA Key Values for Thermodynamics* see http://www.codata.org New York, 1989

[197] P. J. Stephens et al. *J. Phys. Chem.*, **98**: 11623 – 11627, 1994.

[•] In CFOUR this is done with the `RHF` or `ROHF` keyword and the `ECC` algorithm. In MOLPRO , the RHF-UCCSD(T) or RHF-RCCSD(T) default settings are used (RHF-UCCSD(T)-F12b or RHF-RCCSD(T)-F12b for explicitly correlated methods).

[198] CFOUR, a quantum chemical program package written by J.F. Stanton, J. Gauss, M.E. Harding, P.G. Szalay with contributions from A.A. Auer, R.J. Bartlett, U. Benedikt, C. Berger, D.E. Bernholdt, Y.J. Bomble, O. Christiansen, M. Heckert, O. Heun, C. Huber, T.-C. Jagau, D. Jonsson, J. Jusélius, K. Klein, W.J. Lauderdale, D.A. Matthews, T. Metzroth, D.P. O'Neill, D.R. Price, E. Prochnow, K. Ruud, F. Schiffmann, S. Stopkowicz, A. Tajti, J. Vázquez, F. Wang, J.D. Watts and the integral packages MOLECULE (J. Almlöf and P.R. Taylor), PROPS (P.R. Taylor), ABACUS (T. Helgaker, H.J. Aa. Jensen, P. Jørgensen, and J. Olsen), and ECP routines by A. V. Mitin and C. van Wüllen. For the current version, see http://www.cfour.de

[199] J. D. Watts, J. Gauss, and R. J. Bartlett. *J. Chem. Phys.*, **98**: 8718 – 8733, 1993.

obtained with the MOLPRO set of programmes.[200] T_3 as well as (Q) contributions are generated with the MRCC programme suit.[201] It should be noted that for these post-CCSD(T) calculations to open-shell systems are obtained with the respective unrestricted algorithms. Any density functional theory (DFT) calculation is carried out with either the GAUSSIAN or the ORCA programme suits.[202,203]

4.2.2 Photoelectron spectrum simulation

In the present work, all anion photoelectron spectra were simulated by determining the Franck–Condon (FC) factors linking the anion and neutral species vibrational states. FCFs were calculated using the ezSpectrum 3.0 programme code which is made freely available by Mozhayskiy and Krylov.[204] As described in Section 2.1.7, FC factors are obtained as a product of multidimensional FC integrals,[87] where vibrational mode mixing is accounted for by the Duschinsky rotation matrix describing the normal mode displacements.[88]

Input to the code consists of the output from the ab initio calculations, being geometries, vibrational frequencies, and vibrational normal mode vectors. The predicted stick spectra are also convoluted with a Gaussian response function of width 0.002 eV to simulate an experimental spectrum.

4.3 Methanal-oxide: anion and electron affinity

The first part of this carbonyl oxide analysis, focuses on the simplest of all Criegee intermediates, being methanal-oxide and its anion. Geometries, heats of formation, harmonic vibrational transitions of the neutral and anion species as well as a simulated photoelectron spectrum and the electron affinity for the anion are presented and discussed. In addition to these, the barrier height for reaction (R 4.8) is calculated.

$$CH_2OO^- \longrightarrow CH_2O + O^- \qquad \text{(R 4.8)}$$

All properties are obtained using W3-F12 theory,[4] they were published recently.[168]

---

[200] H.-J. Werner et al. MOLPRO*, version 2012.1, a package of ab initio programs* Cardiff, UK, 2012

[201] M. Kállay et al. MRCC*, a quantum chemical program suite* Version: July 10, 2014 Budapest, HU

[202] M. J. Frisch et al. *Gaussian 09 Revision A.1* Gaussian Inc. Wallingford CT 2009

[203] Neese, F. ORCA—an ab initio, Density Functional and Semiempirical program package, Version 3.0.2 Max–Planck-Insitut für Bioanorganische Chemie, Mülheim and der Ruhr, 2014.

[204] V. Mozhayskiy and A. Krylov *ezSpectrum* 2012

4.3.1 Geometries and vibrational frequencies

The geometry of the neutral Criegee intermediate is well known from previous high level calculations (see reference [166] and references cited therein). It has been shown that the C–O and O–O bond lengths are sensitive to the level of theory used, and it is noted that the values predicted from the CCSD(T) / A'VQZ calculations presented in this thesis are in line with those reported in references [165] and [166]. In Figure 4.1, the geometries of the anionic and neutral methanal-oxide structures are depicted.

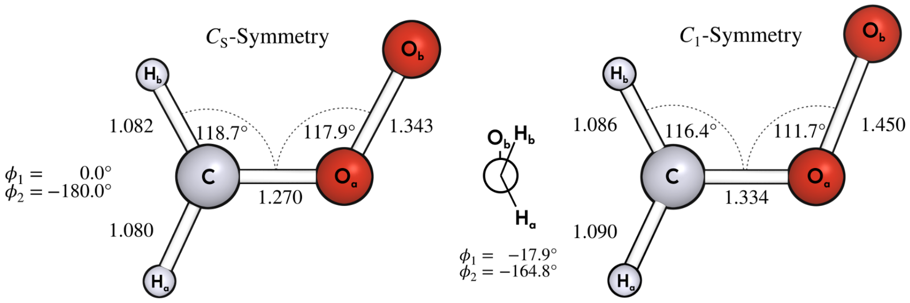

MetOx: methanal-oxide (neutral) **AMetOx**: methanal-oxide (anion)

Figure 4.1 | Anion and neutral species of CH_2OO. Bond lengths are given in Ångström. ϕ_1 refers to the dihedral angle between H_b, C, O_a and O_b; ϕ_2 between H_a, C, O_a and O_b. All geometric parameters obtained from CCSD(T) / A'VQZ calculations. The full geometric data are presented in Table A.2 of the Appendix.

For MetOx, lengths of 1.270 Å for the C–O bond and 1.343 Å for the O–O bond are predicted and are in good agreement with the CCSD(T) / AVTZ calculations of Nguyen et al. (1.275 Å and 1.375 Å from reference [166]). The agreement is also very good between the results presented here and those from Fang et al. (CAS-(8,6)+1+2 / VDZ calculations which showing C–O and O–O bond lengths of 1.280 Å and 1.322 Å respectively).[165]

As can be seen in Figure 4.1, the structure of the anion is similar to the neutral, however it features longer C–O and O–O bond lengths. The C–O bond length increases by 6 pm, while the O–O bond length increases by 11 pm. In addition to these two structural differences, the anionic methanal-oxide (AMetOx) is no longer of C_s symmetry as the hydrogen atoms have moved out of the plane defined by the C–O–O atoms. As presented in Figure 4.1, the H–C–O–O dihedral angles are −17.9° and −164.8° for AMetOx, whereas in the neutral species the values are 0° and 180°.

In order to rationalise the differences in anion and neutral geometries an analysis of the bonding behaviour is necessary. For this reason, a natural bond orbital (NBO) analysis was performed yielding populations of the bonding, anti-bonding, and lone pair natural orbitals.[205] These data, in terms of orbital occupancies, are provided in the Section 4.4 (Table 4.6).

Compared to MetOx, for AMetOx increased electron density is predicted in the lone pair orbitals of the carbon, and for the oxygen bound to carbon. The pyramidal nature of the anion complex, compared with the planar neutral, can be rationalised as the population in the carbon lone pair orbital. The NBO calculations also reveal decreased electron density in C−O and O−O bonding orbitals for AMetOx, leading to the increase in the bond lengths. Additionally, there is a marked decrease in the population of the C−O anti-bonding orbital, whereas the O−O anti-bonding orbital occupancy barely changes. This explains the larger change in the O−O bond length compared with the C−O bond length when going from anion to neutral.

	Anion (AMetOx)		**Neutral (MetOx)**					
Method		CCSD(T)		CCSD(T)		NEVPT2		
Basis Set		A'VQZ		A'VQZ	AVTZ	AVDZ		
Mode	S	Harm.	S	Harm.	Harm.	Harm.	Anharm.	**Mode description**
ω_1	a	3185	a'	3302	3290	3370	3149	Asymmetric CH stretch
ω_2	a	3048	a'	3140	3137	3197	3030	Symmetric CH stretch
ω_3	a	1422	a'	1489	1483	1500	1458	CH_2 scissor / CO stretch
ω_4	a	1252	a'	1316	1306	1338	1302	CO stretch / CH_2 scissor
ω_5	a	1164	a'	1239	1231	1235	1220	CH_2 rocking
ω_6	a	776	a'	945	935	916	892	OO stretch
ω_7	a	466	a'	532	529	536	530	COO deformation
ω_8	a	601	a''	876	862	856	853	CH_2 wagging
ω_9	a	316	a''	651	632	620	606	CH_2 twisting
Ref.		This work		This work	[166]	[5]	[5]	as in [5]

Table 4.4. | Computed vibrational wavenumber values of the CH_2OO anion and neutral species in cm^{-1} at CCSD(T) / A'VQZ level of theory as well as comparisons with other recently published work. The ordering of the modes of the anion has been changed to reflect that of the neutral (and its symmetry S), for direct comparison.

---

[205] E. D. G. J et al. *NBO 6.0.* Theoretical Chemistry Institute, University of Wisconsin, Madison (2013)

In Table 4.4, harmonic vibration frequencies of the neutral and anionic methanal-oxide at a level of theory of CCSD(T) / A'VQZ are presented. The vibrational modes of the neutral species have been ordered according to the usual numbering scheme appropriate for a C_S symmetry molecule (wavenumber descending in a', and then descending in a'' symmetry). For ease of comparison between the anion and neutral modes, the same order was adopted for the anion species even though they are all of a symmetry. In any event, the mode description for each mode is provided in the table. It is noted that the increased O–O bond length in the anion species is reflected in a reduction of the frequency of the O–O stretching mode, ω_6, from $945\,\mathrm{cm}^{-1}$ to $776\,\mathrm{cm}^{-1}$. Similarly the C–O bond length increase is accompanied by a reduction in vibrational frequency of modes ω_3 and ω_4. The CH_2 wagging mode also decreases in frequency in the anion species. A more detailed analysis of the molecular vibrations can be found in Section 4.5.2.

4.3.2 Stability of the anion with respect to dissociation

In order to determine the stability of AMetOx the reaction profile for dissociation to the products formaldehyde and oxide was modelled. This was achieved by optimising the geometry of the transition state (TS) linking the reactant CH_2OO^- and the products CH_2O and O^-. The W3-F12 protocol was applied to the TS, anion, and products with the results shown in Figure 4.2. Geometries of the AMetOx-TS and the methanal molecule are provided in Figure 4.3. It is noted that the C–O bond length (at CCSD(T) / A'VTZ level of theory) for AMetOx is 1.333 Å, for the AMetOx-TS this length is 1.317 Å and for the methanal molecule it is 1.212 Å. A barrier to dissociation clearly exists and it is therefore argued that the anion can survive long enough in a cold, supersonically expanded molecular beam to allow for spectroscopic interrogation.

4.3.3 W3-F12 heat of formation and electron affinity

The components of the W3-F12 total atomisation energies for the CH_2OO and CH_2OO^- species are given in Table 4.5. At the W2-F12 level (W3-F12 without post-CCSD(T) contributions), the relativistic, all-electron CCSD(T) contributions to TAE_0 add up to $1520.9\,\mathrm{kJ\,mol}^{-1}$ for CH_2OO, and $1581.5\,\mathrm{kJ\,mol}^{-1}$ for CH_2OO^-. The TAE_0 for MetOx is by $1.8\,\mathrm{kJ\,mol}^{-1}$ higher than the W1 value published by Nguyen and co-workers.[166] The majority of this difference comes from the valence CCSD(T) components which are closer to the basis set limit when calculated with the W2-F12 protocol. Furthermore, the improved CCSD(T) / A'VQZ geometry, the better ZPVE and DBOC (not included in the W1) contribute to the remainder.

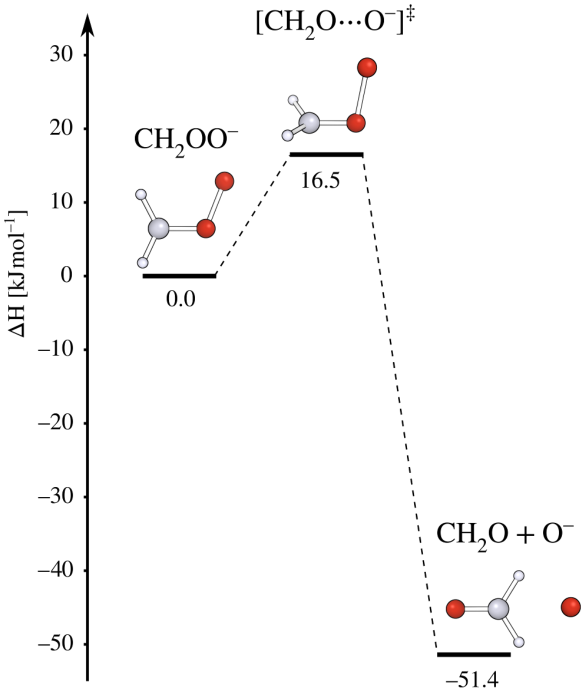

Figure 4.2 | Reaction profile illustrating the dissociation channel of the methanal-oxide anion CH_2OO^- to the products $CH_2O + O^-$ calculated with W3-F12 protocol at 298 K.

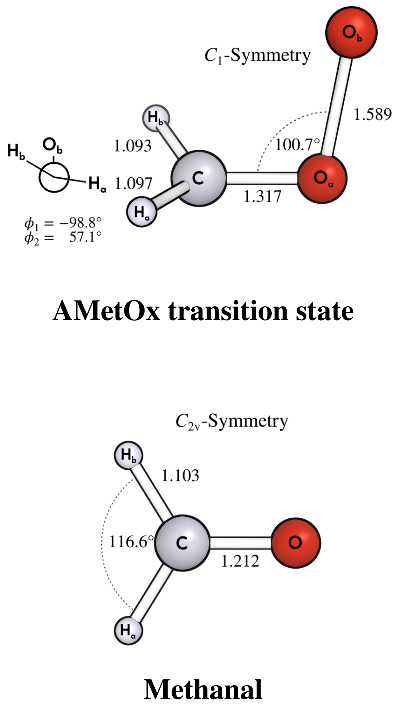

Figure 4.3 | The anionic methanal-oxide transition state and methanal geometries optimised at CCSD(T) / A'VTZ level of theory

As outlined in Section 4.2, the carbonyl oxide class of molecules seem to exhibit some multi-reference character, i.e. the HF is not a good approximation when aiming for chemical accuracy. There are a variety of diagnostics available to test for multi-reference character, e.g. the %TAE[(T)], T_1 or D_1 diagnostics.[172,173,206–209] For a CCSD(T) calculation to be reliable, the threshold criteria for the aforementioned diagnostics are usually as follows: %TAE[(T)]< 10%, $T_1 < 0.02$ and $D_1 < 0.06$.[210] According to Sprague and Irikura, the %TAE[(T)] shows the best performance against their test-set, producing the fewest false negatives and false positives.[211] As well as Martin and Karton,[172] they found that %TAE[(T)] correlates well with the T_4+T_5 contribution. This diagnostic can therefore not only

---

[206] T. J. Lee and P. R. Taylor. *Int. J. Quantum Chem.*, **36**: 199 – 207, 1989.
[207] T. J. Lee et al. *Theor. Chim. Acta*, **75**: 81 – 98, 1989.
[208] M. L. Leininger et al. *Chem. Phys. Lett.*, **328**: 431 – 436, 2000.
[209] T. J. Lee. *Chem. Phys. Lett.*, **372**: 362 – 367, 2003.
[210] W. Jiang, N. J. DeYonker, and A. K. Wilson. *J. Chem. Theory Comput.*, **8**: 460 – 468, 2012.
[211] M. K. Sprague and K. K. Irikura. *Theor. Chem. Acc.*, **133**: 1544(1) – 1544(12), 2014.

be used for a qualitative analysis of the non-dynamical correlation but also serves as a qualitative diagnostic.

The CH_2OO neutral and anion species considered in the present study exhibit mild-to-moderate non-dynamical correlation effects; 53 % to 55 % of the atomisation energy is accounted for at the SCF level, and 3.8 % to 4.6 % by the (T) triples (%TAE[(T)]). T_1 diagnostics return values of 0.034 to 0.045, D_1 diagnostics show values of 0.122 to 0.176, indicating that post-CCSD(T) excitations may have non-trivial contributions. A detailed listing and comparison with the ethanal-oxide species (discussed in Section 4.4) is provided in Table 4.9.

The generally good performance of the CCSD(T) / CBS level of theory in computational thermochemistry can typically be attributed to the large degree of cancellation between higher-order triples contributions, $T_3-(T)$, and post-CCSDT contributions. For systems dominated by dynamical correlation, these contributions are of similar magnitudes, however, the $T_3-(T)$ excitations tend to universally decrease the atomisation energies whereas the post-CCSDT excitations tend to universally increase the atomisation energies. For the CH_2OO^- anion there is a significant degree of cancellation between the $T_3-(T)$ contribution ($-2.7\,\mathrm{kJ\,mol^{-1}}$) and the (Q) contribution ($4.5\,\mathrm{kJ\,mol^{-1}}$), resulting in a post-CCSD(T) contribution of $1.8\,\mathrm{kJ\,mol^{-1}}$. However, for MetOx there is significantly poorer cancellation between the $T_3-(T)$ ($-3.4\,\mathrm{kJ\,mol^{-1}}$) and (Q) contributions ($9.8\,\mathrm{kJ\,mol^{-1}}$). Therefore, the post-CCSD(T) contributions increase the atomisation energy of CH_2OO by as much as $6.4\,\mathrm{kJ\,mol^{-1}}$. It is noted that the inclusion of higher-order quadruple contributions, $T_4-(Q)$, is likely to reduce the magnitude of the connected quadruple excitations, and therefore the CCSDT(Q) / CBS values calculated here should be regarded as upper limits of the TAEs.

Overall, the best relativistic, all-electron CCSDT(Q) / CBS atomisation energies (shown in Table 4.5) are $1527.3\,\mathrm{kJ\,mol^{-1}}$ (CH_2OO) and $1583.3\,\mathrm{kJ\,mol^{-1}}$ (CH_2OO^-). These correspond to heats of formation at 0 K of $109.9\,\mathrm{kJ\,mol^{-1}}$ (CH_2OO) and $53.8\,\mathrm{kJ\,mol^{-1}}$ (CH_2OO^-), and heats of formation at 298 K of $102.8\,\mathrm{kJ\,mol^{-1}}$ (CH_2OO) and $48.1\,\mathrm{kJ\,mol^{-1}}$ (CH_2OO^-). In accordance with the large post-CCSD(T) contributions for MetOx, W3-F12 heats of formation are lower than the W1 values obtained by Nguyen et al. ($\Delta_f H_0 = 113.0\,\mathrm{kJ\,mol^{-1}}$ and $\Delta_f H_{298} = 105.9\,\mathrm{kJ\,mol^{-1}}$).[166]

Using the W3-F12 heats of formation for the CH_2OO neutral and anion species electron affinities of $56.1\,\mathrm{kJ\,mol^{-1}}$ at 0 K and $54.7\,\mathrm{kJ\,mol^{-1}}$ at 298 K were obtained. It is noted that the post-CCSD(T) contributions to the electron affinity add up to as much as $4.5\,\mathrm{kJ\,mol^{-1}}$.

Molecule or property	CH_2OO	CH_2OO^-	$E^{\dagger}_{EA}$	E^{*}_{BH}
SCF	873.4	903.1	29.7	34.0
CCSD	652.0	685.8	33.7	−4.6
(T)	74.4	62.9	−11.5	−5.8
T_3−(T)	−3.4	−2.7	0.8	−1.9
(Q)	9.8	4.5	−5.3	−1.3
Inner-Shell	5.5	5.2	−0.3	0.5
Scalar Relativistic	−1.9	−2.2	−0.3	−0.2
Spin-Orbit	−2.2	−2.2	0.0	0.0
DBOC	0.3	0.1	−0.1	0.1
TAE_e	1608.0	1654.6	46.6	20.7
ZPVE	80.7	71.3	−9.4	4.3
TAE_0	1527.3	1583.3	56.1	16.4
$\Delta_f H_0$	109.9	53.8	56.1	16.4
$\Delta_f H_{298}$	102.8	48.1	54.7	16.5

† Energy for the $CH_2OO^- \longrightarrow CH_2OO + e^-$ reaction.

∗ Barrier height for the $CH_2OO^- \longrightarrow CH_2O + O^-$ reaction.

Table 4.5. | Component breakdown of the W3-F12 TAEs and heats of formation of the CH_2OO neutral and anion species, electron affinity of CH_2OO, and barrier height for the $CH_2OO^- \longrightarrow CH_2O + O^-$ reaction (in kJ mol^{-1}).

4.3.4 Methanal-oxide: photoelectron spectrum

Using the CCSD(T) / A'VQZ geometries, vibrational frequencies, and normal mode vectors as an input for the ezSpectrum 3.0 code it is now possible to predict the form of the anion photoelectron spectrum. The simulation of the vibronic transitions is obtained with a temperature parameter of 10 K, which is appropriate for species entrained in a molecular beam produced via supersonic expansion. Up to 10 quanta were allowed in each excited state vibrational mode (i.e. the modes of the neutral CH_2OO species). In Figure 4.4, a stick spectrum against the electron binding energy, E_{eB}, is presented, where the grey part of the spectrum identifies the combination bands, whereas the red part represents the pure progressions; together they form the fully predicted spectrum. The major progressions are labelled as $P^{v'}_{v''}$, where P represents the vibrational mode of the final state; v'' and v' represent the vibrational quantum number of the initial (anion) and final (neutral) states, respectively.

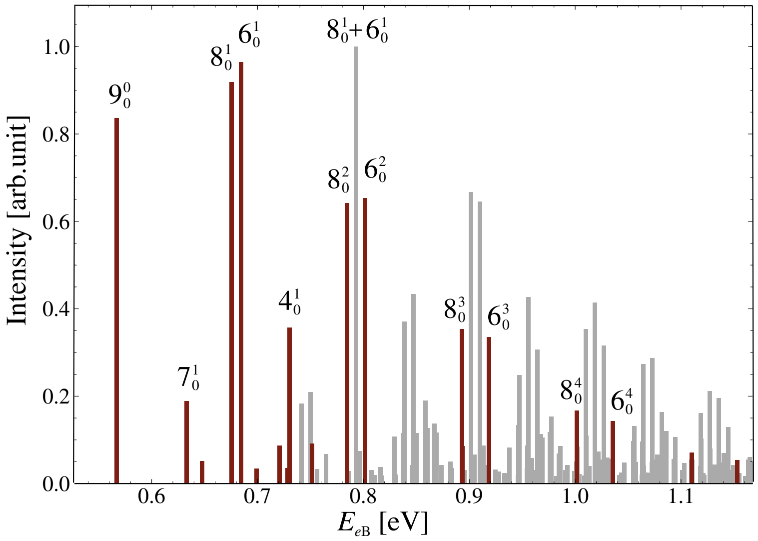

Figure 4.4 | Predicted photoelectron stick spectrum of AMetOx, red colour identifies the pure progressions, grey areas the combination bands.

The majority of the pure progressions (marked red in Figure 4.4) are for the modes ω_6 and ω_8 which correspond to the O–O stretching and CH_2 wagging modes respectively. The fact that these two modes display the longest progressions is consistent with the geometry changes observed between the anion and neutral species. Referring to the data in Figure 4.1, the O–O bond length is predicted to decrease by 11 pm, while the two hydrogen atoms move into the C–O–O plane, with the pair of H–C–O–O dihedral angles changing from −17.9° and −164.8° to 0.0° and 180.0°.

To provide a clearer picture of what an experimental spectrum might look like, the line spectrum was convoluted with a Gaussian response function whose full width at half maximum (FWHM) was set to 0.002 eV and the resulting simulated spectrum is shown in Figure 4.5. This resolution seems appropriate since it is achievable by the state-of-the-art anion photoelectron spectrometers in use today.

As a final note, when considering the mass selected photoelectron spectrum of the CH_2OO^- anion one cannot discount the possibility that a van der Waals complex of the form $O^-\cdots CH_2O$ may also be synthesised in addition to the covalently bound CH_2OO^- anion. This possibility needs to be taken into account, however, fortuitously the ionisation energy of the O^- anion is much larger than for CH_2OO^-, with the most recent determination of the electron affinity of the O neutral measured at 1.439 157 eV.[212] The $O^-\cdots CH_2O$ species should essentially be a perturbed O^- anion, due to the weak interaction in a van der Waals species, and in addition the electron binding energy of the anion generally increases

---

[212] A. Joiner, R. H. Mohr, and J. N. Yukich. *Phys. Rev. A*, **83**: 035401, 2011.

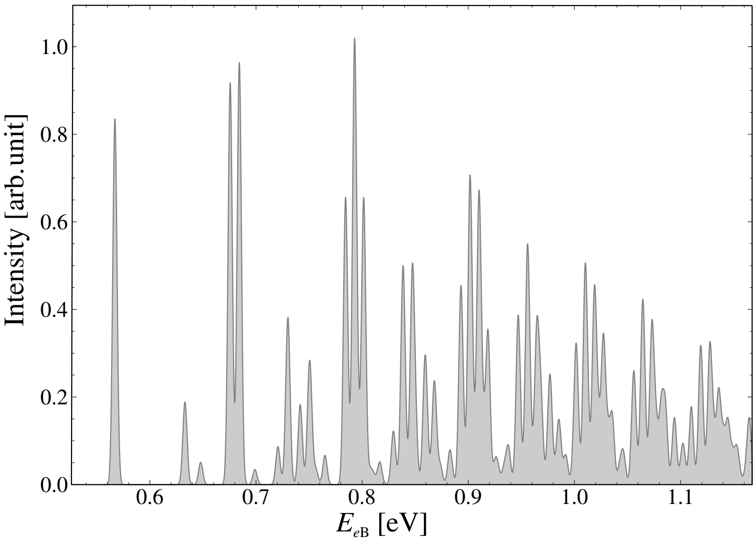

Figure 4.5 | Simulated photoelectron spectrum of AMetOx with the stick spectrum shown in Figure 4.4 (convoluted with Gaussian response function (FWHM of 2 meV).

upon formation of a van der Waals complex. Therefore, AMetOx can be preferentially targeted by selecting a photodetachment photon energy below 1.4 eV.

4.4 Ethanal-oxide: anions and electron affinities

The second part of this carbonyl oxide analysis addresses the ethanal-oxides and their anions. While the neutral isomers are 'reasonable-sized' calculations, the anionic structures – since they are exhibiting lower symmetries and open-shell systems – are challenging to calculate with the W3-F12 method. It was still possible to obtain geometries, heats of formation, harmonic vibrational transitions of the neutrals and anions as well as a simulated photoelectron spectra and the electron affinities for the anions; all of which are presented and discussed in this section. This work was published recently in Chemical Physics Letters.[213]

4.4.1 Geometries and vibrational frequencies

In Figure 4.6, the four ethanal-oxide structures are presented. They are obtained at CCSD(T) / A'VTZ level of theory instead of as recommended with CCSD(T) / A'VQZ, which is due to the immense computational effort involved in carrying out an optimisation for the anions at that level of theory. The expected changes in energy when going to a quadruple zeta geometry are deemed negligible in this case (from prior experience with MetOx). The neutral, closed-shell equilibrium isomers, both feature C_S symmetry and, as shown in the NBO analysis (Table 4.6), both exhibit a C=O double bond. For this reason the neutral species are labelled as *cis*-ethanal-oxide (^{c}EtOx) and *trans*-ethanal-oxide (^{t}EtOx). Due to the electrostatic interaction between H_c and H_d atom of the methyl group with the O_b atom, ^{c}EtOx is by 14.1 kJ mol^{-1} more stable than ^{t}EtOx (These differences are results of W3-F12 calculations, which are expanded upon in Section 4.4.2). A partial charge representation of a natural population analysis is illustrated in Figure 4.7.

Contrary to the neutrals, the anionic structures do not show any symmetry, which can be seen when comparing the dihedral angles ϕ_1 and ϕ_2 in Figure 4.6. For this reason and the fact that according to an NBO analysis the anionic structures do not feature a 'classic' C=O double bond, the molecules are labelled as anionic *syn*-ethanal-oxide (^{s}AEtOx) and anionic *anti*-ethanal-oxide (^{a}AEtOx), respectively. It is also noticed that the ^{a}AEtOx isomer is slightly more stable (by 0.4 kJ mol^{-1}) than the ^{s}AEtOx isomer. For both anionic structures, the C−C bond is lengthened on average by 2 pm, the C−O bond by 7 pm and the O−O bond by 10 pm, compared to their neutral counterparts.

---

[213] M. Kettner et al. *Chem. Phys. Lett.*, **621**: 193 – 198, 2015.

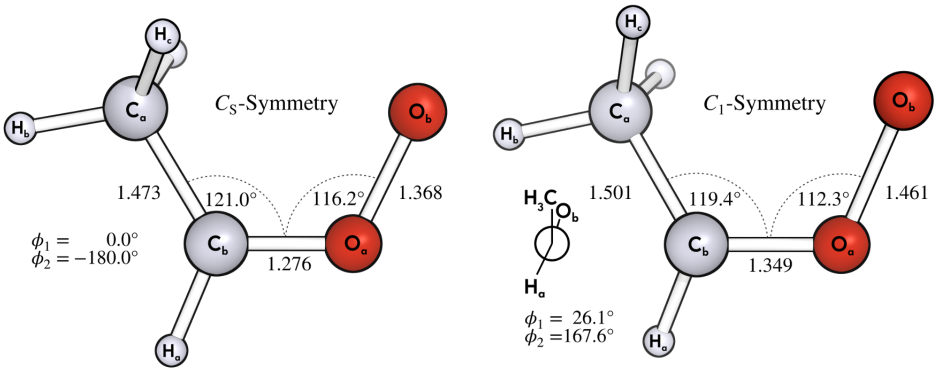

^{c}EtOx: *cis*-ethanal-oxide (neutral) **^{s}AEtOx**: *syn*-ethanal-oxide (anion)

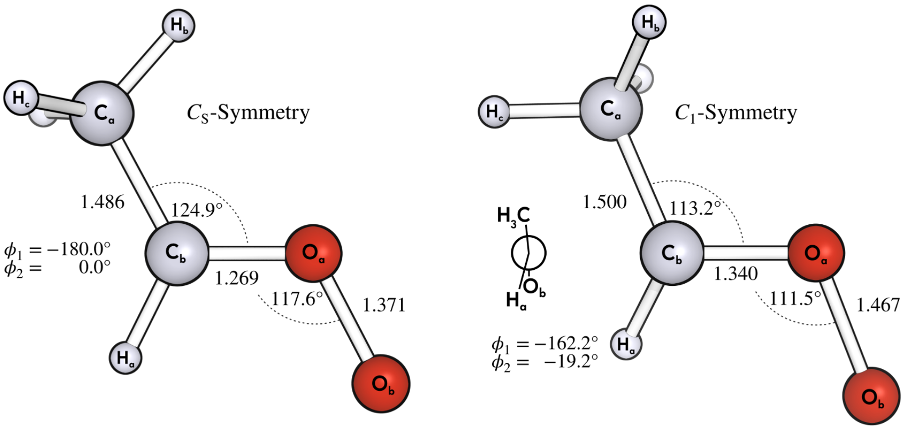

^{t}EtOx: *trans*-ethanal-oxide (neutral) **^{a}AEtOx**: *anti*-ethanal-oxide (anion)

Figure 4.6 | Anion and neutral species of CH_3CHOO. Bond lengths are given in Ångström. ϕ_1 refers to the dihedral angle between C_a, C_b, O_a and O_b; ϕ_2 between H_a, C_b, O_a and O_b. All geometric parameters obtained from CCSD(T) / AVTZ calculations. The full geometric data are presented in Table A.3 of the Appendix.

Both calculated neutral geometries are in good agreement with the CCSD(T)-F12a / AVTZ structures reported by Nakajima and Endo.[162,163] The bond lengths reported by the group in the most extreme case deviate by 12 pm (C–C bond), but on average less than 2 pm. It is also noticed that their experimentally determined rotational constants A_0, B_0 and C_0 agree very well with the equilibrium and ground state rotational constants. A comparison between the experimentally determined and computationally determined rotational constants is presented in Table A.5 of the Appendix. It should be pointed out that there are no literature-reported computational ground state rotational constants for the ethanal-oxides (Nakajima and co-workers only report values at equilibrium position). As discussed in

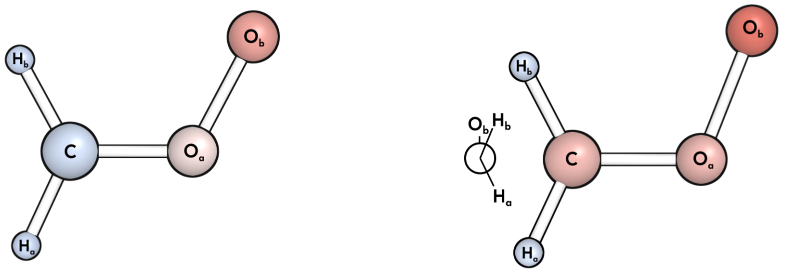

MetOx: methanal-oxide (neutral)

AMetOx: methanal-oxide (anion)

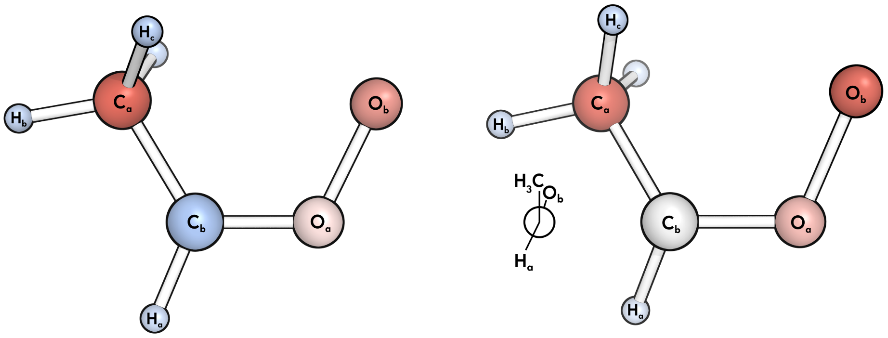

^{c}**EtOx**: *cis*-ethanal-oxide (neutral)

^{s}**AEtOx**: *syn*-ethanal-oxide (anion)

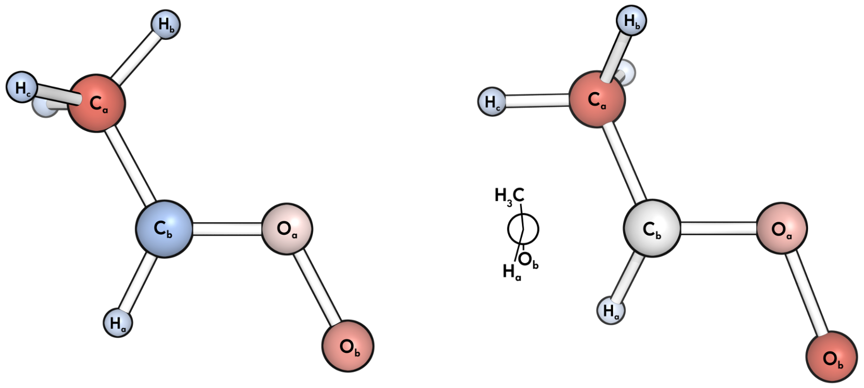

^{t}**EtOx**: *trans*-ethanal-oxide (neutral)

^{a}**AEtOx**: *anti*-ethanal-oxide (anion)

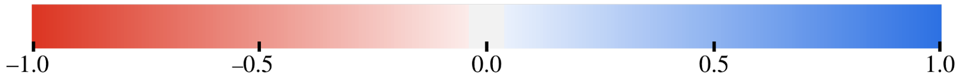

Figure 4.7 | Partial charges for methanal and ethanal oxides. These are obtained from a natural population analysis at B3LYP / AVQZ level of theory.

Section 4.5.3, a VPT2-CCSD(T) / A'VTZ force field is obtained for ^{c}EtOx which is used to obtain the ground state rotational constants reported in Table A.5 of the Appendix.

A B3LYP / 6-31G(d,p) structure for ^{c}EtOx reported by Gutbrod and co-workers,[150] also matches the structure reported in the present work (where the largest difference is the C–O–O angle, deviating by 1.0°). The ^{c}EtOx and ^{t}EtOx geometries also compare well to the neutral form of the simplest carbonyl oxide, MetOx, see Section 4.3.1, which shows very similar bond lengths [r(C–O) = 1.270 Å, r(O–O) = 1.343 Å and θ(C–O–O) = 117.9°].

In the 'anionic case', which has not been explored theoretically before, both molecules, ^{s}AEtOx and ^{a}AEtOx, display similar structural features as AMetOx. As shown in Figure 4.1 AMetOx exhibits bond lengths of 1.334 Å [r(C–O)] and 1.450 Å [r(O–O)]; as well as bond angles of 111.7° [θ(C–O–O)], 164.8° [ϕ_1] and −17.9° [ϕ_2]. The NBO analysis of the ethanal-oxides suggests that the anionic structures harbour the additional electron in the $\mathrm{C_b}$ lone-pair orbital, which explains the change from C_S to C_1 symmetry when going from the neutral to the anion. Additionally, the $\mathrm{C_b}$–$\mathrm{O_a}$ bond is weakened significantly as the summed occupancies of these double bonding orbitals drop from ca. 4.0 for the neutrals to ca. 3.0 in the anions. The remaining electron populates a $\mathrm{O_a}$ lone pair orbital, which also reveals why the $\mathrm{O_a}$–$\mathrm{O_b}$ bond is longer for the anion. It should be noted however that the $\mathrm{C_b}$–$\mathrm{O_a}$ bond orbital and the $\mathrm{O_a}$ lone pair orbital are almost degenerate. Compared to the MetOx and AMetOx electronic structures, the neutrals and anions are very similar; yet due to the methyl group, the $\mathrm{C_b}$–$\mathrm{O_a}$ anti-bonding orbitals in the ethanal-oxide species display slightly higher electron density. The detailed NBO analysis and comparison between the carbonyl oxide structures is presented in Table 4.6.

Molecule	**^{c}EtOx**	**^{t}EtOx**	**MetOx**	**^{s}AEtOx**	**^{a}AEtOx**	**AMetOx**
$\mathrm{O_a}$ lone pair	1.9718	1.9728	1.9780	2.9504	2.9474	2.9706
$\mathrm{O_b}$ lone pair	5.6964	5.7164	5.8510	5.8739	5.8978	5.9699
$\mathrm{C_a}$ lone pair	0.0000	0.0000	0.0000	0.9277	0.9149	0.9933
$\mathrm{C_a}$–$\mathrm{O_a}$ bonding	3.9871	3.9848	3.9959	2.9866	2.9868	2.9960
$\mathrm{C_a}$–$\mathrm{C_b}$ bonding	1.9953	1.9855	–	1.9947	1.9860	–
$\mathrm{O_a}$–$\mathrm{O_b}$ bonding	1.9884	1.9852	1.9913	1.9872	1.9822	1.9873
$\mathrm{C_a}$–$\mathrm{O_b}$ anti-bonding	0.3453	0.3158	0.1316	0.1214	0.0972	0.0180
$\mathrm{C_a}$–$\mathrm{C_b}$ anti-bonding	0.0190	0.0126	–	0.0211	0.0148	–
$\mathrm{O_a}$–$\mathrm{O_b}$ anti-bonding	0.0188	0.0159	0.0085	0.0183	0.0152	0.0088

Table 4.6. | Orbital occupancies for the carbonyl oxide molecules. Results were obtained from NBO 6.0 calculations at B3LYP / A'VQZ level of theory.

Mode	Neutral			Anion			Mode description
	^{c}EtOx	^{t}EtOx	S	^{s}AEtOx	^{a}AEtOx	S	
ω_1	3201	3166	a'	3051	3104	a	C_b–H_a stretch
ω_2	3155	3147	a'	3090	3015	a	C_a–H asymmetric stretch (methyl group)
ω_3	3026	3035	a'	2918	2886	a	C_a–H symmetric stretches (methyl group)
ω_4	1514	1525	a'	1493	1381	a	asymmetric O–C / C–O stretch
ω_5	1470	1462	a'	1402	1500	a	CH_2 scissor / H_b–C_aC_b bend
ω_6	1397	1419	a'	1362	1348	a	methyl inversion / C–O stretch
ω_7	1306	1312	a'	1231	1245	a	in-plane C_b–H_a rocking / C–O stretch
ω_8	1113	1155	a'	1118	1118	a	methyl wagging / C–C stretch
ω_9	974	942	a'	913	938	a	C–C stretch
ω_{10}	905	895	a'	787	785	a	O–O stretch
ω_{11}	669	553	a'	526	478	a	methyl wagging / O–O–C bend
ω_{12}	304	320	a'	221	302	a	C–C–O–O scissor bend / deformation
ω_{13}	3079	3098	a''	3018	3065	a	C_a–H asymmetric stretch (methyl group)
ω_{14}	1454	1480	a''	1446	1467	a	CH_2 twist / C_a–H_b rocking
ω_{15}	1034	1054	a''	1026	1030	a	methyl twisting / C_b–H_a rocking
ω_{16}	724	843	a''	649	654	a	C_b–H_a wagging / methyl rocking
ω_{17}	443	248	a''	306	120	a	C–C–O–O out-of-plane twisting
ω_{18}	209	153	a''	159	196	a	methyl twisting (internal rotation)

All frequencies given in cm^{-1}.

Table 4.7. | Computed harmonic vibrational frequencies of the CH_3CHOO anion and neutral species at the CCSD(T) / A'VTZ level of theory. The ordering of the modes of all other species has been changed to reflect that of ^{c}EtOx (orderded according to the Symmetry S of the modes), for direct comparison. An approximation of the (anharmonic) fundamentals is presented in the appended Table A.4.

The normal mode vibrational frequencies are presented in Table 4.7, where they are sorted in accordance to the standard numbering scheme for the C_S point group. In Section 4.5.3 preliminary results for anharmonic frequenscies (obtained by means of the VPT2 method) are discussed in more detail. It is possible to approximate the (anharmonic) fundamental frequencies by means of applying a linear scaling factor to the harmonic frequencies.[192] These fundamental frequencies are presented in appended Table A.4. The idea behind a linear scaling factor is that anharmonic frequencies are in general smaller than the values derived from the harmonic approximation. In the present case for example the O–O stretching frequency for ^{c}EtOx is reduced by ca. 33 cm^{-1} from 905 cm^{-1} to 872 cm^{-1} after scaling.

In the neutral structures, ^{c}EtOx exhibits a weak interaction between the terminal oxygen O_b and the methyl hydrogen atoms H_c and H_d. Similar to a weak hydrogen bond, this interaction stabilises the molecule by 14.1 kJ mol^{-1}, compared to ^{t}EtOx. This is also the reason why all the vibrations where O_b, H_c and H_d are involved exhibit a red-shift in ^{t}EtOx. The most notable case is the C−C−O−O out-of-plane twisting (ω_{17}) which shows an eigenfrequency of 443 cm^{-1} in ^{c}EtOx and 248 cm^{-1} in ^{t}EtOx. Another example is the methyl wagging / O−O−C bend (ω_{11}) where the red-shift amounts to 116 cm^{-1}. In contrast, the C_b−H_a wagging/methyl rocking vibration (ω_{16}) display a 120 cm^{-1} blue-shift.

The differences in mode frequencies between the anionic and neutral seem quite similar to the differences encountered in the AMetOx. Reflecting the increased stability, the O−O stretches (ω_{10}) blue-shift on average by 114 cm^{-1} when comparing the anion to the neutral. It can be observed however, that the blue-shift for the asymmetric O−C / C−O stretch (ω_4) is much larger when going from ^{a}AEtOx to ^{t}EtOx than when going from ^{s}AEtOx to ^{c}EtOx.

4.4.2 W3-F12 heats of formation and electron affinities

All components of the W3-F12 total atomisation energies for the ethanal-oxide species are given in Table 4.8. At the W2-F12 level, the relativistic, all-electron CCSD(T) contributions to TAE_0 add up to 2724.0 kJ mol^{-1} (^{c}EtOx), 2746.5 kJ mol^{-1} (^{s}AEtOx), 2709.5 kJ mol^{-1} (^{t}EtOx) and 2747.2 kJ mol^{-1} (^{a}AEtOx).

As described in Section 4.3.3, a variety of diagnostics can be applied in order to analyse the extent of non-dynamical correlation effects. Table 4.9 provides these, namely the percentage of the total atomisation energy accounted for by the SCF and (T) triples contributions from W2-F12 theory,[172,173] as well as the coupled cluster T_1 and D_1 diagnostics.[206–209] The CH_3CHOO neutral and anion species considered here exhibit mild-to-moderate non-dynamical correlation effects; 64 % to 66 % of the atomisation energy is accounted for at the SCF level, and 2.7 % to 3.1 % by the perturbative triples. The T_1 diagnostics of 0.029 to 0.040 and D_1 diagnostics of 0.120 to 0.181 also indicate that post-CCSD(T) excitations may have non-trivial contributions. It is therefore necessary to obtain the CCSDT and CCSDT(Q) contributions from W3-F12 theory. The overall post-CCSD(T) contribution to the atomisation energy amount to 5.3 kJ mol^{-1} and 5.7 kJ mol^{-1} in the neutral structures (^{c}EtOx and ^{t}EtOx respectively), and to 1.6 kJ mol^{-1} and 1.9 kJ mol^{-1} in the anions (^{s}AEtOx and ^{a}AEtOx respectively). It is noted that the T_4−(Q), is likely to reduce the magnitude of the connected quadruple excitations, and therefore the CCSDT(Q) / CBS values should be regarded as upper limits of the TAEs.

Molecule or property	**^{s}AEtOx**	**^{c}EtOx**	E_{EA}(T1)	**^{a}AEtOx**	**^{t}EtOx**	E_{EA}(T2)
SCF	1860.0	1877.3	−17.3	1866.8	1874.8	−7.9
CCSD	949.6	907.9	41.7	944.1	897.2	46.8
(T)	79.8	88.3	−8.4	78.8	85.9	−7.1
T_3−(T)	−3.6	−4.6	1.1	−3.6	−4.2	0.6
(Q)	5.5	9.9	−4.4	5.2	9.9	−4.7
Inner-Shell	10.0	10.6	−0.6	10.1	10.6	−0.5
Scalar Relativistic	−3.0	−2.6	−0.3	−3.0	−2.7	−0.3
Spin-Orbit	−2.6	−2.6	–	−2.6	−2.6	–
DBOC	0.4	0.6	−0.3	0.4	0.6	−0.2
TAE_e	2896.2	2884.7	11.5	2896.2	2869.6	26.6
ZPVE	147.8	155.4	−7.6	147.3	154.4	−7.0
TAE_0	2748.4	2729.3	19.1	2748.8	2715.2	33.6
$\Delta_{\mathrm{f}}H_0$	32.2	51.3	19.1	31.7	65.4	33.6
$\Delta_{\mathrm{f}}H_{298}$	20.1	37.8	17.7	20.0	52.6	32.6

Table 4.8. | Component breakdown of the W3-F12 TAEs, heats of formation and electron affinities of the CH_3CHOO neutral and anion species (in kJ mol^{-1}).

Molecule	**MetOx**	**AMetOx**	**^{s}AEtOx**	**^{c}EtOx**	**^{a}AEtOx**	**^{t}EtOx**
%TAE[(T)]	4.6	3.8	2.8	3.1	2.7	3.0
%TAE[SCF]	54.4	54.6	64.4	65.3	64.6	65.6
T_1	0.044	0.034	0.031	0.040	0.029	0.039
D_1	0.176	0.122	0.132	0.181	0.120	0.180

Table 4.9. | Non-dynamical correlation diagnostics for methanal and ethanal-oxides.

The heats of formation for the neutral species at 0 K amount to 51.3 kJ mol^{-1} (^{c}EtOx) and 65.4 kJ mol^{-1} (^{t}EtOx). At 298 K these are 37.8 kJ mol^{-1} (^{c}EtOx) and 52.6 kJ mol^{-1} (^{t}EtOx). For the anionic structures, the following heats of formation are obtained: 32.2 kJ mol^{-1} (^{s}AEtOx) and 31.7 kJ mol^{-1} (^{a}AEtOx) at 0 K; as well as 20.1 kJ mol^{-1} (^{s}AEtOx) and 20.0 kJ mol^{-1} (^{a}AEtOx) at 298 K.

Although it has been tested before,[197] it might be warranted to check whether the enthalpy functions $H_{\mathrm{EF}}(T = 298\,\mathrm{K})$ obtained from B3LYP / A′VTZ calculations give the same result as 'higher-level' calculations (CCSD(T) / A′VQZ for MetOx and AMetOx and CCSD(T) / A′VTZ for the neutral and anionic ethanal-oxides). In Table 4.10, $H_{\mathrm{EF}}(T = 298\,\mathrm{K})$ calculated at these different levels of theory is presented. The largest difference in all cases is smaller than 0.1 kJ mol^{-1}. It can therefore be assumed that the W3-F12 protocol specific method for determining $H_{\mathrm{EF}}(T = 298\,\mathrm{K})$ is sufficient (compared to the CCSD(T) method).

Molecule	**MetOx**	**AMetOx**	**^{c}EtOx**	**^{s}AEtOx**	**^{t}EtOx**	**^{a}AEtOx**
$H_{\mathrm{EF,\,B3LYP}}(T = 298\,\mathrm{K})$	7.1	5.7	13.5	12.1	12.8	11.7
$H_{\mathrm{EF,\,CCSD(T)}}(T = 298\,\mathrm{K})$	7.0	5.8	13.5	12.2	12.7	11.8

Table 4.10. | Enthalpy functions calculated with different methods for methanal and ethanal-oxides.

Using the W3-F12 heats of formation for the CH_3CHOO neutral and anion species, it is now possible to calculate the anion electron affinities, the components of which are presented in Table 4.8. For the ^{c}EtOx ← ^{s}AEtOx transition (T1), the electron affinity amounts to 19.1 kJ mol^{-1} at 0 K and 17.7 kJ mol^{-1} at 298 K; for the ^{t}EtOx ← ^{a}AEtOx transition (T2), an electron affinity of 33.6 kJ mol^{-1} at 0 K and 32.6 kJ mol^{-1} at 298 K was found. It is noted that the post-CCSD(T) contributions to the electron affinity add up to as much as 3.3 kJ mol^{-1} and 4.1 kJ mol^{-1} for the ^{c}EtOx ← ^{s}AEtOx and ^{t}EtOx ← ^{a}AEtOx transitions, respectively.

4.4.3 Ethanal-oxide: photoelectron spectra

If the anionic forms of the ethanal-oxide can be synthesised, it should be possible to measure their photoelectron spectra. The main transitions should be the ^{c}EtOx ← ^{s}AEtOx transition (T1) and the ^{t}EtOx ← ^{a}AEtOx transition (T2). These spectra were simulated employing the ezSpectrum 3.0 code using the geometries, vibrational frequencies, and normal mode vectors of a CCSD(T) / A$'$VTZ harmonic calculation. For both simulations, the temperature was set to 10 K, which is appropriate for species entrained in a molecular beam produced via supersonic expansion. Up to 10 quanta were allowed in each excited state vibrational mode (i.e. the modes of the neutral CH_3CHOO species). The predicted photoelectron spectra against the electron binding energy, $E_{e\mathrm{B}}$, are presented in Figure 4.8, where the grey part of the spectrum identifies the combination bands, whereas the red part represents the pure progressions; together they form the fully predicted spectrum. To provide a clearer picture of what an experimental spectrum might look like, the stick spectra are convoluted with a Gaussian response function whose full width at half maximum was set to 0.002 eV and the resulting simulated spectrum is shown in Figure 4.9.

During the T1 transition, the geometry only changes slightly and most of the normal modes can be cast onto the neutral system. The determinant of the normal modes rotation matrix, $|\mathrm{Det}(\boldsymbol{S})|$, is 0.98

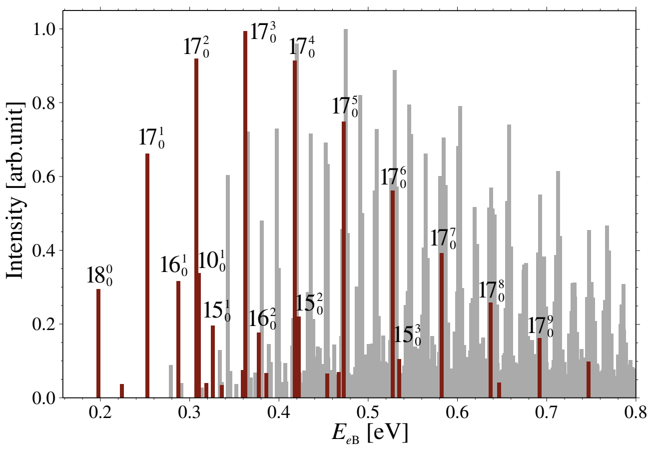

T1: ^{c}EtOx ← ^{s}AEtOx

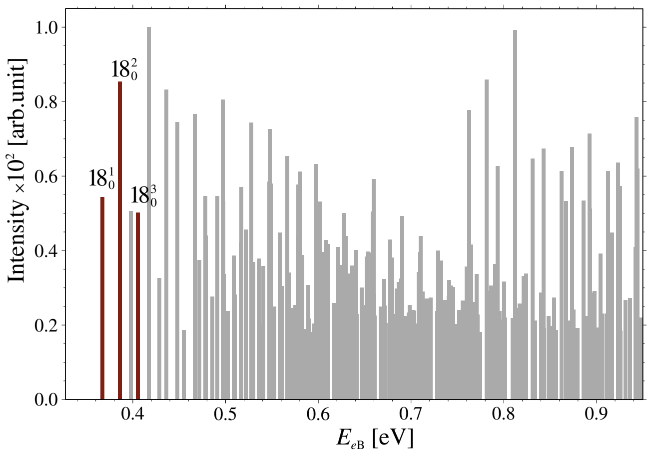

T2: ^{t}EtOx ← ^{a}AEtOx

Figure 4.8 | Predicted anion photoelectron stick spectra of ^{s}AEtOx and ^{a}AEtOx, red areas identify the pure progressions, grey areas the combination bands.

(***S*** is described in the manual of Ref. [204]). For the T2 transition, $|\mathrm{Det}(\boldsymbol{S})|$ is 0.88, yielding much lower transition intensities (on the order of 10^2 times lower).

Most of the pure T1 transitions are due to ω_{17}, the C–C–O–O out-of-plane twisting mode. Other main contributors to the T1 spectrum are the O–O stretch mode ω_{10}, methyl twisting / C_b–H_a rocking mode ω_{15}, C_b–H_a wagging / methyl rocking mode ω_{16} and the methyl twisting mode ω_{18}. The single most important pure progression in the T2 spectrum is the methyl twisting mode ω_{18}; this methyl

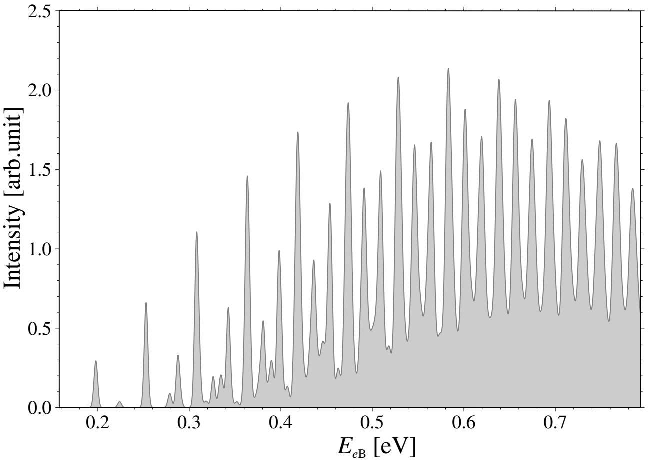

T1: ^{c}EtOx ← ^{s}AEtOx

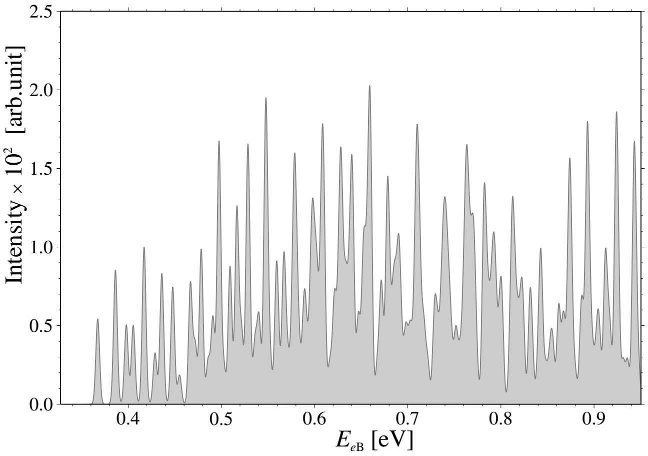

T2: ^{t}EtOx ← ^{a}AEtOx

Figure 4.9 | Simulated photoelectron spectrum of ^{s}AEtOx and ^{a}AEtOx convoluted with Gaussian response function (FWHM of 2 meV).

group is rotated during the transition. In general, these observations are consistent with the shifts in vibrational frequencies and changes in geometry during the transition.

4.5 On the vibrational analysis of carbonyl oxides

The unstable and to some extent multi-reference character of the carbonyl oxides render them ideal for analysing deficiencies within 'high-level' theories; specifically, since Su et al. measured the IR spectrum of MetOx, the prediction of anharmonic vibrational frequencies can be tested. As outlined in Section 2.1.7, there are multiple techniques to obtain such frequencies. While there are approximations used within the anharmonic models, a considerable part of the error associated with those frequencies can arise from the computational method applied. It is therefore reasonable to ask whether the CCSD(T) method (in combination with a certain basis set) can provide an adequate description of the 'shape' of the Born–Oppenheimer potential energy surface (BO-PES) and dipole surface–particularly in the case of MetOx which exhibits a %TAE[(T)] of 4.6 %. Furthermore, it is interesting to see how the VPT2 method compares to the two sets of calculated anharmonic frequencies provided by Su et al. as well as Li and co-workers.[5,169]

In an attempt to understand the influence of different common basis sets on the anharmonic frequencies of MetOx, a variety of basis sets are applied to create CCSD(T) potential energy surfaces for the VPT2 method (presented in Section 4.5.2). It was also possible–as shown in Section 4.5.3–to obtain a CCSD(T) / A'VTZ semi-quartic force field of ^{c}EtOx which was then used to calculate the anharmonic frequencies according to the VPT2 method.

4.5.1 Methanal-oxide geometry

Before addressing the vibrational structure of methanal-oxide, it is worthwhile investigating the effect of different basis sets on the geometry. Partly due to their energy extrapolation behaviour and also due to their popularity, it was decided to focus on the correlation consistent basis sets.

In Table 4.11, the results of CCSD(T) geometry optimisations using different basis sets are presented. From this data it can first be seen that the partial augmented sets of valence only A'V*n*Z and core-correlated A'wCVTZ give the same geometry as their fully augmented versions AV*n*Z and AwCVTZ. It is also apparent that augmentation of the carbon and oxygen is indeed rather important to describe the electronic structure of the species and relatively large negative partial charges (In MetOx, O_b shows a large negative partial charge: see Figure 4.7).[214,215] This is reflected especially in the O_a–O_b

---

[214] T. H. Dunning. *J. Phys. Chem. A*, **104**: 9062 – 9080, 2000.
[215] E. Papajak and D. G. Truhlar. *J. Chem. Theory Comput.*, **7**: 10 – 18, 2011.

Basis Set	N	$r\left(\mathrm{C{-}O_a}\right)$	$r\left(\mathrm{O_a{-}O_b}\right)$	$\measuredangle\left(\mathrm{C{-}O_a{-}O_b}\right)$
VTZ	135	1.279 Å	1.339 Å	117.99°
A'VTZ	195	1.275 Å	1.350 Å	117.81°
AVTZ	215	1.275 Å	1.350 Å	117.76°
wCVTZ	177	1.275 Å	1.337 Å	118.07°
A'wCVTZ	237	1.271 Å	1.348 Å	117.85°
AwCVTZ	257	1.271 Å	1.348 Å	117.83°
VQZ	280	1.272 Å	1.339 Å	118.01°
A'VQZ	385	1.270 Å	1.343 Å	117.94°
AVQZ	425	1.270 Å	1.343 Å	117.92°
wCVQZ	382	1.269 Å	1.336 Å	118.10°
A'wCVQZ	487	1.267 Å	1.341 Å	118.02°
ANO2	280	1.271 Å	1.341 Å	118.00°

Table 4.11. | MetOx geometry optimisations at different basis sets. An optimisation is terminated when the root mean square of the molecular gradient is below 10^{-7}. All calculations were carried out with Cfour's R-CCSD(T) (ECC) optimisation algorithm (N – number of basis functions in CH_2O_2).

bond length which increases by 1.1 pm when adding augmented functions to the triple-ζ type of basis sets and 0.5 pm for the quadruple-ζ type of basis sets. The ANO2 basis (CFOUR notation) has been added to the group of correlation consistent basis sets due to its great performance in other VPT2 related studies of anharmonic frequencies.[58,216,217] Its contraction pattern is the same as VQZ (H: [$4s3p2d1f$], B–Ne: [$5s4p3d2f1g$]), yet the better performance seems to be caused by the greater number of primitive functions (compared to the VQZ).[•] The resulting CCSD(T) / ANO2 optimised MetOx geometry is however very similar to the quadruple-ζ structures.

As expected, the core-correlation causes the bond lengths to decrease, e.g. the $\mathrm{C{-}O_a}$ bond length decreases by 0.4 pm for the triple-ζ cases and by 0.3 pm for the quadruple-ζ cases. The basis set size is of course most relevant for accuracy of the simulation. Hence the best prediction regarding the bond lengths in the methanal-oxide molecule given here are $r\left(\mathrm{C{-}O_a}\right)$ of 1.267 Å and 1.341 Å for

---

[216] J. Vázquez and J. F. Stanton. *Mol. Phys.*, **105**: 101 – 109, 2007.

[217] L. McCaslin and J. Stanton. *Mol. Phys.*, **111**: 1492 – 1496, 2013.

[•] It should be noted that the ANOx ($x = \{0, 1, 2\}$, see Ref. [217] for their definition) do not feature additional augmented functions and are hence not suitable for anionic systems or molecules with more pronounced charge separation.

$r\left(\mathrm{O_a}{-}\mathrm{O_b}\right)$. The geometry corresponds to rotational constants for the ground state of A_0 of 77 602 MHz, B_0 of 12 420 MHz and C_0 of 10 684 MHz,[•] which is in reasonable agreement with the rotational constants observed by Nakajima et al. of A_0 of 77 748.9415(46) MHz, B_0 of 12 465.1742(36) MHz and C_0 of 10 721.3577(46) MHz.[161]

4.5.2 Methanal-oxide anharmonic frequencies

In Section 2.1.7, the advantages and disadvantages of the VPT2 method are outlined which is used for anharmonic analyses throughout this thesis. For such an analysis one first has to carry out a harmonic calculation and subsequently the Hessian force field can be used to find all displacements necessary to obtain the semi-quartic (f_{ijk} and f_{ijkk}, see Equation (2.66a)) force field.[▲] At each of the displaced geometries another harmonic calculation has to be conducted, which again uses analytical gradients, finally the derivatives can be combined to give the sought-after semi-quartic force field.[59] In order to obtain the anharmonic intensities the dipole moment surface is calculated in its cubic expansion.[★]

Treatment of Fermi resonances

All VPT2 frequencies are obtained using the `xguinea` routine provided in the latest CFOUR software suit.[198] Fermi resonance corrections are carried out according to the work of Matthews and co-workers, who developed an improved method for identifying Fermi resonances by taking 'harmonic derivatives' of the perturbation corrections to the fundamental frequencies.[82] As described in their work, the energy correction to a fundamental vibration ν_i, $E_{\nu_i}^{\mathrm{VPT2}}$ depends not only on the force field components f_{abc} or f_{abb} but also on the harmonic frequencies ω_a, ω_b and ω_c of the normal modes a, b and c. Hence, a derivative D_a^i of $E_{\nu_i}^{\mathrm{VPT2}}$ with respect to ω_a can provide insight on whether the fundamental ν_i is influenced by a change of ω_a. In this manner, certain patterns emerge and as Matthews et al. show, for a strong Fermi resonance of the form $\omega_i \approx 2\omega_j$ a part of the derivative matrix $\boldsymbol{D}$ will have the form

$$\begin{pmatrix} D_i^i \\ D_j^i \end{pmatrix} = \begin{pmatrix} -X \\ 2X \end{pmatrix}, \tag{4.4}$$

[•] These rotational constants are obtained from the VPT2-CCSD(T) / A'VQZ force field and are not treated for any resonance effects. The corresponding equilibrium values are A_e: 78 598 MHz, B_e: 12 552 MHz and C_e: 10 824 MHz.

[▲] The MetOx requires 16 displacements from its equilibrium position.

[★] The dipole moment is already a first-order derivative with respect to the energy, therefore a fourth-order force field only yields a third-order correction to the dipole moment.

the weak resonance $\omega_i \approx \omega_j + \omega_k$ emerges as

$$\begin{pmatrix} D^i_i \\ D^i_j \\ D^i_k \end{pmatrix} = \begin{pmatrix} -X \\ X \\ X \end{pmatrix}, \tag{4.5}$$

where X is proportional to the energy correction. Fermi resonances can be accounted for by removing all involved states from the perturbation summations and obtain corrected frequencies as well as intensities from a diagonalised effective Hamiltonian.[79,80,216]

A Fermi resonance interaction is often described through perturbation function W where a matrix element $W_{ni} = \langle \psi_n \,|\, W \,|\, \psi_i \rangle$.[218] For a 2×2 effective Hamiltonian the following equation can be formed:

$$\begin{vmatrix} \nu_n^0 - \nu & W_{ni} \\ W_{in} & \nu_i^0 - \nu \end{vmatrix} = 0\,, \tag{4.6}$$

where ν_n^0 and ν_n^0 are the unperturbed frequencies (note that $W_{ni} = W_{ni}^*$) and the perturbed frequencies ν can be obtained.

In the present calculations involving MetOx, a weak Fermi coupling between at least two states are found and corrected, which is illustrated for the case of the CCSD(T) / A'VTZ calculation, for which the $\boldsymbol{D}$ matrix is given in Table 4.12. From this, X_{389} for the resonance $3_1 \approx 8_1\, 9_1$ is found to be 1.21, X_{367} for $3_1 \approx 6_1\, 7_1$ is 0.15 and X_{499} for $4_1 \approx 9_2$ is 0.3. The latter two values are below the theoretical threshold of 0.5 and therefore, these resonances are not addressed. An overview of all resonances where X_{in} is larger than 0.1, the difference between the harmonic frequencies $\Delta\omega_{in}$ and the perturbation function matrix element W_{in} for each basis set is given in Table 4.13. Apart from the VPT2 calculation involving the ANO2 basis set, the only significant Fermi resonance arises from the coupling between 3_1 and $8_1\, 9_1$. For the ANO2 basis set, the $3_1 \approx 6_1\, 7_1$ yields a much stronger coupling for which the difference between the harmonic frequencies $\Delta\omega = \omega_3 - (\omega_6 + \omega_7)$ is only $-1.4\,\mathrm{cm}^{-1}$.[•]

Continuing with the CCSD(T) / A'VTZ example, a 2×2 effective Hamiltonian is now formed, containing the 'deperturbed' vibrations ($1443\,\mathrm{cm}^{-1}$ for the 3_1 and fundamental and $1459\,\mathrm{cm}^{-1}$ for the $8_1\, 9_1$ overtone, $W_3 89 = -26.3\,\mathrm{cm}^{-1}$). Diagonalisation yields the eigenvalues which are in most cases the

---

[218] G. Herzberg. *Molecular spectra and molecular structure. Vol.2: Infrared and Raman spectra of polyatomic molecules*, 1945.

[•] If ignored, the resulting intensity of fundamental ν_3 ($1367\,\mathrm{cm}^{-1}$) would be unphysically large ($4103.03\,\mathrm{km\,mol}^{-1}$).

D_i^a a i	1	2	3	4	5	6	7	8	9
1	−0.05	0.04	0.04	0.00	0.03	0.01	0.01	0.02	0.03
2	0.02	−0.11	0.19	0.00	0.02	0.00	0.01	0.03	0.02
3	0.00	0.00	−1.37	0.01	0.00	0.15	0.15	1.24	1.21
4	0.00	0.00	0.01	−0.30	0.00	0.01	0.01	0.01	0.63
5	0.00	0.00	0.00	0.01	−0.03	0.01	0.01	0.01	0.04
6	0.00	0.00	0.00	0.00	0.00	0.04	0.01	0.00	0.00
7	0.00	0.00	0.00	0.00	0.00	0.00	0.00	0.00	0.00
8	0.01	0.00	0.00	0.01	0.00	−0.01	0.00	0.00	0.01
9	0.01	0.00	0.00	0.00	0.00	0.00	0.00	0.01	0.01

Table 4.12. | The first harmonic derivative matrix of CCSD(T) / A'VTZ semi-quartic force field. Major resonances arise from contributions $3_1 \approx 8_1\,9_1$, minor ones ($X < 0.5$), from $4_1 \approx 9_2$ and $3_1 \approx 6_1\,7_1$. All quantities are dimensionless.

originating modes. For example the resulting corrected mode $3_1'$ (1424 cm^{-1}) can be interpreted as a superposition of 91 % original 3_1 mode and 9 % $8_1\,9_1$ overtone vibration.[▲]

Basis set		VTZ	A'VTZ	AVTZ	wCVTZ	A'wCVTZ	A'VTZ	ANO2
$\Delta\omega_{389}$	[cm^{-1}]	−30.3	17.8	−15.6	15.8	−28.6	−28.6	−17.1
X_{389}		1.2	3.0	3.0	3.7	0.8	0.9	2.6
W_{389}	[cm^{-1}]	−26.3	−30.8	−26.8	−30.5	−25.7	−26.4	−27.6
$\Delta\omega_{367}$	[cm^{-1}]	17.2	−21.1	17.5	−18.8	19.4	9.9	−1.4
X_{367}		0.1	0.1	0.1	0.1	0.1	0.4	21.8
W_{367}	[cm^{-1}]	N/A	N/A	N/A	N/A	N/A	N/A	−6.5
$\Delta\omega_{49}$	[cm^{-1}]	11.5	29.2	35.7	30.5	34.3	29.8	31.5
X_{49}		0.3	0.4	0.3	0.4	0.3	0.4	0.4
W_{49}	[cm^{-1}]	N/A	N/A	N/A	N/A	N/A	N/A	N/A

Table 4.13. | Overview of potential Fermi resonances from VPT2–CCSD(T) calculations with the respective basis set denoted in the header. Here $\Delta\omega_{in}$ refers to the difference in harmonic frequencies of a mode i and a combination band $j + k$ or an overtone $2j$, while X_{in} denotes the harmonic derivative matrix element and W_{in} is the matrix element of the perturbation function W.

[▲] The corrected overtone $8_1\,9_1'$ (1529 cm^{-1}) is hence 9 % original 3_1 mode and 91 % $8_1\,9_1$ overtone.

Comparison to other studies

In Table 4.14 the fundamental vibrations and intensities of MetOx calculated with the CCSD(T) method and the VTZ, A'VTZ, AVTZ, wCVTZ, A'wCVTZ, A'VQZ, as well as the ANO2 basis set are presented. They are compared to the experimental values given by Su et al. as well as the theoretical predictions made by Li et al. and Su and co-workers.[5,169]

The results from Li et al. were obtained by means of vibrational configuration interaction (VCI) using a potential energy surface fit to ca. 50 000 CCSD(T)-F12a / AVTZ single-point energies. Su et al. generated the vibrational levels from two dimensional VCI using *n*-electron valence second-order perturbation theory (NEVPT2) with an AVDZ basis set to generate their BO-PES. The dipole moment surface was obtained from CASSCF (8, 8) / AVDZ calculations.

As a set, the VCI-5 frequencies compare best to experiment at an RMSD against the experimental frequencies RMSD$_{\mathrm{Exp}}$ of 16.3 cm^{-1} with the largest difference being ν_5 which, as explained in their study, is most likely an incorrect assignment on the experimental side (this was stated in their publication and thus, the ν_5 difference has been dropped form the RMSD$_{\mathrm{Exp}}$ calculation resulting in a new RMSD$_{\mathrm{Exp}}$ of 11.0 cm^{-1} for the VCI-5 set of frequencies). The 2D-VCI method used by Su and co-workers also performs quite well with an RMSD$_{\mathrm{Exp}}$ of 16.3 cm^{-1}, yet the discrepancy with the VCI-5 frequencies is quite striking (RMSD$_{\mathrm{VCI}}$ of 17.5 cm^{-1}) where frequencies of both methods often lie on opposite sides of the experiment.[•]

The results obtained in the present study are quite diverse. Out of the set of five different basis sets, the VPT2 all-electron calculation at CCSD(T) / A'wCVTZ performed best with an RMSD$_{\mathrm{Exp}}$ of 4.3 cm^{-1} followed by the VPT2 frozen-core results at CCSD(T) / A'VTZ (RMSD$_{\mathrm{Exp}}$ of 8.4 cm^{-1}). Unexpectedly, this is a significant improvement over the VCI-5 results. Arguably however, there are more points of comparison needed to draw definite conclusions on which method performs better, yet it is noted that – unlike for 2D-VCI – the difference for each vibration between experiment and method point in the same direction when comparing VCI-5 with VPT2–CCSD(T) / A'wCVTZ and VPT2–CCSD(T) / A'VTZ (RMSD$_{\mathrm{VCI}}$ of 5.7 cm^{-1} and 9.5 cm^{-1}, respectively).

Augmentation of the basis functions seems to be essential, as the comparison between VTZ, A'VTZ and AVTZ suggests. A significant difference occurs for the O–O stretching mode ν_6. While the augmented triple-ζ basis sets describe the mode rather well with a maximum error of 4 cm^{-1}, the non-augmented

---

[•] Note that for the RMSD$_{\mathrm{VCI}}$ calculation, all fundamentals of the VCI-5–CCSD(T)-F12 / AVTZ calculation are used as a basis for comparison.

Method		CCSD(T)							CCSD(T)-F12	NEVPT2		
Anharmonics		VPT2							VCI-5	VCI-2		
Basis Set		VTZ	A'VTZ	AVTZ	wCVTZ	A'wCVTZ	A'VQZ	ANO2	AVTZ[169]	AVDZ[5]	Exp.[5]	
Trans.	S	**Fundamental frequencies** [cm^{-1}]										**normal-mode description**
1_1	a'	3157	3145	3145	3164	3152	3150	3156	3151	3149	–	Asymmetric CH stretch
2_1	a'	3022	3010	3010	3028	3017	3014	3020	3013	3030	–	Symmetric CH stretch
3_1	a'	1467	1424	1422	1414	1431	1437	1424	1434	1458	1435	CH$_2$ scissor / CO stretch
4_1	a'	1264	1275	1274	1272	1282	1287	1283	1285	1302	1286	CO stretch / CH$_2$ scissor
5_1	a'	1211	1207	1205	1215	1211	1213	1213	1212	1220	1241	CH$_2$ rocking
6_1	a'	950	912	911	951	912	921	931	927	892	908	OO stretch
7_1	a'	526	522	522	528	524	527	526	526	530	–	COO deformation
8_1	a''	820	846	847	828	853	863	848	859	853	848	CH$_2$ wagging
9_1	a''	614	615	615	618	618	626	622	622	606	–	CH$_2$ twisting
RMSD$_{\text{Exp}}$		31.84	8.35	9.05	26.92	4.32	10.03	12.73	11.00	16.32	–	
RMSD$_{\text{VCI}}$		20.44	9.20	9.49	16.79	5.74	2.97	5.94	–	17.50	–	
Trans.	S	**Transition intensities** [arb. unit]										**normal-mode description**
1_1	a'	0.2	0.2	0.2	0.2	0.2	0.2	0.3	4	5	–	Asymmetric CH stretch
2_1	a'	3	3	3	3	3	3	3	3	1	–	Symmetric CH stretch
3_1	a'	21	7	22	23	23	20	24	29	52	33	CH$_2$ scissor / CO stretch
4_1	a'	43	47	43	50	41	33	39	54	100	42	CO stretch / CH$_2$ scissor
5_1	a'	14	15	15	14	14	15	14	9	33	39	CH$_2$ rocking
6_1	a'	100	100	100	100	100	100	100	100	100	100	OO stretch
7_1	a'	0.1	0.5	0.1	0.5	0.1	0.1	0.2	29	1	–	COO deformation
8_1	a''	25	37	25	36	25	25	28	29	31	24	CH$_2$ wagging
9_1	a''	5	6	5	6	5	4	5	4	2	–	CH$_2$ twisting
RMSD$_{\text{Exp}}$		19.08	13.80	13.31	15.21	13.54	14.59	13.25	17.09	30.86	–	

Table 4.14. | CH$_2$OO calculated anharmonic and experimental IR frequencies and intensities. All ν_3 frequencies and intensities calculated with the CCSD(T) method are Fermi resonance corrected as described in the text. RMSD$_{\text{Exp}}$ and RMSD$_{\text{VCI}}$ refer to root mean square deviation from the experiment (Su et al.) and the VCI-5 (Li et al.) frequencies, respectively. Note that the experimental frequency of 1241 cm^{-1} is most likely incorrectly assigned as noted by Li and Su and thus dropped from the RMSD calculation.[169] The intensities have been scaled such that their largest intensity is equivalent to 100 arb. unit. This intensity is subsequently removed from the intensity-RMSD calculation. The scaling factors for to obtain the original unscaled VPT2 intensities are {0.93, 1.20, 1.20, 0.94, 1.19, 1.21, 1.12} km/mol for the VTZ, A'VTZ, AVTZ, wCVTZ, A'wCVTZ, A'VQZ, and ANO2 basis set, respectively.

VTZ basis set is off by 42 cm^{-1}. This mode also is responsible for the largest error Li et al. found in their calculation (19 cm^{-1}). The authors suggest it is due to the fact that MetOx is isoelectric to O_3 and that for O_3 the asymmetric stretching frequency is difficult to calculate due to its strong multi-reference character. However, as pointed out before, MetOx does only present a mild-to-moderate case of non-dynamical correlation unlike O_3 which exhibits a much stronger multi-reference character.

It is noted here that there seems to be a strong dependence on the choice of basis set. When comparing the VCI-5 results from Li et al. to the VPT2–CCSD(T) results at quadruple-ζ, it is found that they all yield a similar $\mathrm{RMSD_{Exp}}$ (See Table 4.14). Due to the better convergence properties of the explicitly correlated methods, it is often assumed that a conventional quadruple-ζ energy is similarly 'close' to the complete basis set limit than an energy obtained by an explicitly correlated method with a triple-ζ basis set. If this assumption holds for potential energy surfaces as well, the similar $\mathrm{RMSD_{Exp}}$ and the strikingly close $\mathrm{RMSD_{VCI}}$ of the A'VQZ result might not be a coincidence.

Whether the hydrogen atoms are augmented or not does not seem to plays a vital role; both augmentation schemes A'VTZ and AVTZ perform similarly well. The non-augmented core-correlated calculation (wCVTZ basis set) provides a significant improvement over the frozen-core calculation (VTZ basis set). Nevertheless, it exhibits larger errors than calculations with an augmented basis set. As soon as both, augmentation and core-correlation are accounted for, the results are significantly improved. The largest difference in frequencies between the frozen-core (with A'VTZ basis) and the core-correlated approach (with A'wCVTZ basis) involves the polar C−O bond. This manifests itself in the ν_4 C−O stretching mode. While the frozen-core method (A'VTZ) yields a stretching frequency of 1275 cm^{-1} the core-correlated approach results in 1282 cm^{-1}, when the experimentalists report 1286 cm^{-1} for this mode.

As mentioned before, a VPT2 calculation at CCSD(T) / A'wCVTZ provides most suitable frequencies, yet a computationally much less demanding VPT2–CCSD(T) / A'VTZ still provides reasonable results. This is emphasised even more so by the large difference in computationally expense when comparing the VPT2–CCSD(T) / A'VTZ and A'wCVTZ with the VCI-5 method employed by Li et al. where the former methods use the equivalent of 408 CCSD(T) / A'VTZ single-energy points[•] rather than 50 000 single-point energies used for VCI-5. It can however be argued that it is not necessary to acquire all of these points in order to generate large enough surface for the VCI-5 simulation. Additionally, given that augmented triple-ζ results are (due to fortuitous error cancellation) 'better' compared to experiment

---

[•] It requires the calculation of an initial harmonic force field; at 16 follow-up displaced geometries additional harmonic force fields are generated. Each harmonic force field (it would need an equivalent of 24 single-point energies) is obtained through the second energy derivative with respect to a displacement.

than the augmented triple-ζ results, a surface obtained by means of CCSD(T)-F12 with a double-ζ basis set might pose an improvement as well.

The ANO2 basis set was chosen because of its excellent performance in prior studies;[58,82,216,217] it usually produces similar or better results than a VQZ basis set. For the present case, an $\mathrm{RMSD_{Exp}}$ of 12.7 $\mathrm{cm^{-1}}$ puts it slightly behind the performance of an A'VQZ, which might be due to the lack of additional augmented functions.

Turning now to the calculated intensities, which are presented at the lower part of Table 4.14. Experimental intensities are notoriously hard to measure and are often shifted due to instrument related causes; the relative shifts should however be a good comparison piece.[58] All intensities of a certain set have therefore been scaled in such a way that their most intense band reads 100 arb. unit, this maximum band is also removed from the RMSD calculation.

Of all involved simulations, the VPT2 – CCSD(T) / A'VTZ, A'wCVTZ, AVTZ and ANO2 calculations perform best with respect to experiment with an $\mathrm{RMSD_{Exp}}$ of 13.8 arb. unit, 13.5 arb. unit, 13.3 arb. unit and 13.3 arb. unit respectively. The only significant differences to experiment, aside from the supposedly incorrectly assigned peak ν_5 (which in this case has not been removed from the $\mathrm{RMSD_{Exp}}$ calculation), is the $\mathrm{CH_2}$ scissor mode ν_3. Augmentation of the heavy atoms is necessary as can be seen for the VPT2 – CCSD(T) / wCVTZ and VTZ calculations with the latter one performing worse than all other VPT2 calculations. All VPT2 calculations apart from the CCSD(T) / VTZ simulation performed better than the VCI-5 calculation published by Li and co-workers which exhibits an $\mathrm{RMSD_{Exp}}$ of 17.1 arb. unit.

Usually, it is expected that intensities, which are calculated from the square of dipole moment derivatives, have up to four times larger deviations from experiment than the frequencies.[58] In the present case the observed intensities are described rather well by the applied methods. For further clarification however, more detailed experimental data is necessary, which should entail combination and overtone bands as well as isotopic shifts. At the time of writing a collaborating group led by Allan McKinley is working on a matrix-IR spectra for methanal-oxide and its isotopes, and a second collaborator in Henrik Kjærgaard's group – Kasper Mackeprang – provided local mode model (LMM) calculations at CCSD(T) / A'VTZ level of theory.

In order to identify the transitions within the complex IR spectrum of MetOx unambiguously, the experimental fundamental, overtone and combination bands of $\mathrm{CH_2O_2}$ and its isotopes $\mathrm{CH_2{}^{18}O_2}$, $\mathrm{^{13}CH_2{}^{18}O_2}$ and $\mathrm{CD_2O_2}$ need to be compared to simulations. For this reason, the frequencies and

	Isotope		**CH_2O_2**		**$CH_2{}^{18}O_2$**		**$^{13}CH_2O_2$**		**CD_2O_2**	
	Trans.	S	ν	I	ν	I	ν	I	ν	I
Fundamentals										
	1_1	a'	3145	0.2	3145	0.2	3132	0.3	2393	0.7
	2_1	a'	3010	4	3009	4	3003	3	2189	7
	3_1	a'	1424	25	1419	25	1410	16	1309	53
	4_1	a'	1275	52	1244	48	1259	57	1052	69
	5_1	a'	1207	17	1194	13	1197	21	1011	9
	6_1	a'	912	120	868	112	910	117	853	74
	7_1	a'	522	0.1	505	0.1	518	0.1	464	0.7
	8_1	a''	846	30	844	31	838	31	683	11
	9_1	a''	615	6	610	6	616	6	473	3
Overtones										
	1_2	a'	6224	1	6224	1	6197	1	4748	1
	2_2	a'	5961	0.5	5960	0.5	5948	0.5	4348	0.3
	3_2	a'	2812	0.4	2794	0.5	2808	0.4	2597	2
	4_2	a'	2532	0.8	2493	0.8	2514	0.9	2093	0.2
	5_2	a'	2411	0.1	2386	0.1	2392	0.1	2020	0.3
	6_2	a'	1799	2	1711	2	1795	2	1697	1
	7_2	a'	1043	< 0.05	1010	< 0.05	1036	0.0	928	0.1
	8_2	a''	1684	9	1679	10	1669	9	1362	2
	9_2	a''	1214	49	1202	38	1214	38	941	1
Combinations										
	$2_1 1_1$	a'	6048	0.5	6048	0.5	6029	0.5	4526	0.2
	$3_1 1_1$	a'	4542	2	4531	2	4522	2	3714	0.3
	$3_1 2_1$	a'	4428	0.1	4416	0.2	4412	0.2	3487	0.1
	$4_1 1_1$	a'	4416	0.1	4398	0.1	4396	< 0.05	3445	0.3
	$5_1 1_1$	a'	4341	2	4328	2	4318	2	3395	0.8
	$4_1 2_1$	a'	4279	0.2	4261	0.2	4266	0.2	3236	0.1
	$5_1 2_1$	a'	4205	0.2	4192	0.2	4190	0.2	3188	0.2
	$6_1 1_1$	a'	4051	0.1	4007	0.1	4035	0.1	3241	0.2
	$6_1 2_1$	a'	3917	0.1	3873	0.1	3909	0.1	3038	0.1
	$7_1 1_1$	a'	3664	< 0.05	3648	< 0.05	3647	< 0.05	2854	< 0.05
	$7_1 2_1$	a'	3529	0.1	3512	0.1	3519	0.1	2651	< 0.05
	$4_1 3_1$	a'	2677	0.9	2649	0.7	2666	0.6	2355	1
	$5_1 3_1$	a'	2610	0.7	2587	0.6	2598	0.6	2315	0.5
	$5_1 4_1$	a'	2475	0.5	2443	0.4	2457	0.6	2063	< 0.05
	$6_1 3_1$	a'	2332	0.2	2276	0.2	2326	0.1	2168	< 0.05
	$6_1 4_1$	a'	2194	0.2	2132	0.3	2184	0.2	1888	0.6
	$6_1 5_1$	a'	2112	0.1	2057	0.1	2100	0.1	1864	< 0.05
	$7_1 3_1$	a'	1937	< 0.05	1909	< 0.05	1931	< 0.05	1772	0.1
	$7_1 4_1$	a'	1793	0.1	1757	0.1	1781	0.1	1512	0.8
	$7_1 5_1$	a'	1726	0.3	1697	0.2	1714	0.3	1473	0.5
	$9_1 8_1$	a'	1529	0.7	1472	5	1469	3	1154	4
	$7_1 6_1$	a'	1424	3	1366	0.1	1422	5	1309	48
	$8_1 1_1$	a''	3975	< 0.05	3973	< 0.05	3955	< 0.05	3066	< 0.05
	$8_1 2_1$	a''	3848	< 0.05	3845	< 0.05	3834	< 0.05	2870	< 0.05
	$9_1 1_1$	a''	3755	< 0.05	3749	< 0.05	3741	< 0.05	2863	< 0.05
	$9_1 2_1$	a''	3620	< 0.05	3614	< 0.05	3614	< 0.05	2659	< 0.05
	$8_1 3_1$	a''	2217	< 0.05	2201	< 0.05	2215	< 0.05	1965	0.2
	$8_1 4_1$	a''	2102	0.1	2081	0.1	2085	0.1	1743	0.1
	$8_1 5_1$	a''	2055	< 0.05	2040	< 0.05	2039	< 0.05	1693	< 0.05
	$9_1 3_1$	a''	1999	< 0.05	1979	< 0.05	2002	< 0.05	1777	0.1
	$9_1 4_1$	a''	1903	< 0.05	1906	< 0.05	1912	< 0.05	1522	0.1
	$9_1 5_1$	a''	1817	0.2	1800	0.2	1808	0.2	1486	< 0.05
	$8_1 6_1$	a''	1774	0.1	1728	< 0.05	1764	< 0.05	1542	0.1
	$9_1 6_1$	a''	1528	< 0.05	1478	< 0.05	1526	< 0.05	1327	< 0.05
	$7_1 8_1$	a''	1371	< 0.05	1353	< 0.05	1360	< 0.05	1149	< 0.05
	$7_1 9_1$	a''	1135	< 0.05	1113	< 0.05	1132	< 0.05	937	< 0.05

Table 4.15. | All CH_2OO calculated isotopic VPT2 CCSD(T) / A′VTZ frequencies and intensities containing up to 2 quanta. All frequencies ν are given in cm^{-1}, intensities I are presented in $km\,mol^{-1}$. Mode descriptions are given in Table 4.14.

intensities of these transitions are calculated with the VPT2 method using CCSD(T) / A'VTZ level of theory; the results of which are presented in Table 4.15.

The VPT2 frequencies and intensities are obtained in the same manner as described before. For $CH_2{}^{18}O_2$, two separate Fermi resonances, that are $3_1 \approx 8_1\,9_1$ ($X_{389} = 1.8$) and $4_1 \approx 9_2$ ($X_{49} = 1.5$), emerge. The ^{13}C isotope $^{13}CH_2O_2$, exhibits the same two Fermi resonances ($X_{389} = 0.8$ and $X_{49} = 1.5$ respectively) as well as an additional one for $3_1 \approx 6_1\,7_1$ ($X_{367} = 0.5$). Interestingly, the deuterated isotope CD_2O_2 does not feature any strong Fermi resonances ($X_{in} < 0.5$), which presumably is caused by a lower density of vibrational states due to the doubling in mass of the hydrogen compared to the protium. The Fermi resonance descriptors are given in Table A.8 of the Appendix.

As expected, the $^{18}O{-}^{18}O$ stretching mode ν_6 for $CH_2{}^{18}O_2$ is red-shifted by 44 cm^{-1} for the same reason as to why ν_4 is red-shifted in $^{13}CH_2O_2$ – an increased mass when the bond strength remains approximately the same. In all three species (CH_2O_2, $CH_2{}^{18}O_2$ and $^{13}CH_2O_2$) strong intensity borrowing between either 4_1 and 9_2 or 5_1 and 9_2 are observed, leading to a much more intense 9_2 overtone than the equivalent 9_1 fundamental transition. In CD_2O_2 the 9_2 overtone loses its intensity at the expense of the $9_1\,6_1$ combination band. It is also noted that due to the heavier deuterium, all modes associated with CD stretching (ν_1, ν_2 and ν_3) are strongly red-shifted with respect to protium bearing CH_2O_2.

As explained in Section 2.1.7, the C–H stretching modes are challenging for VPT2 to simulate due to higher-order Darling–Dennison coupling. Therefore, a comparison with LMM calculations at the same level of theory might yield additional insight. In Table 4.16 such a comparison of the isotopic frequencies and intensities of the asymmetric CH stretching mode ν_1, the symmetric CH stretching mode ν_2 and the CH_2 scissoring / CO stretching mode ν_3 as well as all the arising overtone and combination transitions (two quanta excitation) between the VPT2 and the LMM at CCSD(T) / A'VTZ level of theory are presented.

For the LMM approach Mackeprang and Kjærgaard mapped out the pairs of the two CH stretching and HCH bending motions as well as the coupling between the CO stretch and the HCH bend.[219] The one-dimensional part of the BO-PES is constructed from four spline fits through the two CH stretches, the HCH bend and the CO stretch, where the single point energy coordinates are obtained by displacing the equilibrium structure by −0.40 Å to 0.70 Å in steps of 0.05 Å for the stretching motion and −50° to 80° in steps of 5° for the bending motion. Quadratic, cubic and some quartic coupling terms are included in the potential term (see Equation (2.72)). These are calculated by displacing two (displacements: ±0.20 Å in steps of 0.05 Å for stretches, ±20° in steps of 5° for bending) or

---

[219] K. Mackeprang and H. G. Kjærgaard personal communication Feb. 17, 2015

	CH_2O_2		$CH_2{}^{18}O_2$		$^{13}CH_2O_2$		CD_2O_2	
	ν_{VPT2}	ν_{LMM}	ν_{VPT2}	ν_{LMM}	ν_{VPT2}	ν_{LMM}	ν_{VPT2}	ν_{LMM}
Fundamentals								
1_1	3145	3171	3145	3171	3132	3157	2393	2396
2_1	3010	3024	3009	3024	3003	3020	2189	2184
3_1	1424	1440	1419	1440	1410	1428	1309	1267
Overtones								
1_2	6224	6289	6224	6289	6197	6262	4748	4758
2_2	5961	5982	5960	5982	5948	5972	4348	4352
3_2	2812	2868	2794	2866	2808	2844	2597	2220
Combinations								
$2_1 1_1$	6048	6093	6048	6093	6029	6075	4526	4535
$3_1 1_1$	4542	4586	4531	4585	4522	4559	3714	3335
$3_1 2_1$	4428	4451	4416	4450	4412	4433	3487	3125
	I_{VPT2}	I_{LMM}	I_{VPT2}	I_{LMM}	I_{VPT2}	I_{LMM}	I_{VPT2}	I_{LMM}
Fundamentals								
1_1	0.2	4	0.2	4	0.3	4	0.7	2
2_1	4	2	4	2	3	2	7	1
3_1	25	29	25	28	16	24	53	68
Overtones								
1_2	1	0.5	1	0.5	1	0.5	1	0.2
2_2	0.5	0.4	0.5	0.4	0.5	0.4	0.3	0.1
3_2	0.4	0.2	0.5	0.2	0.4	0.2	2	0.6
Combinations								
$2_1 1_1$	0.5	0.7	0.5	0.7	0.5	0.7	0.2	0.3
$3_1 1_1$	2	2	2	2	2	2	0.3	0.5
$3_1 2_1$	0.1	0.1	0.2	0.1	0.2	0.1	0.1	< 0.05

Table 4.16. | CH_2OO calculated isotopic VPT2 and LMM IR frequencies and intensities. All VPT2 an LMM calculations were carried out at the CCSD(T) / A'VTZ level of theory. The LMM results were obtained by Kasper Mackeprang. All frequencies ν are given in cm^{-1}, intensities I are presented in km mol^{-1}. Mode descriptions are given in Table 4.4.

three (displacements: ±0.10 Å in steps of 0.05 Å for stretches, ±10° in steps of 5° for bending) modes simultaneously, yielding coupling term coefficients as described by Mackeprang and co-workers.[220] The pseudo-potential V', as described in Equation (2.72) is not included in the model, since its effect

---

[220] K. Mackeprang et al. *J. Chem. Phys.*, **140**: 184309, 2014.

is in most cases negligible.[221] Solving the one-dimensional Schrödinger equation for each of the four modes by using a variational method,[74] provides the eigenfunctions (using $\boldsymbol{g}$-matrix elements at the equilibrium geometry), the products of which yield basis functions which are subsequently used to set up the Hamiltonian matrix (including up to five quanta of excitation). The resulting Hamiltonian matrix is then diagonalised to obtain the vibrational states and energy levels. All these calculations were performed using an in-house developed code by Mackeprang and co-workers.[219]

A general observation between the two models is that for all isotopes the intensities of each transition agree remarkably well (notice here, that these are unscaled absolute intensities), where the largest difference is the ν_3 mode of the deuterated methanal-oxide. Almost all frequencies disagree by a significant amount; yet they seem to differ by a constant factor, whereby a LMM frequency would always be larger than the equivalent VPT2 frequency. The only major outlier for this theory is the deuterated isotopologues, where differences of up to 362 cm^{-1} are observed. This might be due to a the strong coupling between the CH$_2$ scissor vibration and the C–O stretching motion in ν_3. In order to fully account for this, the LMM potential could not be sufficient in its extend and therefore might benefit from a larger displacement of the two local modes that describe ν_3. Without experimental spectroscopic evidence, the differences between the two models are difficult to judge. This issue should however be resolved in the new future, when the matrix IR data becomes available.

Isotope	Basis set	$E_{\text{ZPVE, Harm}}$	$E_{\text{ZPVE, VPT2}}$	$E_{\text{ZPVE, Total}}$
CH_2O_2	VTZ	80.52	−1.07	79.46
	A'VTZ	80.29	−1.05	79.24
	AVTZ	80.24	−1.03	79.21
	wCVTZ	80.77	−1.06	79.71
	A'wCVTZ	80.58	−1.06	79.52
	A'VQZ	80.70	−1.11	79.58
	ANO2	80.73	−1.07	79.66
$CH_2{}^{18}O_2$	A'VTZ	79.56	−1.04	78.53
$^{13}CH_2O_2$	A'VTZ	79.85	−1.04	78.81
CD_2O_2	A'VTZ	64.10	−0.65	63.45

Table 4.17. | VPT2–CCSD(T) zero-point vibrational energy contributions for MetOx at different basis sets and for different isotopologues. All energies are given in kJ mol^{-1}.

---

[221] T. Salmi et al. *J. Phys. Chem. C*, **112**: 6305 – 6312, 2008.

Equipped with the semi-quartic force fields, it is now possible to obtain corrected ZPVEs according to the formulas provided in Reference [174]. The resulting ZPVE for each basis set and isotopologue is provided in Table 4.17. Since the fundamental frequencies obtained with the A'wCVTZ basis set compare rather well to the experiment, it is possible to use the corresponding ZPVE of 79.5 kJ mol^{-1} to update the TAE$_0$ of MetOx from 1527.3 kJ mol^{-1} to 1528.5 kJ mol^{-1} (see Section 4.3.3). Thus, the heat of formation at 298 K $\Delta_\mathrm{f} H_{298}$ of 102.8 kJ mol^{-1} is updated to a more accurate 101.6 kJ mol^{-1}. It is expected that if an anharmonic analysis of AMetOx were to be carried out, the ZPVE would change by a similar amount, leading to a greater TAE$_0$ and smaller $\Delta_\mathrm{f} H_{298}$ than reported in Section 4.3.3. The electron affinities and barrier heights should however retain their values since the errors cancel out.

4.5.3 Ethanal-oxide anharmonic frequencies

Nakajima and co-workers recently provided evidence that the synthesis described in reaction (R 4.6) yields *cis*-ethanal-oxide ($^\mathrm{c}$EtOx).[162] In the near future, it should therefore be possible to measure the IR spectrum of $^\mathrm{c}$EtOx. In order to provide an improved prediction over the already published harmonic vibrations (see Section 4.4.1),[213] an anharmonic VPT2 vibrational analysis at CCSD(T) / A'VTZ level of theory is carried out. As shown in the previous section, when compared to the sparse experimental data currently available, this combination of methods seem to describe the vibrational structure of the methanal-oxide as well (if not better) as the best available VCI simulation. While there is certainly room for improvement when considering higher-order coupling-prone CH stretching modes, it should serve as a solid foundation to compare to and label upcoming experimental data.

Resonance	X_{in}	$\Delta\omega_{in}$	W_{in}
$9_1 \approx 11_1 + 12_1$	0.5	1.1	0.8
$5_1 \approx 15_1 + 17_1$	2.2	−7.1	−10.7
$3_1 \approx 4_2$	2.4	−2.7	4.1

Table 4.18. | Fermi resonance descriptors of $^\mathrm{c}$EtOx VPT2 calculations at CCSD(T) / A'VTZ. Here $\Delta\omega_{in}$ (in cm^{-1}) refers to the difference in harmonic frequencies of a mode i and a combination band $j+k$ or an overtone $2j$, while X_{in} (unitless) denotes the harmonic derivative matrix element and W_{in} (in cm^{-1}) is the matrix element of the perturbation function W. Mode descriptions are given in Table 4.19.

Compared to the previous MetOx VPT2 calculations, the semi-quartic force field generation of EtOx –obtained by 30 displacements from the equilibrium position–is ca. three times more demanding.

Trans.	S	ν_{VPT2} [cm^{-1}]	I_{VPT2} [km mol^{-1}]	ω_{Harm} [cm^{-1}]	ω'_{Harm} [cm^{-1}]	**Mode description**
1_1	a'	3069	3.4	3201	3085	C_b–H_a stretch
2_1	a'	3009	8.2	3155	3040	C_a–H asymmetric stretch (methyl group)
3_1	a'	2903	1.7	3026	2915	C_a–H symmetric stretches (methyl group)
4_1	a'	1468	34.3	1514	1459	asymmetric O–C / C–O stretch
5_1	a'	1418	3.8	1470	1416	CH_2 scissor / H_b–C_aC_b bend
6_1	a'	1356	7.3	1397	1346	methyl inversion / C–O stretch
7_1	a'	1271	26.3	1306	1258	in-plane C_b–H_a rocking / C–O stretch
8_1	a'	1085	14.8	1113	1073	methyl wagging / C–C stretch
9_1	a'	954	7.9	974	938	C–C stretch
10_1	a'	886	90.0	905	872	O–O stretch
11_1	a'	662	2.6	669	644	methyl wagging / O–O–C bend
12_1	a'	298	8.3	304	293	C–C–O–O scissor bend / deformation
13_1	a''	2928	1.8	3079	2967	C_a–H asymmetric stretch (methyl group)
14_1	a''	1407	10.2	1454	1401	CH_2 twist / C_a–H_b rocking
15_1	a''	1001	0.0	1034	996	methyl twisting / C_b–H_a rocking
16_1	a''	712	17.6	724	697	C_b–H_a wagging / methyl rocking
17_1	a''	434	0.2	443	427	C–C–O–O out-of-plane twisting
18_1	a''	189	2.0	209	201	methyl twisting (internal rotation)

Table 4.19. | Computed anharmonic vibrational frequencies and intensities for trans-ethanal-oxide at CCSD(T) / A'VTZ level of theory. The equivalent harmonic frequencies ω_{Harm} and scaled harmonic frequencies ω'_{Harm} (taken from Table A.4) are also presented for direct comparison. Transitions are ordered according to the Symmetry S of the modes.

At each of these points a harmonic frequency calculation is carried out in order to obtain the quadratic force field at that position. The CFOUR -internal algorithm `xcubic` is used to generate the final semi-quartic force field and dipole moment derivatives which are needed for the subsequent VPT2 calculation. All VPT2 related operations including Fermi resonance corrections are obtained using the `xguinea` routine.[198]

In order to find such Fermi resonance, the method developed by Matthews and co-workers (as described in the previous section) is employed.[82] The VPT2 first harmonic derivative $\boldsymbol{D}$-matrix is shown in Table A.9 of the Appendix. Analysing this matrix, one finds three possible couplings between $9_1 \approx 12_1\, 11_1$: $X = 0.5$, $5_1 \approx 15_1\, 17_1$: $X = 2.2$ and $3_1 \approx 4_2$ $X = 2.4$ (Fermi resonance descriptors are given in Table 4.18), where the mode descriptions can be found in Table 4.19. Table 4.19 also provides an overview of all the obtained VPT2 frequencies and intensities as well as a comparison to the pre-

Combination bands				**Overtones**			
Trans.	S	ν_{VPT2}	I_{VPT2}	**Trans.**	S	ν_{VPT2}	I_{VPT2}
$7_1\,1_1$	a'	4325	0.5	1_2	a'	6026	1.2
$8_1\,2_1$	a'	4090	0.8	4_2	a'	2912	3.3
$8_1\,6_1$	a'	2439	0.5	5_2	a'	2806	0.8
$16_1\,15_1$	a'	1712	5.8	10_2	a'	1752	3.3
$18_1\,14_1$	a'	1608	1.2	11_2	a'	1324	0.5
$17_1\,15_1$	a'	1450	19.5	16_2	a''	1436	6.4
$12_1\,9_1$	a'	1250	2.0	17_2	a''	865	14.7
$18_1\,15_1$	a'	1184	1.6				
$12_1\,11_1$	a'	958	4.7				
$18_1\,16_1$	a'	897	2.9				
$18_1\,17_1$	a'	610	1.3				
$17_1\,9_1$	a''	1387	0.8				

Table 4.20. | Abridged set of anharmonic overtone and combination band transitions for trans-ethanal-oxide at CCSD(T) / A'VTZ level of theory. Only transitions with an intensity of more than 0.5 km mol^{-1} are listed. Transitions are ordered according to the Symmetry S of the modes.

viously obtained harmonic frequencies ω_{Harm} and scaled harmonic frequencies ω'_{Harm} (taken from Table A.4). The overtones and combination bands with an intensity $I \geq 0.5\,\text{km}\,\text{mol}^{-1}$ are presented in Table 4.20.

The most intense transition, as seen previously for the MetOx molecule, can be associated with the O–O stretching mode ν_{10} at 886 cm^{-1}, followed by the asymmetric O–C / C–O stretch ν_4 at 1468 cm^{-1} and the in-plane C_b–H_a rocking / C–O stretch ν_7 at 1271 percm. The geometry referred to here is given in Figure 4.6 of Section 4.4.1. Another interesting feature is that the 17_2 overtone is much more intense than its corresponding fundamental transition, possibly borrowing intensity from the energetically adjacent 16_1 transition. Similarly, the $17_1\,15_1$ transition receives an intensity boost due to the energetic vicinity to the strong 4_1 transition.

When comparing equivalent modes in MetOx and ^{c}EtOx, minor shifts are observed. For example, both the C–O stretching mode (MetOx: ν_3, 1424 cm^{-1}; ^{c}EtOx: ν_3, 1468 cm^{-1}) and the C–O–O bend (MetOx: ν_7, 522 cm^{-1}; ^{c}EtOx: ν_{11}, 662 cm^{-1}) are blue shifted in ^{c}EtOx. The O–O stretch on the other hand (MetOx: ν_6, 912 cm^{-1}; ^{c}EtOx: ν_{10}, 886 cm^{-1}) is red-shifted by 26 cm^{-1}, reflecting the lengthening of the O–O bond.

It is noted that the RMSD between the VPT2 results and the scaled harmonic frequencies does perform reasonably well with 16.2 cm^{-1}. A lower RMSD of 15.17 cm^{-1} can be achieved when using a scaling factor of 0.9602 instead of 0.9635; the latter is taken from the work of Kesharwani and coworkers.[192] The main problem of scaling frequencies remains however, as demonstrated on the case of the strongly anharmonic methyl inversion / C–O stretching mode ν_6, where a difference between the scaled harmonic and VPT2 transition of 39 cm^{-1} emerges.

Although currently, no experimental IR data is available for ^{c}EtOx, the here predicted IR spectrum should provide a good estimate of the molecular vibrations. As described in Section 4.4.2, the ^{c}EtOx exhibits mild-to-moderate non-dynamical correlation effects (^{c}EtOx: %TAE[(T)] = 3.1 %, MetOx: %TAE[(T)] = 4.6 %), Therefore the chosen CCSD(T) method should perform even better for most of the vibrations. It is expected that CH_2 related stretches might not be described with great accuracy, due to possible higher order couplings.

Compared to the harmonic CCSD(T) / A'VQZ simulations for ^{c}EtOx which yielded a scaled ZPVE of 154.4 kJ mol^{-1} the VPT2-CCSD(T) / A'VTZ anharmonic analysis results in a ZPVE of 153.3 kJ mol^{-1}. The TAE_0 of 2729.3 kJ mol^{-1} reported in Section 4.4.2 is therefore updated to 2731.4 kJ mol^{-1}. Subsequently the $\Delta_f H_{298}$ is changed from 37.8 kJ mol^{-1} to a more accurate 35.7 kJ mol^{-1}. Again, although the other heats of formation will most likely also be lower than reported in Section 4.4.2, the electron affinities and energy differences between the ^{c}EtOx, ^{t}EtOx, ^{s}AEtOx and ^{a}AEtOx structures should be retained.

Chapter 5

Concluding remarks and outlook

The work described in this PhD thesis, consisted of two closely related topics–the development of high-resolution spectroscopic tools based on the velocity map imaging (VMI) principle as well as the accurate theoretical prediction of electron affinities and vibronic transitions. As a methodology for the theoretical predictions, the W3-F12 protocol served as a backbone and was tested successfully on methanal-oxide (MetOx), *cis*-ethanal-oxide (^{c}EtOx) and *trans*-ethanal-oxide (^{t}EtOx) as well as their respective anions.

For all of these species, harmonic frequencies, W3-F12 total atomisation energies and heats of formation at 0 K and 298 K have been determined. The electron affinities at 298 K were calculated to be 0.567 eV, 0.183 eV and 0.338 eV for MetOx, ^{c}EtOx and ^{t}EtOx, respectively. For each of the vibronic transitions between the anionic and neutral forms of MetOx, ^{c}EtOx and ^{t}EtOx, Franck–Condon simulations have been presented allowing for comparison with potential anion photoelectron spectra. Acquiring such a spectrum should, at least for the anionic MetOx species, be possible, as it shows a 16.5 kJ mol^{-1} barrier with respect to dissociation into methanal and O^{-}.

Due to apparent discrepancies between the predicted anharmonic frequencies and the gas-phase IR-spectrum of MetOx, vibrational second-order perturbation theory (VPT2) analyses with five different basis sets have been conducted. The VPT2 method at CCSD(T) / A'wCVTZ level of theory performed best out of the test set, showing a similar, if not better agreement with the sparse experimental data available than a much more computationally demanding calculation presented by Li and co-workers.[169] Until more detailed experimental IR data are available for which isotopic anharmonic frequencies were presented, a comparison of the C–H stretching modes between VPT2 and local mode model (LMM) predictions of the same level of theory remains inconclusive. With the new found insights on the prediction performance of VPT2 method in mind, an anharmonic IR simulation of ^{c}EtOx, a molecule for which an experimental microwave spectrum is already available,[162] is also presented.

Next to these theoretical findings, for the experimental part of the project, improved ion optics were implemented into the current 'TOF-MS-PES' apparatus and a new VMI segment was designed and attached. This process involved the addition of an enhanced mass gate, einzel lenses and *x*-*y* deflection plates, the inclusion of an ion decelerator as well as the refinement of the magnetic bottle field, all of which will improve the photoelectron spectroscopic resolution. For the design and construction of the VMI attachment several tasks were completed:

- the design and construction of a 'beam optimisation module' which includes *x*-*y* deflection plates, einzel lenses and an ion buncher;

- the design and testing of a double layered internal µ-metal shield into which the VMI lense is mounted;
- the design of the VMI lens which included simulations of the VMI process as well as the construction of the electron detection system and
- the development of the camera control and image processing software.

All of these tasks were completed and the VMI attachment was successfully assembled and attached to the TOF-MS-PES apparatus; photodetatched neutral particles were already detected with the current set-up. However, due to a limited candidature of 3½ years and unfortunate equipment failure in the later part of the candidature, work in the project was delayed such that a successful VMI spectrum is yet to be recorded. Most of the listed issues (see Section 3.3.3) have been addressed however so that recording the first spectrum is imminent.

In future, a cylindrical lens has to be put in place allowing formation of a focal plane at the laser interaction region of the VMI Furthermore, the camera software has to be matured where for example flat field correction and maximum entropy reconstruction algorithm need to be implemented allowing for higher quality VMI spectra. In order to improve the particle beam characteristics, a new piezoelectric nozzle will be implemented; which also requires a revision of the exact skimmer position. With regard to photoelectron spectroscopy, the magnet responsible for the magnetic field in the detachment region needs to be upgraded and tested with the new decelerator in place, both of which should increase the current spectral resolution.

For the further development of the theoretical methodology an improved protocol for determining the spin-orbit coupling has to be tested. While in order to simulate electron affinities and anion photoelectron spectra it may not be necessary to conduct an anharmonic analysis of the anion (due to its low temperature in experimental conditions), it is definitely beneficial for the neutral. Therefore, it should be investigated whether the Franck–Condon predictions can be expanded to account for an anharmonic neutral surface and dipole moment field.

Through the presented work, it was found that for the carbonyl oxides, the VPT2 obtained frequencies vary greatly with respect to basis set choice and (since CCSD(T) analytical gradients have been used) the linear equations convergence criterion; an effect which requires further investigation. As mentioned previously, more detailed experimental IR-data of MetOx is necessary, which should entail combination and overtone bands as well as isotopic shifts. Similarly, an IR-spectrum of ^{c}EtOx can help finding inconsistencies within the here presented VPT2 CCSD(T) / A'VTZ results.

Appendix

A.1 Theoretical background

A.1.1 Atomic units

Substituting the coordinates $\boldsymbol{r}$ with $\lambda \boldsymbol{r}'$ leads to the following Schrödinger equation for the hydrogen atom.

$$\left[\frac{\hbar^2}{m_\mathrm{e}\lambda^2}\nabla'^2 - \frac{e^2}{4\pi\varepsilon_0\lambda\boldsymbol{r}'}\right]\phi' = E\phi' \tag{A.1}$$

Hence, the atomic unit of energy E_a [*Hartree*] is.

$$E_a = \frac{\hbar^2}{m_\mathrm{e}\lambda^2} = \frac{e^2}{4\pi\varepsilon_0\lambda} \tag{A.2}$$

Therefore, λ is just the Bohr radius a_0, the atomic unit of length [*Bohr*].

$$\lambda = a_0 = \frac{4\pi\varepsilon_0\hbar^2}{m_\mathrm{e}e^2} \tag{A.3}$$

With $E' = E/E_a$, A.2 becomes:

$$\left[-\frac{1}{2}\nabla'^2 - \frac{1}{\boldsymbol{r}'}\right]\phi' = E'\phi' \tag{A.4}$$

A.1.2 Mean-field approximation

At the heart of the Hartree–Fock (HF) approximation lies the approximate treatment of the two electron interaction through effective one electron operators. The exact two electron Coulomb operator can be written as

$$\left\langle ij \middle| \hat{J}_{ij} \middle| ij \right\rangle = \int \int \chi_i \left(\boldsymbol{x}_i\right)^* \chi_j \left(\boldsymbol{x}_j\right)^* \frac{1}{r_{ij}} \chi_i \left(\boldsymbol{x}_i\right) \chi_j \left(\boldsymbol{x}_j\right) d\boldsymbol{x}_j d\boldsymbol{x}_i \tag{A.5}$$

An electron $\boldsymbol{x}_i$ in orbital χ_i is moving in the field of $\boldsymbol{x}_j$ of orbital χ_j. This can be viewed as two *clouds* of electron density interacting with each other.

The exchange interaction however, cannot be cast into such a simple picture, as illustrated in the two electron exchange operator:

$$\left\langle ij \middle| \hat{K}_{ij} \middle| ij \right\rangle = \int \int \chi_i \left(\boldsymbol{x}_i\right)^* \chi_j \left(\boldsymbol{x}_j\right)^* \frac{\hat{P}_{12}}{r_{ij}} \chi_i \left(\boldsymbol{x}_i\right) \chi_j \left(\boldsymbol{x}_j\right) d\boldsymbol{x}_j d\boldsymbol{x}_i \tag{A.6}$$

$\hat{P}_{12}$ causes the permutation of the two electrons $\boldsymbol{x}_i$ and $\boldsymbol{x}_j$. The interaction can therefore not be broken down into densities but must rather be understood as an interconnected–often coined *non-local*–interaction between the orbital wave functions itself and not the squared versions. Understanding then, becomes a matter of philosophy (What is the meaning of a wave function).

In the HF approximation, the two electron Coulomb operator is replaced by an effective one electron Coulomb operator.

$$\hat{J}_i \left| i \right\rangle = \left(\int \chi_j \left(\boldsymbol{x}_j\right)^* \frac{1}{r_{ij}} \chi_j \left(\boldsymbol{x}_j\right) d\boldsymbol{x}_j \right) \left| i \right\rangle \ , \tag{A.7}$$

where the integral term can be viewed as the average potential $\boldsymbol{x}_i$ is experiencing due to $\boldsymbol{x}_j$. Similarly, the effective one electron Exchange operator can be written as

$$\hat{K}_i \left| i \right\rangle = \left(\int \chi_j \left(\boldsymbol{x}_j\right)^* \frac{1}{r_{ij}} \chi_i \left(\boldsymbol{x}_j\right) d\boldsymbol{x}_j \right) \left| j \right\rangle \ , \tag{A.8}$$

which corresponds to the exchange potential $\boldsymbol{x}_i$ is experiencing due to the interaction with $\boldsymbol{x}_j$.

A.1.3 The restricted Hartree–Fock case

In Equation (2.11) the energy expectation value for the electronic Schrödinger equation is shown. Applying the Slater–Condon rules,[10] and the definition of the Slater determinant (Equation (2.9)) this equation can be rewritten as follows.

$$E = \sum_{i}^{N} \langle \chi_i \,|\, \hat{h}_i \,|\, \chi_i \rangle + \sum_{a>b}^{N} \left[\left\langle \chi_i \chi_j \,\middle|\, \frac{1}{r_{ab}} \,\middle|\, \chi_i \chi_j \right\rangle - \left\langle \chi_i \chi_j \,\middle|\, \frac{1}{r_{ab}} \,\middle|\, \chi_j \chi_i \right\rangle \right] \tag{A.9}$$

In the restricted Hartree–Fock (RHF) case it is assumed that all electrons are paired ($n_\alpha = n_\beta$). This means one can account for all the possible combinations of spacial and spin parts, ϕ and α or β, in the one- (two cases) and two-centred integrals (four cases).

$$\begin{aligned} E_{\mathrm{RHF}} = {} & \sum_{i}^{\frac{N}{2}} \langle \phi_i \,|\, \hat{h}_i \,|\, \phi_i \rangle \begin{pmatrix} \langle \alpha_i | \alpha_i \rangle \\ \langle \beta_i | \beta_i \rangle \end{pmatrix} \\ & + \sum_{a>b}^{\frac{N}{2}} \left\langle \phi_i \phi_j \,\middle|\, \frac{1}{r_{ij}} \,\middle|\, \phi_i \phi_j \right\rangle \begin{pmatrix} \langle \alpha_i \alpha_j | \alpha_i \alpha_j \rangle \\ \langle \alpha_i \beta_j | \alpha_i \beta_j \rangle \\ \langle \beta_i \alpha_j | \beta_i \alpha_j \rangle \\ \langle \beta_i \beta_j | \beta_i \beta_j \rangle \end{pmatrix} - \left\langle \phi_i \phi_j \,\middle|\, \frac{1}{r_{ij}} \,\middle|\, \phi_j \phi_i \right\rangle \begin{pmatrix} \langle \alpha_i \alpha_j | \alpha_j \alpha_i \rangle \\ \langle \alpha_i \beta_j | \beta_j \alpha_i \rangle \\ \langle \beta_i \alpha_j | \alpha_j \beta_i \rangle \\ \langle \beta_i \beta_j | \beta_j \beta_i \rangle \end{pmatrix} \end{aligned} \tag{A.10}$$

In the last part of the sum, one can see that $\langle \alpha_i \beta_j | \beta_j \alpha_i \rangle$ and $\langle \beta_i \alpha_j | \alpha_j \beta_i \rangle$ are rendered zero due to the orthonormality of different spin functions, whereas the remaining spin integrals are all equal to 1. This means that Equation (A.10) can be simplified to the following expression.

$$E = 2 \sum_{i}^{\frac{N}{2}} \langle \phi_i \,|\, \hat{h}_i \,|\, \phi_i \rangle + \sum_{i>j}^{\frac{N}{2}} 4 \left\langle \phi_i \phi_j \,\middle|\, \frac{1}{r_{ij}} \,\middle|\, \phi_i \phi_j \right\rangle - 2 \left\langle \phi_i \phi_j \,\middle|\, \frac{1}{r_{ij}} \,\middle|\, \phi_j \phi_i \right\rangle \tag{A.11}$$

A.1.4 Variational method

A very important aspect in electronic structure theory is to find a solution for the time independent non-relativistic Schrödinger Equation (2.1). Solving this eigenvalue problem is merely feasible for the simplest systems, yet by using the variational method, it is possible to approach the exact solution in the following manner:

$$\frac{\left\langle \widetilde{\psi}_{\mathrm{el}} \,\middle|\, \widehat{H}_{\mathrm{el}} \,\middle|\, \widetilde{\psi}_{\mathrm{el}} \right\rangle}{\left\langle \widetilde{\psi}_{\mathrm{el}} \,\middle|\, \widetilde{\psi}_{\mathrm{el}} \right\rangle} = \widetilde{E}_{\mathrm{el}} \geq E_{\mathrm{el,exact}} \tag{A.12}$$

This equation states that the expectation value of the electronic energy, obtained from any well-behaved electronic trial wave function $\widetilde{\psi}_{\mathrm{el}}$, will always be larger or at best equal to the true electronic energy $E_{\mathrm{el,exact}}$ of the considered system. The variation principle can therefore be understood as a tool to find the best trial wave function which would lead to the minimum electronic energy of the system. Formulated as an optimisation problem, the variational method can be written as follows:

$$\frac{\delta \widetilde{E}}{\delta \widetilde{\psi}} = 0 \tag{A.13}$$

A.1.5 Lagrangian multiplier method

In order to obtain the HF equations, one has to minimise the energy of a single determinant wave function with respect to spin orbitals. For this, the spin has to be varied by an infinitesimal amount $\delta \chi_i$

$$\chi_i \to \chi_i + \delta \chi_i \qquad \Rightarrow \qquad \delta \left\langle \psi \,\middle|\, \widehat{H}_{\mathrm{el}} \,\middle|\, \psi \right\rangle = 0 \tag{A.14}$$

From Equation (2.11) and Equation (A.14) one can form the Lagrangian $\mathcal{L}$ which is the difference of objective function (the energy expectation value) and constraint $\langle i \mid j \rangle - \delta_{ij}$ (which is necessary to ensure the orthogonality of the orbitals). The variational theorem requires $\frac{\delta \widetilde{E}}{\delta \widetilde{\psi}} = 0$, therefore one can write:

$$\delta \mathcal{L} = \delta \left(\left\langle \psi \,\middle|\, \widehat{H}_{\mathrm{el}} \,\middle|\, \psi \right\rangle - \sum_{ij}^{N} \lambda_{ji} \left(\langle i \mid j \rangle - \delta_{ij} \right) \right) = 0 \tag{A.15}$$

The variation is treated like a normal differentiation. In the following, the effect of the variation in the orbitals is shown, first the effect on the one electron operator:

$$\begin{aligned} \delta \left\langle \psi \,\middle|\, \sum_{i}^{N} \hat{h}(i) \,\middle|\, \psi \right\rangle &= \sum_{i}^{N} \left\langle \delta i \,\middle|\, \hat{h}(i) \,\middle|\, i \right\rangle + \left\langle i \,\middle|\, \hat{h}(i) \,\middle|\, \delta i \right\rangle \\ &= \sum_{i}^{N} \left\langle \delta i \,\middle|\, \hat{h}(i) \,\middle|\, i \right\rangle + \underbrace{\sum_{i}^{N} \left\langle \delta i \,\middle|\, \hat{h}(i) \,\middle|\, i \right\rangle^{*}}_{\text{complex conjugate}} ; \end{aligned} \tag{A.16}$$

the effect on the two electron operator:

$$\begin{aligned}\delta\left\langle\psi\left|\frac{1}{2}\sum_{ij}^{N}\frac{1}{r_{ij}}\right|\psi\right\rangle &= \frac{1}{2}\sum_{ij}^{N}\langle(\delta i)j\,|\,ij\rangle+\langle i(\delta j)\,|\,ij\rangle+\langle ij\,|\,(\delta i)j\rangle+\langle ij\,|\,i(\delta j)\rangle\\ &\quad-\frac{1}{2}\sum_{ij}^{N}\langle(\delta i)j\,|\,ji\rangle+\langle i(\delta j)\,|\,ji\rangle+\langle ij\,|\,(\delta j)i\rangle+\langle ij\,|\,j(\delta i)\rangle\\ &=\sum_{ij}^{N}\langle(\delta i)j\,|\,ij\rangle-\langle(\delta i)j\,|\,ji\rangle+\underbrace{\sum_{ij}^{N}\langle(\delta i)j\,|\,ij\rangle^{*}-\langle(\delta i)j\,|\,ij\rangle^{*}}_{\text{complex conjugate}}\;;\end{aligned}\tag{A.17}$$

and finally on the constraint.

$$\begin{aligned}\delta\left(\sum_{ij}^{N}\lambda_{ji}\left(\langle i\,|\,j\rangle-\delta_{ij}\right)\right)&=\sum_{ij}^{N}\lambda_{ji}\left(\langle\delta i\,|\,j\rangle+\langle i\,|\,\delta j\rangle\right)\\ &=\sum_{ij}^{N}\lambda_{ji}\,\langle\delta i\,|\,j\rangle+\underbrace{\sum_{ij}^{N}\lambda_{ji}^{*}\,\langle\delta i\,|\,j\rangle^{*}}_{\text{complex conjugate}}\end{aligned}\tag{A.18}$$

All the complex conjugates can be summed up to give $\delta\mathcal{L}_{\mathrm{CC}}$. The complete Lagrangian optimisation problem can then be written as follows.

$$\begin{aligned}\delta\mathcal{L}&=\sum_{i}^{N}\left\langle\delta i\,\middle|\,\hat{h}(i)\,\middle|\,i\right\rangle+\sum_{ij}^{N}\langle(\delta i)j\,|\,ij\rangle-\langle(\delta i)j\,|\,ji\rangle+\sum_{ij}^{N}\lambda_{ji}\,\langle\delta i\,|\,j\rangle+\delta\mathcal{L}_{\mathrm{CC}}\\ &=\sum_{i}^{N}\int d\boldsymbol{x}_i\,\langle\delta i|\left(\hat{h}(i)\,|i\rangle+\sum_{j}^{N}\left(\hat{J}_j(i)-\hat{K}_j(i)\right)|i\rangle+\sum_{j}^{N}\lambda_{ji}\,|j\rangle\right)+\delta\mathcal{L}_{\mathrm{CC}}\\ &=0\,,\end{aligned}\tag{A.19}$$

where the expressions for the effective one electron operators $\hat{J}_j(i)$ and $\hat{K}_j(i)$ from Equations (A.5) to (A.8) were used. From the last equation, one can see that the expression in brackets needs to be zero in order to satisfy the equation. One can therefore write:

$$\begin{aligned}\left[\hat{h}(i)+\sum_{j}^{N}\left(\hat{J}_j(i)-\hat{K}_j(i)\right)\right]|i\rangle &= \sum_{j}^{N}\lambda_{ji}\,|j\rangle \qquad i=\{\,1,2,\ldots,N\,\}\\ \hat{f}(i)\,|i\rangle &= \sum_{j}^{N}\lambda_{ji}\,|j\rangle\,,\end{aligned} \tag{A.20}$$

where the last line represents the non-canonical HF equations. In order to obtain a canonical set of these equations, the spin orbitals must be transformed, which is described briefly in Section 2.1.2.

A.1.6 Adiabatic connection

To connect the non-interacting Kohn–Sham system and the physical system continuously, a coupling constant λ was introduced into the universal functional $F\,[\rho]$, to multiply $\hat{V}_{ee}$:

$$F^{\lambda}\,[\rho] = \min_{\psi\to\rho}\left\langle \psi \,\middle|\, \hat{T}+\lambda\widehat{V_{ee}} \,\middle|\, \psi \right\rangle \tag{A.21}$$

A non-interacting system is represented as $F^{\lambda=0}\,[\rho]$ and a fully interacting system with $F^{\lambda=1}\,[\rho]$. Using the minimising wave function ψ^{λ} and the Kohn–Sham orbitals χ^{λ} for a given λ, $T^{\lambda}\,[\rho]$ and $E^{\lambda}_{ee}\,[\rho]$ can be described as follows.

$$\begin{aligned}T^{\lambda}\,[\rho] &= \left\langle \psi^{\lambda}\,[\rho] \,\middle|\, \hat{T} \,\middle|\, \psi^{\lambda}\,[\rho] \right\rangle\\ E^{\lambda}_{ee}\,[\rho] &= \left\langle \psi^{\lambda}\,[\rho] \,\middle|\, \lambda\hat{V}_{ee} \,\middle|\, \psi^{\lambda}\,[\rho] \right\rangle = \lambda\left\langle \psi^{\lambda}\,[\rho] \,\middle|\, \hat{V}_{ee} \,\middle|\, \psi^{\lambda}\,[\rho] \right\rangle\end{aligned} \tag{A.22}$$

Thus,

$$E^{\lambda}_{XC}\,[\rho] = \left\langle \psi^{\lambda}\,[\rho] \,\middle|\, \hat{T}+\lambda\hat{V}_{ee} \,\middle|\, \psi^{\lambda}\,[\rho] \right\rangle - \left\langle \chi^{\lambda}\,[\rho] \,\middle|\, \hat{T}+\lambda\hat{V}_{ee} \,\middle|\, \chi^{\lambda}\,[\rho] \right\rangle\,. \tag{A.23}$$

The Hellmann–Feynman theorem [48] can then be applied to this equation, giving:

$$F^{\lambda=1}\,[\rho] = F\,[\rho] = \underbrace{F^{\lambda=0}\,[\rho]}_{T_{\text{non-interacting}}[\rho]} + \int_{0}^{1} d\lambda \left\langle \psi^{\lambda}\,[\rho] \,\middle|\, \hat{V}_{ee} \,\middle|\, \psi^{\lambda}\,[\rho] \right\rangle \tag{A.24}$$

Using Equation (A.21) the exchange-correlation energy becomes:

$$E_{\mathrm{XC}}[\rho] = \int_0^1 d\lambda \left\langle \psi^{\lambda}[\rho] \middle| \widehat{V}_{ee} \middle| \psi^{\lambda}[\rho] \right\rangle - J[\rho] \tag{A.25}$$

With Equation (A.22), one can demonstrate that:

$$\begin{aligned}
E_{\mathrm{XC}}[\rho] &= \int_0^1 \frac{d\lambda}{\lambda} \overbrace{\lambda \left\langle \psi^{\lambda}[\rho] \middle| \widehat{V}_{ee} \middle| \psi^{\lambda}[\rho] \right\rangle}^{E_{ee}^{\lambda}[\rho]} - J[\rho] \\
&= \int_0^1 d\lambda \frac{E_{ee}^{\lambda}[\rho]}{\lambda} - \int_0^1 d\lambda J[\rho] = \int_0^1 d\lambda \left(\frac{E_{ee}^{\lambda}[\rho]}{\lambda} - J[\rho] \right) \\
&= \int_0^1 \frac{d\lambda}{\lambda} \underbrace{\left(E_{ee}^{\lambda}[\rho] - \overbrace{\lambda J[\rho]}^{J^{\lambda}[\rho]} \right)}_{E_{\text{non-classical}}[\rho]} = \int_0^1 d\lambda \frac{E_{\text{non-classical}}[\rho]}{\lambda}
\end{aligned}$$

$$E_{\mathrm{XC}}[\rho] = \int_0^1 E_{\text{non-classical}}(\lambda)\, d\lambda \tag{A.26}$$

The last equation is called adiabatic connection formula (related to Equation (2.59)) and it can be shown that:

$$\begin{aligned}
E_{\text{non-classical}}(\lambda = 0) &= E_{\mathrm{X}} \\
E_{\text{non-classical}}(\lambda = 1) &= \underbrace{E_{\mathrm{X}} + E_{\mathrm{C}}}_{E_{\mathrm{XC}}} - T_{\mathrm{C}}
\end{aligned} \tag{A.27}$$

It should be noted that the correlation effects influence the form of the kinetic energy functional directly. Using the adiabatic connection formula, it is now possible to interpret results provided by density functional theory (DFT) methods, using different approximations.

A.2 Carbonyl oxide studies

A.2.1 Weizmann protocols

Comparison of different Weizmann protocols

There is a large variety of Weizmann (W*n*) protocols, the details of which are summarised in table Table A.1; they can roughly be separated into four categories.

The Weizmann-1 protocols aims to obtain the relativistic all-electron CCSD(T) / CBS with small basis sets (no larger than *spdfg*).[172] As an example, W1w is provided in Table A.1.[4] With more complex basis sets (*spdfgh*), the Weizmann-2 protocols are still aimed at relativistic all-electron CCSD(T) / CBS; it is however more precise as shown in Table A.1 (W2w exhibits an $\mathrm{RMSD}_{\mathrm{W4\text{-}11}}$ of 1.76 kJ mol^{-1} vs. 2.64 kJ mol^{-1} for W1w.).[4] Most single reference dominated systems can even show sub-kJ mol^{-1} accuracy. The Weizmann-3 and Weizmann-4 are layered extrapolations to relativistic, all-electron, CCSDTQ / CBS and CCSDTQ5 / CBS, respectively.[172] They account for post-CCSD(T) contributions and can therefore also account for strong non-dynamical correlation (multi-reference character). Both feature sub-kJ mol^{-1} accuracy for most molecules – W4 even reaches below 0.5 kJ mol^{-1} against the W4-11 dataset.[173]

When looking at feasibilities of certain calculations, it is apparent that W4 is only applicable to the smallest of systems. As one goes down in the rung of Weizmann protocols, larger systems can be treated. With the recent development of explicitly correlated methods, it was possible to calculate some of the components even more efficiently. Examples are the W1-F12, W2-F12 and W3-F12 protocols; the later of which is predominantly applied to the carbonyl oxide species occurring in this thesis. One should note that due to the development of W4lite – a protocol that sits somewhat in the middle between W3 and W4 – most of the standard W3 protocols (W3, W3.2, W3w) are rendered obsolete.[173] The reason for this is that W4lite is only marginally more expensive the standard W3 methods, yet shows a much higher precision.

	W1w	W2w	W3-F12	W4lite	W4
Reference Geometry	B3LYP / V(T+d)Z		CCSD(T) / A'V(Q+d)Z		
SCF	HF / A'V({T,Q}+d)Z	HF / A'V({Q,5}+d)Z	HF* / V({T,Q}+d)Z-F12	HF / A'V({5,6}+d)Z	HF / AV({5,6}+d)Z
SCF extrap.	$E(L) = E_\infty + A/L^{5.00}$				
Valence CCSD	CCSD / A'V({T,Q}+d)Z	CCSD / A'V({Q,5}+d)Z	CCSD* / V({T,Q}+d)Z-F12	CCSD / A'V({5,6}+d)Z	CCSD / AV({5,6}+d)Z
Valence CCSD extrap.	$E(L) = E_\infty + A/L^{3.22}$	$E(L) = E_\infty + A/L^{3.00}$	$E(L) = E_\infty + A/L^{5.94}$	$E(L) = E_\infty + A/L^{3.00}$	$E(L) = E_\infty + A/L^{3.00}$
Valence (T)	(T) / A'V({D,T}+d)Z	(T) / A'V({T,Q}+d)Z	(T*) / VTZ-F12 scaled by f	(T) / A'V({T,Q}+d)Z	(T) / A'V({5,6}+d)Z
Valence (T) extrap.	$E(L) = E_\infty + A/L^{3.22}$	$E(L) = E_\infty + A/L^{3.00}$	N/A	$E(L) = E_\infty + A/L^{3.00}$	$E(L) = E_\infty + A/L^{3.00}$
Valence T_3	N/A		CCSDT / V({D,T}+d)Z		CCSDT / V({T,Q}+d)Z
Valence T_3 extrap.	N/A		$E(L) = E_\infty + A/L^{3.00}$		$E(L) = E_\infty + A/L^{3.00}$
Valence (Q)	N/A		(Q) / VDZ		1.10 (Q) / VTZ
Valence T_4	N/A		N/A		1.10 CCSDTQ / VTZ
Valence T_5	N/A		N/A		CCSDTQ5 / DZ
Valence T_6	N/A		N/A		CCSDTQ56 / DZ
CCSD inner shell	CCSD / Mtsmall		CCSD / A'wCV{T,Q}Z	CCSD / ACV{T,Q}Z	CCSD / wCV{T,Q}Z
(T) inner shell	(T) / Mtsmall		(T) / wCVTZ (no f)	(T) / ACV{T,Q}Z	(T) / wCV{T,Q}Z
Scalar relativistics	DKH-CCSD(T) / Mtsmall		DKH-CCSD(T) / AV(Q+d)Z		DKH-CCSD(T) / AV(Q+d)Z
DBOC	HF / A'VTZ		HF / A'VTZ		HF / AVTZ
ZPVE	B3LYP / V(T+d)Z		Best available		
Harmonic ZPVE Scaling	0.985	0.985	N/A		
$\mathrm{RMSD}_{\mathrm{W4\text{-}11}}$ [kJ mol^{-1}]	2.64	1.76	1.13	0.54	0.43

Table A.1. | Comparison of the components of the selected Weizmann protocols. Explanations of the used abbreviations for the basis sets are presented in Table 4.1. Detailed descriptions of the selected protocols can be found in references 172, 173 and 4.

Extrapolation formula

In W*n* theory it is common to apply a two-point extrapolation formula in order to extrapolate to the complete basis set limit. The following equation is used throughout W*n* theory.

$$E\left(L\right)=E_{\infty}+\frac{A}{L^{\alpha}}\quad\Leftrightarrow\quad A=\left(E\left(L\right)-E_{\infty}\right)L^{\alpha}\tag{A.28}$$

Here, $E\left(L\right)$ is the energy resulting a certain basis set (where L is the highest angular momentum quantum number of that basis set). The empirical parameter α depends on the method used. If two single point calculations were done–the second one with a higher angular momentum $L+1$–one can equate the parameter A.

$$\begin{aligned}\left(E\left(L\right)-E_{\infty}\right)L^{\alpha}&=\left(E\left(L+1\right)-E_{\infty}\right)\left(L+1\right)^{\alpha}\\ E\left(L\right)-E_{\infty}&=\left(E\left(L+1\right)-E_{\infty}\right)\underbrace{\left(\frac{L+1}{L}\right)^{\alpha}}_{c}\\ &=cE\left(L+1\right)-cE_{\infty}\end{aligned}$$

Thus one can solve for E_{∞}.

$$\begin{aligned}E_{\infty}&=\frac{E\left(L\right)-cE\left(L+1\right)}{1-c}\\ &=\frac{E\left(L\right)-E\left(L+1\right)+E\left(L+1\right)-cE\left(L+1\right)}{1-c}\\ &=\frac{E\left(L+1\right)\left(1-c\right)}{1-c}+\frac{E\left(L\right)-E\left(L+1\right)}{1-c}\\ E_{\infty}&=E\left(L+1\right)+\frac{E\left(L+1\right)-E\left(L\right)}{c-1}\end{aligned}\tag{A.29}$$

A.2.2 Additional data: Carbonyl oxides

CH$_2$OO: optimised at CCSD(T) / A'VQZ

C	1.074 791	−0.206 576	0.000 000
H	1.979 677	0.382 186	0.000 000
O	−0.001 516	0.468 206	0.000 000
O	−1.165 018	−0.202 933	0.000 000
H	1.010 308	−1.287 088	0.000 000

CH$_2$OO$^-$: optimised at CCSD(T) / A'VQZ

C	1.101 533	−0.229 150	−0.063 060
H	2.016 025	0.292 700	0.217 757
O	0.015 167	0.540 425	0.018 566
O	−1.202 320	−0.247 147	−0.011 696
H	0.965 446	−1.282 405	0.162 485

CH$_2$OO: optimised at CCSD(T) / A'VQZ

C	1.076 819	−0.207 036	0.000 000
H	1.982 960	0.381 980	0.000 000
O	−0.002 619	0.471 610	0.000 000
O	−1.171 292	−0.204 129	0.000 000
H	1.012 374	−1.288 630	0.000 000

CH$_2$OO$^-$: optimised at CCSD(T) / A'VTZ

C	1.103 699	−0.229 596	−0.067 264
H	2.018 368	0.291 711	0.219 638
O	0.014 966	0.544 039	0.019 281
O	−1.208 804	−0.248 724	−0.011 729
H	0.967 622	−1.283 006	0.164 126

[CH$_2$O···O]$^-$: optimised at CCSD(T) / A'VTZ

C	1.074 381	−0.232 703	−0.027 400
H	1.060 087	−1.085 530	−0.710 223
O	0.101 821	0.650 945	−0.116 593
O	−1.165 422	−0.282 943	0.101 191
H	1.618 110	−0.335 490	0.919 673

Table A.2. | Optimised methanal-oxide geometries (Cartesian $\{x, y, z\}$ coordinates in Å).

^{c}**EtOx**: neutral *cis*-ethanal-oxide

C	−0.597 673	−0.679 246	0.000 000
H	−0.958 486	−1.701 138	0.000 000
O	0.676 240	−0.604 866	0.000 000
O	1.207 071	0.655 454	0.000 000
C	−1.427 923	0.537 996	0.000 000
H	−2.486 964	0.288 480	0.000 000
H	−1.162 820	1.145 816	0.871 687
H	−1.162 820	1.145 816	−0.871 687

^{t}**EtOx**: neutral *trans*-ethanal-oxide

C	−0.489 485	−0.428 951	0.000 000
H	−0.216 911	−1.481 387	0.000 000
O	0.469 175	0.402 657	0.000 000
O	1.744 408	−0.099 797	0.000 000
C	−1.879 766	0.095 051	0.000 000
H	−1.873 391	1.184 336	0.000 000
H	−2.415 299	−0.266 933	0.881 923
H	−2.415 299	−0.266 933	−0.881 923

^{s}**AEtOx**: anionic *syn*-ethanal-oxide

C	−0.634 608	0.682 744	−0.158 401
H	−1.056 198	1.638 224	0.165 511
O	0.689 823	0.656 521	0.095 975
O	1.253 705	−0.684 530	−0.042 937
C	−1.449 240	−0.560 551	0.047 675
H	−2.511 168	−0.320 638	−0.089 150
H	−1.159 227	−1.342 463	−0.656 091
H	−1.306 578	−0.985 528	1.056 384

^{a}**AEtOx**: anionic *anti*-ethanal-oxide

C	−0.504 603	0.462 235	−0.166 988
H	−0.220 527	1.444 238	0.209 318
O	0.452 856	−0.471 095	−0.073 743
O	1.780 206	0.133 052	0.087 515
C	−1.885 458	−0.077 265	0.091 903
H	−2.636 575	0.695 245	−0.103 910
H	−2.101 140	−0.929 797	−0.561 805
H	−2.024 023	−0.428 465	1.131 854

Table A.3. | Optimised ethanal-oxide geometries at CCSD(T) / A'VTZ level of theory (Cartesian $\{x, y, z\}$ coordinates in Å).

Mode	Neutral			Anion			Mode description
	^{c}EtOx	^{t}EtOx	S	^{s}AEtOx	^{a}AEtOx	S	
ν_1	3085	3050	a'	2939	2991	a	C_b–H_a stretch
ν_2	3040	3032	a'	2977	2905	a	C_a–H asymmetric stretch (methyl group)
ν_3	2915	2924	a'	2812	2781	a	C_a–H symmetric stretches (methyl group)
ν_4	1459	1469	a'	1438	1331	a	asymmetric O–C / C–O stretch
ν_5	1416	1408	a'	1350	1445	a	CH_2 scissor / H_b–C_aC_b bend
ν_6	1346	1367	a'	1312	1299	a	methyl inversion / C–O stretch
ν_7	1258	1264	a'	1186	1200	a	in-plane C_b–H_a rocking / C–O stretch
ν_8	1073	1113	a'	1077	1078	a	methyl wagging / C–C stretch
ν_9	938	908	a'	880	904	a	C–C stretch
ν_{10}	872	862	a'	758	756	a	O–O stretch
ν_{11}	644	533	a'	507	460	a	methyl wagging / O–O–C bend
ν_{12}	293	308	a'	213	291	a	C–C–O–O scissor bend/deformation
ν_{13}	2967	2985	a''	2908	2953	a	C_a–H asymmetric stretch (methyl group)
ν_{14}	1401	1426	a''	1393	1413	a	CH_2 twist / C_a–H_b rocking
ν_{15}	996	1015	a''	988	992	a	methyl twisting / C_b–H_a rocking
ν_{16}	697	813	a''	625	630	a	C_b–H_a wagging / methyl rocking
ν_{17}	427	239	a''	294	116	a	C–C–O–O out-of-plane twisting
ν_{18}	201	148	a''	153	188	a	methyl twisting (internal rotation)

All frequencies are given in cm^{-1}.

Table A.4. | Computed scaled harmonic vibrational frequencies of the CH_3CHOO anion and neutral species at the CCSD(T) / A'VTZ level of theory. The scaling factor of 0.9635 taken Kesharwani et al. is the scaling factor for CCSD(T) / A'V(T+d)Z calculations. The basis set used in this study is more or less the same; yet we included augmented functions for C and O. This is expected to have a small effect on the scaling factor. The ordering of the modes of all other species has been changed to reflect that of ^{c}EtOx (ordered according to the Symmetry S of the modes), for direct comparison.

$^{\text{c}}$EtOx	CCSD(T)-F12a / AVTZ[162]	CCSD(T) / A'VTZ	VPT2-CCSD(T) / A'VTZ	Experiment[162]
Type	B_e	B_e	B_0	B_0
A	17 613	17 480	17 396	17 587
B	7192	7139	7060	7133
C	5269	5230	5175	5229

$^{\text{t}}$EtOx	CCSD(T)-F12a / AVTZ[163]	CCSD(T) / A'VTZ	VPT2-CCSD(T) / A'VTZ	Experiment[163]
Type	B_e	B_e	B_0	B_0
A	48 855	48 568	–	48 494
B	4452	4418	–	4435
C	4185	4154	–	4167

Table A.5. | Comparison of the calculated and experimental rotational constants of the ethanal-oxides. All constants are given in MHz.

Basis Set		VTZ	A'VTZ	AVTZ	wCVTZ	A'wCVTZ	A'VQZ	ANO2	**normal mode description**
Trans.	S	**Fundamental frequencies** [cm^{-1}]							
1_1	a'	3308	3294	3295	3316	3305	3302	3308	Asymmetric CH stretch
2_1	a'	3149	3132	3137	3156	3145	3141	3147	Symmetric CH stretch
3_1	a'	1489	1483	1483	1494	1488	1491	1490	CH$_2$ scissor / CO stretch
4_1	a'	1297	1306	1306	1305	1312	1317	1314	CO stretch / CH$_2$ scissor
5_1	a'	1239	1232	1231	1243	1237	1240	1241	CH$_2$ rocking
6_1	a'	975	935	934	976	936	946	956	OO stretch
7_1	a'	535	531	531	537	533	535	535	COO deformation
8_1	a''	837	867	863	841	878	876	866	CH$_2$ wagging
9_1	a''	634	647	635	637	639	643	641	CH$_2$ twisting

Table A.6. | CH$_2$OO calculated CCSD(T) harmonic frequencies. The frequencies are obtained from an analytic harmonic force field using the Cfour suite of programmes. Small differences occur between this data set (which was generated using much tighter convergence criteria for the linear equitations) and the A'VTZ as well as A'VQZ frequencies presented in Table 4.4.

Isotope		CH_2O_2	$CH_2{}^{18}O_2$	$^{13}CH_2O_2$	CD_2O_2	**normal mode description**
Trans.	S	**Fundamental frequencies** [cm^{-1}]				
1_1	a'	3294	3296	3281	2470	Asymmetric CH stretch
2_1	a'	3132	3136	3132	2266	Symmetric CH stretch
3_1	a'	1483	1479	1467	1350	CH_2 scissor / CO stretch
4_1	a'	1306	1273	1290	1077	CO stretch / CH_2 scissor
5_1	a'	1232	1219	1224	1027	CH_2 rocking
6_1	a'	935	888	932	870	OO stretch
7_1	a'	531	514	528	471	COO deformation
8_1	a''	867	869	862	699	CH_2 wagging
9_1	a''	647	629	635	486	CH_2 twisting

Table A.7. | CH_2OO harmonic frequencies of the isotopologues at VPT2–CCSD(T) / A'VTZ The frequencies are obtained from an analytic harmonic force field using the Cfour suite of programmes. Small differences occur between this data set (which was generated using much tighter convergence criteria for the linear equitations) and the A'VTZ frequencies presented in Table 4.4.

Isotope		CH_2O_2	$CH_2{}^{18}O_2$	$^{13}CH_2O_2$	CD_2O_2
$\Delta\omega_{389}$	[cm^{-1}]	−30.3	−19.0	−30.3	165.0
X_{389}		1.2	1.8	0.8	< 0.05
W_{389}	[cm^{-1}]	−26.3	−25.6	−26.1	N/A
$\Delta\omega_{389}$	[cm^{-1}]	17.2	76.7	7.1	9.2
X_{389}		0.1	< 0.05	0.5	0.4
W_{389}	[cm^{-1}]	N/A	N/A	−5.2	N/A
$\Delta\omega_{49}$	[cm^{-1}]	11.5	15.6	19.6	105.3
X_{49}		0.3	1.5	1.0	< 0.05
W_{49}	[cm^{-1}]	N/A	−19.5	−19.5	N/A

Table A.8. | Fermi resonance descriptors of isotopic MetOx VPT2 calculations at CCSD(T) / A'VTZ. Here $\Delta\omega_{in}$ refers to the difference in harmonic frequencies of a mode i and a combination band $j + k$ or an overtone $2j$, while X_{in} denotes the harmonic derivative matrix element and W_{in} is the matrix element of the perturbation function W, all of which are discussed in Section 4.5.2. Mode descriptions are given in Table 4.14.

D_i^a a i	1	2	3	4	5	6	7	8	9	10	11	12	13	14	15	16	17	18
1	−0.1	0.0	0.0	0.2	0.0	0.0	0.0	0.0	0.0	0.0	0.0	0.0	0.0	0.0	0.0	0.1	0.0	0.0
2	0.0	−0.1	0.0	0.0	0.0	0.0	0.0	0.0	0.0	0.0	0.0	0.0	0.0	0.1	0.0	0.0	0.0	0.0
3	0.0	0.0	−2.6	4.8	0.2	0.1	0.0	0.0	0.0	0.0	0.0	0.0	0.0	0.1	0.0	0.0	0.0	0.1
4	0.0	0.0	0.0	−0.1	0.0	0.0	0.0	0.0	0.0	0.0	0.0	0.0	0.0	0.0	0.0	0.0	0.0	0.0
5	0.0	0.0	0.0	0.0	−2.3	0.0	0.0	0.0	0.0	0.0	0.0	0.0	0.0	0.0	2.2	0.0	2.2	0.0
6	0.0	0.0	0.0	0.0	0.0	−0.0	0.0	0.0	0.0	0.0	0.0	0.0	0.0	0.0	0.0	0.0	0.0	0.0
7	0.0	0.0	0.0	0.0	0.0	0.0	−0.1	0.0	0.1	0.0	0.0	0.0	0.0	0.0	0.0	0.0	0.0	0.0
8	0.0	0.0	0.0	0.0	0.0	0.0	0.0	−0.0	0.0	0.0	0.0	0.0	0.0	0.0	0.0	0.0	0.0	0.0
9	0.0	0.0	0.0	0.0	0.0	0.0	0.0	0.0	−0.6	0.0	0.5	0.6	0.0	0.0	0.0	0.0	0.0	0.0
10	0.0	0.0	0.0	0.0	0.0	0.0	0.0	0.0	0.0	−0.2	0.0	0.0	0.0	0.0	0.0	0.1	0.3	0.1
11	0.0	0.0	0.0	0.0	0.0	0.0	0.0	0.0	0.0	0.0	−0.2	0.0	0.0	0.0	0.0	0.0	0.2	0.2
12	0.0	0.0	0.0	0.0	0.0	0.0	0.0	0.0	0.0	0.0	0.0	−0.0	0.0	0.0	0.0	0.0	0.0	0.1
13	0.0	0.0	0.0	0.0	0.0	0.0	0.0	0.0	0.0	0.0	0.0	0.0	−0.1	0.0	0.0	0.0	0.0	0.0
14	0.0	0.0	0.0	0.0	0.0	0.0	0.0	0.0	0.1	0.0	0.0	0.0	0.0	−0.1	0.0	0.0	0.1	0.0
15	0.0	0.0	0.0	0.0	0.0	0.0	0.0	0.0	0.0	0.0	0.0	0.0	0.0	0.0	−0.1	0.0	0.0	0.0
16	0.0	0.0	0.0	0.0	0.0	0.0	0.0	0.0	0.0	0.0	0.0	0.0	0.0	0.0	0.0	0.0	0.0	0.0
17	0.0	0.0	0.0	0.0	0.0	0.0	0.0	0.0	0.0	0.0	0.0	0.0	0.0	0.0	0.0	0.0	−0.0	0.0
18	0.0	0.0	0.1	0.0	0.0	0.0	0.0	0.0	0.0	0.0	0.0	0.0	0.0	0.0	0.0	0.0	0.0	0.1

Table A.9. | ^{c}EtOx first harmonic derivative matrix of the CCSD(T) / A'VTZ semi-quartic force field. Major resonances arise from contributions $9_1 \approx 12_1\,11_1$, $5_1 \approx 15_1\,17_1$ and $3_1 \approx 4_2$ ($X > 0.5$). All quantities are dimensionless.

Bibliography

[1] R. Criegee. Mechanism of Ozonolysis. *Angewandte Chemie International Edition in English*, **14**: 745 – 752, 1975. doi: `10.1002/anie.197507451` (see pp. 2, 76, 77)

[2] A. Arneth, S. P. Harrison, S. Zaehle, K. Tsigaridis, S. Menon, P. J. Bartlein, J. Feichter, A. Korhola, M. Kulmala, D. O'Donnell, and et al. Terrestrial biogeochemical feedbacks in the climate system. *Nature Geoscience*, **3**: 525 – 532, 2010. doi: `10.1038/ngeo905` (see pp. 2, 77, 78)

[3] A. T. J. B. Eppink and D. H. Parker. Velocity map imaging of ions and electrons using electrostatic lenses: Application in photoelectron and photofragment ion imaging of molecular oxygen. *Review of Scientific Instruments*, **68**: 3477 – 3484, 1997. doi: `10.1063/1.1148310` (see pp. 2, 43, 44)

[4] A. Karton and J. M. L. Martin. Explicitly correlated Wn theory: W1-F12 and W2-F12. *The Journal of Chemical Physics*, **136**: 124114, 124114, 2012. doi: `10.1063/1.3697678` (see pp. 2, 80, 82, 83, 85, 132, 133)

[5] Y.-T. Su, Y.-H. Huang, H. A. Witek, and Y.-P. Lee. Infrared Absorption Spectrum of the Simplest Criegee Intermediate CH2OO. *Science*, **340**: 174 – 176, 2013. doi: `10.1126/science.1234369` (see pp. 3, 78, 79, 87, 104, 109, 110)

[6] M. Born and R. Oppenheimer. Zur Quantentheorie der Molekeln. *Annalen der Physik*, **389**: 457 – 484, 1927. doi: `10.1002/andp.19273892002` (see p. 7)

[7] N. C. Handy, Y. Yamaguchi, and H. F. Schaefer. The diagonal correction to the Born–Oppenheimer approximation: Its effect on the singlet–triplet splitting of CH_2 and other molecular effects. *The Journal of Chemical Physics*, **84**: 4481 – 4484, 1986. doi: `10.1063/1.450020` (see p. 8)

[8] M. Born and K. Huang. *Dynamical Theory of Crystal Lattices*. Oxford Classic Texts in Physical Sciences Clarendon Press, 1954. (see p. 8)

[9] V. Fock. Näherungsmethode zur Lösung des quantenmechanischen Mehrkörperproblems. *Zeitschrift für Physik*, **61**: 126 – 148, 1930. doi: `10.1007/BF01340294` (see p. 8)

[10] J. C. Slater. The Theory of Complex Spectra. *Physical Review*, **34**: 1293 – 1322, 1929. doi: `10.1103/PhysRev.34.1293` (see pp. 9, 20, 127)

[11] A. Szabo and N. S. Ostlund. In: *Modern quantum chemistry: Introduction to Advanced Electronic Structure Theory*. chap. 2, 68. Dover Publications, 1996. (see p. 10)

[12] J. E. Lennard-Jones. The electronic structure of some diatomic molecules. *Transactions of the Faraday Society*, **25**: 668 – 686, 1929. doi: `10.1039/TF9292500668` (see p. 12)

[13] C. Roothaan. New Developments in Molecular Orbital Theory. *Reviews of Modern Physics*, **23**: 69 – 89, 1951. doi: `10.1103/RevModPhys.23.69` (see p. 12)

[14] G. G. Hall. The Molecular Orbital Theory of Chemical Valency. VIII. A Method of Calculating Ionization Potentials. *Proceedings of the Royal Society of London. Series A. Mathematical and Physical Sciences*, **205**: 541 – 552, 1951. doi: `10.1098/rspa.1951.0048` (see p. 12)

[15] G. Berthier. Extension de la methode du champ moleculaire self-consistent a l'etude des couches incompletes. *Comptes rendus hebdomadaires des séances de l'Académie des sciences*, **238**: 91 – 93, 1954. (see p. 13)

[16] J. A. Pople and R. K. Nesbet. Self-Consistent Orbitals for Radicals. *The Journal of Chemical Physics*, **22**: 571 – 572, 1954. doi: `10.1063/1.1740120` (see p. 13)

[17] C. D. Sherrill 'An Introduction to Configuration Interaction Theory' 1995 (see p. 14)

[18] E. Schrödinger. Quantisierung als Eigenwertproblem. *Annalen der Physik*, **385**: 437 – 490, 1926. doi: `10.1002/andp.19263851302` (see p. 15)

[19] C. Møller and M. S. Plesset. Note on an Approximation Treatment for Many-Electron Systems. *Physical Review*, **46**: 618 – 622, 1934. doi: `10.1103/PhysRev.46.618` (see p. 17)

[20] L. Brillouin. *Conductibilité électrique et thermique des métaux*. Actualités scientifiques et industrielles Hermann et Cie, 1934. (see p. 17)

[21] P. R. Surján. 'The Brillouin Theorem' English in: *Second Quantized Approach to Quantum Chemistry*. Springer Berlin Heidelberg, 1989. 87 – 92 doi: `10.1007/978-3-642-74755-7_11` (see p. 17)

[22] A. Szabo and N. S. Ostlund. In: *Modern quantum chemistry: Introduction to Advanced Electronic Structure Theory*. chap. 6, 352. Dover Publications, 1996. (see p. 17)

[23] Y. Jung, R. C. Lochan, A. D. Dutoi, and M. Head-Gordon. Scaled opposite-spin second order Møller–Plesset correlation energy: An economical electronic structure method. *The Journal of Chemical Physics*, **121**: 9793 – 9802, 2004. doi: `10.1063/1.1809602` (see p. 18)

[24] M. L. Leininger, W. D. Allen, H. F. Schaefer, and C. D. Sherrill. Is Møller–Plesset perturbation theory a convergent ab initio method? *The Journal of Chemical Physics*, **112**: 9213 – 9222, 2000. doi: `10.1063/1.481764` (see p. 18)

[25] J. Čižek. On the Correlation Problem in Atomic and Molecular Systems. Calculation of Wavefunction Components in Ursell-Type Expansion Using Quantum-Field Theoretical Methods. *The Journal of Chemical Physics*, **45**: 4256 – 4266, 1966. doi: `10.1063/1.1727484` (see p. 18)

[26] J. Čižek and J. Paldus. Correlation problems in atomic and molecular systems III. Rederivation of the coupled-pair many-electron theory using the traditional quantum chemical methodst. *International Journal of Quantum Chemistry*, **5**: 359 – 379, 1971. doi: `10.1002/qua.560050402` (see p. 18)

[27] J. Paldus, J. Čížek, and I. Shavitt. Correlation Problems in Atomic and Molecular Systems. IV. Extended Coupled-Pair Many-Electron Theory and Its Application to the BH_3 Molecule. *Physical Review A*, **5**: 50 – 67, 1972. doi: `10.1103/PhysRevA.5.50` (see p. 18)

[28] J. A. Pople, R. Krishnan, H. B. Schlegel, and J. S. Binkley. Electron correlation theories and their application to the study of simple reaction potential surfaces. *International Journal of Quantum Chemistry*, **14**: 545 – 560, 1978. doi: `10.1002/qua.560140503` (see p. 18)

[29] R. J. Bartlett and G. D. Purvis. Many-body perturbation theory, coupled-pair many-electron theory, and the importance of quadruple excitations for the correlation problem. *International Journal of Quantum Chemistry*, **14**: 561 – 581, 1978. doi: `10.1002/qua.560140504` (see p. 18)

[30] T. D. Crawford and H. F. Schaefer. An Introduction to Coupled Cluster Theory for Computational Chemists. *Reviews in Computational Chemistry*, **14**: 33 – 136, 2000. doi: `10.1002/9780470125915.ch2` (see p. 18)

[31] T. Kato. On the eigenfunctions of many-particle systems in quantum mechanics. *Communications on Pure and Applied Mathematics*, **10**: 151 – 177, 1957. doi: `10.1002/cpa.3160100201` (see p. 21)

[32] E. A. Hylleraas. Neue Berechnung der Energie des Heliums im Grundzustande, sowie des tiefsten Terms von Ortho-Helium. *Zeitschrift für Physik*, **54**: 347 – 366, 1929. doi: `10.1007/BF01375457` (see p. 21)

[33] W. Kutzelnigg and W. Klopper. Wave functions with terms linear in the interelectronic coordinates to take care of the correlation cusp. I. General theory. *The Journal of Chemical Physics*, **94**: 1985 – 2001, 1991. doi: `10.1063/1.459921` (see p. 21)

[34] S. F. Boys. The Integral Formulae for the Variational Solution of the Molecular Many-Electron Wave Equations in Terms of Gaussian Functions with Direct Electronic Correlation. *Proceedings of the Royal Society A: Mathematical, Physical and Engineering Sciences*, **258**: 402 – 411, 1960. DOI: `10.1098/rspa.1960.0195` (see p. 21)

[35] K. Singer. The Use of Gaussian (Exponential Quadratic) Wave Functions in Molecular Problems. I. General Formulae for the Evaluation of Integrals. *Proceedings of the Royal Society of London, Series A: Mathematical and Physical Sciences*, **258**: 412 – 420, 1960. DOI: `10.1098/rspa.1960.0196` (see p. 21)

[36] K. A. Peterson, T. B. Adler, and H.-J. Werner. Systematically convergent basis sets for explicitly correlated wavefunctions: The atoms H, He, B–Ne, and Al–Ar. *The Journal of Chemical Physics*, **128**: 084102, 084102, 2008. DOI: `10.1063/1.2831537` (see pp. 21, 81 – 83)

[37] R. G. Parr and W. Yang. *Density-Functional Theory of Atoms and Molecules*. International Series of Monographs on Chemistry Oxford University Press, USA, 1989. (see p. 22)

[38] W. Koch and M. Holthausen. *A chemist's guide to density functional theory*. Wiley-VCH, 2000. (see p. 22)

[39] K. Burke. *The ABC of DFT*. University of California, 2007. (see p. 22)

[40] P. Hohenberg and W. Kohn. Inhomogeneous Electron Gas. *Physical Review*, **136**: B864 – B871, 1964. DOI: `10.1103/PhysRev.136.B864` (see pp. 22, 23)

[41] J. P. Perdew and K. Schmidt. Jacob's ladder of density functional approximations for the exchange-correlation energy. *AIP Conference Proceedings*, **577**: 1 – 20, 2001. DOI: `10.1063/1.1390175` (see pp. 25, 26)

[42] P. A. M. Dirac. Note on Exchange Phenomena in the Thomas Atom. *Mathematical Proceedings of the Cambridge Philosophical Society*, **26**: 376 – 385, 1930. DOI: `10.1017/S0305004100016108` (see p. 25)

[43] S. H. Vosko, L. Wilk, and M. Nusair. Accurate spin-dependent electron liquid correlation energies for local spin density calculations: a critical analysis. *Canadian Journal of Physics*, **58**: 1200 – 1211, 1980. DOI: `10.1139/p80-159` (see p. 25)

[44] J. P. Perdew and Y. Wang. Accurate and simple analytic representation of the electron-gas correlation energy. *Physical Review B*, **45**: 13244 – 13249, 1992. DOI: `10.1103/PhysRevB.45.13244` (see p. 25)

[45] A. D. Becke. Density-functional exchange-energy approximation with correct asymptotic behavior. *Physical Review A*, **38**: 3098 – 3100, 1988. DOI: `10.1103/PhysRevA.38.3098` (see p. 26)

[46] J. P. Perdew. Density-functional approximation for the correlation energy of the inhomogeneous electron gas. *Physical Review B*, **33**: 8822 – 8824, 1986. doi: `10.1103/PhysRevB.33.8822` (see p. 26)

[47] C. Lee, W. Yang, and R. G. Parr. Development of the Colle-Salvetti correlation-energy formula into a functional of the electron density. *Physical Review B*, **37**: 785 – 789, 1988. doi: `10.1103/PhysRevB.37.785` (see p. 26)

[48] R. Feynman. Forces in Molecules. *Physical Review*, **56**: 340 – 343, 1939. doi: `10.1103/PhysRev.56.340` (see pp. 26, 130)

[49] S. Grimme. Semiempirical hybrid density functional with perturbative second-order correlation. *The Journal of Chemical Physics*, **124**: 034108, 034108, 2006. doi: `10.1063/1.2148954` (see p. 26)

[50] L. Goerigk and S. Grimme. A thorough benchmark of density functional methods for general main group thermochemistry, kinetics, and noncovalent interactions. *Physical Chemistry Chemical Physics*, **13**: 6670 – 6688, 2011. doi: `10.1039/C0CP02984J` (see p. 26)

[51] P. W. Atkins and R. Friedman. *Molecular Quantum Mechanics*. Oxford University Press, 2005. (see p. 27)

[52] E. B. Wilson, J. C. Decius, and P. C. Cross. *Molecular Vibrations: The Theory of Infrared and Raman Vibrational Spectra*. Dover Books on Chemistry Series Dover Publications, 1955. (see pp. 27, 31)

[53] H. P. Figeys and P. Geerlings. ‘Some Aspects of the Quantumchemical Interpretation of Integrated Intensities of Infrared Absorption Bands’ English in: *Theoretical Models of Chemical Bonding* ed. by Z. B. Maksić. Springer Berlin Heidelberg, 1991. 25 – 62 doi: `10.1007/978-3-642-58179-3_2` (see pp. 28, 29)

[54] J. E. Del Bene and M. J. T. Jordan. Vibrational spectroscopy of the hydrogen bond: An ab initio quantum-chemical perspective. *International Reviews in Physical Chemistry*, **18**: 119 – 162, 1999. doi: `10.1080/014423599230026` (see p. 29)

[55] J. K. Watson. Simplification of the molecular vibration-rotation hamiltonian. *Molecular Physics*, **15**: 479 – 490, 1968. doi: `10.1080/00268976800101381` (see p. 30)

[56] D. Papoušek and M. R. Aliev. *Molecular Vibrational-rotational Spectra: Theory and Applications of High Resolution Infrared, Microwave, and Raman Spectroscopy of Polyatomic Molecules*. Studies in physical and theoretical chemistry 17 Elsevier Scientific Publishing Company, 1982. (see p. 30)

[57] R. D. Amos, N. C. Handy, W. H. Green, D. Jayatilaka, A. Willetts, and P. Palmieri. Anharmonic vibrational properties of CH_2F_2 : A comparison of theory and experiment. *The Journal of Chemical Physics*, **95**: 8323 – 8336, 1991. doi: `10.1063/1.461259` (see p. 30)

[58] J. Vázquez and J. F. Stanton. Simple(r) algebraic equation for transition moments of fundamental transitions in vibrational second-order perturbation theory. *Molecular Physics*, **104**: 377 – 388, 2006. doi: `10.1080/00268970500290367` (see pp. 30, 105, 112)

[59] J. Breidung, W. Thiel, J. Gauss, and J. F. Stanton. Anharmonic force fields from analytic CCSD(T) second derivatives: HOF and F_2O. *The Journal of Chemical Physics*, **110**: 3678 – 3696, 1999. doi: `10.1063/1.478258` (see pp. 30, 106)

[60] J. M. Bowman. Self-consistent field energies and wavefunctions for coupled oscillators. *The Journal of Chemical Physics*, **68**: 608 – 610, 1978. doi: `10.1063/1.435782` (see p. 30)

[61] R. Gerber and M. Ratner. A semiclassical self-consistent field (SC SCF) approximation for eigenvalues of coupled-vibration systems. *Chemical Physics Letters*, **68**: 195 – 198, 1979. doi: `10.1016/0009-2614(79)80099-8` (see p. 30)

[62] P. Jensen and P. R. Bunker. *Computational Molecular Spectroscopy*. Wiley, 2000. (see p. 30)

[63] J. M. Bowman, K. Christoffel, and F. Tobin. Application of SCF-SI theory to vibrational motion in polyatomic molecules. *The Journal of Physical Chemistry*, **83**: 905 – 912, 1979. doi: `10.1021/j100471a005` (see p. 30)

[64] H. Romanowski, J. M. Bowman, and L. B. Harding. Vibrational energy levels of formaldehyde. *The Journal of Chemical Physics*, **82**: 4155 – 4165, 1985. doi: `10.1063/1.448858` (see p. 30)

[65] F. Culot and J. Liévin. A multiconfigurational SCF computational method for the resolution of the vibrational Schrödinger equation in polyatomic molecules. *Theoretica chimica acta*, **89**: 227 – 250, 1994. doi: `10.1007/BF01225116` (see p. 30)

[66] F. Culot, F. Laruelle, and J. Liévin. A vibrational CASSCF study of stretch-bend interactions and their influence on infrared intensities in the water molecule. *Theoretica chimica acta*, **92**: 211 – 226, 1995. doi: `10.1007/BF01125947` (see p. 31)

[67] J. O. Jung and R. B. Gerber. Vibrational wave functions and spectroscopy of $(H_2O)_n$, $n = 2, 3, 4, 5$: Vibrational self-consistent field with correlation corrections. *The Journal of Chemical Physics*, **105**: 10332 – 10348, 1996. doi: `10.1063/1.472960` (see p. 31)

[68] O. Christiansen. Vibrational coupled cluster theory. *The Journal of Chemical Physics*, **120**: 2149 – 2159, 2004. doi: `10.1063/1.1637579` (see p. 31)

[69] O. Christiansen. Vibrational structure theory: new vibrational wave function methods for calculation of anharmonic vibrational energies and vibrational contributions to molecular properties. *Physical Chemistry Chemical Physics*, **9**: 2942 – 2953, 2007. doi: `10.1039/B618764A` (see p. 31)

[70] O. S. Mortensen, B. R. Henry, and M. A. Mohammadi. The effects of symmetry within the local mode picture: A reanalysis of the overtone spectra of the dihalomethanes. *The Journal of Chemical Physics*, **75**: 4800 – 4808, 1981. doi: `10.1063/1.441916` (see p. 31)

[71] M. S. Child and R. T. Lawton. Local and normal vibrational states: a harmonically coupled anharmonic-oscillator model. *Faraday Discussions of the Chemical Society*, **71**: 273 – 285, 1981. doi: `10.1039/DC9817100273` (see p. 31)

[72] H. G. Kjærgaard, H. Yu, B. J. Schattka, B. R. Henry, and A. W. Tarr. Intensities in local mode overtone spectra: Propane. *The Journal of Chemical Physics*, **93**: 6239 – 6248, 1990. doi: `10.1063/1.458993` (see p. 31)

[73] B. R. Henry and H. G. Kjærgaard. Local modes. *Canadian Journal of Chemistry*, **80**: 1635 – 1642, 2002. doi: `10.1139/v02-188` (see p. 31)

[74] R. Meyer and E. B. Wilson. Rotational Constants of Torsionally Excited Molecules. *The Journal of Chemical Physics*, **53**: 3969 – 3980, 1970. doi: `10.1063/1.1673867` (see pp. 31, 116)

[75] H. M. Pickett. Vibration—Rotation Interactions and the Choice of Rotating Axes for Polyatomic Molecules. *The Journal of Chemical Physics*, **56**: 1715 – 1723, 1972. doi: `10.1063/1.1677430` (see p. 31)

[76] P. Piecuch, S. A. Kucharski, K. Kowalski, and M. Musiał. Efficient computer implementation of the renormalized coupled-cluster methods: The R-CCSD[T], R-CCSD(T), CR-CCSD[T], and CR-CCSD(T) approaches. *Computer Physics Communications*, **149**: 71 – 96, 2002. doi: `10.1016/S0010-4655(02)00598-2` (see p. 31)

[77] D. A. Matthews, J. Vázquez, and J. F. Stanton. Calculated stretching overtone levels and Darling–Dennison resonances in water: a triumph of simple theoretical approaches. *Molecular Physics*, **105**: 2659 – 2666, 2007. doi: `10.1080/00268970701618424` (see pp. 31, 32)

[78] V. Barone. Anharmonic vibrational properties by a fully automated second-order perturbative approach. *The Journal of Chemical Physics*, **122**: 014108, 2005. doi: `10.1063/1.1824881` (see p. 32)

[79] E. Fermi. Über den Ramaneffekt des Kohlendioxyds. *Zeitschrift für Physik*, **71**: 250 – 259, 1931. doi: `10.1007/BF01341712` (see pp. 32, 107)

[80] B. T. Darling and D. M. Dennison. The Water Vapor Molecule. *Physical Review*, **57**: 128–139, 1940. doi: `10.1103/PhysRev.57.128` (see pp. 32, 107)

[81] S. Califano. *Vibrational states*. Wiley, 1976. (see p. 32)

[82] D. Matthews and J. F. Stanton. Quantitative analysis of Fermi resonances by harmonic derivatives of perturbation theory corrections. *Molecular Physics*, **107**: 213–222, 2009. doi: `10.1080/00268970902769463` (see pp. 32, 106, 112, 118)

[83] J. Franck and E. G. Dymond. Elementary processes of photochemical reactions. *Trans. Faraday Soc.*, **21**: 536–542, 1926. doi: `10.1039/TF9262100536` (see p. 32)

[84] E. Condon. A Theory of Intensity Distribution in Band Systems. *Phys. Rev.*, **28**: 1182–1201, 1926. doi: `10.1103/PhysRev.28.1182` (see p. 32)

[85] E. U. Condon. Nuclear Motions Associated with Electron Transitions in Diatomic Molecules. *Phys. Rev.*, **32**: 858–872, 1928. doi: `10.1103/PhysRev.32.858` (see p. 32)

[86] E. Hutchisson. Band Spectra Intensities for Symmetrical Diatomic Molecules. *Phys. Rev.*, **36**: 410–420, 1930. doi: `10.1103/PhysRev.36.410` (see p. 33)

[87] H. Kupka and P. H. Cribb. Multidimensional Franck–Condon integrals and Duschinsky mixing effects. *The Journal of Chemical Physics*, **85**: 1303–1315, 1986. doi: `10.1063/1.451216` (see pp. 33, 85)

[88] F. Duschinsky. On the interpretation of electronic spectra of polyatomic molecules. *Acta Physicochimica URSS*, **7**: Translation by Christian W. Müller `http://www.ruhr-uni-bochum.de/pc2/mam/duschinsky_translation.pdf`, 551–566, 1937. (see pp. 33, 85)

[89] C. Melania Oana and A. I. Krylov. Dyson orbitals for ionization from the ground and electronically excited states within equation-of-motion coupled-cluster formalism: Theory, implementation, and examples. *The Journal of Chemical Physics*, **127**: 234106, 234106, 2007. doi: `10.1063/1.2805393` (see p. 33)

[90] W. Demtröder. *Laser Spectroscopy Vol.2: Experimental techniques*. Laser Spectroscopy Springer, 2008. (see pp. 34, 35)

[91] J. Koperski and E. S. Fry. Molecules in the cold environment of a supersonic free-jet beam: from spectroscopy of neutral–neutral interactions to a test of Bell's inequality. *Journal of Physics B: Atomic, Molecular and Optical Physics*, **39**: S1125–S1150, 2006. doi: `10.1088/0953-4075/39/19/S22` (see p. 35)

[92] C. Vallence 'Molecular Reaction Dynamics Lectures 1–4' Accessed on 01/03/2013 (see p. 35)

[93] M. D. Morse. 'Supersonic Beam Sources' in: *Atomic, Molecular, and Optical Physics: Atoms and Molecules* ed. by F. Dunning and R. G. Hulet. vol. 29, Part B Experimental Methods in the Physical Sciences Academic Press, 1996. chap. 2, 21 – 47 doi: `10.1016/S0076-695X(08)60784-X` (see p. 36)

[94] J. P. Toennies and K. Winkelmann. Theoretical studies of highly expanded free jets: Influence of quantum effects and a realistic intermolecular potential. *The Journal of Chemical Physics*, **66**: 3965 – 3979, 1977. doi: `10.1063/1.434448` (see p. 36)

[95] T. Märk. 'Ionization of Molecules by Electron Impact' in: *Electron-Molecule Interactions and their Applications* ed. by L. Christophorou. Academic Press, 1984. chap. 3, 251 – 334 doi: `10.1016/B978-0-12-174401-4.50008-0` (see p. 37)

[96] L. Christophorou, D. McCorkle, and A. Christodoulides. 'Electron Attachment Processes' in: *Electron-Molecule Interactions and their Applications* ed. by L. Christophorou. Academic Press, 1984. chap. 6, 477 – 617 doi: `10.1016/B978-0-12-174401-4.50011-0` (see p. 37)

[97] A. E. Cameron and D. F. Eggers. An Ion "Velocitron". *Review of Scientific Instruments*, **19**: 605 – 607, 1948. doi: `10.1063/1.1741336` (see p. 38)

[98] W. C. Wiley and I. H. McLaren. Time-of-Flight Mass Spectrometer with Improved Resolution. *Review of Scientific Instruments*, **26**: 1150 – 1157, 1955. doi: `10.1063/1.1715212` (see p. 38)

[99] M. Guilhaus. Special feature: Tutorial. Principles and instrumentation in time-of-flight mass spectrometry. Physical and instrumental concepts. *Journal of Mass Spectrometry*, **30**: 1519 – 1532, 1995. doi: `10.1002/jms.1190301102` (see p. 38)

[100] B. Brehm, M. Gusinow, and J. Hall. Electron Affinity of Helium Via Laser Photodetachment of its Negative Ion. *Physical Review Letters*, **19**: 737 – 741, 1967. doi: `10.1103/PhysRevLett.19.737` (see pp. 40, 48)

[101] P. Kruit and F. H. Read. Magnetic field paralleliser for 2π electron-spectrometer and electron-image magnifier. *Journal of Physics E: Scientific Instruments*, **16**: 313 – 324, 1983. doi: `10.1088/0022-3735/16/4/016` (see p. 41)

[102] O. Cheshnovsky, S. H. Yang, C. L. Pettiette, M. J. Craycraft, and R. E. Smalley. Magnetic time-of-flight photoelectron spectrometer for mass-selected negative cluster ions. *Review of Scientific Instruments*, **58**: 2131 – 2137, 1987. doi: `10.1063/1.1139475` (see pp. 41, 42)

[103] K. Müller-Dethlefs, M. Sander, and E. W. Schlag. Two-colour photoionization resonance spectroscopy of NO: Complete separation of rotational levels of NO^+ at the ionization threshold. *Chemical Physics Letters*, **112**: 291 – 294, 1984. doi: `10.1016/0009-2614(84)85743-7` (see p. 43)

[104] K. Müller-Dethlefs and E. W. Schlag. High-Resolution Zero Kinetic Energy (ZEKE) Photoelectron Spectroscopy of Molecular Systems. *Annual Review of Physical Chemistry*, **42**: 109 – 136, 1991. doi: `10.1146/annurev.pc.42.100191.000545` (see p. 43)

[105] T. Kitsopoulos, I. Waller, J. Loeser, and D. Neumark. High resolution threshold photodetachment spectroscopy of negative ions. *Chemical Physics Letters*, **159**: 300 – 306, 1989. doi: `10.1016/0009-2614(89)87488-3` (see p. 43)

[106] I. M. Waller, T. N. Kitsopoulos, and D. M. Neumark. Threshold photodetachment spectroscopy of the iodine atom + hydrogen iodide transition-state region. *The Journal of Physical Chemistry*, **94**: 2240 – 2242, 1990. doi: `10.1021/j100369a009` (see p. 43)

[107] C. Bässmann, U. Boesl, D. Yang, G. Drechsler, and E. Schlag. Mass selective anion-ZEKE spectroscopy of the iodine-water cluster. *International Journal of Mass Spectrometry and Ion Processes*, **159**: Special Issue: Ion Spectroscopy, 153 – 167, 1996. doi: `10.1016/S0168-1176(96)04448-5` (see p. 43)

[108] V. Distelrath and U. Boesl. Mass selective gas phase study of ClO, OClO, ClOO and ClAr by anion-ZEKE-photoelectron spectroscopy. *Faraday Discussions*, **115**: 161 – 174, 2000. doi: `10.1039/A909618C` (see p. 43)

[109] G. F. Gantefor, D. M. Cox, and A. Kaldor. High resolution photodetachment spectroscopy of jet-cooled metal cluster anions: Au_2^- and Ag_3^-. *The Journal of Chemical Physics*, **93**: 8395 – 8396, 1990. doi: `10.1063/1.459272` (see p. 43)

[110] T. Lenzer, I. Yourshaw, M. R. Furlanetto, G. Reiser, and D. M. Neumark. Zero electron kinetic energy spectroscopy of the $ArCl^-$ anion. *The Journal of Chemical Physics*, **110**: 9578 – 9586, 1999. doi: `10.1063/1.478923` (see p. 43)

[111] F. Schlicht, M. Entfellner, and U. Boesl. Anion ZEKE-Spectroscopy of the Weakly Bound Iodine Water Complex†. *The Journal of Physical Chemistry A*, **114**: 11125 – 11132, 2010. doi: `10.1021/jp102508f` (see p. 43)

[112] D. M. Neumark. Slow Electron Velocity-Map Imaging of Negative Ions: Applications to Spectroscopy and Dynamics†. *The Journal of Physical Chemistry A*, **112**: 13287 – 13301, 2008. doi: `10.1021/jp807182q` (see pp. 43, 44)

[113] E. Wigner. On the Behavior of Cross Sections Near Thresholds. *Physical Review*, **73**: 1002–1009, 1948. doi: `10.1103/PhysRev.73.1002` (see p. 43)

[114] I. Wolf, S. Ronen, R. Giniger, and O. Cheshnovsky. A new action photoelectron spectroscopy for anions. *The Journal of Chemical Physics*, **122**: 141101, 2005. doi: `10.1063/1.1890885` (see p. 43)

[115] T. Suzuki and B. J. Whitaker. Non-adiabatic effects in chemistry revealed by time-resolved charged-particle imaging. *International Reviews in Physical Chemistry*, **20**: 313–356, 2001. doi: `10.1080/01442350110045046` (see p. 44)

[116] A. Stolow, A. E. Bragg, and D. M. Neumark. Femtosecond Time-Resolved Photoelectron Spectroscopy. *Chemical Reviews*, **104**: PMID: 15080710, 1719–1758, 2004. doi: `10.1021/cr020683w` (see p. 44)

[117] M. N. R. Ashfold, N. H. Nahler, A. J. Orr-Ewing, O. P. J. Vieuxmaire, R. L. Toomes, T. N. Kitsopoulos, I. A. Garcia, D. A. Chestakov, S.-M. Wu, and D. H. Parker. Imaging the dynamics of gas phase reactions. *Physical Chemistry Chemical Physics*, **8**: 26–53, 2006. doi: `10.1039/B509304J` (see p. 44)

[118] A. Sanov and R. Mabbs. Photoelectron imaging of negative ions. *International Reviews in Physical Chemistry*, **27**: 53–85, 2008. doi: `10.1080/01442350701786512` (see p. 44)

[119] S. Cavanagh, S. Gibson, M. Gale, C. Dedman, E. Roberts, and B. Lewis. High-resolution velocity-map-imaging photoelectron spectroscopy of the O^- photodetachment fine-structure transitions. *Physical Review A*, **76**: 052708, 2007. doi: `10.1103/PhysRevA.76.052708` (see pp. 44, 57, 64)

[120] A. Osterwalder, M. J. Nee, J. Zhou, and D. M. Neumark. High resolution photodetachment spectroscopy of negative ions via slow photoelectron imaging. *The Journal of Chemical Physics*, **121**: 6317–6322, 2004. doi: `10.1063/1.1787491` (see p. 44)

[121] E. W. Hansen and P.-L. Law. Recursive methods for computing the Abel transform and its inverse. *Journal of the Optical Society of America A*, **2**: 510–519, 1985. doi: `10.1364/JOSAA.2.000510` (see p. 44)

[122] V. Dribinski, A. Ossadtchi, V. A. Mandelshtam, and H. Reisler. Reconstruction of Abel-transformable images: The Gaussian basis-set expansion Abel transform method. *Review of Scientific Instruments*, **73**: 2634–2642, 2002. doi: `10.1063/1.1482156` (see p. 45)

[123] B. Dick. Inverting ion images without Abel inversion: maximum entropy reconstruction of velocity maps. *Physical Chemistry Chemical Physics*, **16**: 570–580, 2013. doi: `10.1039/C3CP53673D` (see pp. 45, 70)

[124] K. M. Ervin, J. Ho, and W. C. Lineberger. Ultraviolet photoelectron spectrum of nitrite anion. *The Journal of Physical Chemistry*, **92**: 5405 – 5412, 1988. doi: `10.1021/j100330a017` (see p. 48)

[125] G. Markovich, S. Pollack, R. Giniger, and O. Cheshnovsky. Photoelectron spectroscopy of Cl^-, Br^- and I^- solvated in water clusters. *The Journal of Chemical Physics*, **101**: 9344 – 9353, 1994. doi: `10.1063/1.467965` (see p. 48)

[126] A. W. Castleman and K. H. Bowen. Clusters: Structure, Energetics, and Dynamics of Intermediate States of Matter. *The Journal of Physical Chemistry*, **100**: 12911 – 12944, 1996. doi: `10.1021/jp961030k` (see p. 48)

[127] R. LaMacchia. *Towards Anion Photoelectron Spectroscopy of Complexes and Clusters*. MA thesis. University of Western Australia, 2008. (see pp. 48, 49, 59)

[128] K. Lapere, R. LaMacchia, L. Quak, A. McKinley, and D. Wild. Anion photoelectron spectroscopy and ab initio calculations of the gas phase chloride-carbon monoxide complex: $Cl^- \cdots CO$. *Chemical Physics Letters*, **504**: 13 – 19, 2011. doi: `10.1016/j.cplett.2011.01.034` (see p. 48)

[129] K. M. Lapere, R. J. LaMacchia, L. H. Quak, M. Kettner, S. G. Dale, A. J. McKinley, and D. A. Wild. The Bromide–Carbon Monoxide Gas Phase Complex: Anion Photoelectron Spectroscopy and Ab Initio Calculations. *Australian Journal of Chemistry*, **65**: 457 – 463, 2012. doi: `10.1071/CH12007` (see p. 48)

[130] K. M. Lapere, R. J. LaMacchia, L. H. Quak, M. Kettner, S. G. Dale, A. J. McKinley, and D. A. Wild. Anion Photoelectron Spectra and Ab Initio Calculations of the Iodide–Carbon Monoxide Clusters: $I^- \ldots (CO)_n$, n = 1-4. *The Journal of Physical Chemistry A*, **116**: 3577 – 3584, 2012. doi: `10.1021/jp300471x` (see pp. 48, 56)

[131] D. Beckham, S. Conran, K. Lapere, M. Kettner, A. McKinley, and D. Wild. Anion photoelectron spectroscopy and high level ab initio calculations of the halide-acetylene dimer complexes. *Chemical Physics Letters*, **619**: 241 – 246, 2015. doi: `10.1016/j.cplett.2014.11.058` (see p. 48)

[132] K. M. L. Lapere. *Anion photoelectron spectroscopy of halide complexes and clusters*. PhD thesis. University of Western Australia: School of Chemistry and Biochemistry, 2014. (see p. 50)

[133] J. F. Archard and A. M. Taylor. Improved Glan–Foucault Prism. *Journal of Scientific Instruments*, **25**: 407 – 409, 1948. doi: `10.1088/0950-7671/25/12/304` (see p. 53)

[134] R. J. Peláez, C. Blondel, C. Delsart, and C. Drag. Pulsed photodetachment microscopy and the electron affinity of iodine. *Journal of Physics B: Atomic, Molecular and Optical Physics*, **42**: 125001, 2009. doi: `10.1088/0953-4075/42/12/125001` (see pp. 56, 67)

[135] K. M. Ervin, I. Anusiewicz, P. Skurski, J. Simons, and W. C. Lineberger. The only stable state of O_2^- is the X $^2\Pi_g$ Ground State and it (still!) has an adiabatic electron detachment Energy of 0.45 eV. *The Journal of Physical Chemistry A*, **107**: 8521 – 8529, 2003. doi: `10.1021/jp0357323` (see p. 56)

[136] M. Kopczynski. *Femtosekunden Photodetachment-Photoelektronenspektroskopie an isolierten und massenselektierten Halogen-Edelgas-Clustern*. PhD thesis. Georg-August-Universität Göttingen, 2010. (see p. 59)

[137] A. Mager. Magnetic shields. *IEEE Transactions on Magnetics*, **6**: 67 – 75, 1970. doi: `10.1109/TMAG.1970.1066714` (see p. 63)

[138] D. Dubbers. Simple formula for multiple mu-metal shields. *Nuclear Instruments and Methods in Physics Research Section A: Accelerators, Spectrometers, Detectors and Associated Equipment*, **243**: 511 – 517, 1986. doi: `10.1016/0168-9002(86)90989-7` (see p. 63)

[139] D. C. McGilvery and D. A. Dahl *Simion 8.1.1.1* 2012 (see p. 65)

[140] U. Berzinsh, M. Gustafsson, D. Hanstorp, A. Klinkmüller, U. Ljungblad, and A.-M. Mårtensson-Pendrill. Isotope shift in the electron affinity of chlorine. *Phys. Rev. A*, **51**: 231 – 238, 1995. doi: `10.1103/PhysRevA.51.231` (see p. 67)

[141] H. Uehara and K. Horiai. Infrared-microwave double resonance of atomic chlorine on laser-magnetic-resonance fine-structure transitions. *Journal of the Optical Society of America B*, **4**: 1217 – 1221, 1987. doi: `10.1364/JOSAB.4.001217` (see p. 67)

[142] C. Blondel, P. Cacciani, C. Delsart, and R. Trainham. High-resolution determination of the electron affinity of fluorine and bromine using crossed ion and laser beams. *Phys. Rev. A*, **40**: 3698 – 3701, 1989. doi: `10.1103/PhysRevA.40.3698` (see p. 67)

[143] A. I. Chichinin. Chemical Properties of Electronically Excited Halogen Atoms $X(^2P_{1/2})$ (X=F,Cl,Br,I). *Journal of Physical and Chemical Reference Data*, **35**: 869 – 928, 2006. doi: `10.1063/1.2137724` (see p. 67)

[144] J. R. Gascooke. *Energy transfer in polyatomic rare gas collisions and van der Waals molecule dissociation*. PhD thesis. Flinders University of South Australia, 2000. (see pp. 68, 70)

[145] R. J. Bentley-Moyse. *Towards velocity map imaging: Implementation of a self-centering inverse Abel transform script*. MA thesis. University of Western Australia, 2014. (see p. 70)

[146] R. Criegee and G. Wenner. Die Ozonisierung des 9,10-Oktalins. *Justus Liebigs Annalen der Chemie*, **564**: 9 – 15, 1949. doi: `10.1002/jlac.19495640103` (see p. 76)

[147] G. T. Drozd, J. Kroll, and N. M. Donahue. 2,3-Dimethyl-2-butene (TME) Ozonolysis: Pressure Dependence of Stabilized Criegee Intermediates and Evidence of Stabilized Vinyl Hydroperoxides. *The Journal of Physical Chemistry A*, **115**: 161 – 166, 2011. doi: `10.1021/jp108773d` (see pp. 76, 77)

[148] D. Johnson and G. Marston. The gas-phase ozonolysis of unsaturated volatile organic compounds in the troposphere. *Chemical Society Reviews*, **37**: 699 – 716, 2008. doi: `10.1039/B704260B` (see p. 76)

[149] R. Gutbrod, R. N. Schindler, E. Kraka, and D. Cremer. Formation of OH radicals in the gas phase ozonolysis of alkenes: the unexpected role of carbonyl oxides. *Chemical Physics Letters*, **252**: 221 – 229, 1996. doi: `10.1016/0009-2614(96)00126-1` (see p. 76)

[150] R. Gutbrod, E. Kraka, R. N. Schindler, and D. Cremer. Kinetic and Theoretical Investigation of the Gas-Phase Ozonolysis of Isoprene: Carbonyl Oxides as an Important Source for OH Radicals in the Atmosphere. *Journal of the American Chemical Society*, **119**: 7330 – 7342, 1997. doi: `10.1021/ja970050c` (see pp. 76, 78, 97)

[151] Y.-T. Su, H.-Y. Lin, R. Putikam, H. Matsui, M. C. Lin, and Y.-P. Lee. Extremely rapid self-reaction of the simplest Criegee intermediate CH_2OO and its implications in atmospheric chemistry. *Nature Chemistry*, **6**: 477 – 483, 2014. doi: `10.1038/nchem.1890` (see p. 77)

[152] O. Welz, J. D. Savee, D. L. Osborn, S. S. Vasu, C. J. Percival, D. E. Shallcross, and C. A. Taatjes. Direct Kinetic Measurements of Criegee Intermediate (CH_2OO) Formed by Reaction of CH_2I with O_2. *Science*, **335**: 204 – 207, 2012. doi: `10.1126/science.1213229` (see pp. 77, 78)

[153] H. G. Kjærgaard, T. Kurtén, L. B. Nielsen, S. Jørgensen, and P. O. Wennberg. Criegee Intermediates React with Ozone. *The Journal of Physical Chemistry Letters*, **4**: 2525 – 2529, 2013. doi: `10.1021/jz401205m` (see p. 77)

[154] T. Berndt, T. Jokinen, M. Sipilä, R. L. M. III, H. Herrmann, F. Stratmann, H. Junninen, and M. Kulmala. H_2SO_4 formation from the gas-phase reaction of stabilized Criegee Intermediates with SO_2: Influence of water vapour content and temperature. *Atmospheric Environment*, **89**: 603 – 612, 2014. doi: `10.1016/j.atmosenv.2014.02.062` (see p. 77)

[155] C. A. Taatjes, O. Welz, A. J. Eskola, J. D. Savee, A. M. Scheer, D. E. Shallcross, B. Rotavera, E. P. F. Lee, J. M. Dyke, D. K. W. Mok, D. L. Osborn, and C. J. Percival. Direct Measurements of Conformer-Dependent Reactivity of the Criegee Intermediate CH_3CHOO. *Science*, **340**: 177 – 180, 2013. doi: `10.1126/science.1234689` (see pp. 77, 78)

[156] L. Vereecken and J. S. Francisco. Theoretical studies of atmospheric reaction mechanisms in the troposphere. *Chemical Society Reviews*, **41**: 6259 – 6293, 2012. doi: `10.1039/C2CS35070J` (see pp. 77, 78)

[157] N. M. Donahue, G. T. Drozd, S. A. Epstein, A. A. Presto, and J. H. Kroll. Adventures in Ozoneland: Down the Rabbit-hole. *Physical Chemistry Chemical Physics*, **13**: 10848 – 10857, 2011. doi: `10.1039/C0CP02564J` (see p. 77)

[158] W. H. Bunnelle. Preparation, properties, and reactions of carbonyl oxides. *Chemical Reviews*, **91**: 335 – 362, 1991. doi: `10.1021/cr00003a003` (see p. 77)

[159] C. A. Taatjes, G. Meloni, T. M. Selby, A. J. Trevitt, D. L. Osborn, C. J. Percival, and D. E. Shallcross. Direct Observation of the Gas-Phase Criegee Intermediate (CH_2OO). *Journal of the American Chemical Society*, **130**: 11883 – 11885, 2008. doi: `10.1021/ja804165q` (see p. 77)

[160] J. M. Beames, F. Liu, L. Lu, and M. I. Lester. Ultraviolet Spectrum and Photochemistry of the Simplest Criegee Intermediate CH2OO. *Journal of the American Chemical Society*, **134**: 20045 – 20048, 2012. doi: `10.1021/ja310603j` (see p. 78)

[161] M. Nakajima, Q. Yue, J. Li, H. Guo, and Y. Endo. An experimental and theoretical study on rotational constants of vibrationally excited CH_2OO. *Chemical Physics Letters*, **621**: 129 – 133, 2015. doi: `10.1016/j.cplett.2014.12.039` (see pp. 78, 106)

[162] M. Nakajima and Y. Endo. Communication: Spectroscopic characterization of an alkyl substituted Criegee intermediate syn-CH_3CHOO through pure rotational transitions. *The Journal of Chemical Physics*, **140**: 011101, 2014. doi: `10.1063/1.4861494` (see pp. 78, 95, 117, 122, 137)

[163] M. Nakajima, Q. Yue, and Y. Endo. Fourier-transform microwave spectroscopy of an alkyl substituted Criegee intermediate anti-CH_3CHOO. *Journal of Molecular Spectroscopy*, **310**: Spectroscopy of Radicals and Ions in Memory of Marilyn Jacox, 109 – 112, 2015. doi: `10.1016/j.jms.2014.11.004` (see pp. 78, 95, 137)

[164] F. Liu, J. M. Beames, A. S. Petit, A. B. McCoy, and M. I. Lester. Infrared-driven unimolecular reaction of CH_3CHOO Criegee intermediates to OH radical products. *Science*, **345**: 1596 – 1598, 2014. doi: `10.1126/science.1257158` (see p. 78)

[165] D.-C. Fang and X.-Y. Fu. CASSCF and CAS+1 + 2 Studies on the Potential Energy Surface and the Rate Constants for the Reactions between CH_2 and O_2. *The Journal of Physical Chemistry A*, **106**: 2988 – 2993, 2002. doi: `10.1021/jp014129m` (see pp. 78, 79, 86)

[166] M. T. Nguyen, T. L. Nguyen, V. T. Ngan, and H. M. T. Nguyen. Heats of formation of the Criegee formaldehyde oxide and dioxirane. *Chemical Physics Letters*, **448**: 183 – 188, 2007. DOI: `10.1016/j.cplett.2007.10.033` (see pp. 78, 86 – 88, 90)

[167] J. M. L. Martin and G. de Oliveira. Towards standard methods for benchmark quality ab initio thermochemistry—W1 and W2 theory. *The Journal of Chemical Physics*, **111**: 1843 – 1856, 1999. DOI: `10.1063/1.479454` (see pp. 78, 80)

[168] A. Karton, M. Kettner, and D. A. Wild. Sneaking up on the Criegee intermediate from below: Predicted photoelectron spectrum of the CH_2OO^- anion and W3-F12 electron affinity of CH_2OO. *Chemical Physics Letters*, **585**: 15 – 20, 2013. DOI: `10.1016/j.cplett.2013.08.075` (see pp. 79, 85)

[169] J. Li, S. Carter, J. M. Bowman, R. Dawes, D. Xie, and H. Guo. High-Level, First-Principles, Full-Dimensional Quantum Calculation of the Ro-vibrational Spectrum of the Simplest Criegee Intermediate (CH 2 OO). *The Journal of Physical Chemistry Letters*, **5**: 2364 – 2369, 2014. DOI: `10.1021/jz501059m` (see pp. 79, 104, 109, 110, 122)

[170] J. M. Anglada, J. González, and M. Torrent-Sucarrat. Effects of the substituents on the reactivity of carbonyl oxides. A theoretical study on the reaction of substituted carbonyl oxides with water. *Physical Chemistry Chemical Physics*, **13**: 13034 – 13045, 2011. DOI: `10.1039/C1CP20872A` (see p. 80)

[171] A. Tajti, P. G. Szalay, A. G. Császár, M. Kállay, J. Gauss, E. F. Valeev, B. A. Flowers, J. Vázquez, and J. F. Stanton. HEAT: High accuracy extrapolated ab initio thermochemistry. *The Journal of Chemical Physics*, **121**: 11599 – 11613, 2004. DOI: `10.1063/1.1811608` (see p. 80)

[172] A. Karton, E. Rabinovich, J. M. L. Martin, and B. Ruscic. W4 theory for computational thermochemistry: In pursuit of confident sub-kJ/mol predictions. *The Journal of Chemical Physics*, **125**: 144108, 144108, 2006. DOI: `10.1063/1.2348881` (see pp. 80, 89, 99, 132, 133)

[173] A. Karton, S. Daon, and J. M. Martin. W4-11: A high-confidence benchmark dataset for computational thermochemistry derived from first-principles W4 data. *Chemical Physics Letters*, **510**: 165 – 178, 2011. DOI: `10.1016/j.cplett.2011.05.007` (see pp. 80, 89, 99, 132, 133)

[174] Y. J. Bomble, J. Vázquez, M. Kállay, C. Michauk, P. G. Szalay, A. G. Császár, J. Gauss, and J. F. Stanton. High-accuracy extrapolated ab initio thermochemistry. II. Minor improvements to the protocol and a vital simplification. *The Journal of Chemical Physics*, **125**: 064108, 064108, 2006. DOI: `10.1063/1.2206789` (see pp. 80, 117)

[175] M. E. Harding, J. Vázquez, B. Ruscic, A. K. Wilson, J. Gauss, and J. F. Stanton. High-accuracy extrapolated ab initio thermochemistry. III. Additional improvements and overview. *The Journal of Chemical Physics*, **128**: 114111, 114111, 2008. doi: `10.1063/1.2835612` (see p. 80)

[176] A. D. Boese, M. Oren, O. Atasoylu, J. M. L. Martin, M. Kállay, and J. Gauss. W3 theory: Robust computational thermochemistry in the kJ/mol accuracy range. *The Journal of Chemical Physics*, **120**: 4129 – 4141, 2004. doi: `10.1063/1.1638736` (see p. 80)

[177] T. H. Dunning. Gaussian basis sets for use in correlated molecular calculations. I. The atoms boron through neon and hydrogen. *The Journal of Chemical Physics*, **90**: 1007 – 1023, 1989. doi: `10.1063/1.456153` (see p. 81)

[178] R. A. Kendall, T. H. Dunning, and R. J. Harrison. Electron affinities of the first-row atoms revisited. Systematic basis sets and wave functions. *The Journal of Chemical Physics*, **96**: 6796 – 6806, 1992. doi: `10.1063/1.462569` (see p. 81)

[179] T. H. Dunning, K. A. Peterson, and A. K. Wilson. Gaussian basis sets for use in correlated molecular calculations. X. The atoms aluminum through argon revisited. *The Journal of Chemical Physics*, **114**: 9244 – 9253, 2001. doi: `10.1063/1.1367373` (see p. 81)

[180] D. E. Woon and T. H. Dunning. Gaussian basis sets for use in correlated molecular calculations. V. Core-valence basis sets for boron through neon. *The Journal of Chemical Physics*, **103**: 4572 – 4585, 1995. doi: `10.1063/1.470645` (see p. 81)

[181] K. A. Peterson and T. H. Dunning. Accurate correlation consistent basis sets for molecular core–valence correlation effects: The second row atoms Al–Ar, and the first row atoms B–Ne revisited. *The Journal of Chemical Physics*, **117**: 10548 – 10560, 2002. doi: `10.1063/1.1520138` (see p. 81)

[182] S. Yockel and A. K. Wilson. Core-valence correlation consistent basis sets for second-row atoms (Al–Ar) revisited. *Theoretical Chemistry Accounts*, **120**: 119 – 131, 2007. doi: `10.1007/s00214-007-0309-3` (see p. 81)

[183] J. Almlöf and P. R. Taylor. General contraction of Gaussian basis sets. I. Atomic natural orbitals for first- and second-row atoms. *The Journal of Chemical Physics*, **86**: 4070 – 4077, 1987. doi: `10.1063/1.451917` (see p. 81)

[184] W. A. de Jong, R. J. Harrison, and D. A. Dixon. Parallel Douglas–Kroll energy and gradients in NWChem: Estimating scalar relativistic effects using Douglas–Kroll contracted basis sets. *The Journal of Chemical Physics*, **114**: 48 – 53, 2001. doi: `10.1063/1.1329891` (see p. 81)

[185] S. Ten-no. Initiation of explicitly correlated Slater-type geminal theory. *Chemical Physics Letters*, **398**: 56 – 61, 2004. doi: `10.1016/j.cplett.2004.09.041` (see p. 82)

[186] G. Knizia and H.-J. Werner. Explicitly correlated RMP2 for high-spin open-shell reference states. *The Journal of Chemical Physics*, **128**: 154103, 154103, 2008. doi: `10.1063/1.2889388` (see p. 82)

[187] T. B. Adler, G. Knizia, and H.-J. Werner. A simple and efficient CCSD(T)-F12 approximation. *The Journal of Chemical Physics*, **127**: 221106, 221106, 2007. doi: `10.1063/1.2817618` (see p. 82)

[188] H.-J. Werner, G. Knizia, and F. R. Manby. Explicitly correlated coupled cluster methods with pair-specific geminals. *Molecular Physics*, **109**: 407 – 417, 2011. doi: `10.1080/00268976.2010.526641` (see p. 82)

[189] G. Knizia, T. B. Adler, and H.-J. Werner. Simplified CCSD(T)-F12 methods: Theory and benchmarks. *The Journal of Chemical Physics*, **130**: 054104, 054104, 2009. doi: `10.1063/1.3054300` (see p. 82)

[190] M. Douglas and N. M. Kroll. Quantum electrodynamical corrections to the fine structure of helium. *Annals of Physics*, **82**: 89 – 155, 1974. doi: `10.1016/0003-4916(74)90333-9` (see p. 83)

[191] B. A. Hess. Relativistic electronic-structure calculations employing a two-component no-pair formalism with external-field projection operators. *Phys. Rev. A*, **33**: 3742 – 3748, 1986. doi: `10.1103/PhysRevA.33.3742` (see p. 83)

[192] M. K. Kesharwani, B. Brauer, and J. M. L. Martin. Frequency and Zero-Point Vibrational Energy Scale Factors for Double-Hybrid Density Functionals (and Other Selected Methods): Can Anharmonic Force Fields Be Avoided? *The Journal of Physical Chemistry A*, PMID: 25296165, 141021073335006, 2014. doi: `10.1021/jp508422u` (see pp. 83, 98, 120)

[193] B. Ruscic, R. E. Pinzon, M. L. Morton, G. von Laszevski, S. J. Bittner, S. G. Nijsure, K. A. Amin, M. Minkoff, and A. F. Wagner. Introduction to Active Thermochemical Tables: Several “Key” Enthalpies of Formation Revisited. *The Journal of Physical Chemistry A*, **108**: 9979 – 9997, 2004. doi: `10.1021/jp047912y` (see p. 84)

[194] W. R. Stevens, B. Ruscic, and T. Baer. Heats of Formation of $C_6H_5\cdot$, C_6H_5+, and C_6H_5NO by Threshold Photoelectron Photoion Coincidence and Active Thermochemical Tables Analysis. *The Journal of Physical Chemistry A*, **114**: 13134 – 13145, 2010. doi: `10.1021/jp107561s` (see p. 84)

[195] B. Ruscic, R. E. Pinzon, M. L. Morton, N. K. Srinivasan, M.-C. Su, J. W. Sutherland, and J. V. Michael. Active Thermochemical Tables: Accurate Enthalpy of Formation of Hydroperoxyl Radical, HO_2. *The Journal of Physical Chemistry A*, **110**: 6592 – 6601, 2006. doi: `10.1021/jp056311j` (see p. 84)

[196] J. D. Cox, D. D. Wagman, and V. A. Medvedev *CODATA Key Values for Thermodynamics* see http://www.codata.org New York, 1989 (see p. 84)

[197] P. J. Stephens, F. J. Devlin, C. F. Chabalowski, and M. J. Frisch. Ab Initio Calculation of Vibrational Absorption and Circular Dichroism Spectra Using Density Functional Force Fields. *The Journal of Physical Chemistry*, **98**: 11623 – 11627, 1994. doi: `10.1021/j100096a001` (see pp. 84, 100)

[198] CFOUR, a quantum chemical program package written by J.F. Stanton, J. Gauss, M.E. Harding, P.G. Szalay with contributions from A.A. Auer, R.J. Bartlett, U. Benedikt, C. Berger, D.E. Bernholdt, Y.J. Bomble, O. Christiansen, M. Heckert, O. Heun, C. Huber, T.-C. Jagau, D. Jonsson, J. Jusélius, K. Klein, W.J. Lauderdale, D.A. Matthews, T. Metzroth, D.P. O'Neill, D.R. Price, E. Prochnow, K. Ruud, F. Schiffmann, S. Stopkowicz, A. Tajti, J. Vázquez, F. Wang, J.D. Watts and the integral packages MOLECULE (J. Almlöf and P.R. Taylor), PROPS (P.R. Taylor), ABACUS (T. Helgaker, H.J. Aa. Jensen, P. Jørgensen, and J. Olsen), and ECP routines by A. V. Mitin and C. van Wüllen. For the current version, see http://www.cfour.de (see pp. 84, 106, 118)

[199] J. D. Watts, J. Gauss, and R. J. Bartlett. Coupled-cluster methods with noniterative triple excitations for restricted open-shell Hartree–Fock and other general single determinant reference functions. Energies and analytical gradients. *The Journal of Chemical Physics*, **98**: 8718 – 8733, 1993. doi: `10.1063/1.464480` (see p. 84)

[200] H.-J. Werner, P. J. Knowles, G. Knizia, F. R. Manby, M. Schütz, et al. Molpro*, version 2012.1, a package of ab initio programs* Cardiff, UK, 2012 (see p. 85)

[201] M. Kállay, Z. Rolik, J. Csontos, I. Ladjánszki, L. Szegedy, B. Ladóczki, and G. Samu Mrcc*, a quantum chemical program suite* Version: July 10, 2014 Budapest, HU (see p. 85)

[202] M. J. Frisch, G. W. Trucks, H. B. Schlegel, G. E. Scuseria, M. A. Robb, J. R. Cheeseman, G. Scalmani, V. Barone, B. Mennucci, G. A. Petersson, H. Nakatsuji, M. Caricato, X. Li, H. P. Hratchian, A. F. Izmaylov, J. Bloino, G. Zheng, J. L. Sonnenberg, M. Hada, M. Ehara, K. Toyota, R. Fukuda, J. Hasegawa, M. Ishida, T. Nakajima, Y. Honda, O. Kitao, H. Nakai, T. Vreven, J. A. Montgomery Jr., J. E. Peralta, F. Ogliaro, M. Bearpark, J. J. Heyd, E. Brothers, K. N. Kudin, V. N. Staroverov, R. Kobayashi, J. Normand, K. Raghavachari, A. Rendell, J. C. Burant, S. S. Iyengar, J. Tomasi, M. Cossi, N. Rega,

J. M. Millam, M. Klene, J. E. Knox, J. B. Cross, V. Bakken, C. Adamo, J. Jaramillo, R. Gomperts, R. E. Stratmann, O. Yazyev, A. J. Austin, R. Cammi, C. Pomelli, J. W. Ochterski, R. L. Martin, K. Morokuma, V. G. Zakrzewski, G. A. Voth, P. Salvador, J. J. Dannenberg, S. Dapprich, A. D. Daniels, Ö. Farkas, J. B. Foresman, J. V. Ortiz, J. Cioslowski, and D. J. Fox *Gaussian 09 Revision A.1* Gaussian Inc. Wallingford CT 2009 (see p. 85)

[203] Neese, F. ORCA—an ab initio, Density Functional and Semiempirical program package, Version 3.0.2 Max–Planck-Insitut für Bioanorganische Chemie, Mülheim and der Ruhr, 2014. (See p. 85)

[204] V. Mozhayskiy and A. Krylov *ezSpectrum* 2012 (see pp. 85, 102)

[205] E. D. G. J, K. Badenhoop, A. E. Reed, J. E. Carpenter, J. A. Bohmann, C. M. Morales, C. R. Landis, and F. Weinhold *NBO 6.0.* Theoretical Chemistry Institute, University of Wisconsin, Madison (2013) (see p. 87)

[206] T. J. Lee and P. R. Taylor. A diagnostic for determining the quality of single-reference electron correlation methods. *International Journal of Quantum Chemistry*, **36**: 199 – 207, 1989. doi: `10.1002/qua.560360824` (see pp. 89, 99)

[207] T. J. Lee, J. E. Rice, G. E. Scuseria, and H. F. Schaefer III. Theoretical investigations of molecules composed only of fluorine, oxygen and nitrogen: determination of the equilibrium structures of FOOF, $(NO)_2$ and FNNF and the transition state structure for FNNF cis-trans isomerization. *Theoretica chimica acta*, **75**: 81 – 98, 1989. doi: `10.1007/BF00527711` (see pp. 89, 99)

[208] M. L. Leininger, I. M. Nielsen, T. Crawford, and C. L. Janssen. A new diagnostic for open-shell coupled-cluster theory. *Chemical Physics Letters*, **328**: 431 – 436, 2000. doi: `10.1016/S0009-2614(00)00966-0` (see pp. 89, 99)

[209] T. J. Lee. Comparison of the T1 and D1 diagnostics for electronic structure theory: a new definition for the open-shell D1 diagnostic. *Chemical Physics Letters*, **372**: 362 – 367, 2003. doi: `10.1016/S0009-2614(03)00435-4` (see pp. 89, 99)

[210] W. Jiang, N. J. DeYonker, and A. K. Wilson. Multireference Character for 3d Transition-Metal-Containing Molecules. *Journal of Chemical Theory and Computation*, **8**: 460 – 468, 2012. doi: `10.1021/ct2006852` (see p. 89)

[211] M. K. Sprague and K. K. Irikura. Quantitative estimation of uncertainties from wavefunction diagnostics. *Theoretical Chemistry Accounts*, **133**: 1544, 1544(1) – 1544(12), 2014. doi: `10.1007/s00214-014-1544-z` (see p. 89)

[212] A. Joiner, R. H. Mohr, and J. N. Yukich. High-resolution photodetachment spectroscopy from the lowest threshold of O^-. *Physical Review A*, **83**: 035401, 2011. doi: `10.1103/PhysRevA.83.035401` (see p. 92)

[213] M. Kettner, A. Karton, A. McKinley, and D. Wild. The CH_3CHOO "Criegee intermediate" and its anion: Isomers, infrared spectra, and W3-F12 energetics. *Chemical Physics Letters*, **621**: 193 – 198, 2015. doi: `10.1016/j.cplett.2014.12.037` (see pp. 94, 117)

[214] T. H. Dunning. A Road Map for the Calculation of Molecular Binding Energies. *The Journal of Physical Chemistry A*, **104**: 9062 – 9080, 2000. doi: `10.1021/jp001507z` (see p. 104)

[215] E. Papajak and D. G. Truhlar. Convergent Partially Augmented Basis Sets for Post-Hartree−Fock Calculations of Molecular Properties and Reaction Barrier Heights. *Journal of Chemical Theory and Computation*, **7**: 10 – 18, 2011. doi: `10.1021/ct1005533` (see p. 104)

[216] J. Vázquez and J. F. Stanton. Treatment of Fermi resonance effects on transition moments in vibrational perturbation theory. *Molecular Physics*, **105**: 101 – 109, 2007. doi: `10.1080/00268970601135784` (see pp. 105, 107, 112)

[217] L. McCaslin and J. Stanton. Calculation of fundamental frequencies for small polyatomic molecules: a comparison between correlation consistent and atomic natural orbital basis sets. *Molecular Physics*, **111**: 1492 – 1496, 2013. doi: `10.1080/00268976.2013.811303` (see pp. 105, 112)

[218] G. Herzberg. *Molecular spectra and molecular structure. Vol.2: Infrared and Raman spectra of polyatomic molecules*. Molecular Spectra and Molecular Structure Van Nostrand, 1945. (see p. 107)

[219] K. Mackeprang and H. G. Kjærgaard personal communication Feb. 17, 2015 (see pp. 114, 116)

[220] K. Mackeprang, H. G. Kjærgaard, T. Salmi, V. Hänninen, and L. Halonen. The effect of large amplitude motions on the transition frequency redshift in hydrogen bonded complexes: A physical picture. *The Journal of Chemical Physics*, **140**: 184309, 2014. doi: `10.1063/1.4873420` (see p. 115)

[221] T. Salmi, V. Hänninen, A. L. Garden, H. G. Kjærgaard, J. Tennyson, and L. Halonen. Calculation of the O–H Stretching Vibrational Overtone Spectrum of the Water Dimer. *The Journal of Physical Chemistry A*, **112**: PMID: 18572900, 6305 – 6312, 2008. doi: `10.1021/jp800754y` (see p. 116)